The University Of Sheffield.

In vitro photodynamic therapy screening with carbon dot-protoporphyrin IX conjugates

Thesis submitted in partial fulfilment of the requirements for the degree of

Doctor of Philosophy

Jose Ricardo Aguilar Cosme

Department of Materials Science and Engineering

February 2020

Acknowledgements

I would like to acknowledge my primary supervisor, Dr. Frederik Claeyssens. Thank you for allowing me to act so independently while working on the project I put forward, which certainly changed quite a bit during these years. Your guidance has helped me understand what it means to be a researcher. I would also like to thank Dr. Helen Bryant for her continuous help with all things related to experimental design and PDT. Your insightful suggestions helped make this work what it is, and I am very grateful. Finally, I would like to thank Dr. Nicola Green for her help with learning how to use the microscopes: you helped me discover something new which I really enjoyed and was extremely useful for my work.

I would also like to acknowledge CONACyT and the Mexican Federal Government for funding throughout these years. Likewise, the University of Sheffield and INSIGNEO generously provided a great deal of financial support which enabled collaborations and sponsored summer student projects – thanks Chad, Qian Ni, Leonid, Hannah and Ewan for your hard work.

Thank you to all who helped and accompanied me throughout these years in the Biomaterials Lab in Kroto, PGSoc, Biomedical Science, and Hadfield. You've made my PhD journey significantly more enjoyable and made me feel at home.

En especial, dedico esta tesis a mis personas más queridas.

A mi familia: gracias por siempre creer en mí. Ustedes me mostraron que podría lograr cualquier cosa que me propusiera. Mi sueño de ser científico y conocer el mundo se han vuelto realidad gracias a su apoyo.

> Papá, gracias por siempre escucharme y apoyarme. Tu eres mi modelo a seguir.
> Mamá, gracias por tus consejos y ayuda. Tu cariño y amor me han cambiado la vida.
> Dany, gracias por las pláticas divertidas y memes de gatos. ¡Tonki forever!
> Carlos (Karl), gracias por siempre levantarme el ánimo. ¡Espero verte en los Oscars!
> Sin ustedes, yo no estaría aquí. ¡Gracias!

Y sobre todo a quien me ha acompañado a través de todo mi doctorado: ¡a mi hermosa novia Iris!

> Piñita hermosa, tú me has mostrado que es el verdadero amor. Esta tesis es dedicada singularmente para ti. Gracias por tu apoyo en todo, sin ti no podría haber hecho este trabajo. ¡Juntos llegaremos a las estrellas y el doctorado es solo el primer paso!
> Hoy y siempre tuyo, tu Mangurazno.

Statement of originality

I hereby state that all work presented in this thesis is entirely my own.

Abstract

Cancer is a leading cause of death, being responsible for over 9.6 million deaths worldwide in 2018. Photodynamic therapy (PDT) is an alternative cancer treatment with FDA approval. It is based on the use of photosensitisers (PS) such as protoporphyrin IX (PpIX), which are activated through light and produce singlet oxygen when irradiated, leading to tumour ablation. Highly controlled light dosimetry and rapid drug uptake maximizes the PDT effect while protecting surrounding tissue from damage. However, it is limited by inefficient drug accumulation in target tissue, light scattering, variable oxygen gradients, and high toxicity. Carbon dots (CDs) are carbon-based fluorescent nanoparticles that have gained attention due to their interesting photophysical properties, low toxicity, tuneable surface functionality and adaptable synthesis making them ideal candidates for drug delivery, bioimaging, and theragnostics applications. CDs have been previously used for PDT as PS carriers and have shown great success in improving treatment efficiency. However, to date, no comparison between conjugates with different drug loading strategies has been made to determine the best-performing methodology. This research aimed to produce PpIX-loaded conjugates capable of an enhanced PDT effect. Conjugates should be water-dispersible and produce singlet oxygen, demonstrating enhanced photoluminescence, fast intracellular uptake, low dark toxicity, and high light toxicity. In this work, carbon dot (CD) and protoporphyrin IX (PpIX) conjugates were fabricated using microwave-assisted pyrolysis. PpIX loading was carried out using the one-pot reaction method of host-guest encapsulation (PpIX@CD) and previously established amide crosslinking (soluble fraction PpIX-CD and insoluble fraction (PpIX-CD)p). Characterization showed conjugates have a loading efficiency of 34–48%, with similar singlet oxygen production and surface chemistry to PpIX. PpIX-containing CDs showed a 2.2 to 3.7-fold decrease in dark toxicity. PpIX-CD and PpIX@CD showed equivalent light-induced toxicity to PpIX in C8161 human melanoma cell monolayers at concentrations >1 μg/ml, leading to a 3.2 to 4.1-fold

increase in photo-toxicity index (PI). The less soluble fraction of cross-linked conjugates (PpIX-CD)p did not show significant difference from PpIX. Confocal light scanning microscopy demonstrated rapid intracellular uptake and accumulation of conjugates. *In vitro* PDT evaluation of conjugates was continued using multicellular cancer spheroids (MCTS). Spheroids showed increased resistance to conjugate toxicity and PDT effect. Light doses were adjusted to 2.5 – 10 J/cm^2, which caused significant cell death without photobleaching the samples. Parameter screening confirmed light doses >5 J/cm^2 and concentrations >5 μg/mL were the most effective, greatly decreasing in cell viability and total dsDNA content. Light fractionation, also known as sequential light exposure, was shown to greatly increase cell membrane damage and slightly lower dsDNA content in comparison to single light treatments. Light sheet fluorescence microscopy (LSFM) was used to observe PDT-induced morphological changes to spheroids, showing ablation and significant damage throughout their structures. Finally, computer-assisted analysis (AnaSP) was used to extract morphometric data from spheroid images taken with widefield microscopy. Morphological parameters were then used to reduce variability between spheroids by monitoring sphericity and area during their growth. Spheroids subjected to various PDT combinations showed parameters like convexity, solidity, and sphericity had low usefulness for differentiating sample viability. Conversely, area and volume showed better results, being able to predict spheroid PDT response in various conditions. In summary, this work showed the importance of selecting loading strategies for drug delivery applications. CDs were shown to be highly useful and effective carriers for PpIX, demonstrating an enhanced PDT effect through advantageous intracellular localization and decreased cytotoxicity. Furthermore, the use of cancer spheroids and morphometric parameter acquisition demonstrated how multiple treatment parameters can be simultaneously screened to determine optimum ranges for further experiments.

Publications

Aguilar Cosme, JR., Bryant, HE., and Claeyssens, F. **Carbon dot-protoporphyrin IX conjugates for improved drug delivery and bioimaging.** PLoS ONE 14,7 (2019)

Liu, G., Zhao, P., Liu, N., Yoshino, F., Qin, H., Zou, Y., Shi, S., Amano, T., Aguilar Cosme, JR., Nagano, Y., Tamiaki, H., and Komatsu, N. **Photosensitizer and anticancer drug-loaded 2D nanosheet: Preparation, stability and anticancer property.** 2D Materials 6,4 (2019)

List of abbreviations

1-ethyl-3-(3-dimethylaminopropyl) carbodiimide (EDC)

1-hydroxybenzotriazole (HOBt)

1,2-Distearoyl-sn-glycero-3-phosphoethanolamine-poly(ethylene glycol) (DSPE-PEG)

2-((E)-2-((E)-2-chloro-3-((E)-2-(1-(2-hydroxyethyl)-3,3-dimethylindolin-2-ylidene) ethylidene)cyclohex-1-en-1-yl)vinyl)-1-(2-hydroxyethyl)-3,3-dimethyl-3H-indol-1-ium iodide (CyOH)

4-morpholinoethanesulfonic acid (MES)

4′,6-diamidino-2-phenylindole (DAPI)

5-aminolevulenic acid (5-ALA)

Adsorption, distribution, metabolism, and excretion (ADME)

Amide crosslinked CDs (low solubility) ((PpIX-CD)p)

Amide crosslinked CDs (PpIX-CD)

amine functionalized silica nanoparticles (ASNPs)

ANAlyse SPheroids (AnaSP)

Antimicrobial photodynamic therapy (A-PDT)

Antimicrobial photothermal therapy (A-PTT)

Arbitrary unit (A.U.)

Arginyl-Glycyl-Aspartic acid (RGD)

Aspirin-coated CDs (FACDs)

Atom transfer radical polymerization (ATRP)

B-cell lymphoma 2 (Bcl-2)

Biotin-decorated CD (B-CD)

Blood-brain barrier (BBB)

Body weight (BW)

Carbon dots (CDs)

Carbon nanotubes (CNTs)

Carbon nitride (C_3N_4)

CD-based nanosphere (CDNS)

Chick chorioallantoic membrane (CAM)

Chlorin e6 (Ce6)

Cisplatin (IV) (PtIV)

Citric acid (CA)

Citric acid-based CDs (CA-EDA)

Cancer stem-like cell (CSC)

Cancer tissue-originated organoids (CTOS)

Computed tomography (CT)

Computed tomography (CT)

Confocal laser scanning microscopy (CLSM)

Copper (Cu^{II})

Cresyl violet (CV)

Degrees Celsius (°C)

Dicyclohexylcarbodiimide (DCC)

Differential interference contrast (DIC)

Diketopyrrolopyrrole (DPP)

Dimethylmaleic acid (DMMA)

Doxorubicin (DOX)

dsDNA (dual-stranded DNA)

Dulbecco's Modified Eagle's Medium (DMEM)

Eicosapentaenoic acid (EPA)

Enhanced permeability and retention (EPR)

Ethylenediamine (EDA)

Excitation wavelength (λ_{ex})

Foetal bovine serum (FBS)

Fibroblast growth factor (FGF)

Fluence (J/cm^2)

Fluorescence resonance energy transfer (FRET)

Fluorine-doped CDs (F-CDs)

Folic acid (FA)

Fourier-transform infrared spectroscopy (FTIR)

Graphene quantum dots (GQDs)

High-throughput screening (HTS)

Hollow CDs (HCDs)

Host-guest embedded CDs (PpIX@CD)

Hours post-fertilisation (hpf)

Human hepatocellular carcinoma cell line (HUH7)

Human melanoma cell line (C8161)

Human osteosarcoma cell line (U2OS)

Human ovarian adenocarcinoma cell line (NCI-ADR-RES)

hyaluronate (HA)

Hydroxylphenyl triphenylporphyrin (TPP)

Hyperbranched poly(amido amine) (HPAP)

Irradiance or power output (W/cm^2)

Joule (J)

Lactate dehydrogenase (LDH)

Lanthanides (Ln)

Lauryl betaine (BS-12)

Length of Major Diameter Through Centroid (LMajorDTC)

Length of Minimum Diameter Through Centroid (LMinDTC)

Lethal concentrations (LC50)

Light microscopy (LM)

Light sheet fluorescence microscopy (LSFM)

Light treatment (LT)

m-phenylenediamine (mPD)

Magnetic iron (III) oxide (Fe_3O_4)

Magnetic resonance imaging (MRI)

Manganese (II) phthalocyanine (Mn-Pc)

Mass spectrometry (MS)

Mesenchymal stem cells (MSCs)

Metal organic frameworks (MOFs)

Methotrexate (MTX)

Methyl-5-aminolevulinate (MAL)

Microgram (μg)

Microlitre (μl)

Micrometre (μm)

Micromolar (μM)

Milligram (mg)

Mitogen-activated protein kinases (MAPK)

Molecular weight cut-off MWCO

Monomethoxypolyethylene glycol (mPEG)

Multicellular tumour spheroids (MCTS)

N-hydroxysuccinimide (NHS)

N-hydroxysulfosuccinimide (sulfo-NHS)

Nanodiamonds (NDs)

Nanoscale MOFs (NMOFs)

Near-infrared (NIR)

Neodymium (Nd^{+3})

Nile blue (NB)

Nitric oxide (NO)

Nitrogen-doped CDs (N-CDs)

Nuclear factor kappa-light-chain-enhancer of activated B cells (NF-κB)

o-phenylenediamine (oPD)

Oxaliplatin (IV) (Oxa(IV))

P-phenylenediamine (pPD)

Phenalenone (PH)

Phosphate buffered saline (PBS)

Photo-toxicity index (PI)

Photodynamic diagnosis (PDD)

Photodynamic therapy (PDT)

Photoluminescence (PL)

Photon upconversion (UC)

Photosensitisers (PS)

Photosensitizer fluorescence detection (PFD)

Photosensitizers (PS)

Photothermal therapy (PTT)

PicoGreen (PG)

Plasmid SOX9 (pSOX9)

Poly(allyamine) (PAH)

Poly(ethylene) glycol (PEG)

Polycyclic aromatic hydrocarbons (PAH)

Polyethylene glycol diacrylate (PEGDA)

Polyethyleneimine (PEI)

Polyethyleneimine average molecular weight 25 kDa (PEI25k)

Positron emission tomography (PET)

Protoporphyrin IX (PpIX)

Prussian blue (PB)

Reactive oxygen species (ROS)

Reconstruction and Visualization from a Single Projection (ReViSP)

Resazurin reduction (RR)

Rotations per minute (rpm)

Scanning electron microscopy (SEM)

Standard error of the mean (SEM)

Short interfering RNA Tumour Necrosis Factor

alpha (si*Tnfα)*

Singlet oxygen ($^1O_2$)

Short interfering RNA (siRNA)

Standard deviation (SD)

Succinic acid (SA)

Sucrose (S)

Sucrose-based CDs (S-EDA)

Sulfosuccinimidyl 4-(N-maleimidomethyl) Cyclohexane-1-carboxylate (sulfo-SMCC)

Surface plasmon resonance (SPR)

Temozolomide (TMZ)

Tetracycline (TC)

Tetraplatinated porphyrin complex (PtPor)

Thermogravimetric analysis (TGA)

Thermogravimetric analysis (TGA)

Three-dimensional (3D)

TNF-related apoptosis-inducing ligand (TRAIL)

Total light exposure (H_e)

Transmission electron microscopy (TEM)

Triphenylphosphonium (TPP)

triplet oxygen ($^3O_2$)

Tumour necrosis factor receptor (TNFR)

Tungsten disulphide (WS_2)

Two-dimensional (2D)

Three-dimensional (3D)

Two-photon (2P)

U.S. Food and Drug Administration (FDA)

Ultraviolet (UV)

Ultraviolet-Visible (UV-Vis)

Tn-doped CDs (UCDs)

Upconverting nanoparticles (UCNPs)

Vascular endothelial growth factor (VEGF)

Watt (W)

Weight/weight ratio (w/w)

X-ray photoelectron spectroscopy (XPS)

X-ray photoelectron spectroscopy (XPS)

Ytterbium (Yb^{+3})

Zeolitic imidazolate frameworks (ZIFs)

Zinc phthalocyanine (ZnPc)

β-cyclodextrin (b-TC)

List of figures

Chapter 1

From left to right, images were taken with differential interference contrast (DIC), fluorescence (λex = 405 nm) and a merged image.

1.14 Zebrafish embryos incubated with 2.5 mg/ml CDs show uptake at 3 hours post-fertilisation (hpf) (A). Fluorescence gradually decreases at various timepoints, being observable until 60 hpf (F).

1.15 *Ex ovo* CAM assay can also be achieved by cracking fertilised eggs and placing the embryos in plastic containers. The appearance of the membrane can be seen on embryonic development day (EDD) 5 and is shown with black arrows on days 7 and 8. CAM assay has a maximum of 17 days for development before termination.

1.16 Multicellular tumour spheroids can replicate some in vivo cancer parameters such as hypoxia, diffusion, and ECM formation. Cell phenotype, protein expression, and drug response are more like in vivo tumours.

1.17 Cancer stem cell (CSC)-derived organoids. Organoids can be obtained from cancerous tissue after excising samples, digesting them to form single-cell suspensions, and suspending cells in an appropriate medium. Cancer tissue-originated spheroids (CTOS) are prepared through incomplete cell dissociation. Clusters of cells are suspended and rapidly form CTOS. It is currently unclear how interchangeable CTOS and CSC organoid results are between each other.

1.18 Discovery and development of new drugs is a multistep process with huge experimental and regulatory hurdles. Many drugs show positive results prior to clinical trials but fail due to unexpected side effects before Phase III.

1.19 Ciproflaxin-loaded CDs showed controlled release over a period of 24 hrs. S. cerevisiae showed quick uptake and no toxicity from Ciproflaxin release.

1.20 CDs were shown to be capable of substantial photothermal conversion, increasing temperature over 30° in a 1-minute timescale. Heat generation was used to destroy E. coli in exponential and stationary phases.

1.21 CDs crosslinked with heparin were shown to efficiently bind doxorubicin and were capable of controlled intracellular release triggered by low pH in tumour microenvironment.

1.22 CD charge can be influenced through passivation to introduce additional amine groups. Nitrogen-containing compounds can also be used as carbon sources for CD formation.

1.23 FA-mediated uptake and targeting has been shown to be effective in treatments against cancer. DOX release is significantly improved after carrier internalization.

1.24 Phosphorus and nitrogen-doped hollow carbon dots entered cells through endocytosis and showed efficient doxorubicin release near nuclei.

1.25 CDs@ZIF-8 show similar photoluminescence and surface chemistry, indicating complexation. TEM images show ZIF morphology is not affected by CD/DOX loading.

1.26 Schematic showing immune response to PDT. Irradiation causes PS excitation and producing ROS such as singlet oxygen (1O2). Continuous 1O2 production leads to cell damage and eventual death, inciting an immune response in the affected area.

1.27 Schematic representation of EDC/NHS crosslinking. Compound 1, containing carboxylic acid, is prepared for binding as an amine-reactive ester is formed. The intermediate o-acylisourea is protected from hydrolysis by NHS/Sulfo-NHS. Conjugation with a stable primary amine group leads to the formation of an amide bond.

1.28 Host-guest encapsulation of Nile Blue (NB) and Zinc phthalocyanine (ZnPc) within CDs changes optical properties, enhancing emissions in red and NIR regions.

1.29 Ce6 was conjugated with CDs and covered with hyaluronic acid to improve dispersibility in water and improve tissue penetration. NIR excitation enabled transdermal PS activation.

1.30 Schematic representation of CD and NO photodonor linking. Nitric oxide can be produced in environments with low partial oxygen pressure.

1.31 Alternate strategies for PDT in hypoxic environments can make use of other nanomaterials, such as carbon nitride. Water-splitting produced sufficient oxygen in hypoxic regions for effective PDT with PpIX.

1.32 Photoactivation with an 808 nm NIR laser of copper-doped CDs can produce a simultaneous PDT and PTT effect.

1.33 Gene delivery typically makes use of a vector or carrier to aid cellular uptake while avoiding degradation.

1.34 Fluorescence imaging was used to monitor real-time siRNA uptake in human mesenchymal stem cells. While fluorescein-labelled siRNA was used, this system could be utilised with only CD-SMCC fluorescence.

1.35 ATRP was used to graft zwitterionic polymers onto CDs, functioning as multicolour imaging probes with high DNA condensation efficiency. Outer layers protected DNA from degradation and nonspecific interactions. Transfection efficiency was improved 13 to 28-fold in comparison to lipofectamine 2000.

1.36 siRNA-loaded CDs showed fast complexation, retention, and effective gene silencing

in mosquito larvae compared to chitosan and silica-complexed siRNA.

1.37 Fluorine-doped CDs showed improved gene delivery efficiency compared to undoped CDs (UCDs) and the gold standard lipofectamine 2000.

1.38 CD photoluminescence is excitation-dependent and increased with PEG1500N passivation. Multicolour PL can be observed after excitation at various wavelengths using a ban-pass filter. Adapted from

1.39 N-O doped CDs show strong NIR absorption due to the presence of pyrrolic and graphitic residues on surface edges. IR imaging and PPT were shown to be effective using an 808 nm laser at the absorption maxima.

1.40 CDs are versatile and can be doped with complexed iron ions before synthesis. In vitro and in vivo imaging can be done due to their excellent water dispersibility and biocompatibility.

Chapter 2

2.1 Schematic detailing PDT mechanism. Reactive oxygen species produced by photosensitizers lead to cell death and eventual tumour ablation.

2.2 Porphyrins and phthalocyanines are well-known PS families. The abundance of pyrrole groups and facile modification has led to many the formation of numerous derivatives and conjugates.

2.3 **CD synthesis is highly versatile**. Fabrication of samples can be top-down: produced from a pre-existing structure such as carbon allotropes, or bottom-up: based on the pyrolysis of organic compounds.

2.4 **CD conjugates were synthesised with two distinct loading strategies.** Host-guest encapsulated (PPIX@CD) samples were produced in a one-pot reaction. CA-EDA CDs were used to produce amide bond-linked (PPIX-CD and (PpIX-CD)p) conjugates. S-EDA CDs were embedded with PpIX in a one-pot encapsulation step.

2.5 **Samples produced through domestic microwave synthesis.** CD samples obtained by domestic microwave-assisted pyrolysis of sucrose and PEG-400. The colour change can be observed from the precursor solution (left) to CD solutions. Char formation after carbonization can be seen at the bottom of the beaker (right).

2.6 **Microwave reactor synthesis setup.** Precursor solution is placed within vessel with metal-reinforced cap (left). The solution is pyrolysed with the Discover SP microwave

reactor setup (middle) and recovered after cooling (right).

2.7 **PpIX@CD samples change according to wt%.** Lower percentages such as 0.5 and 1% (a) showing decreased aggregate formation compared to 2% (b).

2.8 **Freeze-dried PpIX@CD conjugates**. A noticeable colour change can be seen as PpIX wt% increases.

2.9 **Crosslinked conjugates are separated by centrifugation**. The solution gradually separated into two fractions: PpIX-CD and (PpIX-CD)p.

2.10 **Schematic detailing newly synthesized PpIX-loaded conjugates.**

2.11 **Dialysis was repeated to remove contaminants**. The process was repeated until no colour change could be observed.

2.12 **Dialysis significantly changes end product quality.** The repetition of this process successfully removed most contaminants from the suspension and prevented sample rehydration after freeze-drying.

2.13 **Sequential rounds of freeze-drying ensured complete removal of residual water**. CDs were recovered and stored to prevent rehydration due to ambient moisture.

2.14 **PpIX conjugates show variable dispersibility in water.** After initial addition to solution, PpIX@CD and (PpIX-CD)p remained suspended and remained as such until mixed. PpIX-CD readily formed a slightly reddish suspension without observable precipitation.

2.15 **Comparison of emission at 300 and 400 nm excitation with various molecules used for passivation.** EDA-coated CDs demonstrated significantly higher photoluminescence at both 300 and 400 nm excitation compared to PEG and PEI.

2.16 **Fluorescence spectra of synthesized CD samples from various carbon sources using excitation wavelengths ranging from 300-500 nm**. PEG-coated samples showed drastically reduced photoluminescence in comparison to amine-rich PEI and EDA.

2.17 Fluorescence spectra of conjugates separated by CD subtype.

2.18 **Drug loading in conjugates was calculated using a PpIX calibration curve.** The curve was based on PpIX fluorescence at the absorbance maximum (λ_{max} = 405 nm). Conjugates were diluted and compared to estimate PpIX content.

2.19 **Fluorescence spectra of PpIX host-guest encapsulated conjugates.** All samples show fluorescence corresponding to the characteristic emission bands. PpIX loading efficiency was calculated as previously detailed.

2.20 Absorbance spectra of PpIX, PpIX-CD, (PpIX-CD)p and PpIX@CD in water.

2.21 **FT-IR spectra comparing surface chemistry of CA-EDA samples**. The characteristic amine band (N-H) does not appear in PpIX-CD, indicating complete crosslinking using EDC/NHS.

2.22 **FT-IR spectra comparing surface chemistry of S-EDA sample PpIX@CD**. Amine groups are available as PpIX was noncovalently bound through host-guest chemistry.

2.23 **Full FT-IR spectra of CA-EDA and S-EDA conjugates**.

2.24 **FT-IR spectra comparing surface chemistry of PpIX host-guest encapsulated samples**.

2.25 **CDs form small aggregates in water suspension.** TEM images of CDs at 690× (a) and 68,000× (b). CDs form small aggregates (<200 nm) at higher concentration (a). Individual particles can be seen after diluting stock solutions and sonicating samples (b).

2.26 **CD-PS conjugates show decreased aggregation in water.** TEM images of conjugates at 30,000× (A) and 68,000× (B). Conjugates show irregular morphology and less aggregation in comparison to PpIX (30,000× and 18,500×).

2.27 **PpIX-loaded CDs can form aggregates depending on synthesis conditions.** PpIX@CD formed some separate porous nanoparticles, seen at 49,000× (right). PpIX-CD aggregates caused by dimerization could be seen at 49,000× (right).

2.28 **PpIX@CD self-assembles at higher concentrations.** TEM images of PpIX@CD show tendril-like structures forming from aggregates, with individual particles becoming clearer at higher magnifications.

2.29 **(PpIX-CD)p rapidly forms large aggregates in water.** TEM image at 18,500X, individual particles can be observed around the edges of the aggregate.

2.30 **Singlet oxygen yield of conjugates in DMF.** Corrected initial amplitude of lifetime generated singlet oxygen against the power of a 355 nm Nd:YAG laser to calculate singlet oxygen yield of each sample. Phenalenone was used as a control for 95% production.

2.31 **Drug loading increases CD thermal stability.** TGA demonstrates CDs decompose at lower temperatures compared to PpIX and its conjugates.

2.32 **TGA of CDs and drug loaded conjugates.** Conjugates show slight variation from PpIX. PpIX@CD showed increased weight loss around 200 °C.

Chapter 3

3.1 **Schematic detailing conjugates used for *in vitro* PDT**. PpIX-CD and (PpIX-CD)p were fabricated through amide crosslinking. The latter corresponds to the insoluble (precipitate) fraction separated from PpIX-CD after centrifugation. PpIX@CD was obtained using a one-pot reaction.

3.2 **CDs and PpIX have significantly different effects on metabolic activity due to dark toxicity.** PpIX shows a sharp drop in viability after 10 μg/ml (a). In comparison, CD cytocompatibility can be clearly seen, with cells maintaining high metabolic activity (>80%) at ultrahigh concentrations of 100 μg/ml (b). All samples were compared to the negative control to determine differences at each concentration. (N=3, n=3)

3.3 **Conjugates show significantly improved biocompatibility in comparison to PpIX.** The improvement was observed regardless of crosslinking strategy. PpIX@CD was slightly more toxic than PpIX-CD or (PpIX-CD)p at lower concentrations (<5 μg/ml). Each conjugate was compared to the positive control PpIX. (N=3, n=3)

3.4 **CDs and conjugates have lower dark toxicity than PpIX.** PpIX-CD and PpIX@CD show similar trends with increasing concentrations. (PpIX-CD)p appears to be the most biocompatible conjugate, closely mirroring CA-EDA until around 50 μg/ml. (N=3, n=3)

3.5 **PpIX-adjusted concentrations show improved biocompatibility in conjugates.** Samples demonstrated decreased dark toxicity after changing values to %PpIX (μg/ml). Conjugates showed a similar drop in metabolic activity to PpIX until 4 – 5 μg/ml.

3.6 **Heatmap indicating variation in phototoxicity.** The position of the LED spot was adjusted to cover most of the 96 well plate. Wells on the top right corner show a reduced PDT effect due to insufficient light exposure. Outer rows and columns were not used as media evaporation causes variance in cell growth.

3.7 **Phototoxicity varies according to total light exposure duration.** A 2-fold increase in light exposure duration leads to increased variability at higher conjugate concentrations. Each conjugate was compared to the positive control PpIX. (N=3, n=3)

3.8 **Light-activated toxicity of CA-EDA conjugates (3-minute light exposure, 24-hour post light).** (PpIX-CD) showed markedly diminished PDT efficiency in comparison to other samples. PpIX-CD and PpIX@CD showed equal performance to PpIX at concentrations >1 μg/ml ($p < 0.05$). (N=3, n=3)

3.9 **Light-activated toxicity of CA-EDA conjugates varies after PDT.** 3 minutes of light

exposure reduces metabolic activity by over 75% after 24 hours of treatment, but slowly recovers over a 72-hour period. (N=3, n=3)

3.10 **PpIX-CD and PpIX@CD show similar PDT efficiency to PpIX at concentrations >1 µg/ml**. In contrast, (PpIX-CD)p shows a constant difference at all timepoints with concentrations >1 µg/ml. Each comparison was made between the control (PpIX) and conjugates. (N=3, n=3)

3.11 **CD-PS conjugates can be used as probes for fluorescence imaging.** CSLM images of U2-OS osteosarcoma. PpIX-CD and PpIX@CD have similar emissions to both CDs and PpIX, while (PpIX-CD)p has greatly decreased fluorescence emission. Conjugates appear to aggregate near the nuclei.

3.12 **CD-PS conjugates show non-specific intracellular localisation.** CSLM of conjugates show accumulation in the perinuclear area and cytosol. However, particles do not penetrate within the nucleus, which can be seen through the various z-slices. Lower z-slices (left) do not show brightness with DAPI staining while CD and PpIX fluorescence is high. Conversely, higher z-slices (right) clearly show cell nuclei with no overlapping signal from 488 or 543 nm.

Chapter 4

4.1 ***In vivo*** **mouse models are the current gold standard for cancer drug testing.** Typically, there are two distinct approaches: human xenografts make use of cancer cell lines, while syngeneic models use allografts from immortalised mouse cancerous tissue.

4.2 **3D cell culture models improve the relevance of *in vitro* drug evaluation**. Cancer spheroids can replicate relevant morphophysiological characteristics of in vivo tumours like hypoxia and increased drug resistance. They have also been widely used in high-throughput screening and are easily produced with inexpensive reagents. Nonetheless, their single cell line lineage and inability of long-term culture limit their usefulness in comparison of organoids.

4.3 **Schematic detailing conjugates used for in vitro PDT**. PpIX-CD and (PpIX-CD)p were fabricated through amide crosslinking. The latter corresponds to the insoluble (precipitate) fraction separated from PpIX-CD after centrifugation. PpIX@CD was obtained using a one-pot reaction.

4.4 **Spheroid growth kinetics based on initial seeding density**. Diameter was measured using

images taken with an AE2000 inverted light microscope and ImageJ. Growth reached a slowed after spheroids passed 600 μm.

4.5 **Progression of spheroid growth after initial aggregation.** Spheroids reach a maximum diameter (~600 μm) and maintain their morphology until decaying.

4.6 **Multicellular tumour spheroids react differently to PDT.** Spheroids were selected for use in PDT after reaching ~450 μm (A). Prolonged exposure to environmental stress in addition to conjugate dark toxicity caused slight damage to the outer cell layer (B). PDT caused significantly more damage, resulting in large seen as debris surrounding the spheroid (C). Debris can be removed to reveal the spheroid (D).

4.7 **LDH release varies according to sample type and dose (μg/ml).** PpIX-adjusted values show samples have similar dark toxicity in spheroids. Each sample was compared to the positive control PpIX. (N=3, n=6)

4.8 **Total dsDNA concentration shows less variability between samples and concentrations.** PpIX-adjusted concentrations show similar behaviour to LDH release, with no significant difference between conjugates and PpIX. Each sample was compared to the positive control PpIX. (N=3, n=6)

4.9 **Effect of prolonged exposure to environmental stress on spheroid viability.** Spheroids showed no significant difference in LDH release and total DNA content after a 2-hour period outside the incubator. Each sample was compared to spheroids left within incubation conditions. (n=3, N=3)

4.10 **PDT-induced phototoxicity in spheroids after 24 hrs (PpIX-CD 5 μg/ml, 5 J/cm2, 1LT).** Cell debris precipitates to the bottom of the well, obscuring the spheroid. Removal must be done with care to avoid spheroid disruption.

4.11 **Light fractionation improves PDT outcome.** Fractionated treatments (2LT) showed significant differences from single treatments (1LT) at concentrations >5 μg/ml. Higher irradiance and drug concentration significantly increased damage to spheroids regardless of sample type. (N=3, n=6)

4.12 **Fractionation of light exposure increases PDT effectiveness**. Treatments with 1LT show slightly decreased damage to spheroids in comparison to 2LT, even with lower fluence in each repeat exposure. (N=3, n=6)

4.13 **PpIX-adjusted values show similar behaviour between PpIX and conjugates**. This trend can be seen in LDH release and total DNA content in samples treated with single (top) and double (bottom) light treatments. (N=3, n=6)

4.14 **Heatmap of all treatment combinations**. Values correspond to % viability (LDH

release) or %dsDNA (DNA quantification). Treatments with best outcomes are shown in green.

4.15 **Schematic of 405 nm laser setup**. The laser was controlled through software (a) and directed towards the spheroids using a mirror (b).

4.16 **PDT effect does not scale with high irradiance.** The increase of irradiance does not lead to significantly different treatment outcomes in multicellular tumour spheroids using a 405 nm laser (25 and 100 J/cm^2). (N=3, n=6)

4.17 **Conjugate uptake in spheroids at 1 µg/ml.** Drug uptake with 1 µg/ml is an insufficient dose for PDT as uptake is limited to outer spheroid layers.

4.18 **Conjugate uptake in spheroids at 5 µg/ml** Drug uptake and signal emission are significantly improved after increasing dose to 5 µg/ml. PpIX@CD shows signs of aggregation or quenching.

4.19 **Conjugate uptake in spheroids at 10 µg/ml**. PpIX-based emissions with 10 µg/ml show drug uptake throughout the spheroid diameter and within the hypoxic core.

4.20 **Sample rotation within LSFM permits more detailed evaluation of spheroid morphology.** Live (green) and dead(red) cells can be seen throughout the spheroid at all angles (top). PDT damage can be seen in some samples, with spheroids showing sloughing and loss of sphericity after treatment (bottom). Image at 0° corresponds to the point of view seen with light microscopy.

4.21 **Live LSFM imaging of spheroid treated with lysis buffer**. Images were separated by channel (calcein-AM, ethidium homodimer-1, and the merged image).

4.22 **Spheroids show directional ablation after PDT.** Post-PDT morphology varies according to viewing angle, with parts of spheroids becoming ablated due to significant cell death.

4.23 **Drug dose increases damage to spheroids.** Increased drug doses destabilise spheroid morphology and cause ongoing cell death after 24 hours of PDT.

4.24 **Spheroids showed prolonged response to phototoxicity**. Continuous cell death could be observed up to 48 hours after the final light treatment. Initial damage was similar to that found in 1LT (top) and continued to reduce spheroid size while increasing cell death (bottom).

4.25 **3LT causes significant PDT damage compared to 1LT and 2LT.** Live imaging of 3LT PDT (24 hrs) shows significantly increased cell death and localised damage on the top section of the spheroid. Outer layers begin to detach after sequential light treatments.

4.26 **Standard C8161 melanoma spheroid imaged using SEM**. Slight damage visible in the top right corner due to manipulation during fixation.

4.27 **PDT-induced damage is visible using SEM.** In comparison to the previously shown untreated spheroid (Fig. 4.25), treated spheroids show a significantly reduced size and loss of sphericity. PDT caused sloughing of outer layers as damage increased due to fractionated light treatments, indicated with arrows for all samples.

4.28 **Cancer spheroid microscopy for evaluating PDT damage.** Fractionated light treatments significantly alter spheroid morphology, greatly reducing their size.

Chapter 5

5.1 **Automated parameter acquisition using multicellular tumour spheroids.** Spheroids were cultured, pre-screened, and treated with various PDT combinations. Image acquisition was done using widefield microscopy and automatic segmentation with AnaSP led to parameter extraction. Finally, morphometric parameters were compared with in vitro assays.

5.2 **– Spheroid growth and morphology depends on agarose coating quality.** Spheroids initially may show irregular morphology as cells begin to aggregate in Day 1. Steady growth eventually leads to a more spherical shape with no irregularities by Day 3. Defects in the agarose coating or incubation conditions led to irregular morphology.

5.3 **Automatic segmentation reduces variability during image pre-processing**. Manual segmentation results for area, perimeter, and volume showed high variation after multiple segmentation attempts with the same image.

5.4 **Parameter extraction improves as debris is cleared from the well**. Automatic segmentation depends on initial binary conversion and accuracy decreases as more opaque objects are present in the foreground alongside spheroids.

5.5 **Group variability was lowered with spheroid pre-screening.** Area values from extracted morphological data did not show significant variability between spheroid and treatment groups. (N=3, n=6).

5.6 **Variability in spheroid morphology at 24 hours post-PDT.** Greater variations in colours indicate which parameters can be used to distinguish treatments known to cause significantly different damage to spheroids, such as 5 μg 1LT versus 10 μg 3LT.

5.7 **PpIX and PpIX-CD show similar reductions to viability and area with equivalent**

treatment conditions (a, b). Light fractionated treatments caused very similar effects regardless of drug dosages (c).

5.8 **Spheroid area can be used to predict viability and DNA content**. Each point on the graph corresponds to an independent repeat; the same spheroid was monitored through imaging (parameter acquisition) and biological assays (LDH release and total dsDNA content). (N=3, n=6)

5.9 **Spheroid curvature is not linked to viability.** Morphological parameters based on spheroid curvature (sphericity) and diameter (LMinDTC) showed significant variability compared to area or volume.

5.10 **Variations in surface roughness based on different models for 3D projection**: (a) roughness and (b) mixed from Zeiss ZEN 2014 software. Data such as total fluorescence intensity, size, and volume can be extracted from each Z-stack.

List of tables

Chapter 2

Chapter 3

Chapter 4

Chapter 5

Table of contents

Chapter 1 – Literature review: Carbon dot conjugates for biomedical and biomaging applications

Introduction

Nanomaterials in biomedical applications

Carbon-based nanomaterials have unique photophysical properties which have been used in research for a wide variety of biomedical applications including drug delivery, bioimaging, and sensing. Carbon dots (CDs), also known as C-dots and carbon quantum dots, are quasispherical fluorescent nanoparticles which have received continuous attention and research interest since their serendipitous discovery during the purification of single-walled carbon nanotubes in 2004 [1]. The term "carbon dot" has also been used to describe several different types of particles such as carbon nanoparticles, amorphous carbon dots, and polymer dots.

In general, CDs have key characteristics such as excellent biocompatibility, tuneable photoluminescence, photostability, and facile surface group modification that make them ideal candidates for several applications [2]. Moreover, synthesis routes for CDs are highly adaptable and inexpensive, leading to greater control over several photophysical characteristics through mechanisms like surface passivation, which is the process by which reactive surfaces are coated to prevent changes. CDs typically are passivated with compounds such as branched polymers or glycerol, which maintain photoluminescence and prevent surface oxidation [3]. However, there are contradictory reports regarding key properties such as photoblinking, [4] photon upconversion, [5] pH-dependent photoluminescence, and size-dependent photoluminescence [6,7], indicating that they are a much more complex material than initially expected (Fig. 1.1).

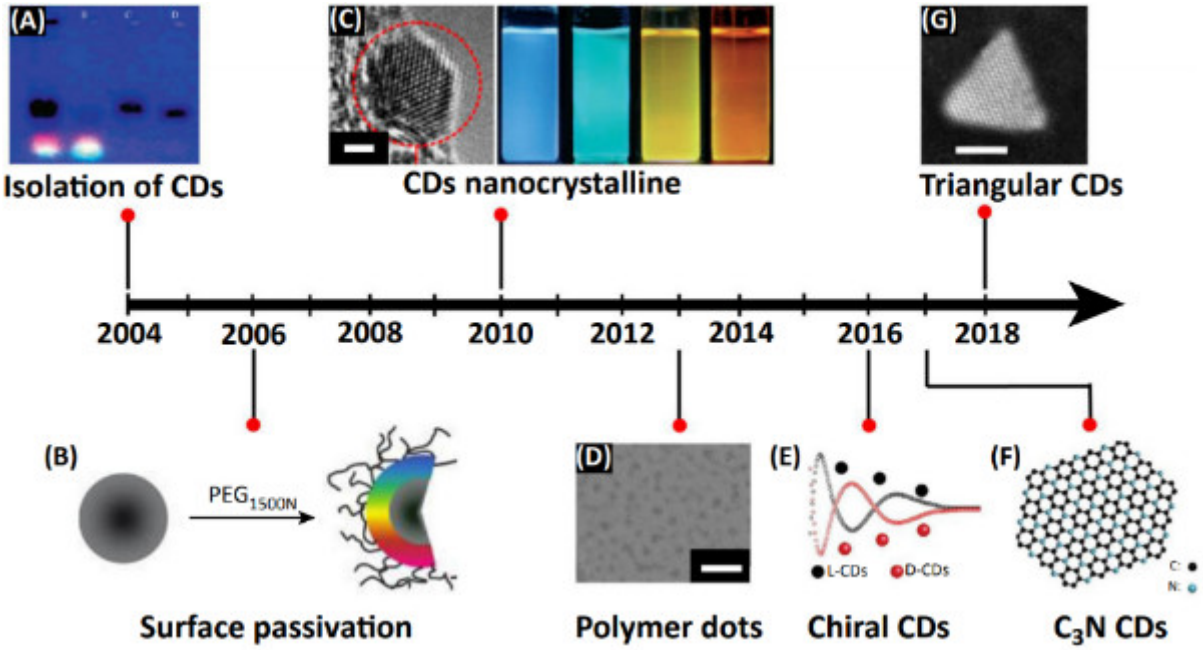

Fig. 1.1 – Timeline of improvements in CD synthesis and modification. Reprinted from Yao et al. (2019) with permission from Elsevier [8].

Carbon nanotubes (CNTs)

Currently there are many competing technologies within the field of nanoparticle conjugates for biomedical applications, particularly from the same carbon allotrope family. Carbon nanotubes (CNTs) are one of the most widely known nanomaterials and have been exhaustively investigated for biomedical applications. Though they have excellent electrical, mechanical, and chemical properties, they have been continuously limited in their use due to ongoing concerns regarding toxicity. CNTs have been shown to be cytotoxic mainly because of their shape and length, which pierce cells. This can lead to abnormalities in phagocytosis, which is commonly observed in cancer and malignant lymphoid cells [9,10]. Additionally, metal catalyst impurities have been investigated as important factors in toxicity [11].

Nanodiamonds (NDs)

Nanodiamonds exhibit very similar properties to carbon dots with intrinsic photoluminescence and excellent biocompatibility. However, they have a crystalline structure and synthesis conditions are limited as conventional methods require high pressure and temperature for initial

growth or require additional solvents (Fig. 1.2) [12]. Furthermore, they suffer from poor colloidal stability in water unless coated with PEG or a similar polymer and tend to aggregate non-specifically with other biomolecules [13]. However, this is a common problem for all nanoparticles which are used as colloidal dispersions.

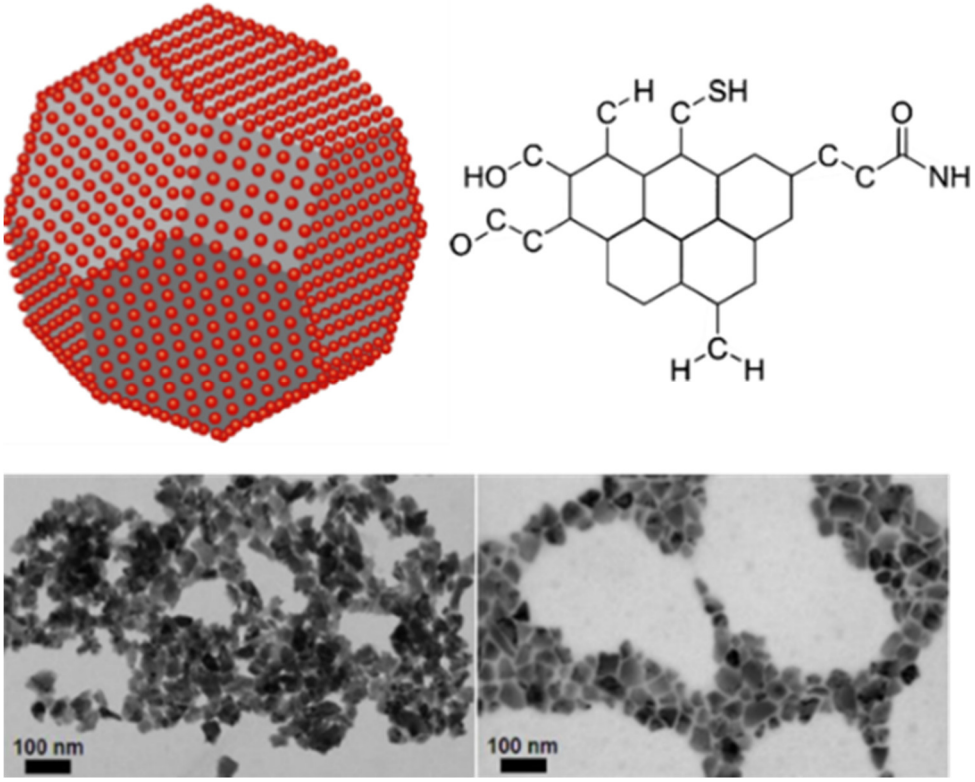

Fig. 1.2 – Nanodiamonds have a core-shell geometrical structure with many available surface groups. They can be used without modifications (bottom left) or functionalised to improve biocompatibility and other properties (bottom right). Adapted from Zhao et al. (2004) through the Creative Commons CC BY license [14].

Graphene quantum dots (GQDs)

Graphene quantum dots have also seen increased research interest thanks to their intriguing optoelectronic properties. This zero-dimensional luminescent material is formed by small (3-20 nm) fragments of graphene that exhibit high photoluminescence while maintaining biocompatibility and semiconducting behaviour (Fig. 1.3). However, GQDs typically suffer from aggregation due to their limited solubility and require further modification to surface

groups. [15].

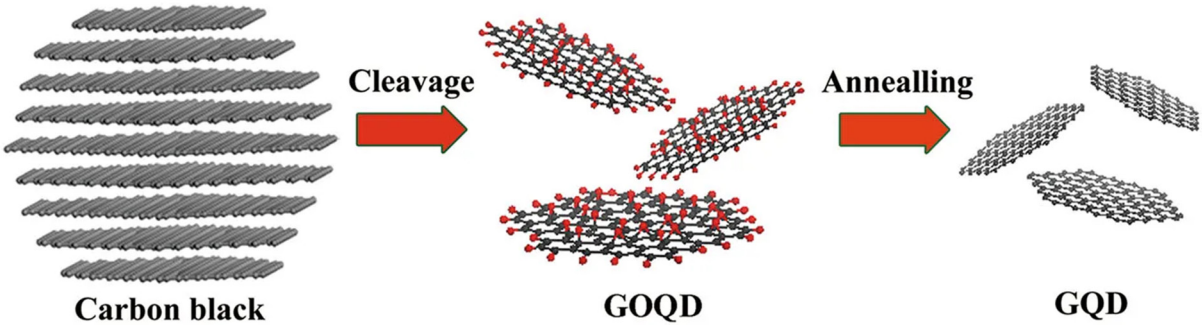

Fig. 1.3 – GQDs are obtained from the cleavage of graphite or carbon black and treated with heat to remove oxide from the surface. Reprinted from Sun et al. (2017) through the Creative Commons CC BY license [16].

Inorganic nanoparticles

Inorganic nanoparticles have also been shown to have suitable properties to act as both carriers and contrast agents. Semiconductor quantum dots have excellent photoluminescence and have been widely explored for use in similar biomedical applications to CDs. Despite their high performance due to their excellent photophysical properties, many have raised concerns about possible toxicity and side effects caused by heavy metals such as cadmium, selenium, tellurium, and lead [17]. Metallic nanoparticles have shown great versatility due to their strong optical properties and high magnetic susceptibility. They can be subdivided into four categories based on their composition: metallic, bimetallic (also known as alloy), metal oxide, and magnetic nanoparticles. However, they suffer from instability in physiological environments, size and shape-dependent toxicity, and impurities present as a result of their synthesis [18].

Upconverting nanoparticles (UCNPs)

Nanoparticles containing uncommon elements open up many possibilities due to their intriguing optical properties such as photon upconversion (UC). This phenomenon is based on the conversion of higher wavelength (lower energy) light to lower wavelength (higher energy)

light as a result of their unusually high absorption cross section [19]. Upconverting nanoparticles are made up of a crystalline matrix in which lanthanide ions are embedded (Fig. 1.4). Although they are excellent candidates for bioimaging and light-based therapeutics, they are limited as their excitation maximum (980 nm) overlaps with water and is relatively low in brightness [20]. Nonetheless, all these materials have shown varying degrees of success in biomedical and bioimaging applications due to their innate properties like high surface area and photoluminescence [21].

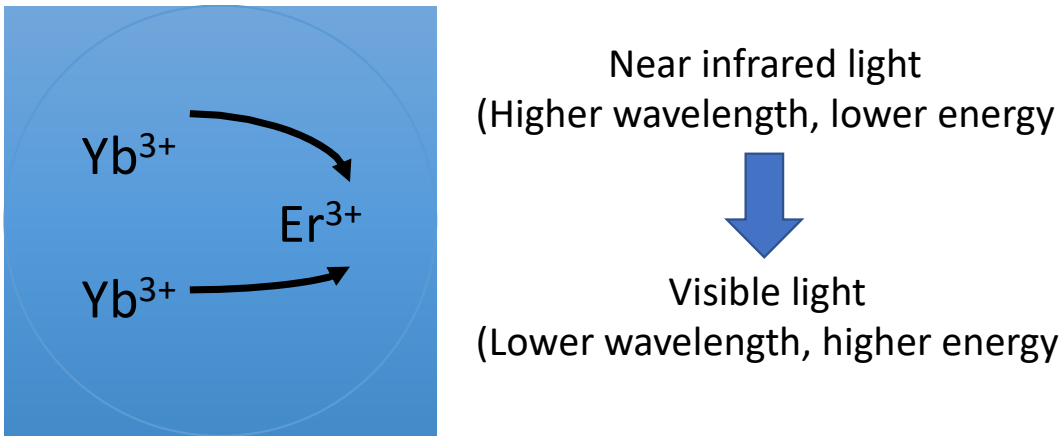

Fig. 1.4 – Upconversion nanoparticles can convert near-infrared light into visible light. These crystals are often composed of fluorides such as $NaYF_4$ or oxides like Gd_2O_3.

Table 1.1 - Commonly utilised molecules and nanoparticles in biomedical applications.

	Material	Size	Ease of conjugation	Quantum yield %	FWHM	Photostability	PL lifetime	Ease of multiplexing	2PE
Organic fluorophores	Dye molecules or proteins	<1 nm – 4 nm	N/A	Variable	Broad, red tailed	+	< 10 ns	+	+
Dye-doped silica NPs	Silica	2 - 200 nm	++	Variable		++	<10 ns	++	+
Nanodiamonds	Carbon	5-20 nm	+	10 – 80	> 60 nm	+++	10 – 20 ns	+	+
Graphene quantum dots	Carbon	Variable height and length	+	<10	> 80 nm	+++	<10 ns	+	++
Carbon dots	Carbon	<10 nm	+	5 – 60	> 60 nm	+++	<10s	++	++
Carbon nanotubes	Carbon	Variable	+	< 25	> 60 nm	+++	<5 ns	+	+
Metal nanoparticles	Metals (e.g. gold, silver, iron)	Variable	+	<20	> 60 nm	+++	>100 ns	+	++
Upconverting nanoparticles	Lanthanide-doped	20 – 50 nm	+	Variable	Variable	+++	>100 ns	++	+++
Quantum dots	Semiconductor (e.g. CdSe)	2 – 10 nm	++	10 – 90	25 – 35 nm	++	>10 ns	++	++

Carbon dots (CDs)

Initially, CDs were thought to be an alternative to semiconductor quantum dots because of their high photostability, tuneable emission spectra, and low toxicity. However, the extreme variability of photoluminescence and toxicity has somewhat limited the application of CDs in several fields [22]. Furthermore, the prediction of CD photophysical characteristics remains a great challenge due to their complex chemical structure; the relationship between contributions of bulk and surface-derived effects on these properties has not been completely understood [8].

In recent years, there has been much progress in regards with the general properties and application of CDs which has been succinctly summarized in several review articles [23–25]. This review will focus on describing the recent progress of CDs in biomedical applications as nanoparticle-drug conjugates, focusing on the many variations in synthesis, modifications, crosslinking, and drug delivery strategies.

Evaluation of *in vitro* and *in vivo* toxicity

Biocompatibility is one of the most important properties for biomedical applications. However, it should be noted that the concept of "biocompatible" has been in constant change since its introduction and is often thought to be the opposite of cytotoxicity. Williams (2008) proposed that biocompatibility is the ability of a system or material to perform intended function without causing localised or systemic damage *in vivo* [26]. In contrast, cytotoxicity generally refers to a broad range of effects that lead to accidental (necrosis) and regulated (apoptosis) cell death. These differ according to the mechanism by which cell death occurs; typically regulated cell death is the end result of multiple signalling pathways and a combination of multiple events within cells (Fig. 1.5) [27].

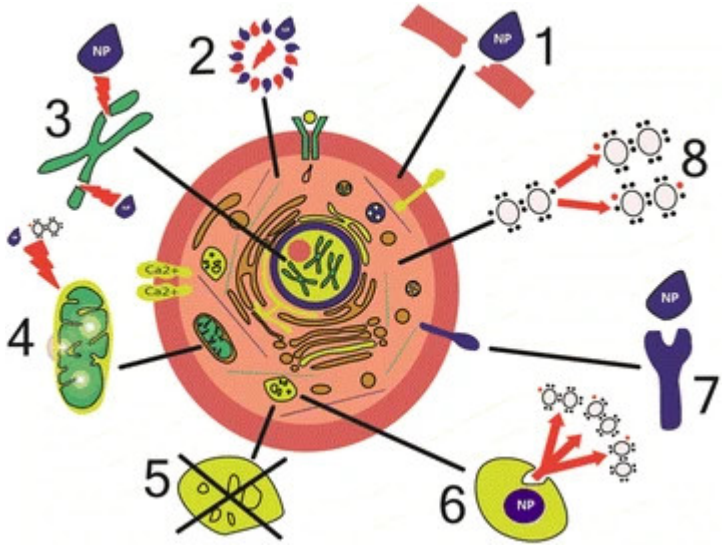

Fig. 1.5 – Cell damage from nanoparticles is multifaceted and occurs simultaneously in various sites. Damage can occur within the membrane (1), cytoskeleton (2), DNA (3) , mitochondria (4), lysosomes (5), production of reactive oxygen species (6), and through the expression of pro-inflammatory components (7) . Reprinted from Sukhanova et al. (2018) through the Creative Commons CC BY license [28].

The evaluation of toxicity of carbon nanomaterials has proven to be difficult as their behaviour is highly variable depending on factors like surface chemistry, dispersion properties, hydrophilicity, and particle size. The toxicity of nanoparticles is the combination of a multitude of effects which determine how these materials interact with cells. Nanoparticle-mediated toxicity has been linked to several stress-related cellular events caused by the alteration of homeostasis.

In particular, the physiochemical properties of particles have been shown to be crucial in determining cytotoxicity *in vitro*, and include surface charge [29], size, shape [30], and elemental composition [31]. Furthermore, nanoparticles can arrest the cell cycle by disrupting the cell-division cycle. As cells cannot repair the damage that is caused, they can become necrotic or apoptotic, which continuously supresses proliferation [32]. Extensive testing is a key step in understanding the mechanism of cellular toxicity in any nanomaterial.

Determination of cytotoxicity is essential for nanomaterial development

There is a wide variety of protocols used to determine cytotoxicity, from simpler cell viability assays like live/dead staining, metabolic activity, membrane damage, or total DNA content, up to more complex immunoassays for detecting various biomolecules as markers for alterations in key cellular pathways [33]. The model used for evaluating toxicity greatly impacts the quality and relevance of obtained data. These can be either *in* vitro, which includes cell monolayers and various 3D cell culture models, or *in vivo* models like rats, mice, chick chorioallantoic membrane.

Panessa-Warren et al. (2006) suggest a combination of *in vitro* and *in vivo* assays is the ideal method to maintain the balance of cost-benefit in cytotoxicity evaluation. In particular, the use of immortalized cell lines with high passages or brief exposure times may not reflect physiological conditions and should be used alongside another more complex model to obtain complementary data [34]. Additionally, Moore et al. (2019) showed nanoparticle-cell interactions are affected by the administration method – as particles can be in a concentrated solution, pre-mixed, or mixed *in situ* [35]. Therefore, cytocompatibility results should be compared only after a careful observation of the experimental design that was utilised.

The general consensus across several studies is that CDs generally possess a very low toxicity, mainly as a result of their hydrophilicity [36]. CDs have previously shown widely varied results related to a multitude of experimental factors such as cell line used, synthesis route, chemical modifications, and incubation times. LD50 values for cell viability are extremely variable, ranging from 15.625 µg/ml to 10 mg/ml in cell monolayers (Table A2.1, Chapter 2 Annex). Therefore, CD-based conjugates can be greatly affected by the variability seen in cytocompatibility, indicating the need for extensive toxicological evaluation prior to their use.

In vitro (cytocompatibility)

CDs show low cytotoxicity though high dose range is variable

A key factor in the evaluation of cytotoxicity is determining what concentration is considered as a "high dose" – this can be particularly difficult as this varies according to each application and author. Tao et al. (2012) showed a comparison of *in vitro* and *in vivo* accumulation of graphite or carbon nanotube-derived CDs and determined no appreciable toxicity even at "ultrahigh" concentrations of 0.5 mg/ml. These CDs are highly hydrophilic possibly due exceptionally high oxygen content (55%) and many carbonyl and hydroxyl surface groups, which makes them similar to hydrophilic carbon clusters [37]. Similarly, Huang et al. (2014) did not observe significant changes in cell viability of cultured AD-923 cells with extremely high concentrations of up to 2 mg/ml with histidine-derived CDs. [38]

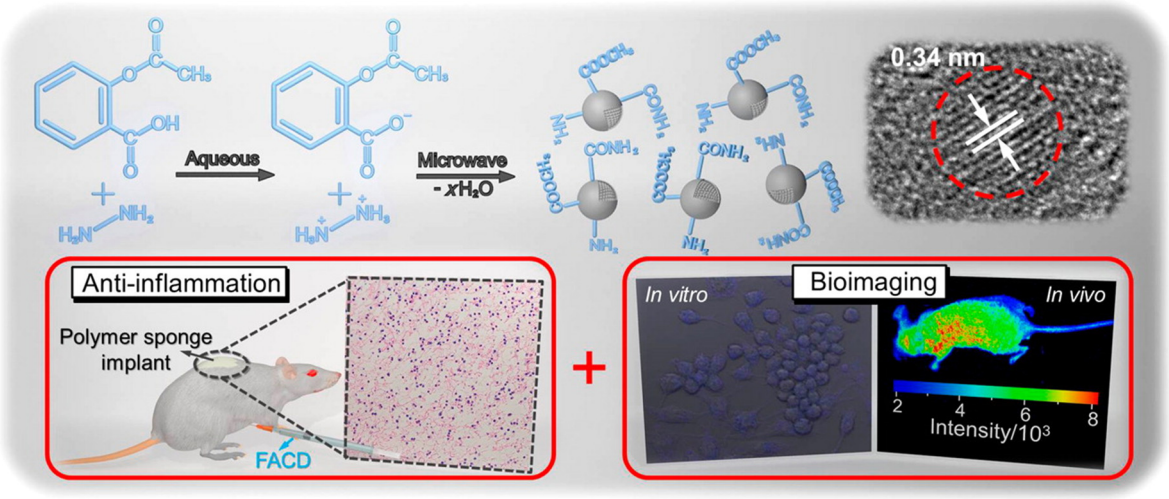

Fig. 1.6 – The anti-inflammatory properties of aspirin were maintained after CD synthesis. Concentrations up to 100 µg/ml were not shown to cause observable *in vitro* and *in vivo* toxicity. Reprinted with permission from Xu et al. (2016) [39]. Copyright (2016) American Chemical Society.

In comparison, Jiang et al. (2015) used a lower range of 0 – 50 µg/ml to test the CD toxicity with MCF-7 cells and observed >95% viability in all concentrations up to 50 µg/ml, noting that samples showed "excellent biocompatibility" [40]. Likewise, Xu et al. (2016) determined

aspirin-based CDs do not cause significant cell death in RAW264.7 cells at concentrations up to 100 μg/ml [39]. These results highlight excellent CD cytocompatibility but suggest there are more factors involved in predicting CD-based cellular toxicity. It is possible that the synthesis protocol leads to specific surface chemistry which improve cytocompatibility, as seen in Fig. 1.6. These variations in lethal concentrations (LC50) are likely caused by variations in synthesis conditions, reagents, and sample processing.

Cytotoxicity evaluation depends on various assays

Cell viability and proliferation assays are also varied across the literature, with most evaluations being carried out using the MTT assay. However, other assays such as MTS, resazurin reduction, CCK-8 or CellTiter96 have been used to evaluate CD cytotoxicity. Ray et al. (2009) combined MTT and Trypan blue assays to determine the cytotoxicity of 2 – 6 nm CDs obtained by nitric acid oxidation of carbon soot and found minimal cell death at concentrations under 1 mg/ml [41]. Cui et al. (2015) also showed high cytocompatibility of CDs fabricated by the hydrothermal processing of ammonium citrate and ammonium hydroxide. Particles were evaluated in concentrations up to 2 mg/ml with CKK-8 and did not impact cellular morphology or proliferation [42]. Nanoparticle incubation time for cytotoxicity evaluation in cell monolayers is mostly the same across the literature, with most work coinciding at 24-hour exposure periods immediately followed by a metabolic activity assay. However, the use of longer timescales is useful as it may show additional data regarding changes to proliferation after several cell division cycles. Hill et al. (2016) evaluated the cytotoxic effect of amine-functionalized CDs over a lengthier timescale of 1 to 7-day exposure with live/dead staining and resazurin reduction assays. The reductive metabolism per cell (RMPC) was calculated by comparing the total metabolic activity with the number of live cells estimated with staining. Amine-coated CDs showed elevated RMPC at 1-hour exposure, with significant cell death apparent at concentrations above 250 μg/ml. Lactose-coated CDs showed

increased RMPC levels consistently across all time points, which suggest glycans could be useful for improving the cytocompatibility of CDs [43]. Yang et al. (2011) evaluated the toxicity of CDs synthesized by the hydrothermal treatment of monopotassium phosphate and glucose. HepG2 cells did not show appreciable cytotoxicity after incubation with CDs, up to a total of 72 hours of exposure [44].

Variations in cell lines lead to different outcomes for toxicity

There are reports of variation between *in vitro* CD toxicity when utilising different cell lines in similar experiments. Shereema et al. (2014) showed CDs fabricated by combustion of styrene produce highly variable LD50 concentrations between HEK 293 (>250 µg/ml) and A549 (15.625 µg/ml) cells [45]. Similarly, Yang et al. (2009) fabricated CDs by laser ablation of ^{13}C and graphite cement and evaluated toxicity in MCF-7 and HT-29 cells. CDs *in vitro* were shown to decrease around 25% of cell proliferation and viability at concentrations over 50 µg/ml (HT-29) and 100 µg/ml (MCF-7). HT-29 cells showed decreased mortality in comparison to MCF-7. It is possible that cancer cells are capable of higher rates of cellular uptake and storage due to the EPR (enhanced permeability and retention) effect [46]. Throughout literature there are conflicting results regarding variations between cell lines, which indicates that the evaluation of CD cytotoxicity should be thoroughly evaluated with a standardized method.

Synthesis method may affect cytotoxicity as surface chemistry changes

CD synthesis and carbon sources used in their production could also be a source of variability between samples. Vedamalai et al. (2014) synthesized CDs through hydrothermal decomposition of *o*-phenylenediamine and observed cells showed toxicity leading to cell death mainly through apoptosis in A549 (~250 µg/ml), MCF-10A and MDA-MB-231 cells (>300 µg/ml). Additionally, the addition of CDs did not cause significant change in intracellular pH

values [47]. Zhang et al. (2013) utilised CCK-8 for evaluating cell viability in both NIH-3T3 fibroblasts and A549 cells with nanodiamond-derived CDs. They did not observe adverse effects in cell morphology and viability up to concentrations of 320 μg/ml in both cell lines. Additionally, there was no significant difference in cell viability between NIH-3T3 and A549 cells at all concentrations regardless of incubation times. Bright field microscopy shows the outline of carbon dot aggregates in the cytoplasm, with normal cellular morphology at 50 μg/ml [48]. Zhang et al. (2015) showed minimal variation between the toxicity of iodine-doped CDs in A549 and 4T1 cancer cell lines [49]. Likewise, Liu et al. (2012) showed CD cytocompatibility varies only slightly between HepG2 and COS-7 cells. Additionally, it was found that microwave irradiation time greatly affected CD cytotoxicity at concentrations over 4 μg/ml. It is possible that as synthesis time increases the majority of positively-charged groups in polyethyleneimine (PEI) are either destroyed during the passivation or are located within the nanoparticle core, thus reducing membrane damage [50].

Passivation can greatly increase photoluminescence and cytocompatibility

Surface passivation has been shown to be an important factor in CD cytocompatibility. Havrdova et al. (2016) found surface charge greatly influences soot-derived CD toxicity in NIH/3T3 fibroblasts. Polyethylene glycol-coated nanoparticles showed no significant effect on cell viability up to a concentration of ~300 μg/ml and began to affect morphology at similar concentrations. In comparison, negatively charged pristine CDs were found to disrupt part of the cell cycle and decrease proliferation at around 200 μg/ml, while positively charged PEI-coated CDs caused significant changes to cell viability at concentrations around 100 μg/ml. As can be seen in Fig. 1.7, cell cycle homeostasis can be disrupted by CDs at various stages. Flow cytometry analysis of cell populations suggest free PEI molecules interact with various organelles and intracellular components such as DNA, contributing to increased cell death [51]. Likewise, Li et al. (2010) utilised silica spheres as carriers for CD synthesis via nitric acid

oxidation and compared the effect of polymer surface passivation on cytotoxicity. CD3 (particles passivated with PEI-PEG-PEI polymer chains) showed increased binding to cell membranes due to its positive zeta potential of +3.35 mV, while non-passivated CDs led to decreased cytotoxicity as a result of their negative charge [52].

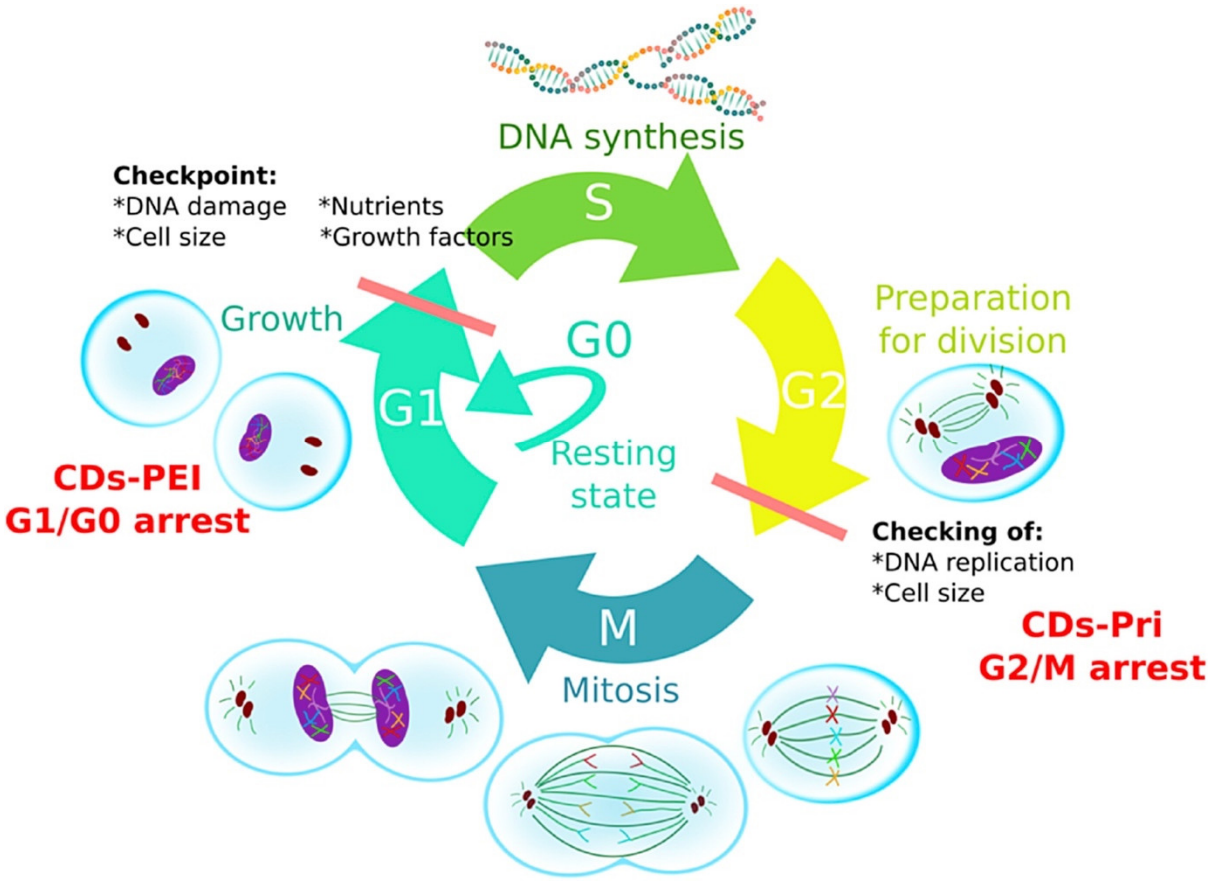

Fig. 1.7 – Cell cycle homeostasis is impacted by CDs at different stages depending on charge. Reprinted from Havrdova et al. (2016) with permission from Elsevier [51].

Heteroatom doping improves photoluminescence in CDs

The introduction of elements other than carbon, hydrogen, and oxygen in CDs has been shown to be an adaptable and facile method of increasing photoluminescence. Typically, this is done using nitrogen and phosphorous-containing compounds for particle synthesis. The main advantage of one-pot synthesis combined with heteroatom doping is the lack of any other external additives like passivating agent, alkali, acid, or salt which may be disadvantageous for

cytocompatibility and quantum yield, as can be seen in Fig. 1.8. Zhai et al. (2012) showed the very low toxicity in N-doped CDs with high quantum yields (30.2%) at unusually high concentrations of >10 mg/ml. The additional passivation with amine-rich compounds such as 4,7,10-trioxa-1,13-tridecanediamine or PEI was not found to significantly impact particle toxicity and increased quantum yield. CDs did not have an effect cell morphology even at 2 mg/ml, with concentrations metabolic activity remaining unchanged at 3 mg/ml (100%) and a slight decrease when increased to 6 mg/ml (84%) [53]. Zhou et al. (2014) demonstrated P-doping of CDs increased photoluminescence and quantum yield in a similar manner to N-doping by forming more isolated sp^2 carbon clusters. P-doped CDs show reduced greatly cytocompatibility in HeLa cells (~100 μg/ml) due to this modification [54]. Parvin and Mandal (2017) evaluated the toxicity of nitrogen and phosphorous co-doped CDs in RAW264.7 cells. PN-CQDs were determined to be highly fluorescent and non-cytotoxic with concentrations up to 1 mg/ml not significantly affecting cell metabolism, proliferation, and survival [55].

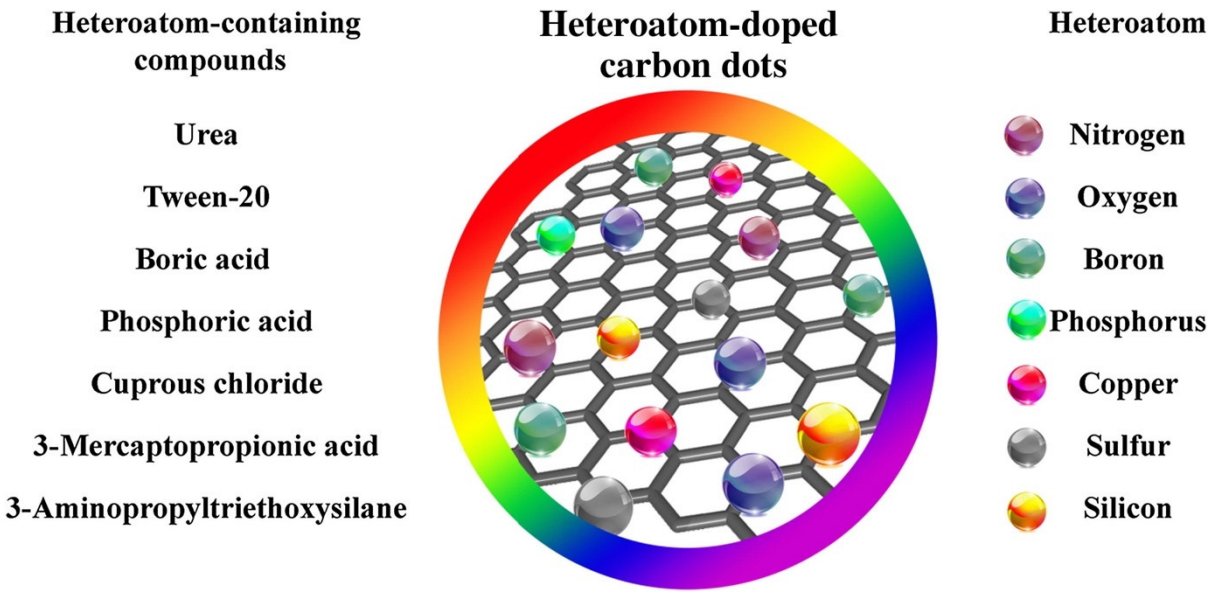

Fig. 1.8 – CDs can be doped with various compounds during synthesis, influencing photophysical properties as surface chemistry is altered. Reprinted from Mohammadinejad et al. (2019) through the Creative Commons CC-BY-NC-ND license [56].

Postprocessing samples leads to improved photoluminescence and cytocompatibility

Interestingly, the separation of CDs via HPLC has revealed the presence of distinct groups of more homogeneous particles within a single sample. Vinci et al. (2013) resolved a mixture of CDs obtained from graphite nanofibers and found a complex mix of 12 individual fractions. They observed highly variable quantum yield (<1 – 7%) plus unique absorption bands and emission wavelengths. Furthermore, the toxicological profile of each fraction was evaluated, with several fractions showing significantly improved cytocompatibility in comparison to the unprocessed mixed CD solution [57].

***In vivo* (biocompatibility)**

CDs have continuously shown excellent biocompatibility *in vitro* with a large variety of cell lines. However, there are clear limitations when utilising *in vitro* studies for toxicological screening of compounds. Although conditions such as oxidative stress, pro-inflammatory response, and NF-κB (nuclear factor kappa-light-chain-enhancer of activated B cells) activation have been linked to particle toxicity in cell culture, the replication of pathogenic effects seen *in vivo* has not yet been achieved. This has led to false positives (e.g. glass microfibres) or negatives (e.g. purified single-walled carbon nanotubes) during initial testing phases [58]. *In vivo* evaluation of nanoparticle toxicity with various animal models, including mice, rats, and zebrafish, can provide more clinically relevant data. The toxicity assessment typically includes haematological analysis, particle clearance, biodistribution, and histological evaluation of various tissues. *In vivo* and *ex vivo* imaging and other similar techniques can also be used to determine particle uptake in organs.

Fig. 1.9 shows two commonly used compounds for surface passivation, both with amine groups. These molecules cover the reactive CD surface and preserve photoluminescence while improving uptake. This effect has been found both *in vivo* and *in vitro* [51]. Yang et al. (2009)

demonstrated accumulation of subcutaneous and intravenous-injected CDs passivated with PEG_{1500N} and PPEI-EI in several key organs of DBA/1 mice. Kidneys demonstrated stronger fluorescence consistent with the urinary excretion pathway of compounds, while the liver only showed low particle accumulation. Although increased hepatic uptake has been previously observed in other nanoparticles, PEG passivation may have reduced protein affinity [59]. However, contrary to expectations, zeta potential did not significantly change *in vivo* toxicity at the concentrations that were evaluated.

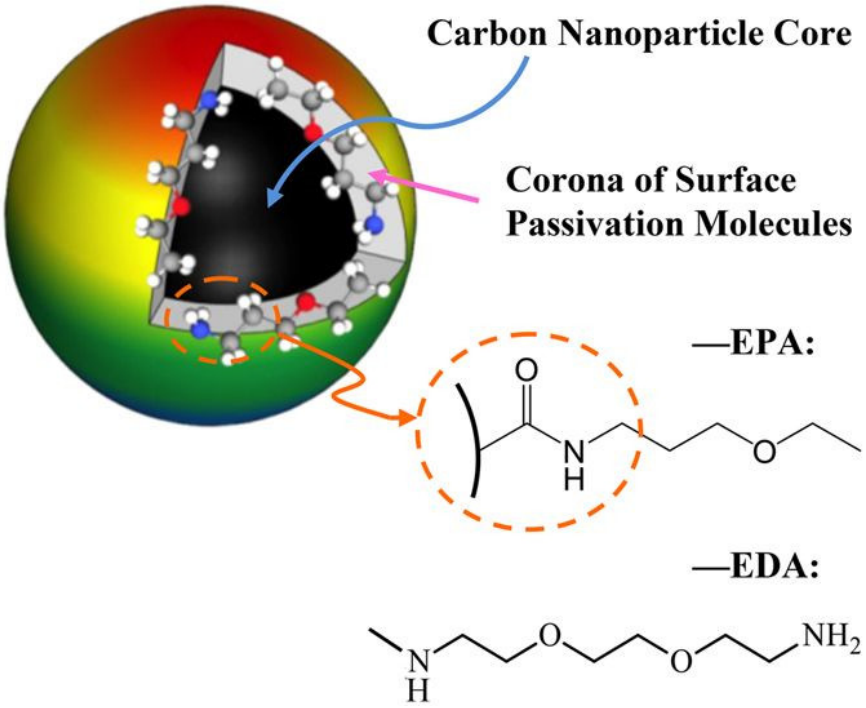

Fig. 1.9 – CDs can be passivated with molecules such as eicosapentaenoic acid (EPA) or ethylenediamine (EDA). Passivation can impact circulation lifetime and colloidal stability. Reprinted from Dong et al. (2017) through the Creative Commons CC BY license [60].

Route of administration impacts in vivo efficiency

The use of different administration routes directly impacts *in vivo* distribution, clearance, and tumour uptake of nanoparticles and has been found to be one of the main factors in determining compound toxicity. Furthermore, animal models provide great versatility in the tools used for observing nanoparticle accumulation both *in vivo* and *ex vivo*. Huang et al. (2013) performed

a thorough evaluation of the effects of different subcutaneous, intravenous, and intramuscular injection of CDs on their *in vivo* distribution, clearance, and tumour uptake in BALB/c mice. CDs were passivated with diamine-terminated oligomeric PEG_{1500N} and crosslinked to ZW800 (near-infrared dye) through EDC-NHS chemistry to enhance optical properties, which can be seen in Fig. 1.10 [61]. Additionally, ^{64}Cu was used for CD radiolabelling to monitor uptake via dynamic positron emission tomography (PET) scanning. SCC-7 cells were injected into BALB/c mice to promote tumour growth. Blood clearance rates were shown to vary according to the administration route, with particle concentration dropping dramatically 1 hour after intravenous injection, in comparison to increases with both subcutaneous and intramuscular injections.

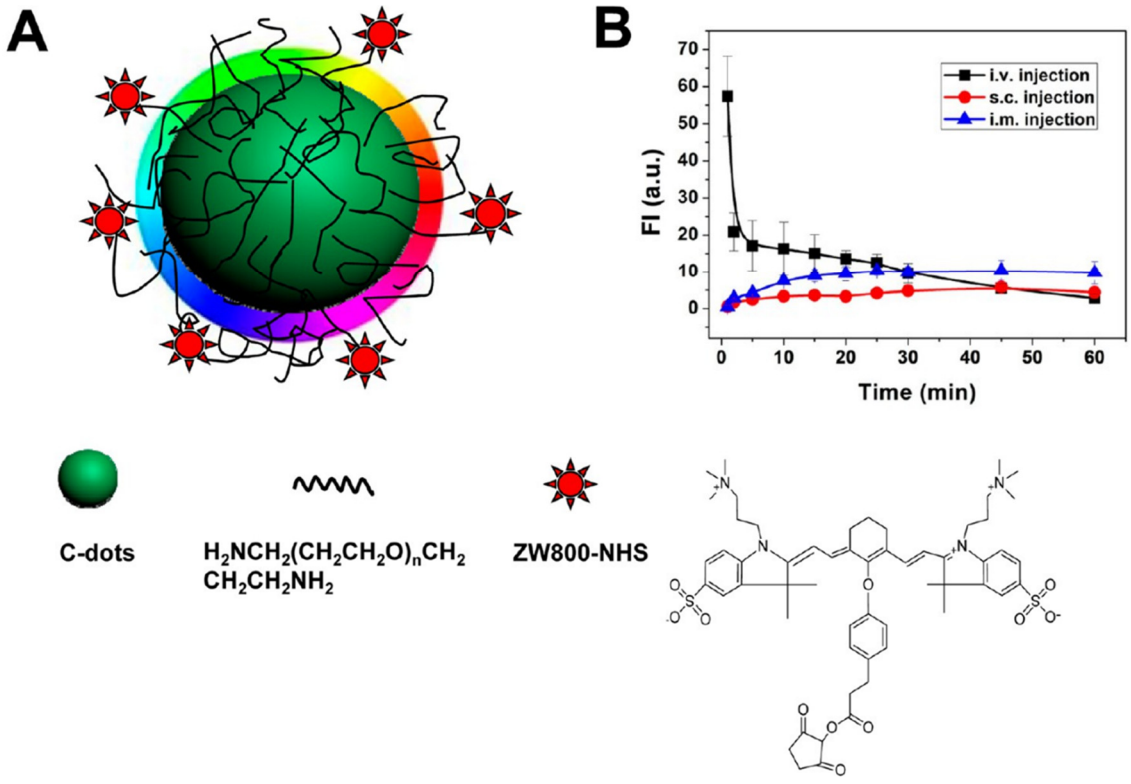

Fig. 1.10 – ZW800 increases CD absorption in the NIR region after amide crosslinking (A). CD-ZW800 particles were mainly cleared through kidneys, resulting in rapid urinary excretion (B). Adapted with permission from Huang et al. (2013). Copyright (2013) American Chemical Society [61].

It is possible rapid blood clearance could be due to rapid protein adsorption to CDs, leading to removal via the reticuloendothelial system. This is a widespread problem with nanoparticle suspensions: circulation lifetime is limited due to increased aggregation and clearance. Histology and *ex vivo* fluorescence imaging demonstrated high CD concentrations in kidneys compared to the liver in all administration routes. Intramuscular injection showed higher particle retention in kidneys followed by subcutaneous and intravenous injection. PET scanning confirmed low accumulation of CDs in the reticuloendothelial system, with less than 1% ID/g radioactivity in all organs measured. Urine clearance was shown to be rapid for all samples, repeating the pattern of blood clearance rate. CDs were shown to not accumulate at injection sites. Tumours showed significantly higher fluorescence from other tissue at 2, 4, and 24 hours post injection [61]. However, these results do not accurately reflect CD distribution as they were previously conjugated with ZW800, changing pharmacokinetics.

In vivo nanoparticle distribution can be monitored

Imaging tools such as CT and PET scanning are key for the study of *in vivo* distribution and retention over longer timescales. Furthermore, rapid renal clearance has been widely reported for CDs and other nanoparticles such as semiconductor quantum dots. This is highly desirable for imaging applications to decrease signal to noise ratios while reducing background toxicity [62]. Zhang et al. (2015) reported the synthesis of iodine-doped CDs for use as X-ray computed tomography (CT) contrast agents for Sprague Dawley rats. I-doped CDs were shown to be extremely hydrophilic and biocompatible with almost no adverse effects up to 200 μg/ml while showing superior X-ray attenuation capacity to commercial contrast agents. *In vivo* biodistribution was studied using rats with an intravenous injection of 40 mg/kg BW. Kidney and bladder showed a strong signal 10 minutes post injection, indicating rapid distribution and urinary excretion of nanoparticles. Histological analysis of susceptible organs did not reveal any obvious abnormalities [49]. Similarly, drug delivery applications benefit from rapid

clearance as treatment typically takes place 24 – 72 hours post nanoparticle administration.

Dosage is also an important factor in drug toxicity *in vivo*, which has to be carefully evaluated to enhance treatment efficiency. In this context, toxicity refers to the dose where deleterious effects start occurring. Wang et al. (2013) performed a systematic evaluation of CD toxicity and accumulation in rat and mouse models and did not find significant toxic effects or abnormalities in a wide range of concentrations. The high dose values are below the range of commercially available fluorescent imaging compounds like FDA-approved indocyanine green which has an LD50 of 50 – 80 mg/kg BW in mice. However, it should be noted the maximum recommended dose for humans is tenfold lower (5 mg/kg BW, body weight), which further reveals discrepancies between animal models and clinical data [63]. Acute toxicity was evaluated by comparing body weight and blood sample analysis of BALB/c mice injected with 5.1 and 51 mg/kg body weight in a 14-day period with no significant toxicological effects or mortality. Biochemical and haematological analysis determined no variation in the levels of biomolecules such as urea, cholesterol, blood glucose, and albumin. Histological analysis of major organs showed similar results to acute toxicity studies, with no apparent lesions or damage caused by 20 mg/kg BW. CDs did not show signs of genotoxicity (damage to genes by chemical or physical agents) after a single tail injection in low, middle, and high doses (2.04, 5.01, and 51 mg/kg BW) with 40 mg/kg Cytoxan as a positive control [64]. Fig. 1.11 shows no significant differences between control and test tissues excised from mice.

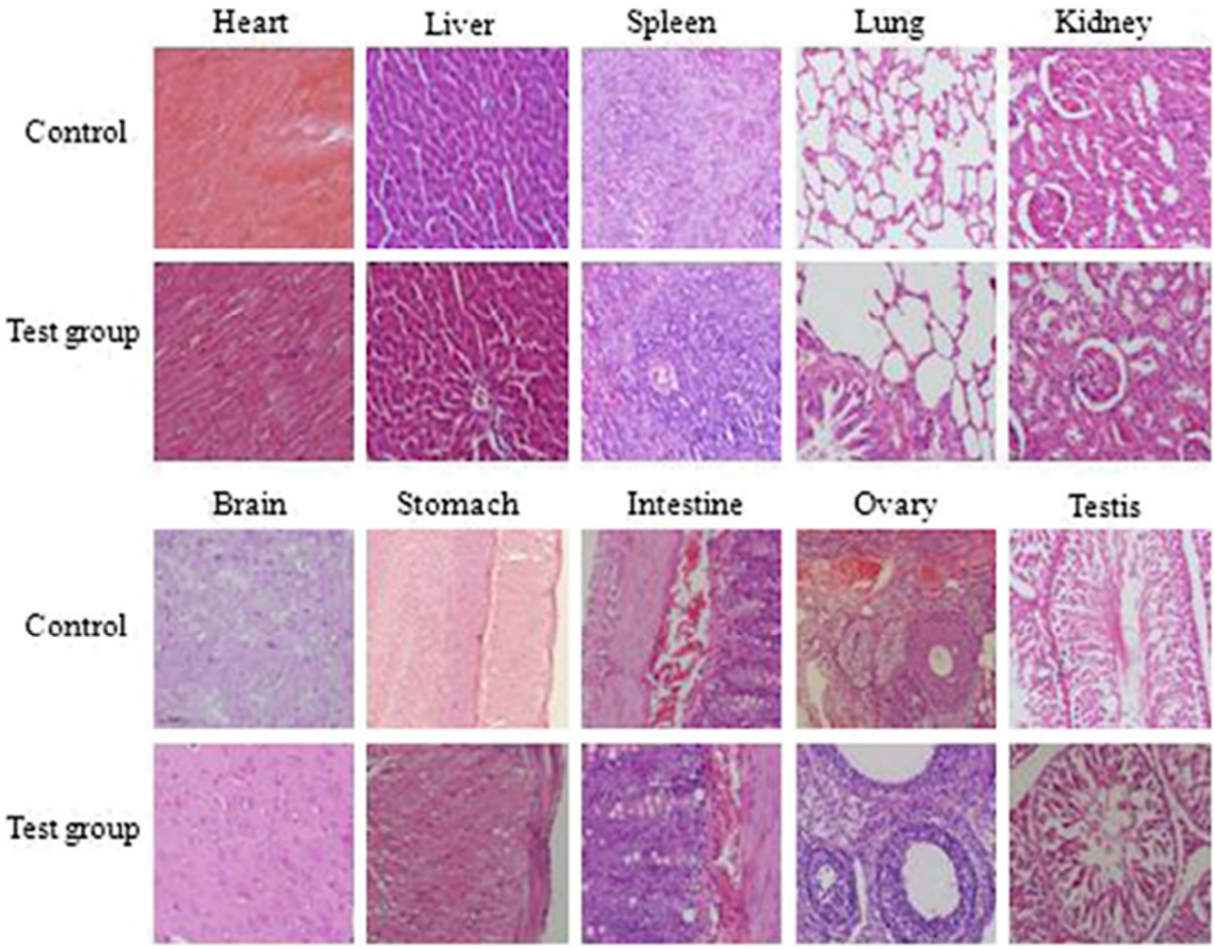

Fig. 1.11 – Histological evaluation of various tissues excised from mice treated with 20 mg/kg BW produced by nitric acid oxidation showed no observable morphology change or genotoxicity. Reprinted from Wang et al. (2013) through the Creative Commons CC BY license [64].

CD accumulation does not cause a significant toxic effect

Nanoparticle accumulation can lead to changes in tissue morphology, function, and expression of proteins. Organs with higher particle concentrations can provide insight about the adsorption, distribution, metabolism, and excretion (ADME) routes. Animal models can be combined with a wide variety of imaging technologies to more accurately determine drug concentration at key time points both *in vivo* and *ex vivo*. Tao et al. (2012) used carbon nanotube-derived CDs in athymic mice to observe *in vivo* accumulation. CD radiolabelling was used to study the pharmacokinetics, comparing blood radioactivity levels after an intravenous

injection over a 7-day period and followed a two-compartment model indicating slowed distribution within the body. Reticuloendothelial organs showed higher particle accumulation in comparison to others after injection, like other nanomaterials previously tested *in vivo*. BALB/c mice did not show BW drop or any obvious toxic side effect from CDs at concentrations of 20 mg/kg BW within 90 days of administration. Histological analysis demonstrated normal tissue behaviour with no observable lesions in any organ at the highest dosage that was evaluated [37].

These results were like those reported by Yang et al. (2009) as they used CD-1 mice to evaluate *in vivo* toxicity of laser-ablated CDs at 8 and 40 mg/kg BW. Mice exposed to high dosage (40 mg/kg BW) were used to observe CD uptake and accumulation in several organs. Histopathological analyses of liver, spleen, and kidney tissue did not show altered morphology. CDs fabricated with ^{13}C were detected using isotope-mass spectrometry analysis and a total carbon core-equivalent content of 20 μg in liver and 2 μg in spleen were calculated [46]. Studies suggest CDs are highly biocompatible and cause minimal alterations in normal metabolism even at concentrations of up to 40 mg/kg BW. Radiolabelling and isotope-mass spectrometry analysis determined minimal CD retention in tissue at longer exposure periods.

Mouse models can be used to study drug distribution and inflammatory response

In vivo models are also highly useful to study distribution and toxicity in cancer tumours and are highly tied to the evaluation of CD-based conjugates for drug delivery. Murine models are widely used in cancer research through the use xenografts, chemical induction, or genetic engineering and are very advantageous due to rapid disease progression and shorter lifespans. He et al. (2015) investigated the *in vivo* tissue staining and tumour uptake of CDs synthesised from the hydrothermal treatment of citric acid (CA) and ethylenediamine (EDA). CDs were conjugated with the Arginyl-Glycyl-Aspartic acid (RGD) peptide to target integrin $\alpha_v\beta_3$ which

is highly expressed in new blood vessels and cancerous tissue. They were able to observe tumours despite strong tissue autofluorescence at 405 nm. Mice were intravenously injected with 8 mg/ml CDs after tumours reached a size of 100 – 120 mm^3. Bladder and tumour tissue showed high fluorescence indicating rapid uptake after 24 hours, while other organs (including liver) showed decreased intensity [65]. These results are consistent with observations from Bao et al. (2018), where they observed NIR fluorescence from CDs co-doped with sulphur and nitrogen during PTT [66]. Particles passively accumulated in cancerous tissue and kidneys, showing high performance with rapid excretion (Fig. 1.12).

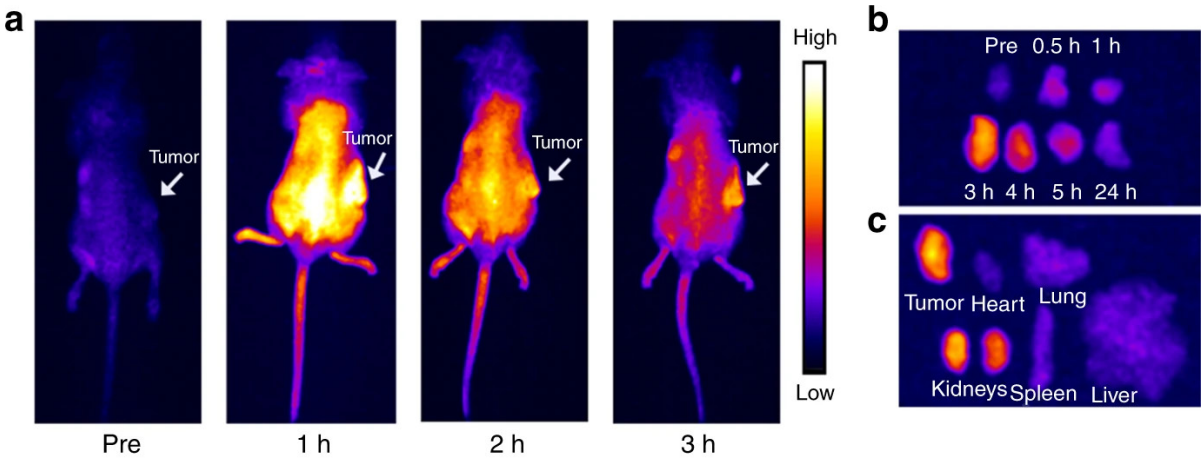

Fig. 1.12 – NIR fluorescence at 655 nm was observed in mice after an intravenous CD injection (0.2 mL, 1000 µg mL) (a). *Ex vivo* imaging of tumours at various timepoints show gradual uptake until 3 hours post injection (b). Kidneys were the only other organ which showed similar signal strength (c). Reprinted from Bao et al (2018) through the Creative Commons CC BY license [66].

Zheng et al. (2016) showed a simple one-pot synthesis protocol could produce CDs with near-infrared absorption and emission using PEG_{400} and a hydrophobic cyanine dye [2-((E)-2-((E)-2-chloro-3-((E)-2-(1-(2-hydroxyethyl)-3,3-dimethylindolin-2-ylidene) ethylidene)cyclohex-1-en-1-yl)vinyl)-1-(2-hydroxyethyl)-3,3-dimethyl-3H-indol-1-ium iodide, CyOH]. CyCDs demonstrated increased water dispersibility and preferential uptake in tumours. BALB/c mice with CT26-induced tumours were used as a model for CyCD distribution. *In vivo* fluorescence

imaging demonstrated accumulation of CyOH and CyCDs after an intravenous injection of 4 mg/kg BW. Tumours and kidneys retained higher concentrations of nanoparticles than liver, spleen and heart in a period of 48-72 hours. [67] These results reveal preferential CD uptake in cancerous tissue regardless of the inclusion of conjugated targeting motif. Furthermore, they suggest particles can avoid the reticuloendothelial system for fast renal clearance.

Nanoparticle-induced oxidative stress can lead to chronic inflammation as particles cannot be cleared from tissue. Therefore, the study of inflammatory response to CD administration is crucial. Xu et al. (2016) investigated the toxicity, accumulation, and anti-inflammatory properties of aspirin-coated CDs (FACDs) *in vivo* compared with 1% carrageenan-soaked polyester sponges implanted Wistar rats. FACDs were evaluated for possible anti-inflammatory effects by comparing the decreased production of prostaglandins *in vivo*. FACDs and aspirin significantly decreased PGE_2 levels in serum indicating an effective anti-inflammatory effect in tissue. *In vivo* toxicity was evaluated by haematological analyses, with no statistically significant differences on days 1, 3, and 7. Histological analysis of various organs showed no abnormalities for all samples at 25 mg/kg BW [39].

Alternative models for evaluating novel nanomaterials

Recently there has been work on alternate models aside from mice and rats for the evaluation of CD biocompatibility and biodistribution. These models aim to maintain the relevance of acquired data while reducing costs and increasing repeatability and high-throughput capacity.

Nematode

The nematode (*C. elegans*) is an attractive *in vivo* model for toxicological evaluation that provide data from an organism with various active systems including digestive, endocrine, muscular, neuronal, and reproductive. Thus, they are a model meant to bridge *in vitro* work and mammalian toxicity testing by optimising drug concentrations. Although it has several

limitations due to its lower complexity compared murine models, it has consistently predicted mammalian LD50 values for a wide variety of compounds [68]. Fig. 1.13 shows nematodes readily uptake CDs throughout their bodies with no adverse effects.

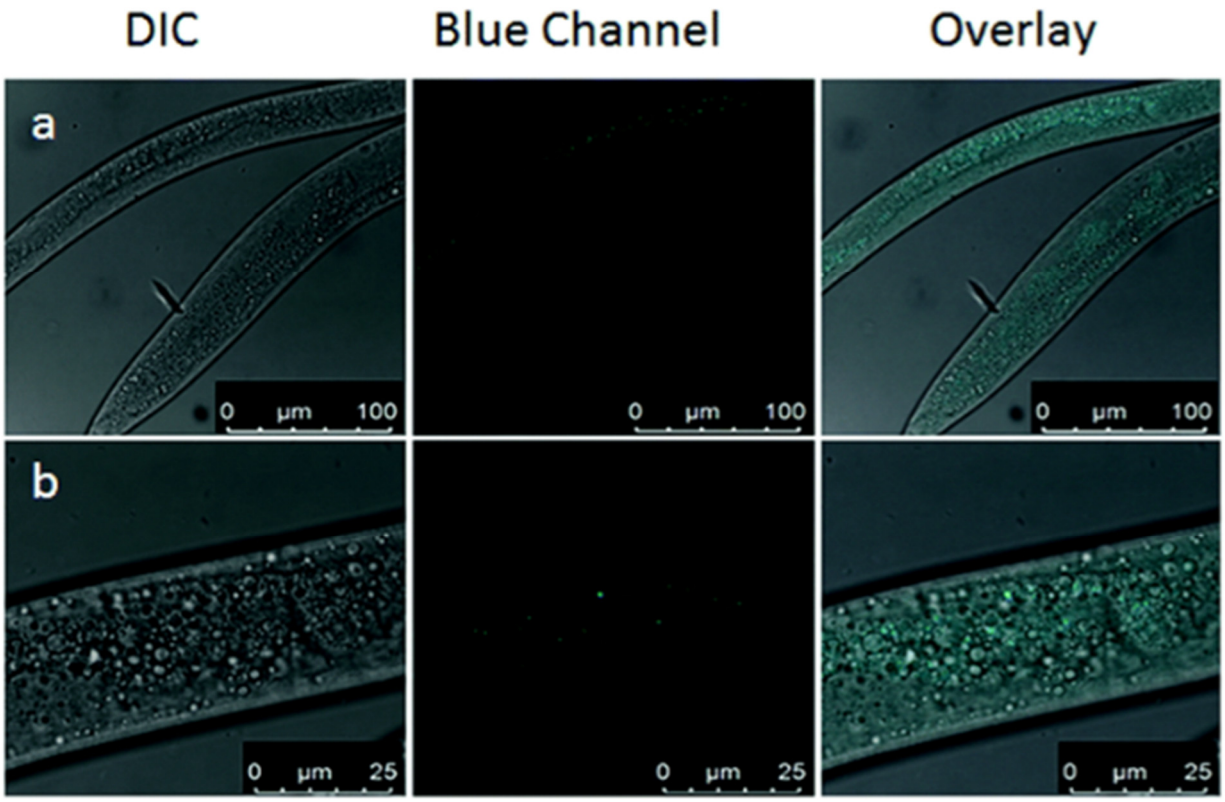

Fig. 1.13 – CD accumulation in wild-type (N2) nematodes can be observed with confocal imaging. From left to right, images were taken with differential interference contrast (DIC), fluorescence (λex = 405 nm) and a merged image. Adapted from Singh et al. (2018) with permission from Elsevier [69].

Singh et al. (2018) reported the cytotoxic evaluation of highly fluorescent and photostable of blue (B-CQDs) and green (G-CQDs) particles produced by hydrothermal treatment of beetroot extract in nematodes and BALB/c mice. Nematodes were fed using 1.5 mg/ml CDs mixed with *E. coli* OP50 and observed using confocal laser scanning microscopy. Treated specimens showed strong fluorescence in the gut and surrounding tissue, indicating systemic absorption of nanoparticles [69].

Zebrafish

Zebrafish is a well-known and established animal model due to their great similarity to the human toxicological profile, low cost, tissue transparency, and convenient drug delivery to embryos and larvae. In particular, zebrafish have great potential for drug delivery and toxicology because of variety of toxicological endpoints that can be observed throughout embryonic and larval development [70].

Kang et al. (2015) described an alternate method for the evaluation of CD distribution and toxicity in zebrafish. Embryos and larvae showed different biodistribution when exposed to CDs by microinjection and soaking. Embryos showed CDs possibly have different tissue affinities as they are mainly deposited in the yolk sac, tail, and head, being excreted at around 60 hours post exposure. There is also a slight accumulation in the dorsal aorta which may indicate nanoparticle entry through the circulatory system. Interestingly, CDs can cross the blood-ocular barrier and accumulate in the lens but were incapable of crossing the blood-brain barrier. The ADME route of CDs was shown to be primarily based on swallowing and skin-based absorption, followed by transfer through the cardiovascular system and excretion by urine or faeces. Zebrafish embryos revealed slight variations in survivability according to the administration route at 24- and 48-hours post exposure.

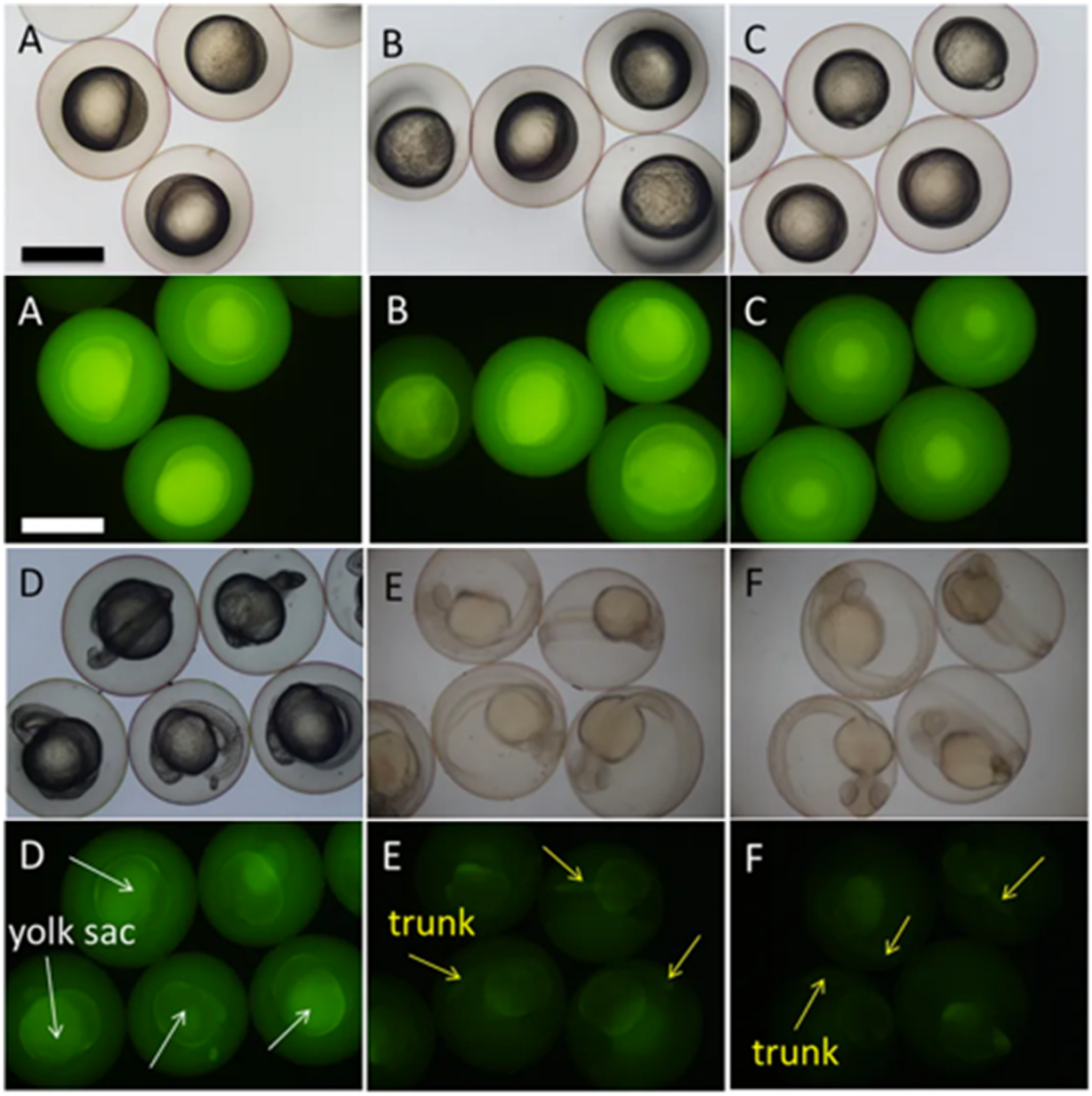

Fig. 1.14 – Zebrafish embryos incubated with 2.5 mg/ml CDs show uptake at 3 hours post-fertilisation (hpf) (A). Fluorescence gradually decreases at various timepoints, being observable until 60 hpf (F). Adapted from Kang et al. (2015) through the Creative Commons CC BY license [71].

Fig. 1.14 shows zebrafish embryos subjected to microinjections had a small decrease in survival rate, down to 80% at 1.5 mg/ml and 50% at 2.5 mg/ml. In comparison, embryos soaked in CDs at 1.5 mg/ml and 2.5 mg/ml were 85% and 55% respectively. Concentrations under 0.625 mg/ml demonstrated no significant effect on embryo survival rate. Zebrafish larvae developed normally and did not have adverse effects at solutions of 1.5 mg/ml [71].

Li et al. (2016) demonstrated low quantum yield CDs prepared from carbon nanopowder have a strong affinity and retention to zebrafish bones. Intracardiac injection of zebrafish larvae showed a strong fluorescence of skeletal structures after only 30 minutes post-injection. Furthermore, larvae were able to tolerate CDs and retain fluorescence in tissue until day 8. *In vivo* fluorescence emission was found to be excitation wavelength-dependent, following a similar shifting pattern as observed with CDs in an aqueous solution. Skeletal tissue was identified with Alizarin red staining for co-localization with CDs showing high affinity and specificity with calcified bone. In comparison, non-mineralized tissue such as cartilage was not extensively stained. Immunohistochemistry was used to observe fluorescein-labelled CDs in calcified cleithrum and ceratobranchial bones. CD binding to mineralized tissue was shown to be dependent on bone ossification by modifying retinoic acid levels for larvae [72]. In summary, zebrafish have been shown to be a reliable predictive model for the evaluation of CD-related pharmacokinetics at longer timescales post fecundation. Nonetheless, there is still a wide variability between experimental procedures and standards used in literature.

Chick chorioallantoic membrane (CAM) assay

CAM assay is an *in vivo* model which uses the extraembryonic vasculature and membrane of developing chicken eggs. This model has several advantages for high-throughput drug screening as it is low-cost, versatile, and reproducible. Furthermore, this model has the capability of supporting tumour growth due to its immunodeficiency at early developmental stages, which is not possible in murine models [73]. CAM assays have additional adaptability by being able to be cultivated outside of the eggshell, in comparison to the traditional use of windowing. This approach enables easier performance of xenograft-based studies using mammalian stem and cancer cells throughout the various chick developmental stages, which can be seen in Fig. 1.15 [74]. Shereema et al. (2015) evaluated the biocompatibility and angiogenic effect of styrene soot-based CDs via CAM assay and compared results with *in vitro*

toxicity assays performed with HEK 293 cells. The estimation of total haemoglobin as measure of vascular density and angiogenesis after an intravenous injection of 100 μg CDs suggested particles have an antiangiogenic effect. The reduction of angiogenic cytokines vascular endothelial growth factor (VEGF) and fibroblast growth factor (FGF) and the comparison of vascular densities through photomicrographic analysis further proved this reduction of blood vessel formation from days 4 to 12. Additionally, there was no observable toxic effects during the 14-day incubation period [45].

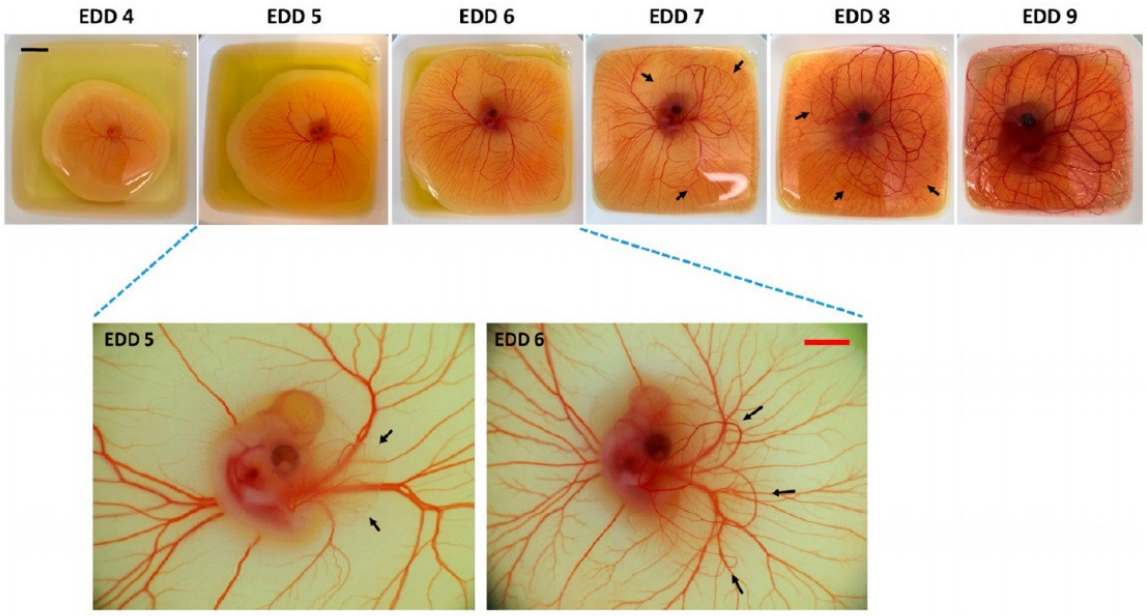

Fig. 1.15 – *Ex ovo* CAM assay can also be achieved by cracking fertilised eggs and placing the embryos in plastic containers. The appearance of the membrane can be seen on embryonic development day (EDD) 5 and is shown with black arrows on days 7 and 8. CAM assay has a maximum of 17 days for development before termination. Reprinted from Mangir et al. (2019). Copyright (2019) American Chemical Society [75].

Three-dimensional (3D) cell culture models as alternatives for drug studies

Together, *in vitro* and *vivo* models have provided highly useful information regarding CD toxicity. However, the comparison of both models has consistently shown negligible correlation in results. This demonstrates the need for an evaluation of an *in vitro* model that can be easily validated and compared to *in vivo* data [76]. 3D-cell culture models have been intensely pursued as the next step in drug discovery and are expected to address the shortcomings of traditional monolayer cell culture models [77].

Scaffolds for tissue engineering and cell-derived matrices

The use of scaffolds for cell culture has proven to be extremely useful to replicate physiological conditions. Strategies are typically based on mimicking *in vivo* cell microenvironment, particularly the extracellular matrix. This is achieved using a variety of materials, such as hydrogels, porous scaffolds, fibrous scaffolds, or cell-derived materials like alginate or decellularized scaffolds [78]. An advantage of scaffolds is the possibility of forming controlled structures through a variety of methods such as emulsion templating, electrospinning, or salt leaching [79]. Chandra and Singh (2017) showed CDs were nontoxic to cells growing in a 3D microgel environment made with 10% (w/v) polyethylene glycol diacrylate (PEGDA) (molecular weight: 10 kDa) and 1% (w/v) Irgacure 2959 in PBS. CDs were loaded onto the gels at 0.5 mg/ml by dispersing them in CD-PEGDA solution prior to photopolymerization. HeLa cells and NIH-3T3 cells showed negligible toxicity at concentrations up to 1 mg/ml within the gels. Furthermore, CDs were observed to remain loaded onto microgels for up to 12 days after formation [80]. In addition to biochemical composition, another advantage of scaffolds is the similitude with mechanical properties of target tissue. Mechanical stimuli can lead to various responses in cells such as differentiation, migration, and signalling, among others [81]. Stiffness vastly differs depending on the type of tissue, and has been linked with drug resistance in cancerous tissue [82].

Multicellular tumour spheroids (MCTS)

MCTS, also known as spheroids, have been widely used in the evaluation of nanoparticle toxicity screening due to their similarities to *in vivo* conditions such as increased drug resistance, cell-cell interactions, and hypoxia (Fig. 1.16). They are cellular aggregates from cell line monocultures which represent a single type of tissue component [83]. Spheroids can be used to study cancer microenvironment due to the presence of hypoxic areas, cell-cell interactions, and increased drug resistance [84]. Furthermore, they have been used high-throughput drug screening [85]. Scialabba et al. (2019) demonstrated MCTS could be used to monitor biotin-decorated CD (B-CD) delivery through fluorescence imaging. Comparisons between 2D and 3D cell cultures revealed selective uptake through overexpressed biotin receptors in MCTS compared to monolayers [86]. Spheroids were shown to be a suitable alternative to animal models for the study of nanoparticle penetration across tissue.

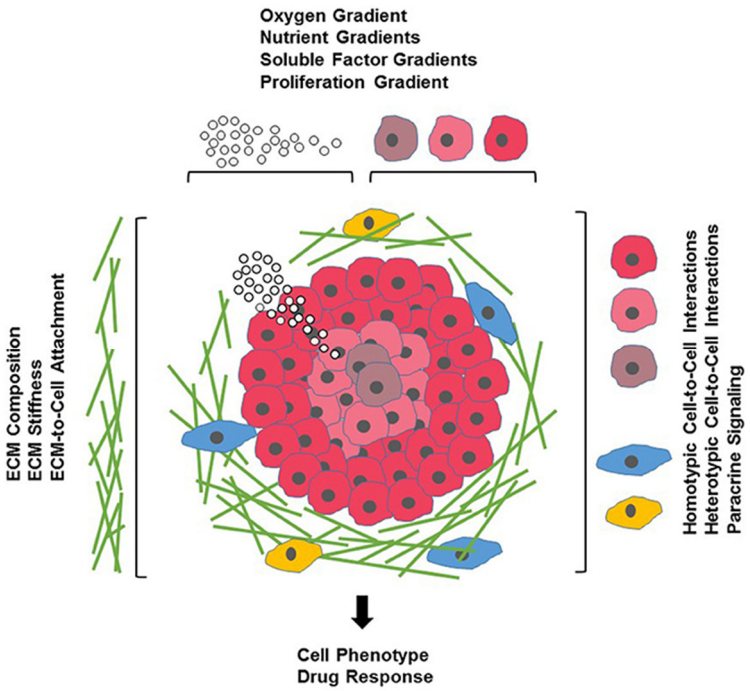

Fig. 1.16 – Multicellular tumour spheroids can replicate some *in vivo* cancer parameters such as hypoxia, diffusion, and ECM formation. Cell phenotype, protein expression, and drug response are more like *in vivo* tumours. Reprinted from Langhans (2018) through the Creative Commons CC BY license [77].

However, MCTS has inherent variability in morphology between individual samples due to differences in growth conditions. Most importantly, this affects diffusion rates across different spheroid layers. Both ellipsoidal or irregular spheroids show significantly reduced hypoxic areas and varied oxygen distribution, influencing drug resistance. Wang et al. (2017) demonstrated a reduction of spheroid size after survivin siRNA silencing and doxorubicin (DOX) delivery with amphiphilic CDs (ACD/Sur), with PEI-coated CDs acting as a comparison. Confocal microscopy demonstrated particle uptake on the spheroid surface and interior and significant size reduction after 48 hours transfection[87]. However, ACD/Sur *in vitro* toxicity was not evaluated using biological assays with spheroids. Instead, the mean diameter from each condition was used as an indicator of uptake and gene silencing. CDs showed high toxicity compared to the literature, with around 80% viability at 25 μg/ml and only 25% viability at 50 μg/ml. This is likely due to the hydrophobic nature of the particle combined with the use of polyethyleneimine (PEI) as a passivating agent. Although spheroids showed a significant size reduction, it is unclear if it is caused by the action of siRNA or the possible toxicity of PEI-coated CDs, which have a zeta potential of +35 mV.

Organoids

Although spheroids are a well-known model, they suffer from clear limitations. They are only partially representative of physiological parameters due to their single cell lineage and are difficult to keep in culture conditions for extended periods of time (>2 weeks). In contrast, organoids are a much more complex 3D cell culture model, which essentially function as miniature versions of different organs, hence their name. They are capable of accurately replicating organ microanatomy, signalling pathways, protein expression, and drug response while comprising multiple cell lineages. Organoids are obtained from either single adult stem cells, embryonic stem cells, induced pluripotent stem cells, patient tumours, or xenograft

tumours (Fig. 1.16). Cancer organoids are typically obtained from tissue samples, as shown in Fig. 1.17. Additionally. organoids have been shown to be excellent platforms for high throughput drug screening in PDT [88].

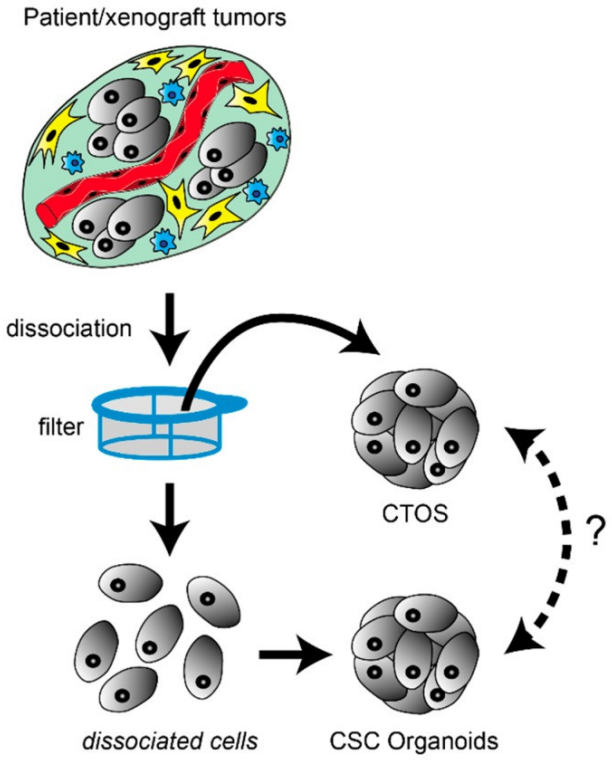

Fig. 1.17 – Cancer stem cell (CSC)-derived organoids. Organoids can be obtained from cancerous tissue after excising samples, digesting them to form single-cell suspensions, and suspending cells in an appropriate medium. Cancer tissue-originated spheroids (CTOS) are prepared through incomplete cell dissociation. Clusters of cells are suspended and rapidly form CTOS. It is currently unclear how interchangeable CTOS and CSC organoid results are between each other. Reprinted from Kondo et al. (2019) through the Creative Commons BY license [89].

However, the cancer organoid model has some significant drawbacks. Their generation is made difficult due to logistical and technical challenges, particularly when scaling production. In a sense, they are highly affected by the "craftsmanship" of each individual. Special care has to be taken during manipulation as tissue rapidly undergoes anoikis, which is a type of programmed cell death caused due to loss of adhesion to a surface [90]. The establishment of

a reproducible protocol for organoid generation in a laboratory typically requires large amounts of resources for validation and optimisation. Access to primary tissue from hospitals is also a limiting factor. Finally, the costs for organoid development are much higher than those for spheroids [89]. Nonetheless, organoids are still an attractive 3D cell model which has been steadily gaining research interest in the field of drug delivery and photodynamic therapy.

Summary

In summary, *in vitro* models should ideally be highly reproducible, resemble *in vivo* physiological conditions, and be adaptable to high-throughput screening (HTS) of compound libraries or experimental conditions. *In vivo* studies have shown all CD samples do not show appreciable toxicity and are readily cleared from the body after short periods of time. However, further testing is necessary to elucidate the mechanism of CD uptake and retention, both *in vitro* and *in vivo*. The use of models such as *C.* elegans, zebrafish, and CAM assay have been shown to provide clinically relevant data while reducing costs and complexity associated with murine models. Additionally, 3D cell culture models for the evaluation of CD-based toxicity have not yet been widely explored. CDs have been shown to have widely varied toxicity *in vitro*, with synthesis conditions possibly contributing the most to this parameter. Therefore, the use of CDs in conjugates should consider previous synthesis conditions to maximize efficiency and decrease adverse effects.

Drug delivery with carbon dot conjugates

Current limitations with drug discovery and development

Drug development is costly and time-consuming, with approximately 90% of new drugs failing to pass clinical trials and subsequently gain FDA approval (Fig. 1.18). Therefore, improvement of drug safety is essential in order to overcome the high failure rate in phase I and II studies

[91]. There are several key factors in drug toxicity, most notably the poor pharmacokinetics of new drugs as over 95% of new potential therapeutic compounds found through drug discovery are not found to be suitable for further evaluation. Conventional drug delivery has several issues that limit the effectiveness of treatments and use of various compounds clinically. The development of new drug delivery approaches has shown drugs can be made safer and more effective [92]. The use of natural products, chemical modifications [93], and computational methods for drug design and discovery have made great impact in this area [94].

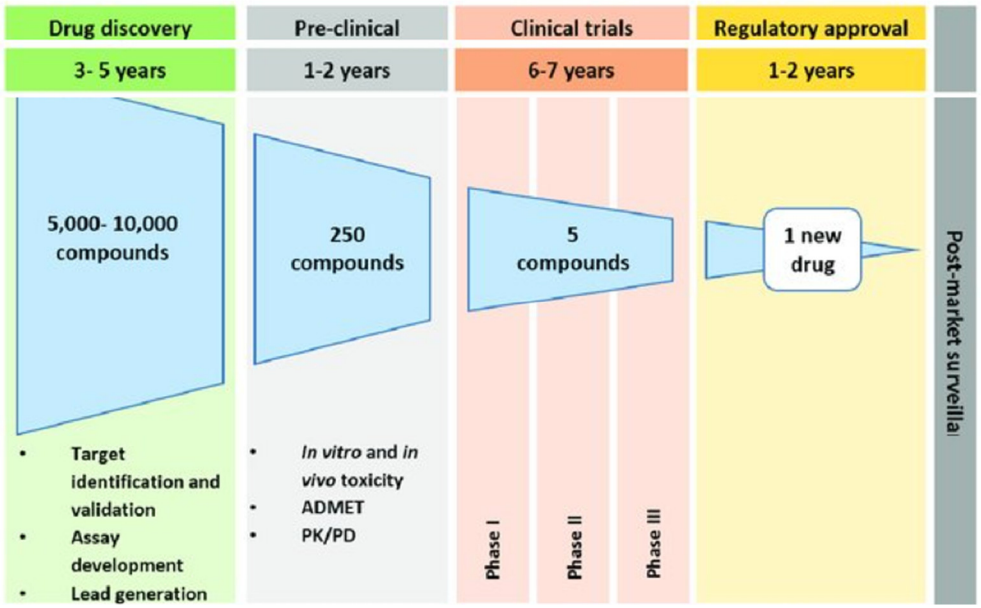

Fig. 1.18 – Discovery and development of new drugs is a multistep process with huge experimental and regulatory hurdles. Many drugs show positive results prior to clinical trials but fail due to unexpected side effects before Phase III. Adapted from Hu et al. (2011) through the Creative Commons CC BY license [95].

Nanomaterials as carriers for improving drug delivery

Drug delivery can be achieved through several different formulations consisting of a carrier and cargo. These can be divided into categories such as virus, immunoconjugates, vesicle-based systems, emulsions, nanoparticles, and polymers, among others [96]. Nanoparticle-drug formulations have been widely studied due to the advantages these systems have such as

increased solubility, bioavailability, efficacy enhancement, and protection from degradation. In particular, nanoparticles can be manufactured and customized for various drug delivery applications including controlled drug release [97]. Furthermore, new nanoparticle-drug formulations are highly attractive as previously unwanted compounds suffering from low solubility, decreased efficiency or specificity, and high toxicity can be evaluated for use in a clinical setting [98]. Nanoparticles also benefit from facile addition of other components such as PEG to improve circulation lifetime during intravascular administration, as it hinders protein adsorption to the conjugate envelope [99].

CDs have been widely studied as part of drug delivery systems in the literature due to their physiochemical properties like high water solubility, interchangeable surface functional groups, photostability, and tuneable fluorescence [100]. For example, fluorescence-based drug tracking is able to provide additional insight to therapeutic efficiency, intracellular localization, and *in vivo* distribution, which is not immediately possible with traditional drug carriers. [101]

Antimicrobial applications

Nanoparticles have several antimicrobial mechanisms such as the production of reactive oxygen species (ROS), destabilization of cell membranes, and interruption of enzyme activity or DNA synthesis. Nanoantibiotics are a promising tool for circumventing the problems of broad-spectrum antibiotics as they simultaneously act against multiple targets. Furthermore, conjugates possess high temperature stability, controlled release, enhanced intracellular uptake, and improved solubility. However, the long-term effects are not yet understood as their interactions with tissue have yet to be completely detailed [102]. Conjugates have been evaluated in both gram positive and negative bacteria.

A key advantage of nanoparticle-based carriers is their high loading capacity due to their

extremely elevated surface area, which can be exploited to achieve high loading ratios while maintaining low toxicity with carriers such as CDs, as can be seen in Fig. 1.19. Thakur et al. (2014) also showed promising results as ciproflaxin-loaded CDs showed drug loading efficiency of >99%, low toxicity in mammalian cells, and pH-dependent controlled release. Prolonged exposure to the antibiotic due to sustained release over a period of 24 hours (up to 18 μM) inhibited the growth of gram-negative bacteria *P. aeuroginosa* and *B. subtilis*. [103].

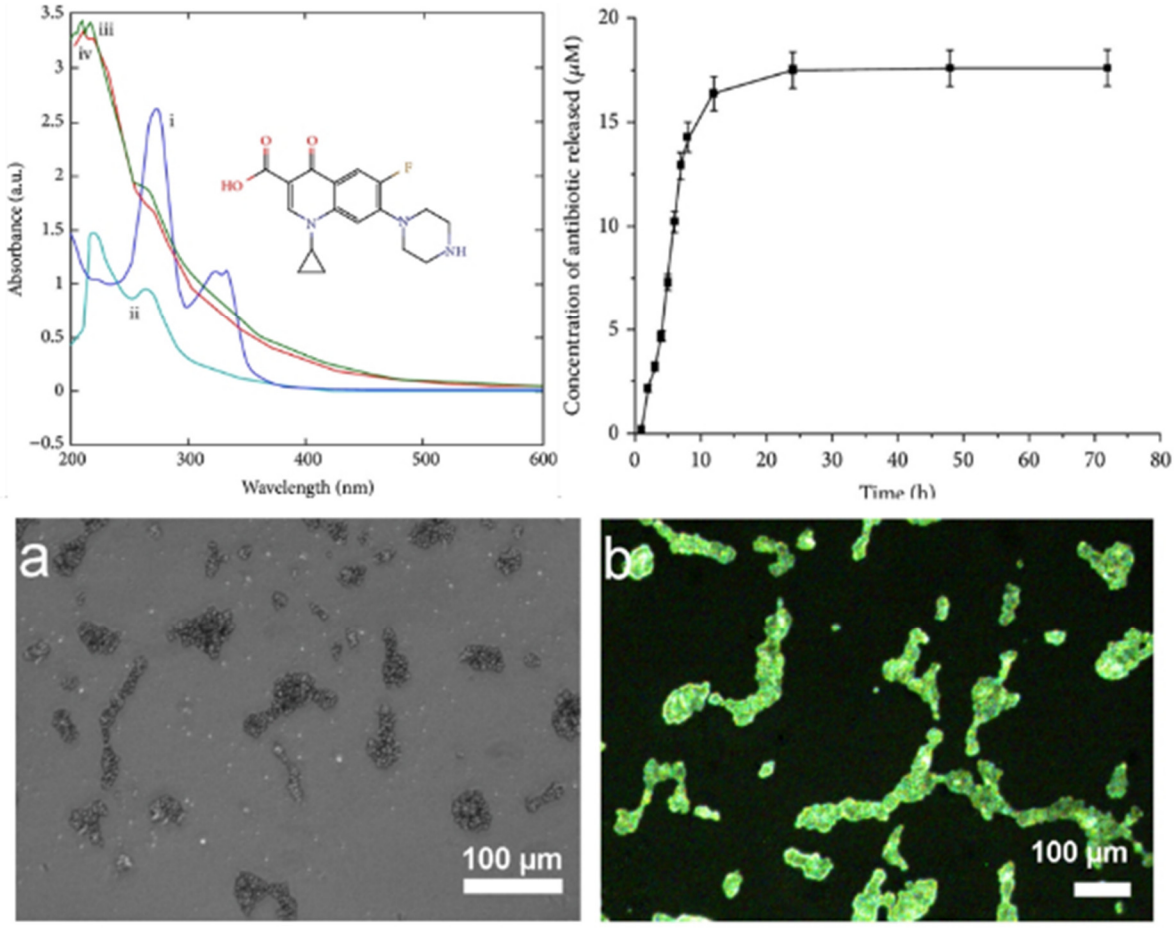

Fig. 1.19 – Ciproflaxin-loaded CDs showed controlled release over a period of 24 hrs. *S. cerevisiae* showed quick uptake and extremely low toxicity from Ciproflaxin release. Adapted from Thakur et al. (2014) through the Creative Commons CC BY license [103].

Yang et al. (2016) demonstrated a 17-fold increase in efficiency against gram-negative *S. aureus* using CDs loaded with lauryl betaine (BS-12), a quaternary ammonium compound. This growth inhibition occurred mostly during the first twelve hours of incubation, while free

BS-12 did not show significant antimicrobial effect at concentrations lower than 30 μg/ml. Likewise, CDs did not show any cytotoxic effect, which indicates there may be a synergistic effect between CDs and BS-12 even with a fraction of the concentration [104]. Gogoi and Chowdhury (2014) also showed CDs could be used to coat calcium alginate beads (CA-CDs) through electrostatic interactions. Tetracycline (TC) and tetracycline associated with β-cyclodextrin (b-TC) were shown to have higher loading efficiency in CA-CDs in comparison to CA hydrogels alone. This system was also shown to be highly adaptable, being capable of sustained drug release across a wide range of pH values [105]. Nonetheless, the loading capacity between Ciproflaxin, TC, b-TC, and BS-12 was highly variable, ranging from 1 to 17-fold loading ratios.

Metal ions improve antimicrobial properties in CDs

Heteroatom doping has also shown positive results with CDs for antibiotic-based applications. Elements such as silver, copper, brass, and gold have been shown to have antimicrobial properties, known as the oligodynamic effect [106]. Metal-doped CDs are an emerging research area which requires further investigation on the interactions between intrinsic CD properties (shape, charge, surface chemistry) and the antimicrobial properties gained through doping. Fang et al. (2019) showed silver-carbon nanocomposites could be synthesized through a facile one-pot reaction. C-dot/Ag composites demonstrated a significant antibacterial effect against *E. coli*, likely due to the release of silver ions causing cell membrane damage. [107] Similarly, Priyadarshini et al. (2017) demonstrated size-dependent toxicity of gold nanoparticles and CDs (Au@CD) in *Candida albicans* at concentrations of 250 – 500 μg/ml. CDs were used to stabilize gold nanoparticles after their synthesis, with nucleation being controlled through varying the amount of tetrachloroauric acid. In addition to their antifungal properties, Au@CDs showed a wide range of properties including surface plasmon resonance (SPR) and tuneable fluorescence [108]. Although these nanocomposites have shown high

efficiency, there are some concerns regarding long-term toxicity and accumulation, limiting their use.

Antimicrobial photodynamic therapy (A-PDT) and photothermal therapy (A-PTT)

A-PDT has been explored as a tool for rapid wound healing, taking advantage of rapid uptake and cell death. Photodynamic therapy is based on the production of reactive oxygen species (ROS) through photoactivation of a sensitizing compound. Kumari et al. (2019) demonstrated CDs could be used as crosslinkers for hydrogels along with cytosine-rich ssDNA and protoporphyrin IX (PpIX). CDs were used as fluorescence resonance energy transfer (FRET) donors for enhanced A-PDT. Interestingly, the ssDNA chain could be modified to adjust FRET efficiency and diminish PpIX quenching. The hydrogel showed sustained drug release over a period of 10 days, with over 90% of the drug being released before 96 hours [109].

There have been reports of CDs with intrinsic ROS production which could be used for A-PDT. Meziani et al. (2016) evaluated CD visible light-induced microbial toxicity. Interestingly, ambient light was sufficient to significantly reduce *E. coli* growth after a 1-hour exposure time while no significant change was seen in the dark [110]. It is possible that highly efficient surface passivation is the key for producing particles with higher ROS production, as fluorescence emission is based on the presence of emissive excited states after light absorption. Jijie et al. (2018) also demonstrated effective A-PDT utilising ampicillin-loaded CDs capable of ROS production, with concentration-dependent bacterial killing after irradiation with 260 nm light (0.3 W, 10/20 min). Ampicillin-CDs inhibited the growth of K12-MG 1655 *E. coli* at 14 μg/ml in comparison to 25 μg/ml of free ampicillin. In comparison, conjugates did not show toxicity to HeLa cells even at concentrations of up to 200 μg/ml, indicating suitability for antimicrobial applications [111].

Photothermal therapy (PTT) is a process similar to PDT in which light-sensitive compounds transform energy from light into heat, causing cell death as local temperature rises over 30° more than standard conditions [113]. This increase can be seen in Fig. 1.20, where temperature steadily rises until the laser source is switched off. Similarly, Kang et al. (2018) demonstrated A-PTT using CDs loaded with IR825, an infrared dye capable of NIR absorption and heat generation. CDs acted as carriers for IR825, which was released in both acidic and basic conditions within cells and enabled targeted A-PTT. This led to nearly 100% drug release after 1 hour of incubation. Approximately 99% of bacteria in a water sample were killed as temperature rose 37 °C [114].

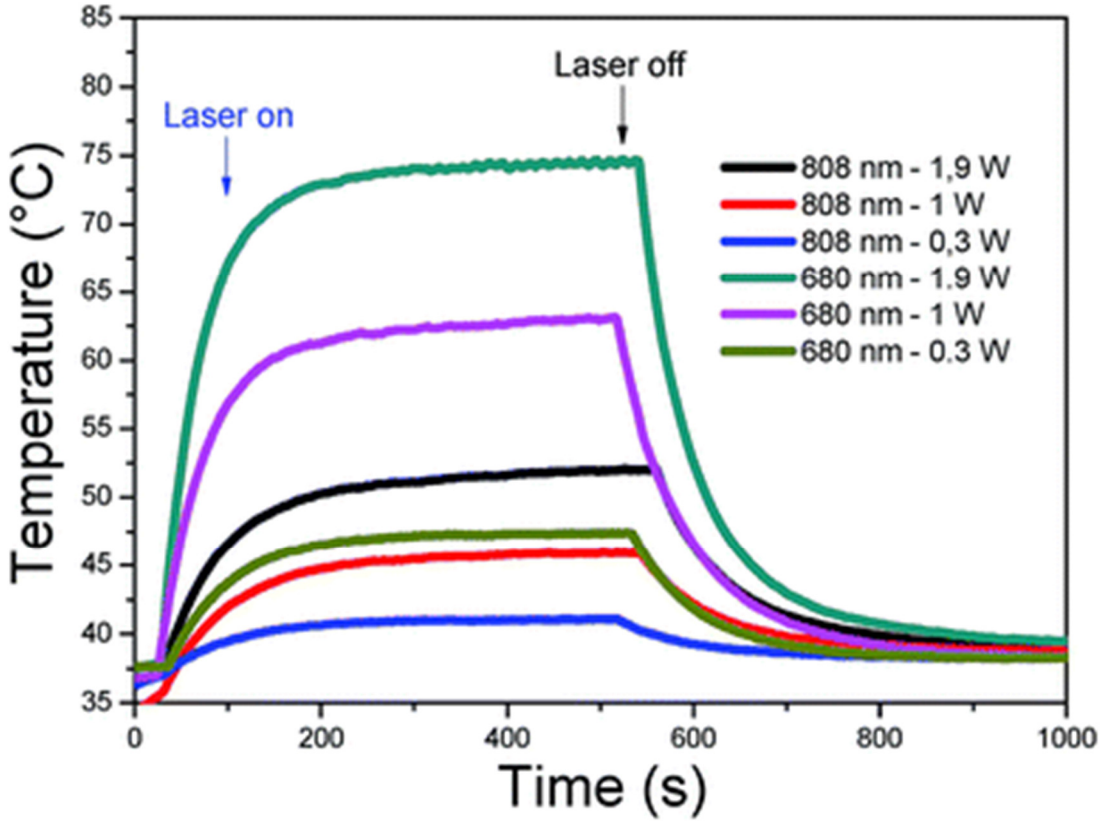

Fig. 1.20 – CDs were shown to be capable of substantial photothermal conversion, increasing temperature over 30° in a 1-minute timescale. Heat generation was used to destroy *E. coli* in exponential and stationary phases. Belkhala et al. (2019) through the Creative Commons CC BY-NC license [112].

Chemotherapy

Chemotherapy has been limited by the inherent drug toxicity and subsequent side effects to patients, as there is cytotoxicity in both healthy and diseased tissue. Therefore, drug toxicity reduction is one of the main benefits of nanoparticle-drug formulations. Drug solubility has always been a key concern as many compounds rapidly aggregate in aqueous media or with high serum concentrations. The formation of aggregates commonly leads to false positives in enzyme-based assays and negatives in cell-based assays, lowering the effectiveness of early screening during drug discovery; improved colloidal stability in serum has been linked to blood circulation lifetime *in vivo* [115]. This has been shown in model systems such as simulated intestinal fluid, where 22 out of 29 drugs rapidly formed aggregates and interfered with enzyme assays [116]. Therefore, the use of model drugs for *in vitro* and *in vivo* evaluation is a crucial part of research in the field of nanomedicine.

Drugs retain activity after loading on CDs

The preservation of drug activity in adverse physiological conditions is crucial for ensuring high treatment efficiency. CDs are highly versatile nanoparticles which can be tailored to have specific surface chemistry and photoluminescence, which has been used to potentiate their efficiency within drug delivery applications. Recent work has shown various biomolecules can be effectively incorporated within CDs and retain their biological activity (Fig. 1.21). Xu et al. (2016) demonstrated FA-CDs retained and enhanced the anti-inflammatory effects of aspirin *in vivo* even after pyrolysis. It is likely that the acetyl groups from the aspirin remain on the CD surface, which interact with the serine residue of cyclooxygenases 1 and 2, effectively blocking oxygenation and avoiding inflammation. Synthesis was adjusted by adding hydrazine for increased solubility and dispersion prior to FACD formation [39]. Likewise, Zhang et al. (2017) utilised CDs with heparin to increase cellular uptake while maintaining the biological

activity and stability of heparin in physiological conditions. The amine-rich CDs and heparin outer shell allowed an extremely high DOX loading efficiency (32.3%) through electrostatic interactions. CD-Hep-DOX showed an increased anticoagulant effect, decreased haemolysis, and steady drug release within acidic vesicles [117].

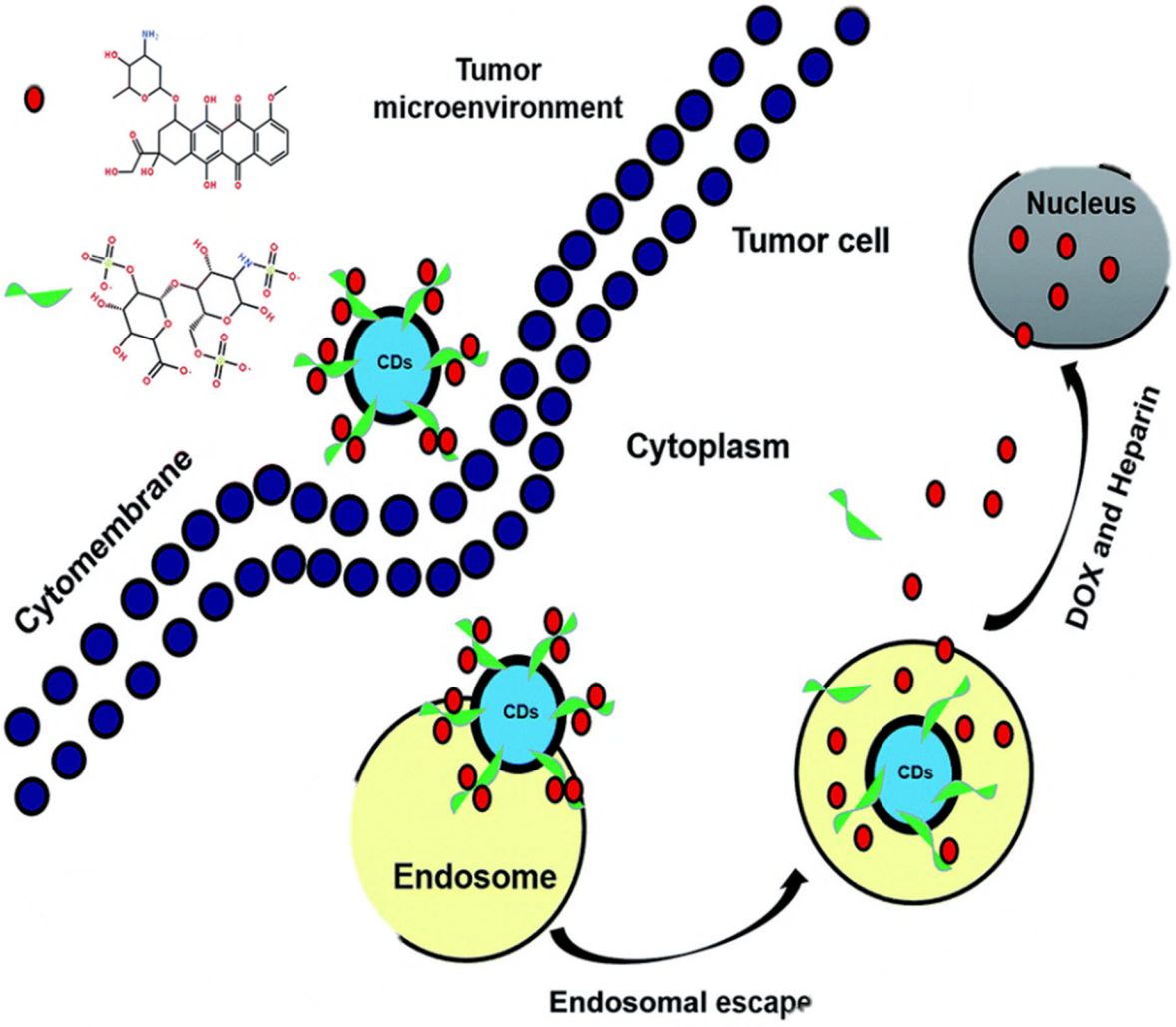

Fig. 1.21 – CDs crosslinked with heparin were shown to efficiently bind doxorubicin and were capable of controlled intracellular release triggered by low pH in tumour microenvironment. Adapted from Zhang et al. (2017) through the Creative Commons CC BY license [117].

Charge-reversible conjugates offer improved pH stability

Drug loading strategies based on CDs as carriers are varied, ranging from covalent crosslinking to electrostatic interactions. Although covalent linking is useful for increasing drug solubility

and stability, electrostatic interactions allow conjugates to display new characteristics based on charge conversion in various physiological conditions, as can be seen in Fig. 1.22. Feng et al. (2016) evaluated *in vitro* and *vivo* uptake and toxicity of charge-reversible CDs (CDs–Pt(IV)@PEG-(PAH/DMMA); CDs were bound with cisplatin (IV) [PtIV] and complexed with a combination of dimethylmaleic acid (DMMA) and poly(ethylene) glycol (PEG)-functionalized poly(allyamine) (PAH) or succinic acid (SA). CDs–Pt(IV)@PEG-(PAH) showed variable toxicity in A2780 cells at pH 7.4 (>11.4 μM) in comparison to 6.7 (5.72 μM), while CDs–Pt(IV)@PEG-(SA) showed no appreciable toxicity at concentrations up to 11.4 μM[118].

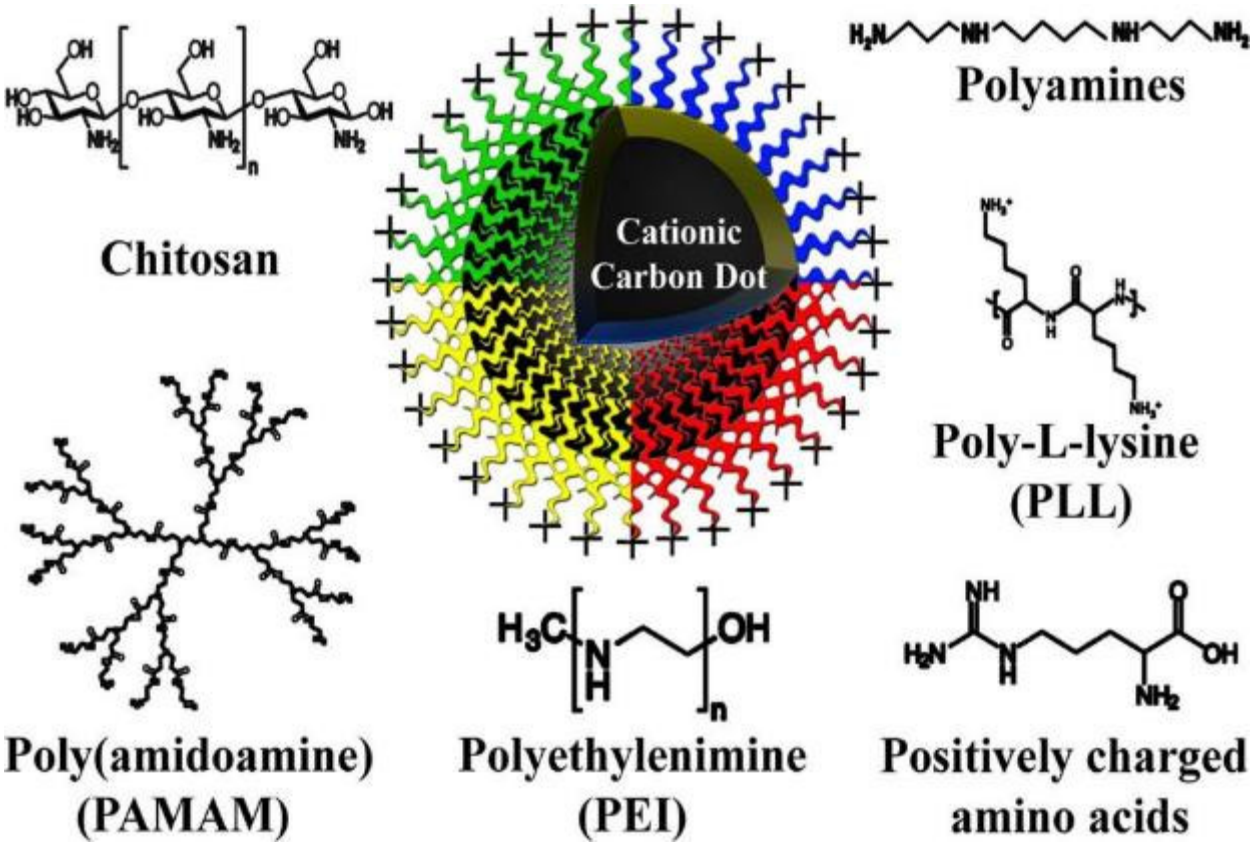

Fig. 1.22 – CD charge can be influenced through passivation to introduce additional amine groups. Nitrogen-containing compounds can also be used as carbon sources for CD formation. Reprinted from Mohammadinejad et al. (2019) through the Creative Commons CC-BY-NC-ND license [56].

Likewise, Wang et al. (2017) reported the synthesis of amphiphilic CDs (ACDs) from PEI capable of forming micelles in water. ACDs showed a low critical micelle concentration value, which suggest they can load hydrophobic drugs such as DOX effectively. DOX@ACDs showed high drug loading ratios and increased efficiency *in vitro*. Additionally, the conjugates were stable in water at 4 °C for several months [87]. Zeng et al. (2016) demonstrated pH dependent DOX release loaded on CDs via electrostatic interactions. DOX loading was optimised by varying citric acid and urea ratios to obtain a predominantly carboxylic acid (-COOH) surface. Conjugates showed a very effective pH response, varying DOX release from 24.2% (pH 7.4) to 86.5% (pH 5). CD-DOX was shown to be more effective against cancer cells (HepG2) in comparison to normal cells (HL-7702) due to the intracellular pH difference triggering selective release[119].

Release profiles can be adjusted based on pH

The adaptability of drug release combined with rapid cellular uptake is important to mitigate the toxicity of chemotherapy drugs such as doxorubicin (DOX), temozolomide (TMZ), or methotrexate (MTX). The possibility of multiple drug release profiles based on pH-sensitive systems would limit release in healthy tissue and improve treatment outcomes in patients, particularly in compounds with high inherent toxicity. Kong et al. (2018) showed DOX loading on CDs using electrostatic interactions, obtaining a 57.5% loading efficiency. Furthermore, the conjugates showed faster release rates at pH 5.0 in comparison to 6.8 or 7.2, likely impacted by changes in CD zeta potential. CDs-DOX showed greatly increased anti-cancer effect and higher apoptosis ratio in comparison to free DOX *in vitro*, possibly due to higher internalization speed of complexed DOX. However, intracellular uptake did not appear to be significantly improved through CD complexation after a 4-hour incubation period [120]. Wang et al. (2015) demonstrated DOX loading with constant drug release and an equal effect to free DOX at concentrations under 320 µg/ml [121]. Variations in loading efficiency and rapid intracellular

uptake could also be influenced by CD size and surface chemistry. These results highlight the importance of controlled CD synthesis in order to achieve both higher efficiency and increase experimental reproducibility.

Controlled drug release is another key component of an ideal nanoparticle-based drug delivery system. Their adaptability makes the use microenvironmental cues for rapid release possible, such as the case with pH gradients in the tumour microenvironment. Yang et al. (2016) demonstrated DOX could be loaded on CDs using 4-hydrazinobenzoic acid as a linker, which formed a pH-sensitive bond capable of cleavage. Conjugates showed improved efficiency *in vitro* and *in vivo* compared to free DOX [122]. Likewise, Yuan et al. (2017) demonstrated CDs loaded with DOX with high loading efficiency and selective release in acidic environments, with the highest release at pH 5. CD-DOX conjugates showed rapid accumulation and cell death. The ratio of apoptosis to necrosis was higher with conjugates in comparison to free DOX. Higher rates of apoptosis are linked to an increased therapeutic efficiency in cancer drugs [123]. However, there have been reports of no significant difference in drug release between slightly acidic and alkaline environments. Pandey et al. (2013) used CDs separated by centrifugation to decorate gold nanorods and load doxorubicin through both covalent and non-covalent bonding. NIR (near-infrared) irradiation also triggered a burst release of DOX (~60%) and no significant differences were observed when pH was adjusted [124].

Combining targeting and efficient delivery improves treatments

There has also been research into crossing the blood-brain barrier (BBB), which represents a significant challenge for drug delivery. Limited accumulation and uptake limit the efficiency of current treatments, leading to complications in conditions such as glioblastoma. Hettiarachchi et al. (2018) demonstrated triple-conjugated CDs (C-DT) based on amide crosslinking of transferrin, temozolomide, and epirubicin can efficiently cross the BBB. The

efficacy of various combinations of conjugates was tested including dual systems with transferrin-temozolomide (C-TT) and transferrin-epirubicin (C-ET), with the triplet system C-DT exhibiting the highest cytotoxic effect against SJ-GBM2 glioblastoma [125].

This work was continued as Hettiarachchi et al. (2019) demonstrated a triple-conjugated system based on CDs, transferrin, and either epirubicin or temozolomide could increase therapeutic efficiency. Non-transferrin drug conjugated CDs did not efficiently reduce cell viability due to poor uptake as the nanoparticles were likely ejected by cell membrane drug efflux pumps. On the contrary, CD-transferrin-drug conjugates showed a drastic reduction in cell viability even at low concentrations. A synergistic effect between both drugs was observed at all concentrations that were evaluated. [125] However, the use of various components with covalent crosslinking requires a multi-step approach to conjugate fabrication. In particular, sequential coupling is less efficient as only approximately half of the available carboxylic acids are converted to amide [126]. Therefore, experimental conditions should be thoroughly standardised in order to maximize drug loading and minimise conjugate loss after sample purification.

Targeted drug delivery can improve treatment efficiency

Currently, it is generally accepted that drug diffusion through lipid membrane is the dominant process for delivery. Lipinski's rule of 5 is used to predict pharmacokinetics of unknown compounds based on 5 criteria. Ideally, compounds should have a molecular mass <500 Daltons, <5 hydrogen bond donors (C-O or N-O bonds), <10 oxygen or nitrogen atoms, and a partition coefficient <5. However, these considerations can be circumvented through the use of carrier-mediated uptake [127].

Targeted drug delivery using receptor-mediated uptake is a very effective strategy to circumvent high compound toxicity and low water solubility. Molecules such as folic acid (FA)

have been used to guide conjugates with great efficiency (Fig. 1.23). Although many drugs are highly effective against cancer, there is a widespread lack of selectivity towards target tissue. Li et al. (2016) also demonstrated delivery across the blood-brain barrier was possible using cancer-targeting transferrin decorated CDs. MALDI-TOF mass spectrometry (MS) was used to estimate the loading of a single molecule of DOX per transferrin. Although DOX-loaded CDs showed higher efficiency in comparison to free DOX, the exact mechanism of cell death is not completely understood. [129] Tang et al. (2013) used a carbon dot and folic acid system to monitor doxorubicin delivery *in vitro* by monitoring FRET. The energy transfer between CDs and DOX is easily detected and was used to quantify drug release. The direct coupling of PEG on the CD surface allowed DOX entrapment through $\pi - \pi$ stacking and showed pH-dependent release. Additionally, real-time monitoring of drug release was achieved in tissue (65 - 300 μm thickness) [130]. Mewada et al. (2014) used bovine serum albumin and folic acid (FA) to coat CDs for improved DOX delivery. Conjugates showed a high drug loading efficiency and pH-dependent release; combined with FA-mediated targeting, they showed great potential in therapeutic applications [131].

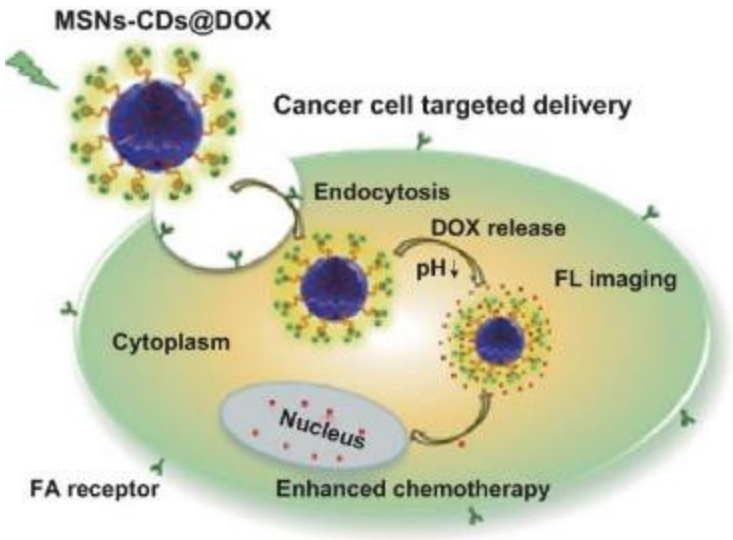

Fig. 1.23 – FA-mediated uptake and targeting has been shown to be effective in treatments against cancer. DOX release is significantly improved after carrier internalization. Zhao et al. (2019) through the Creative Commons CC-BY license [128].

Platinum-based cancer drugs are highly effective and currently used clinically in over 50% of patients. However, they are limited in efficiency in a similar manner to DOX: side effects due to unspecific accumulation in non-target tissue, rapid aggregation, low blood circulation lifetime, and drug resistance. Zheng et al. (2014) showed Oxaliplatin (IV) [Oxa(IV)] loading on CDs through EDC/NHS crosslinking could efficiently be reduced to Oxa(II) and produce significant cell death. Real-time monitoring the fluorescence from the conjugates allowed quantification of gradual drug release with low signal-to-noise ratios [132]. Feng et al. (2016) also demonstrated the benefits of dual responsive drug delivery systems by combining CDs with an RGD targeting ligand, monomethoxypolyethylene glycol (mPEG), and Cisplatin(IV). PEGylation ensured the conjugate was protected at neutral pH, while acidic conditions exposed the RGD peptide for enhanced tumour targeting capability in cells overexpressing $\alpha_v\beta_3$. [133]

Hollow CDs (HCDs) can be used to increase drug loading ratio

HCDs have a display a similar amorphous carbon phase to CDs and an internal cavity with pores. It has been hypothesized that HCDs be used to increase drug loading efficiency as their surface area is larger. Wang et al. (2013) reported the synthesis of HCDs prepared from bovine serum albumin after increasing the time for the solvothermal reaction. Although DOX was adsorbed onto the surface, it showed a decreased loading ratio (6 wt.%) in comparison to other previously mentioned conjugates, as can be seen in Fig. 1.24. Nonetheless, HCDs did not interfere in the pharmacodynamic activity of DOX and showed rapid drug release in acidic pH (<5) [134].

Equally, Gong et al. (2016) reported hollow CDs (HCDs) with high drug loading capacity and demonstrated effective DOX complexing through electrostatic interactions. PNHCDs-DOX composites showed remarkable pH-sensitive release, with only ~3% release at physiological pH in comparison to 96% at pH 5 after a 24-hour period. Conjugates also showed increased

inhibition against cancer cell proliferation and similar *in vivo* efficiency in comparison to free DOX [135]. However, despite positive results HCDs have not yet achieved widespread use, possibly due to complications during synthesis and sample postprocessing.

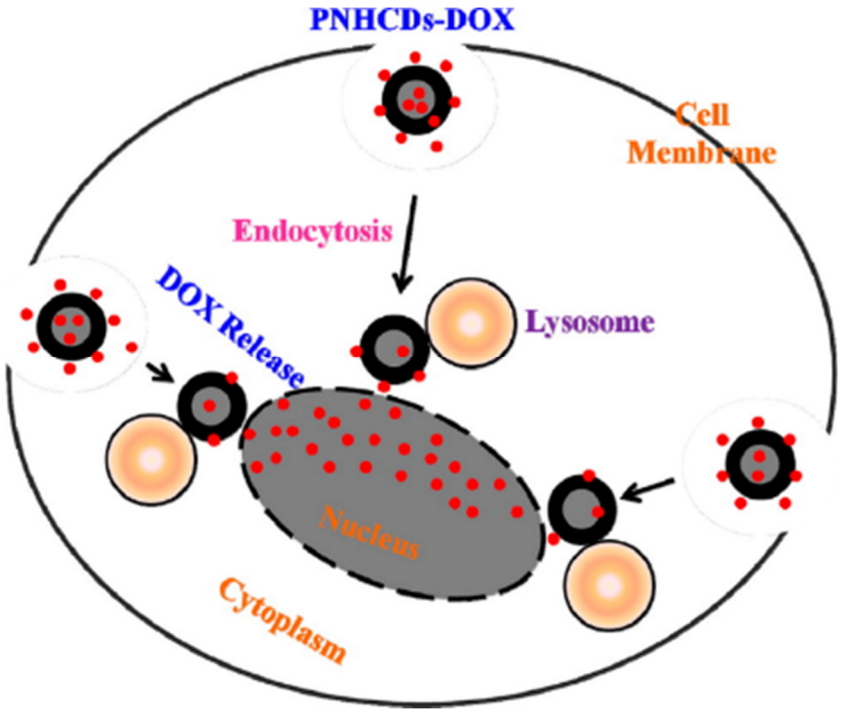

Fig. 1.24 – Phosphorus and nitrogen-doped hollow carbon dots entered cells through endocytosis and showed efficient doxorubicin release near nuclei. Reprinted with permission from Gong et al. (2016). Copyright (2016) American Chemical Society [135].

CDs can be used within multicomponent drug delivery systems

In addition to nanoparticle-based systems, pH-responsive drug delivery has also been explored using other structures. Wang et al. (2017) showed the versatility of CD-DOX conjugates within chitosan nanogels for drug delivery with NIR and pH-triggered release. Conjugates were shown to easily cross the blood-brain barrier due to their small hydrodynamic size (~78 nm) and surface charge (+20.2 mV). The mechanism of uptake is speculated to be adsorptive transcytosis due to similarities with chitosan or albumin-based nanocarriers. *In vivo* drug delivery was highly effective, with a significant reduction of tumour volume at day 18 post injection [136].

Inorganic compounds such as metal organic frameworks (MOFs) and nanoscale MOFs (NMOFs) have also been utilised for this application, taking advantage of their high porosity, tuneable properties, and tailorable structures; these highly crystalline and microporous structures such as zeolitic imidazolate frameworks (ZIFs) have high surface area and have been explored as drug carriers. He et al. (2014) reported the synthesis of C-dots@ZIF-8 nanocomposites for pH-responsive delivery of chemotherapy drug 5-fluorouracil and bioimaging. Cumulative drug release after 48 hours was higher in acidic conditions (92% at pH 5.5) in comparison to physiological conditions (67% at pH 7) [137]. Interestingly, this work was extremely similar to that carried out by Xu et al. (2016) in which ZIF-8 was used as a carrier for DOX-loaded CDs in a one-pot reaction [138]. Fig. 1.25 shows ZIF-8 and the composite CDs@ZIF-8 are similar in surface chemistry but drastically different in photoluminescence. Fahmi et al. (2015) reported the synthesis of composites consisting of manganese ferrite nanoparticles (CM), CDs, and DOX for dual-mode MRI/fluorescence imaging and drug delivery. Drug-loaded composites (DCCM) was shown to enter cells through receptor-mediated endocytosis, with pH-selective drug release. Neutral conditions showed significantly reduced DOX release (22%) after 72 hours in comparison to acidic conditions (pH 5, 75% and pH 6, 60%)[139].

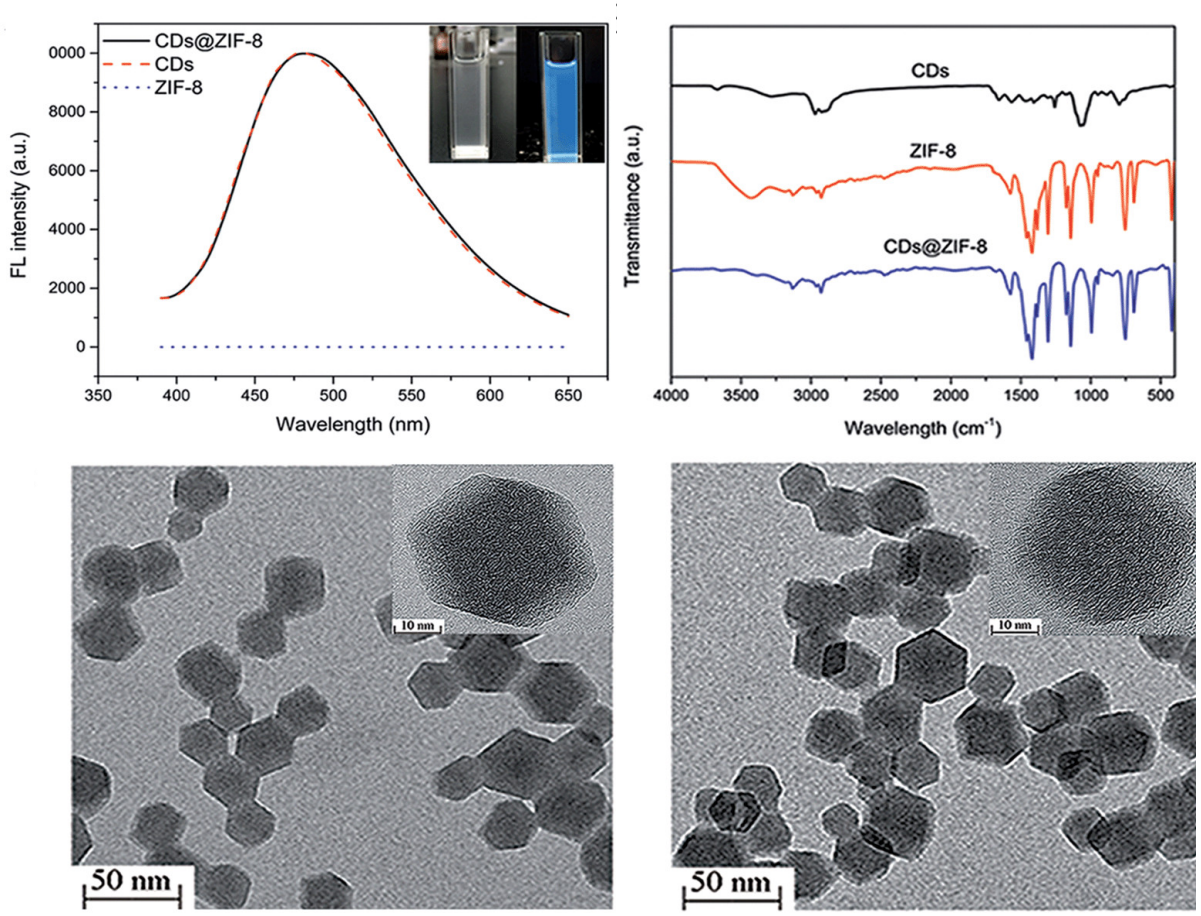

Fig. 1.25 – CDs@ZIF-8 show similar photoluminescence and surface chemistry, indicating complexation. TEM images show ZIF morphology is not affected by CD/DOX loading. Adapted from Xu et al. (2016) with permission the Royal Society of Chemistry[138].

Photodynamic (PDT) and photothermal (PTT) therapy

As previously described, PDT is an FDA-approved non-invasive cancer treatment which makes use of light-sensitive molecules called photosensitisers (PS) that accumulate in tissue. These compounds are capable of producing ROS under irradiation, leading to cell death in the affected area [140]. ROS production is the result of a PS passing from an excited triplet state after absorbing energy to a ground state, passing energy to nearby oxygen (Fig. 1.26). Likewise, PTT employs photoactive compounds to generate heat and ablate cancerous tissue [113]. These treatments have gained increased research interest due to their high specificity,

spatial-temporal selectivity due to light activation, and ease of application.

Nanoparticle synthesis often leads to undesired outcomes such as surface contamination with salts, inconsistent functionalisation, and wide size dispersions, which can affect their properties. Furthermore, nanoparticles are dynamic, changing their behaviour constantly and depending on time after synthesis, environmental conditions such as temperature and humidity, and mode of storage. For example, silver nanoparticles were shown to "age", with surface chemistry changing over time and subsequently leading to variations in toxicity after periods of 1-6 months of storage [141]. These changes are commonly not immediately apparent and are often not taken into account and reported in the literature, leading to issues with inconsistent and unreproducible results [142].

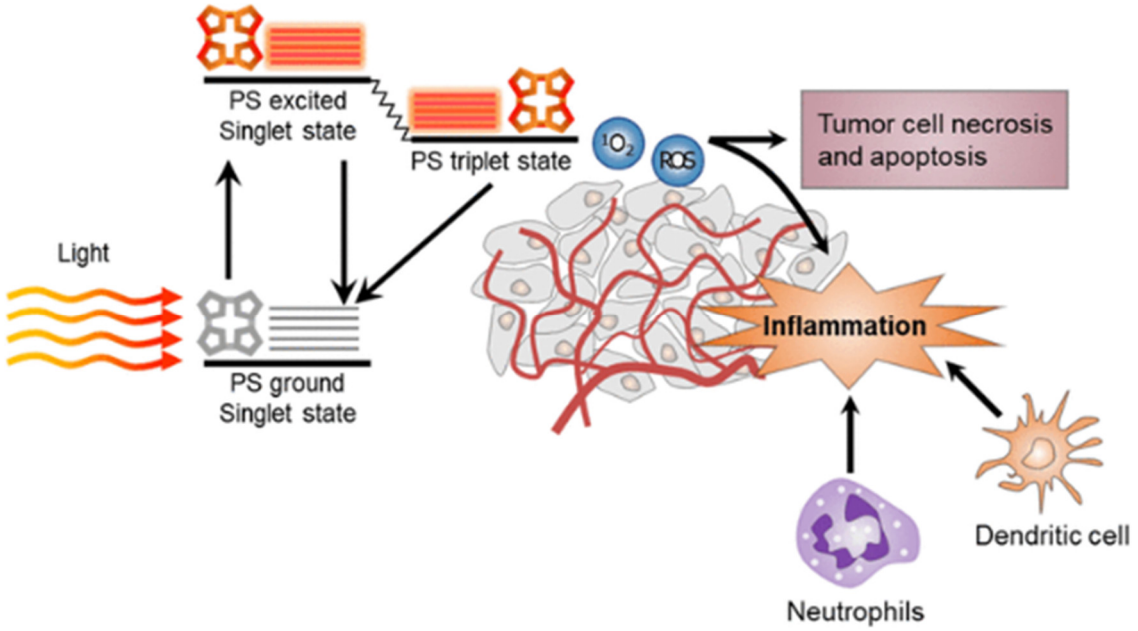

Fig. 1.26 – Schematic showing immune response to PDT. Irradiation causes PS excitation and producing ROS such as singlet oxygen ($^1O_2$). Continuous $^1O_2$ production leads to cell damage and eventual death, inciting an immune response in the affected area. Reprinted from Hwang et al. (2018) through the Creative Commons CC-BY license [143].

Drug loading strategies

PS can be loaded through covalent crosslinking

Covalent crosslinking is a common method for conjugating nanoparticles with other molecules. Reactions are varied and can be adapted for use with a wide variety of functional groups and include hydrazide-aldehyde, amine-carboxyl, thiol-maleimide, thiol-thiol, and gold-thiol bonding, among others. Fowley et al. (2015) showed covalent crosslinking could be used to conjugate CDs to protoporphyrin IX (PpIX), a porphyrin sensitizer used in PDT that produces singlet oxygen [144]. Amide crosslinking based on EDC/NHS (1-ethyl-3-(3-dimethylaminopropyl)carbodiimide/N-hydroxysuccinimide) chemistry showed excellent results as it made use of the high density of carboxyl groups on CD surface to bind molecules at concentrations ranging from 10 to 30 µM, which can be seen in Fig. 1.27. Intriguingly, they observed a fluorescence resonance energy transfer (FRET) from CDs to PpIX. This likely caused quenching of CD-based fluorescence but did not significantly change to singlet oxygen production.

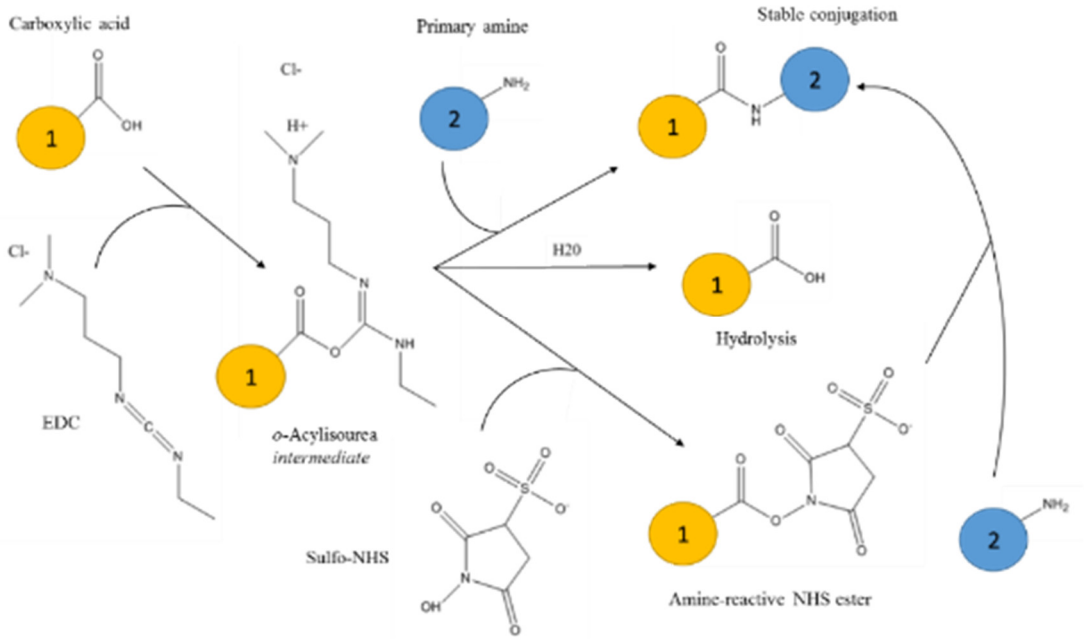

Fig. 1.27 – Schematic representation of EDC/NHS crosslinking. Compound 1, containing carboxylic acid, is prepared for binding as an amine-reactive ester is formed. The intermediate *o*-acylisourea is protected from hydrolysis by NHS/Sulfo-NHS. Conjugation with a stable primary amine group leads to the formation of an amide bond.

Electrostatic interactions can increase loading efficiency

In comparison, loading through electrostatic interactions is an easier and more cost-effective method of drug loading on CDs. Wu et al. (2018) used a tetraplatinated porphyrin complex (PtPor) bound to CDs by electrostatic interactions (CQDs@PtPor) to improve its solubility and cytocompatibility. Singlet oxygen production of CQDs@PtPor increased in comparison to PtPor, likely caused by decreased aggregation in water [145]. In addition to the crosslinking strategies, other modifications can be made to improve or add properties to CDs based on external stimuli. Wu et al. (2015) evaluated the PDT efficiency of 5-aminolevulenic acid (5-ALA), a precursor of PpIX, alongside CDs and triphenylphosphonium (TPP), a coumarin derivative which can target mitochondria. 5-ALA was bound to CDs through a photocleavable carbamate bond to enable intracellular release which can be triggered by one or two-photon excitation. Although two-photon irradiation was slightly less effective than single-photon, the increased tissue penetration and specificity for 5-ALA/PpIX makes it a valuable tool for PDT. However, the time required for 5-ALA release can vary from 10 minutes (5% release) to >120 min (80% release), which may limit its effectiveness. Annexin V-FITC/PI staining confirmed the proapoptotic effect of PDT-induced cell death. Furthermore, it was shown that both violet (400-450 nm) and red (645-655 nm) light irradiation after 30 minutes were able to trigger 5-ALA release through photolysis and cause significant cell death [146].

PS can be embedded within CDs through host-guest chemistry

Host-guest encapsulation is the result of various non-covalent interactions arising from the entrapment of a “guest” molecule within a larger “host”, which envelops it. The formation of these complexes gives rise to new nanomaterials with intriguing properties that can be exploited for theranostic applications, which can be seen in Fig. 1.28 [148]. Typically, CDs are synthesized through microwave-assisted pyrolysis. The addition of a “guest” to the precursor solution allows CDs to form around these molecules, eventually encapsulating them. However,

only molecules which are not affected by synthesis temperatures can be used. Previously, CDs have been used as hosts red/near-NIR dyes cresyl violet (CV), Nile blue (NB), and zinc phthalocyanine (ZnPc) to enhance their optical properties while retaining water solubility and surface chemistry [148]. Zheng et al. (2016) fabricated a host-guest embedded CD composite (CyCD) with the hydrophobic cyanine dye CyOH [2-((E)-2-((E)-2-chloro-3-((E)-2-(1-(2-hydroxyethyl)-3,3-dimethylindolin-2-ylidene) ethylidene)cyclohex-1-en-1-yl)vinyl)-1-(2-hydroxyethyl)-3,3-dimethyl-3H-indol-1-ium iodide] alongside PEG800 for PTT. CyCDs showed improved dispersibility in media and high photothermal conversion efficiency (38%) under 808 nm laser irradiation. Furthermore, composites exhibited significantly reduced dark toxicity caused by CyOH uptake and could be detected using NIR imaging [67].

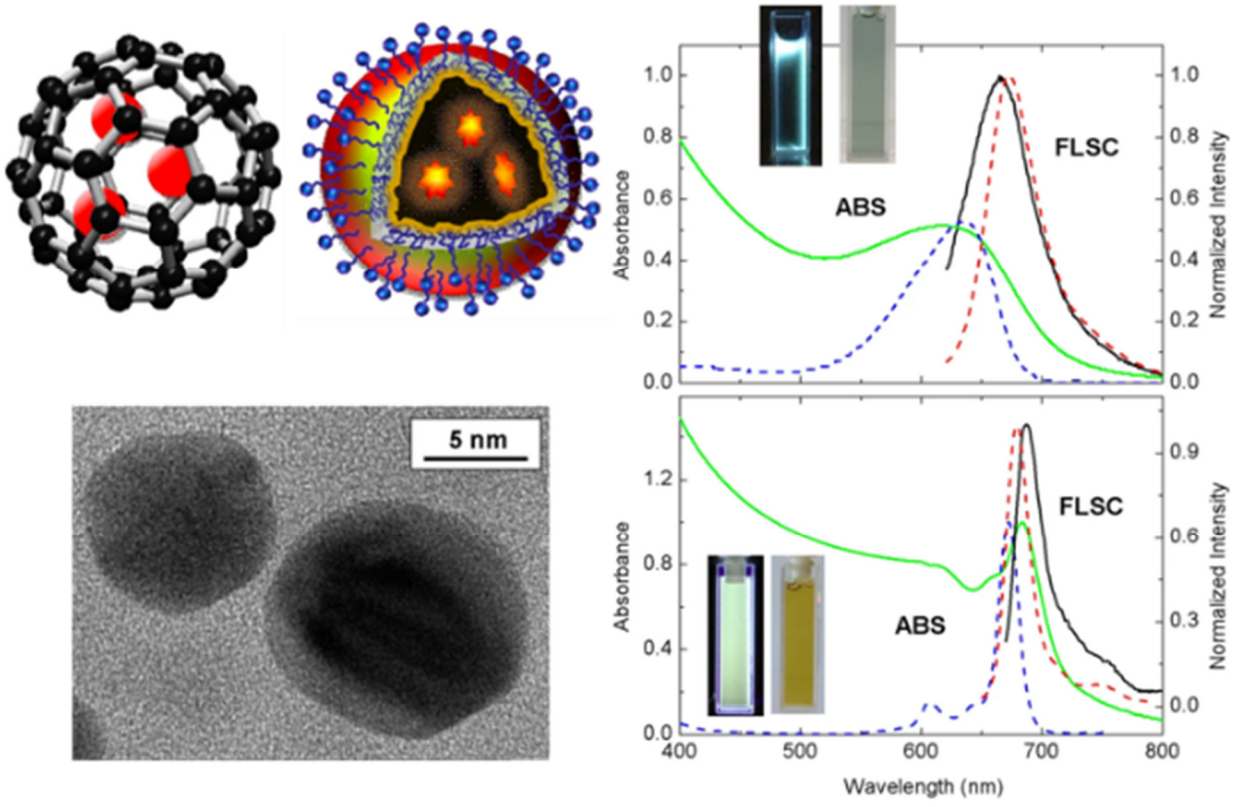

Fig. 1.28 – Host-guest encapsulation of Nile Blue (NB) and Zinc phthalocyanine (ZnPc) within CDs changes optical properties, enhancing emissions in red and NIR regions. Adapted from Sun et al. (2015) through the Creative Commons CC-BY license [148].

He et al. (2018) also showed host-guest embedding with CDs significantly improved diketopyrrolopyrrole (DPP) solubility in water. Singlet oxygen production in DPP CDs was approximately 26.7%, which was very similar to that of free DPP at 31.2%. Confocal microscopy showed conjugates entered cells primarily through endocytosis and escaped lysosomes, residing in the cytoplasm. DPP CDs showed high cytocompatibility (IC50 = 820 μg/ml) in the absence of light irradiation. *In vivo* PDT experiments demonstrated a significant reduction of tumour size after irradiation with a 540 nm laser [149]. Li et al. (2017) also synthesised photosensitiser-loaded CDs in a one-pot reaction using chitosan and mono-hydroxylphenyl triphenylporphyrin (TPP-CDs). This composite material shows larger and more hydrophobic compounds can be effectively incorporated into the amorphous carbon core of CDs while maintaining its single oxygen production and other photophysical properties. Irradiation with 625 nm light (16 mW/cm^2, 1 hr) showed significant cell death *in vitro* after internalization through endocytosis [150]. The above results confirm guest CyOH and DPP molecules are capable of PTT and PTT even while embedded within a carbon core. Additionally, CD-based fluorescence can be used for image-based diagnosis *in vivo* after composite accumulation, improving treatment efficiency.

Treatment efficiency may vary according to loading strategy

Previous studies have demonstrated the effectiveness of CD-based conjugates for PDT. However, it is unclear which loading strategy is preferable to use as both covalent crosslinking and host-guest chemistry have shown exceptional results. Aguilar Cosme et al. (2019) demonstrated the versatility of CDs as carriers by fabricating two different protoporphyrin IX (PpIX) conjugates based on amide crosslinking (PpIX-CD) and host-guest embedding (PpIX@CD). Conjugates were loaded with 34-48% PpIX and were capable of efficient singlet oxygen production after loading. Additionally, conjugates showed decreased aggregation in water compared to free PpIX due to the abundant hydrophilic groups on the CD surface.

Furthermore, PpIX-CD and PpIX@CD demonstrated an equivalent PDT effect in C8161 melanoma cells to PpIX at lower concentrations and decreased dark toxicity. [151] Interestingly, there was no significant difference between crosslinked and host-guest encapsulated conjugates. However, host-guest chemistry required greater control over the reaction conditions to ensure homogeneity and reproducibility. In contrast, amide crosslinking yielded more consistent results but suffered from low product yield and increased cost due to the additional reaction and purification steps required for fabrication.

PDT uptake and efficiency benefit from targeting

As previously stated, targeted drug delivery using carrier systems has been shown to improve PDT treatment efficiency. Small molecule targeting has several advantages such as ease of linkage, stability, and low cost. Choi et al. (2014) synthesised folic acid-coated PEG-CDs and successfully loaded ZnPc through π-π interactions (CD-PEG-FA/ZnPc) to improve PDT. HeLa cells showed rapid CD-PEG-FA/ZnPc and CD-PEG-FA internalization in comparison to CD-PEG particles, which did not enter cells despite prolonged incubation. Conjugates displayed comparable singlet oxygen yield to ZnPc after cell lysate was added to the cell culture, likely due to the competitive displacement of ZnPc from conjugates to other biomolecules [152].

Beack et al. (2015) reported similar results, demonstrating the effectiveness of chlorin e6 (Ce6), CD and hyaluronate (HA) composite for improved transdermal delivery. This system took advantage of the overexpressed HA receptors on cancerous tissue to improve targeting and uptake. Amide coupling was used to bind ce6 and HA to CDs in two different reactions. Improved solubility and singlet oxygen generation was observed in conjugates, with Ce6 and Ce6-CD conjugates did not show significant phototoxicity after irradiation, suggesting HA-mediated endocytosis significantly improved intracellular uptake. Fig. 1.29 shows how Ce6-CD-HA conjugates increased transdermal delivery in mice with B16F10 cancer cells [153].

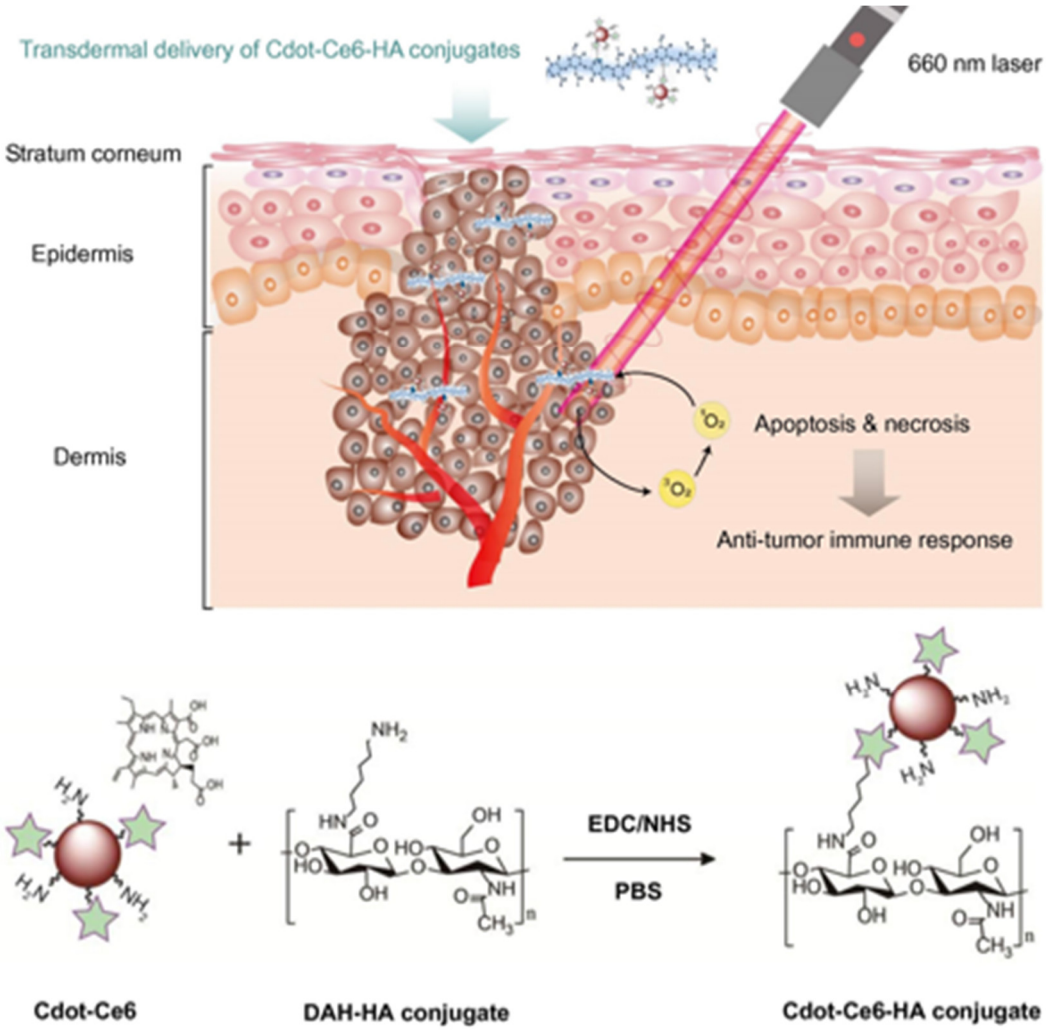

Fig. 1.29 – Ce6 was conjugated with CDs and covered with hyaluronic acid to improve dispersibility in water and improve tissue penetration. NIR excitation enabled transdermal PS activation. Reprinted from Beack et al. (2015) with permission from Elsevier [153].

Nonetheless, the ultrasmall size of CD-based conjugates may not always ensure binding to extracellular domains for receptor-mediated endocytosis. Multivalent targeting, or the use of multiple targeting moieties, could increase the affinity between both molecules and ensure rapid uptake.

CDs may possess intrinsic cell targeting

Although there have been many reports of targeting molecules being used in CD-based systems, CDs may also possess inherent targeting abilities for different organelles. Hua et al. (2014) fabricated CDs with intrinsic passive mitochondria tracking and formed a composite with photosensitiser Rose Bengal. Although compounds such as TPP can be used for mitochondria targeting, there are concerns regarding their cytotoxicity and lack of tracking capabilities. Unlike previously described conjugates, Rose Bengal was conjugated through DCC/HOBt chemistry. CDs showed better performance compared to the commercially available MitoTracker Green dye commonly used for staining. Furthermore, the loading efficiency of Rose Bengal was determined to be 12.5%, with singlet oxygen production and decreased aggregation being observed after conjugation. CDs-RB showed efficient PDT effect after irradiation with a 532 nm laser at intensities ranging from 10 – 50 mW/cm^2 for a total of 5 minutes [154].

Huang et al. (2012) demonstrated nucleus-targeting CDs could be used to improve the photosensitizer fluorescence detection (PFD) of Ce6. This system is capable of direct and indirect Ce6 excitation through FRET. Confocal microscopy confirmed conjugate uptake and accumulation near the nuclei using the characteristic Ce6 fluorescence peaks as reference. CD-Ce6 also showed low cytotoxicity and high laser-triggered phototoxicity. Mice with subcutaneous MGC803 gastric cancer xenografts showed rapid compound accumulation and NIR fluorescence imaging was used to monitor PDT *in vivo*. The fluorescence intensity was used to estimate the optimal time for PDT (based on particle accumulation): 8 hours post injection paired with 671 nm laser excitation. Conjugation with CDs alone improved both the circulation lifetime and the tumour uptake through the EPR effect [155]. However, the exact mechanism by which CDs exhibit targeting is unclear, though it appears to be passive in nature as opposed to active.

PDT in hypoxic microenvironments requires nitric oxide

PDT efficiency in hypoxic microenvironments is a challenging prospect primarily due to low oxygen availability for ROS production and low light penetration into tissue. Nitric oxide (NO) based treatments have seen success in these cases, bypassing the need for oxygenation. Fowley et al. (2015) continued their previous work by demonstrating hypoxic tumours could be treated using CDs loaded with a nitroaniline derivative NO photodonor by irradiation with NIR light at 800 nm, shown in Fig. 1.30. The main advantage of this system is the coupling of CDs in order to use FRET for two-photon based excitation of the photodonor, as their absorption windows typically are outside the therapeutic window (650 – 1350 nm). NO release was not significantly affected after conjugation and there was no evidence of aggregation in water. BxPC-3 induced tumours in mice were shown to be susceptible to two-photon activated NO release [156].

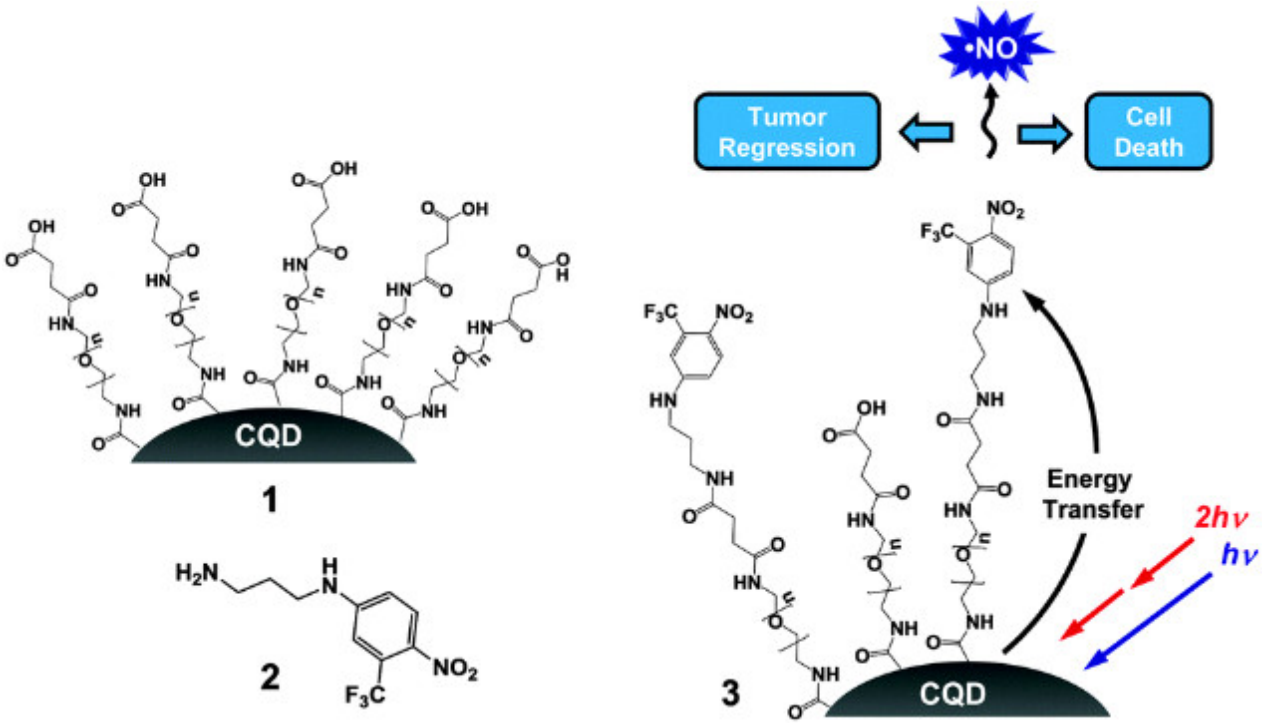

Fig. 1.30 – Schematic representation of CD and NO photodonor linking. Nitric oxide can be produced in environments with low partial oxygen pressure. Reprinted from Fowley et al. (2015) with permission from the Royal Society of Chemistry [156].

In situ oxygen production is also an alternative for improving photosensitiser efficiency in hypoxia. Jia et al. (2018) synthesised a new conjugate by combining CDs (Mn-CD) formed by manganese (II) phthalocyanine (Mn-Pc) alongside 1,2-Distearoyl-sn-glycero-3-phosphoethanolamine-poly(ethylene glycol) (DSPE-PEG). Mn-CDs showed catalytic activity in the presence of H_2O_2, generating oxygen and improving PDT effectiveness. The manganese within the phthalocyanine can also be used to detect conjugate accumulation through bimodal fluorescence/magnetic resonance imaging. Mn-CDs showed red-shifted absorption spectra due to the aromatic moieties of Mn-Pc. DSPE-PEG increased colloidal stability in water, phosphate buffered saline (PBS), and serum-supplemented Dulbecco's Modified Eagle's Medium (DMEM). Irradiation with a 635 nm laser produced significant cell death *in vitro* and *in vivo*, with an enhanced PDT effect in hypoxia confirming the catalytic activity of Mn-CDs [157].

NIR absorption can overcome light scattering in tissue

Light scattering within deep tissue is a key limiting factor in PDT as efficiency is directly tied to the amount of energy that can be delivered efficiently. Indirect photosensitiser excitation is a strategy that has been used to compensate for the low red-NIR absorption of some compounds, although it is limited due to their low two-photon cross section of many dye-based PDT agents. In comparison, CDs have a cross section around three orders of magnitude higher, making them ideal carriers for a PDT nanocomposite system. Fowley et al. (2013) demonstrated CDs could effectively be loaded onto CDs for PDT through indirect excitation via FRET. Singlet oxygen was shown to be generated through both one and two-photon irradiation and conjugates remained stable in a wide range of pH values. PpIX-loaded CDs exhibited significantly reduced dark toxicity and enhanced PDT effect, possibly due to the decreased intracellular aggregation [144].

Composite nanomaterials can improve CD-based conjugates in PDT

CD synthesis with one-pot reactions in contact with organic and inorganic materials have produced novel composites with intriguing photophysical properties that can be used in biomedical applications. Zheng et al. (2016) also showed carbon nitride (C_3N_4) doped CDs (PCCN) bound with PpIX and targeting peptide RGD could be used for efficient PDT in hypoxic cell microenvironments. Carbon nitride is capable of water splitting, which was used to increase the oxygen concentration upon light irradiation at 630 nm (Fig. 1.31). This enhanced the cancer killing capabilities of PpIX, with PCCN showing positive results compared to PpIX when used in an oxygen concentration of 1% in comparison to the physiological levels of 2 – 13%. Oxygen production was shown to be faster than consumption through PDT. *In vivo* biodistribution showed preferential uptake in tumour tissue, decreased accumulation in nonspecific tissue, and improved PDT efficiency [158].

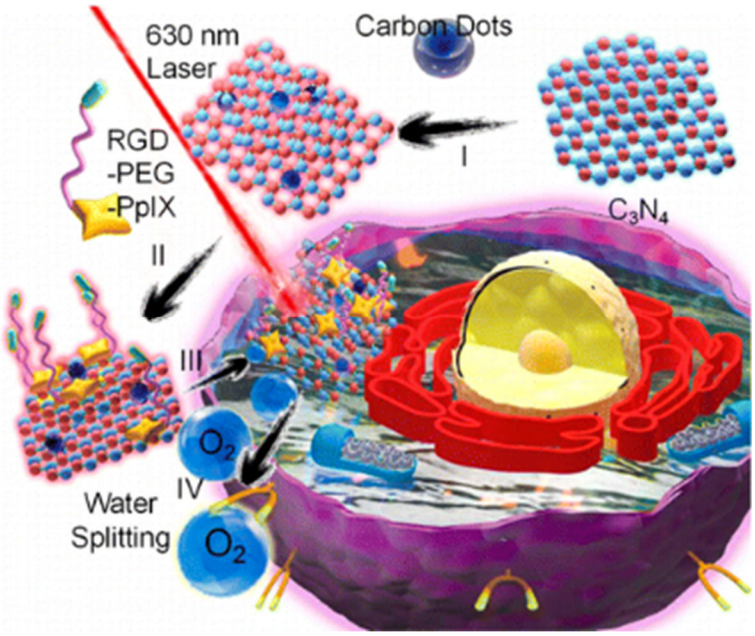

Fig. 1.31 – Alternate strategies for PDT in hypoxic environments can make use of other nanomaterials, such as carbon nitride. Water-splitting produced enough oxygen in hypoxic regions for effective PDT with PpIX. Reprinted with permission from Zheng et al. (2016). Copyright (2016) American Chemical Society [158]

Combination of PDT and PTT can produce a synergistic effect

Embedded compounds maintain their specific properties while benefitting from increased cytocompatibility and hydrophilicity in a similar manner to host-guest encapsulation. Wang et al. (2014) combined the functionality of magnetic iron (III) oxide (Fe_3O_4) nanocrystals and the low cytotoxicity of CDs to form a multifunctional composite capable of multimodal imaging, PTT, and drug delivery. The mesoporous shell of the nanoparticles allowed high efficiency loading of doxorubicin to form a dual anticancer treatment, which could be released with or without NIR excitation. However, composites were shown to have slightly high dark toxicity at concentrations over 40 μg/ml. Nonetheless, a combination treatment of DOX with PTT significantly reduced cell viability and was able to be used alongside magnetic resonance imaging [159].

Guo et al. (2018) used transition metal doping with copper (Cu^{II}) through N-Cu-N complexation to endow CDs with NIR absorption, photothermal conversion, and singlet oxygen production capabilities according to the amount of Cu present in the particle (Cu,N-CDs). Changes in the hydrothermal synthesis significantly affected the PDT/PTT properties as they are likely linked to both particle size and surface chemistry. Fig. 1.32 shows the mechanism for simultaneous PDT/PTT in CDs. NIR absorption was achieved by increasing the available Cu content on the CD surface and 808 nm laser excitation (1 W/cm^2) showed both singlet oxygen production and photothermal conversion [160]. Peng et al. (2018) utilised the photothermal conversion ability of Prussian blue nanoparticles (PBNPs) along with the hydrophilicity of CDs to form conjugates for enhanced PDT and imaging. CD/PBNPs showed a slightly deformed cubic shape, with Fe^{2+}–CN–Fe^{3+} functional groups on their surface. CD/PBNPs did not show significant cytotoxicity at concentrations of up to 0.6 mg/ml and *in vivo* blood chemistry tests did not find any adverse effects. *In vitro* and *in vivo* PTT with 808 nm laser irradiation showed effective cell killing and tumour ablation after 10 minutes as

temperature increased up to 55 °C due to the high photothermal conversion (30%) [161]. Nandi et al. (2017) used CDs to improve the cytocompatibility of tungsten disulphide (WS_2) nanorods for PTT and bioimaging. WS_2-CDs showed increased colloidal stability in water and blue-shifted fluorescence after covalent conjugation. Composites also showed increased cytocompatibility in comparison to WS_2 and other similar metal chalcogenide structures. PTT was carried out using a 700 nm laser and verified by observing the Raman shift at the characteristic peak for WS_2 (352 nm) [162].

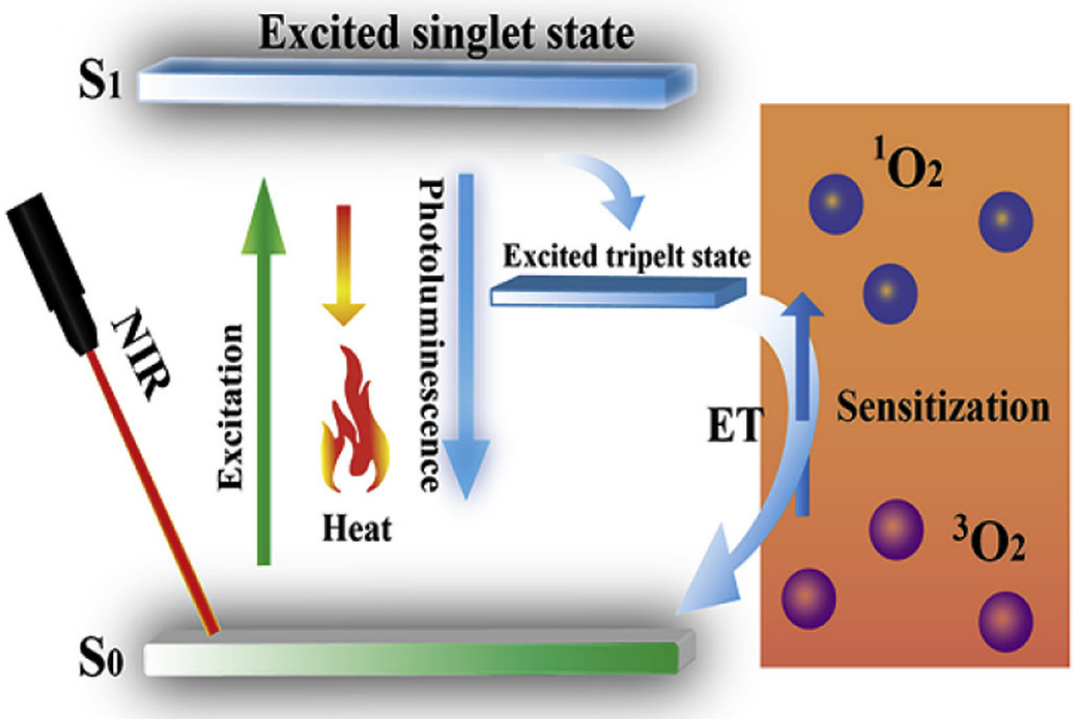

Fig. 1.32 – Photoactivation with an 808 nm NIR laser of copper-doped CDs can produce a simultaneous PDT and PTT effect. Adapted from Guo et al. (2018) with permission from Elsevier [160].

Variations in synthesis lead to CDs capable of PDT/PTT

CDs have been shown to have extremely heterogeneous photophysical properties which are affected by a multitude of factors including the fabrication route and reagents, leading to changes in surface chemistry and size. Recently, CDs have been shown to be capable of PDT

and PTT effects as red and near-infrared emissions were achieved. Ge et al. (2016) fabricated CDs capable of singlet oxygen production and photothermal conversion under laser irradiation at 635 nm. CDs showed very high photostability and sustained singlet oxygen production. Photothermal conversion was also shown to be effective, with a maximum of 50 °C reached after 10-minute irradiation (635 nm, 2 W/cm^2). Dual PDT/PTT treatments showed significant cell death in comparison to single PDT or PTT groups. HeLa-bearing nude mice showed accumulation of CDs in tumours, kidneys, and liver within 10 hours post injection. Although the combined PDT/PTT effect from CDs was not sufficient to cause complete tumour ablation, tissue damage was apparent through the appearance of scar tissue [163]. However, variations in synthesis conditions can also lead to changes that can affect therapeutic efficiency *in vivo*, such as stability in serum. Jia et al. (2017) designed a CD-based nanosphere (CDNS) through ionic self-assembly in the presence of sodium dodecylbenzenesulphonate and passivated with (PEG)-NH_2. These CDs are capable of singlet oxygen production but suffer from inefficient accumulation in target tissue and low circulation lifetimes in blood. [164].

PTT-capable CDs have also been used as part of a hybrid system for simultaneous PDT/PTT. Sun et al. (2019) utilised ce6 and red-emissive CDs (RCDs) capable of photothermal conversion to form composites (Ce6-RCDs). Ce6 was conjugated on RCDs through an amide condensation reaction and showed broad absorption up to the NIR region along with effective singlet oxygen production. Cell viability assays demonstrated high efficiency even at low laser power intensity (671 nm, 0.5 W/cm^2). Additionally, ce6-RCDs also showed potential as multimodal bioimaging with fluorescence, photoacoustic imaging, and photothermal-guided imaging. The laser-triggered PDT/PTT treatment combined with imaging-guided treatment makes this strategy highly interesting [165]. Although reproducibility is a key factor as many of these effects are size and surface-dependent, the prospect of CDs as a new type of PDT/PTT agents is highly interesting due to their excellent stability and cytocompatibility.

Gene delivery

Gene delivery has a wide variety of applications such as antisense and RNAi therapy in addition to cell transfection with plasmid DNA (Fig. 1.33). There have been various systems for delivery that have been investigated, which can be separated into three main categories: modified siRNA, viral vectors, and non-viral vectors. Although viral vectors show very high efficiency, there are various concerns regarding the immunological response caused by residual viral elements. In contrast, non-viral vectors can be designed with biocompatible materials with tuneable properties to enhance gene delivery. These systems need to be capable of preventing degradation, serum inactivation, and be capable of nuclear targeting [166]. Carriers have typically been based on positively charged polymer or lipid carriers such as polyethyleneimine (PEI25k) due to their facile binding to DNA and advantageous intracellular trafficking leading to rapid uptake. However, these systems are typically highly cytotoxic as their delivery efficiency increases. This is possibly caused by the interaction of cationic compounds to mitochondria which cause impaired function and ultimately cell death [167].

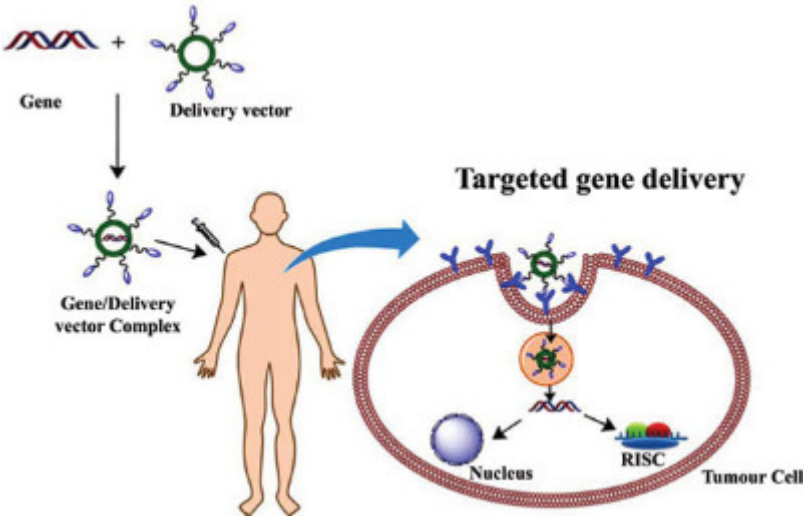

Fig. 1.33 – Gene delivery typically makes use of a vector or carrier to aid cellular uptake while avoiding degradation. Reprinted from Begum et al. (2019) through the Creative Commons CC BY license [168].

DNA and RNA effectively bind to cationic CDs

Carrier systems using nanoparticles have seen increasing research interest as efficiency reaches or even surpasses the current gold standards for gene delivery, such as Lipfectamine2000. Cao et al. (2018) used cationic CDs to condense gene plasmid SOX9 (pSOX9). CD/pSOX9 transfection showed a significant change in chondrogenic differentiation after delivery to mouse embryo fibroblasts [169]. Zhou et al. (2016) utilised a different approach for CD synthesis, using alginate as both a carbon source and cationization agent. CD/pDNA complexes showed equivalent transfection efficiency to Lipofectamine2000 and significantly more than PEI, while maintaining high water solubility and cytocompatibility. Composite internalization was shown to begin through caveolae and clathrin-mediated endocytosis. As mentioned previously, weight ratios under 20:1 (CD/pDNA) showed significantly increased delivery efficiency [170]. Furthermore, modification of surface chemistry through other chemical reactions has been shown to be highly efficient at increasing DNA binding affinity. Dou et al. (2015) demonstrated PEI-functionalised CDs could be used for simultaneous antimicrobial properties and gene delivery capabilities. Particles were further modified using benzyl bromide to quaternize the amine groups on the surface for increased bactericidal effect against gram-negative bacteria. Quaternary linear PEI passivated CDs showed increased inhibition of both Gram positive (*E. coli*) and negative (*S. aureus*) bacteria at a minimum inhibitory concentration of 16 μg/ml. Quaternization also improved the gene transfection capability of CDs by a factor of 10^4-fold after optimising loading ratios [171].

Carriers can shield genetic material and prevent degradation

The degradation of genetic material before arrival in the target site significantly impacts effectiveness. Nanoparticles have been previously used to circumvent these limitations by providing protection while maintaining low toxicity. Kim et al. (2017) utilised PEI-passivated CDs for siRNA (short interfering RNA) delivery through electrostatic interactions. CD/siRNA

complexes protected the cargo from ribonuclease-mediated degradation, prolonging the circulation lifetime and delivery efficiency. *In vitro* studies demonstrated rapid intracellular uptake and low cytotoxicity within HeLa and MDA-MB-231 cells. Furthermore, *in vivo* gene silencing experiments showed efficient GFP knockdown and tumour growth inhibition. Real-time fluorescence imaging was used to observe the gradual intracellular siRNA release over a period of 12 hours [172]. Liu et al. (2019) also used a protein crosslinker sulfosuccinimidyl 4-(N-maleimidomethyl)cyclohexane-1-carboxylate (sulfo-SMCC) to bind si*Tnfα* and CDs for the enhancement of chondrogenesis in mesenchymal stem cells (MSCs). CD-SMCC-si*Tnfα* showed reduced inflammatory response after MSC transfection and effective gene silencing as siRNA was protected from nucleases. This system was shown to be more cytocompatible and stable in comparison to bPEI25k. Additionally, an *in vivo* mouse model showed positive results in cartilage defect healing [173]. Fig. 1.34 shows siRNA delivery in real time could be achieved using CDs as additional imaging probes.

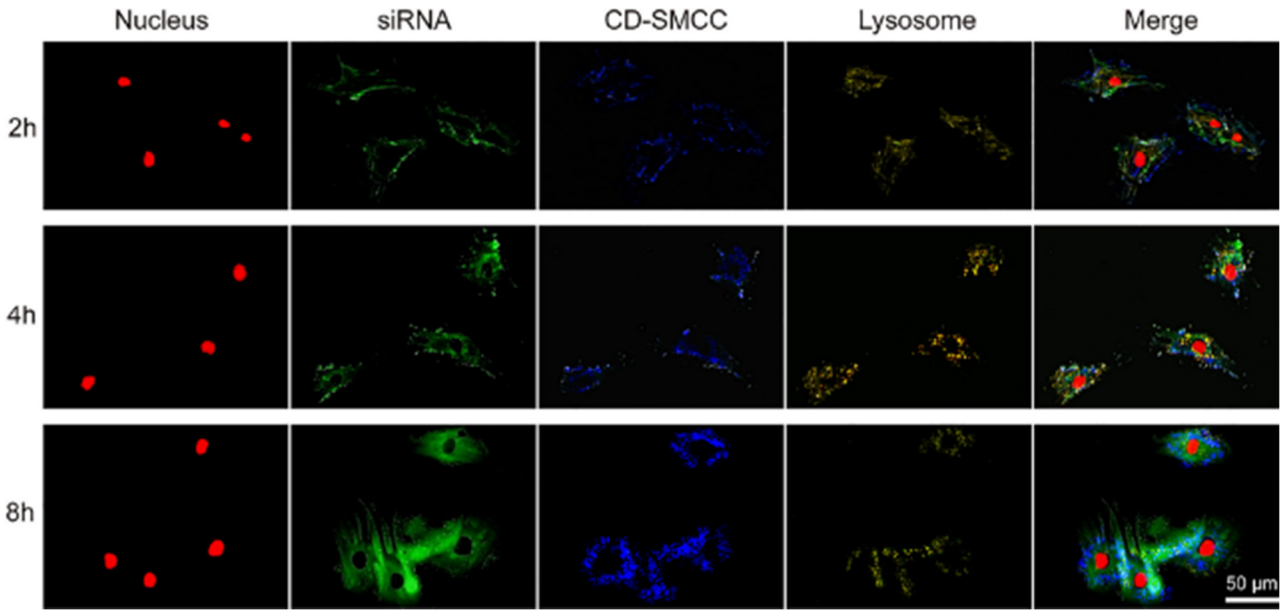

Fig. 1.34 – Fluorescence imaging was used to monitor real-time siRNA uptake in human mesenchymal stem cells. While fluorescein-labelled siRNA was used, this system could be utilised with only CD-SMCC fluorescence. Reprinted from Liu et al. (2019) through the Creative Commons CC BY-NC-ND license [173].

Shell-based systems have also shown great success as controlled release can be adjusted to react in different environmental cues. Zhao et al. (2018) used hyperbranched PEI end-capped disulfide-bond-bearing hyperbranched poly(amido amine) (HPAP) functionalised CDs for improving TNF-related apoptosis-inducing ligand (TRAIL) gene delivery. An outer shielding layer of mPEG-PEI_{600} increased the circulation lifetime of the composite. The HPAP shell can be degraded by glutathione, triggering intracellular DNA release in target cells. Furthermore, dimethlymaleic acid (DMMA) was used to form a charge-convertible particle (PPD@HPAP-CDs/pDNA) by covalently binding it to mPEG-PEI_{600}. Complexes showed *in vivo* tumour growth inhibition and high cytocompatibility with PPD@HPAP-CDs/pDNA obtaining the highest efficiency [174].

CD surface chemistry impacts gene delivery through surface charge

CD-based gene delivery systems primarily make use of electrostatic interactions for DNA loading, taking advantage of high cationic functional group density on CD surfaces. Liu et al. (2012) fabricated PEI-functionalised CDs for plasmid delivery making use of the branched amine-rich polymer to bind DNA in a one-pot reaction. This system was shown to be capable of condensing DNA at very low concentrations but was affected by zeta potential variations as synthesis conditions were adjusted. Longer reaction times showed decreased gene delivery efficiency, possibly due to the destruction of amine groups leading to faster DNA degradation while bound to PEI-CDs. PEI-CD-DNA complexes showed more efficient delivery and lower toxicity in comparison to pristine PEI25k [50]. Wang et al. (2017) showed similar results with carbon dots used for plasmid DNA and siRNA delivery. CDs were modified using 2-((dodecyloxy)methyl)oxirane to produce amphiphilic particles (ACDs) which were able to condense plasmid DNA at an ACD/DNA ratio of 4:1, whereas non-modified PEI-CDs were not capable of this even at an 8:1 ratio. ACDs were shown to have significantly higher transfection efficiency than commercially-available reagent Lipofectamine 2000. [87]

Inorganic and supramolecular structures have been shown to work in tandem with CDs to improve their properties for gene delivery. Cheng et al. (2014) grafted poly[2-(dimethylamino) ethyl methacrylate]-b-poly[N-(3-(methacryloylamino) propyl)-N,N-dimethyl-N-(3-sulfopropyl) ammonium hydroxide] (PDMAEMA-b-PMPDSAH) to CDs through surface-initiated atom transfer radical polymerization (ATRP) to fabricate a gene delivery system (CD-PDMA-PMPD), which is detailed in Fig. 1.35. DNA condensation was achieved in weight ratios of 0.8 to 1.2, with an average particle zeta potential of 30 mV. Furthermore, this conjugate demonstrated reduced protein adsorption and increased transfection efficiency in comparison to PEI25k, which was adversely affected by increasing protein concentration in media. [175].

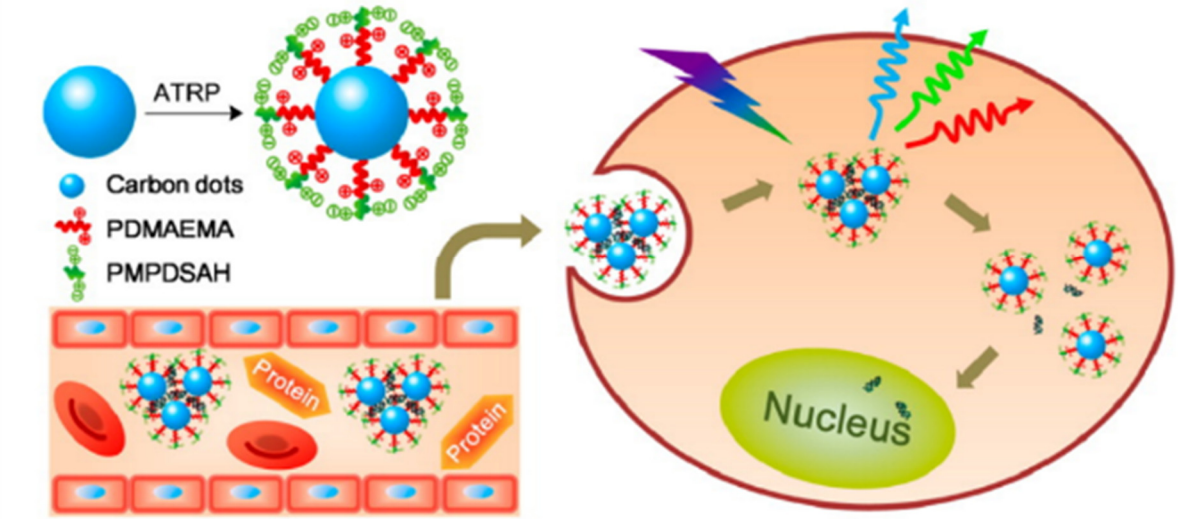

Fig. 1.35 – ATRP was used to graft zwitterionic polymers onto CDs, functioning as multicolour imaging probes with high DNA condensation efficiency. Outer layers protected DNA from degradation and nonspecific interactions. Transfection efficiency was improved 13 to 28-fold in comparison to lipofectamine 2000. Reprinted with permission from Cheng et al. (2014). Copyright (2014) American Chemical Society [175].

Similarly, Das et al. (2015) compared chitosan/amine functionalized silica nanoparticles (ASNPs) and CDs as carriers to compensate for the low half-life of dsRNA. CDs were passivated using PEI which allowed highly effective siRNA complexation and loaded with *SRC* and *SNF7* genes, shown in Fig. 1.36. These samples showed the best results in *A. aegypti* larvae transfection compared to ANSPs. CDs were found to retain 100% of dsRNA up to 72 hours after loading regardless of pH and particles could be tracked *in vivo* using fluorescence imaging systems [176].

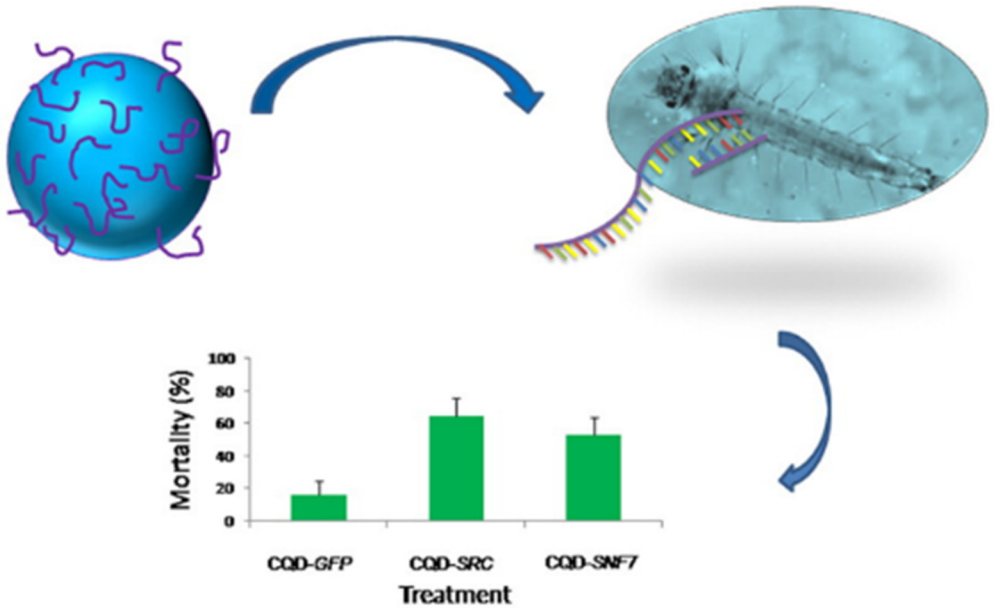

Fig. 1.36 – siRNA-loaded CDs showed fast complexation, retention, and effective gene silencing in mosquito larvae compared to chitosan and silica-complexed siRNA. Reprinted with permission from Das et al. (2015). Copyright (2015) American Chemical Society [176].

Targeted delivery with CDs as carriers can reduce immune response

Gene delivery with nanoparticles can reduce or eliminate the immune response found with viral vectors. In some cases, this strategy can be more efficient as larger payloads can be administered. Targeted delivery can be used to further improve this as it improves cargo release within a specific site [177]. Jaleel et al. (2019) utilised folate-functionalised CDs to decorate graphene-reinforced chitosan nanoparticles coated with diamine PEG for tumour-targeted delivery of pDNA containing *Tnfα*. CDs were shown to be effective at guiding the conjugate

and could be used to monitor uptake in real time [178]. Wu et al. (2016) used a similar approach, with folate-conjugated CDs passivated with PEI for siRNA delivery. Simultaneous siRNA loading and intracellular delivery was confirmed using EGFR and cyclin B1 in H460 lung cancer cells. A synergistic gene silencing effect was observed when loading both siRNAs in comparison to single-loaded particles. In addition, nude mice bearing H460 tumours showed growth inhibition after aerosol-based delivery of nanoparticles, as inhalation rapidly led to accumulation within the lungs [179].

Bioimaging for detection of successful gene delivery

Image-based detection of gene delivery has been shown to be highly successful at evaluating DNA/RNA internalization and accumulation within specific cells. Gene-carrying vectors with fluorescence can be used to monitor gene uptake in real-time and elucidate more specific mechanisms of nanoparticle trafficking using tools such as confocal laser scanning microscopy (CLSM). Its high spatial resolution combined with multiple imaging modes for fluorescence probes has been used to resolve gene delivery in both human cells and animal tissues up to a single-particle level [180]. Therefore, highly fluorescent imaging probes capable of gene delivery are suitable for this application. Pierrat et al. (2015) fabricated CDs with high quantum yield with bPEI25, a hyperbranched cationic polymer, for improving pulmonary nucleic acid delivery. Compared to PEI/plasmid-based transfection, CDs showed similar efficiency and cytotoxicity. However, bPEI25k/siRNA complexes caused significantly more cell death compared to CD/siRNA. This suggests CD surface chemistry and synthesis protocol play an important role in toxicity. Nonetheless, CD/pDNA complexes showed enhanced transgene expression *in vivo* compared to bPEI25k. They also displayed an equivalent efficiency to the cationic lipid formulation GL67A, which is considered to be a gold standard for transfection [181].

Likewise, Hu et al. (2014) fabricated CDs with extremely high quantum yields (54.3%) for EGFP plasmid delivery. It was shown that the loading weight ratio was a key factor in the improvement of transfection efficiency as CD/DNA complexes were formed [182]. Fluorescence-based imaging can also be useful for quantifying cargo release at various time points. Noh et al. (2013) used negatively charged CDs to form covalently bound conjugates with a double-stranded DNA oligonucleotide to monitor miRNA124a expression during neuronal differentiation *in vitro* using fluorescence imaging. The fold expression change was obtained by comparing total fluorescence intensity at various timepoints in CHO cells at concentrations up to 100 pmol [183].

CDs doped with heteroatoms show higher loading efficiency. It has been shown that CDs can be doped with heteroatoms to improve their existing properties or introduce new ones. Nitrogen and phosphorus doping have been used to increase CD photoluminescence by introducing additional surface defects, while simultaneously conferring a positive charge suitable for loading DNA/RNA [184].

Wang et al. (2018) evaluated the effect of nitrogen/phosphate ratios in CDs on siRNA loading. Cy3-labelled siRNA was shown to be increasingly more effective as the N/P ratio was increased. The available siRNA was completely complexed by CDs at a 20:1 ratio [185]. Zuo et al. (2018) synthesised fluorine-doped CDs (F-CDs) from tetrafluoroterephthalic acid and branched PEI. Fluorination has been previously shown to decrease the surface energy of cationic polymers, making electrostatic interactions more favourable at lower concentrations. EGFP transfection efficiency was shown to increase two-fold after fluorine doping. Additionally, it was shown that the incorporation of fluorine atoms in aromatic rings increased F-CD fluorescence without compromising the electrostatic interactions for gene delivery. F-CDs showed improved stability and carrying efficiency in high serum concentrations and low

DNA concentrations, outperforming both Lipofectamine2000 and PEI25k (Fig. 1.37) [186].

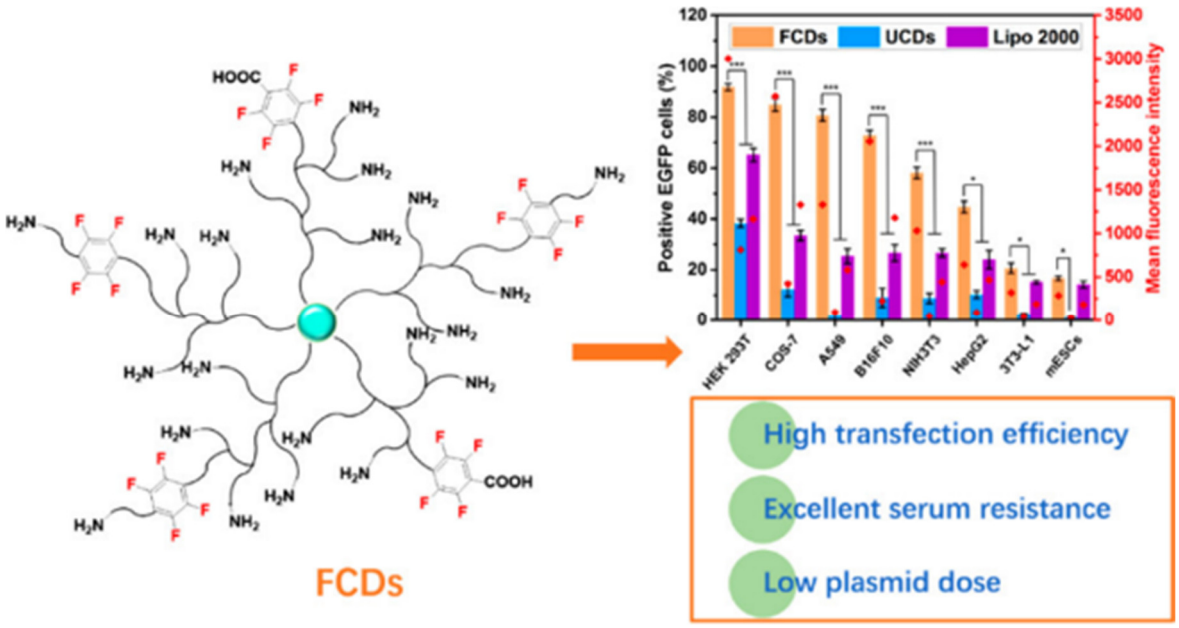

Fig. 1.37 – Fluorine-doped CDs showed improved gene delivery efficiency compared to undoped CDs (UCDs) and the gold standard lipofectamine 2000. Reprinted with permission from Zuo et al (2018). Copyright (2018) American Chemical Society [186].

Bioimaging

Advantages of CDs as bioimaging probes

Biomedical imaging has seen great advances as nanotechnology has been used to fabricate new contrast agents with exceptional performance. Multimodal imaging has grown as a tool for medical diagnosis as contrast agents can be simultaneously detected through techniques such as magnetic resonance imaging (MRI), fluorescence microscopy, or computed tomography (CT). Luminescent nanoparticles are poised to be an integral part of a new generation of theranostics systems, integrating therapy, imaging, and diagnosis. Nanoparticle-based probes have several advantages including increased stability in physiological conditions, resistance to photobleaching, high quantum yield, and resistance to degradation. Conventional dyes are severely limited by their rapid bleaching and low water solubility in addition to increased

toxicity after intracellular uptake [187].

Photoluminescence in CDs varies according to synthesis conditions

Intrinsic fluorescence is one of the most important properties of CDs and has attracted research interest since they were first reported. Their photoluminescence has been shown to be a multifaceted process affected by the amorphous carbon core with sp^2 hybridization and C=O/C-N functional groups (Fig. 1.38). Surface passivation with polymers like PEG and PEI, or with small molecules like EDA have been shown to efficiently enhance photoluminescence in CDs and can be readily linked to other bioactive molecules [188].

Zhai et al. investigated the role of various passivating agents in the amine/carboxyl ratios of microwave-synthesized CDs. Quantum yield was shown to increase with total reaction time, though overheating the solution led to the destruction of many surface functional groups, thus lowering photoluminescence [53]. Guo et al. (2018) made use of an oil/water interface based on $CuSO_4$-H_2O_2 catalytic-oxidation to control CD surface chemistry during synthesis. This allowed them to obtain more control over their photoluminescence, though the use of styrene could limit their solubility in water [189]. While surface passivation is certainly useful, non-passivated CDs can also exhibit improved quantum yields. Bhunia et al. (2013) demonstrated the effect of pristine CD photoluminescence based on synthesis temperature. They were able to fabricate CDs with distinct emission maxima using the same reagents, with quantum yields ranging from 6 – 30% [190].

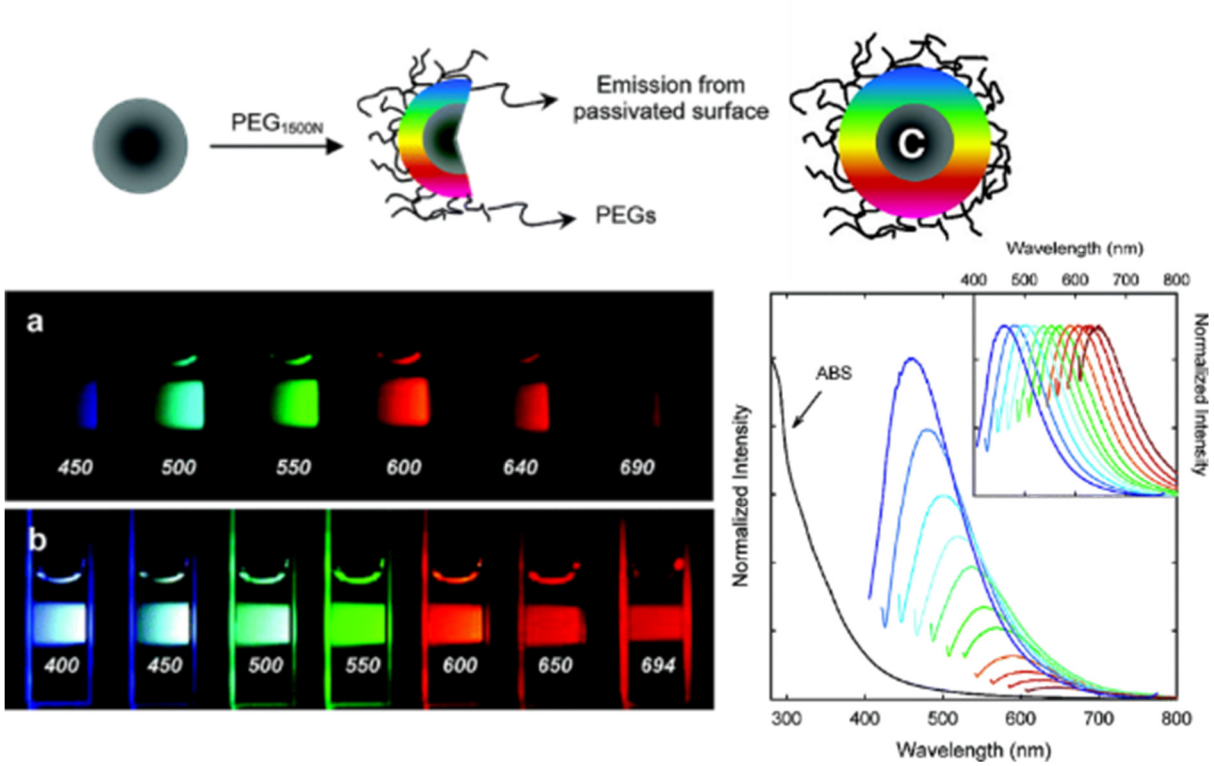

Fig. 1.38 – CD photoluminescence is excitation-dependent and increased with PEG_{1500N} passivation. Multicolour PL can be observed after excitation at various wavelengths using a ban-pass filter. Adapted with permission from Sun et al. (2006). Copyright (2006) American Chemical Society [191].

Multiphoton imaging with CDs

Multiphoton imaging is another key area of opportunity for CDs, as they intrinsically possess high two-photon cross sections. This property has been used to extend their capabilities within bioimaging applications, particularly in confocal laser scanning microscopy [192]. Yang et al. (2009) showed CDs could be readily used as imaging probes with both single and two-photon excitation. Their efficiency as contrast agents was determined to be similar to commercially available CdSe/ZnS PEG-functionalised quantum dots while showing high cytocompatibility and photostability [46]. In addition to multiphoton imaging, high-intensity NIR femtosecond lasers have also been used to indirectly excite loaded molecules through FRET [130,153,156].

Tuneable photoluminescence is influences by multiple factors

Nonetheless, multicolour tuneable photoluminescence in CDs has been difficult to achieve due to limited control over surface chemistry and nanoparticle dimensions. Lu et al. (2014) utilised a rapid screening approach for CD synthesis based on the variation of synthesis conditions and reagents using a microreactor. Their evaluation of 89 combinations of reagents, time, and temperature indicated that these factors do not cause a significant change in photoluminescence. However, it was determined that the addition of nitrogen-containing compounds effectively improved quantum yield [193]. There have been reports indicating specific reagents can be used to obtain blue, green, or red emission. Jiang et al. (2015) observed variations in CDs fabricated using three phenylenediamine isomers [*o*-phenylenediamine (oPD), *m*-phenylenediamine (mPD), and *p*-phenylenediamine (pPD)]. Solvothermal synthesis using the same conditions led to drastically different PL spectra, with green (oPD-CDs), blue (mOPD-CDs), and red (pPD-CD) emissions obtained at 365 nm excitation [194]. Likewise, Meiling et al. (2016) observed the use of Tris-acetate buffer with starch as a precursor greatly improved CD quantum yield. They also observed an increase in absorbance as reaction time was increased from 5 to 120 minutes [195].

Near-infrared (NIR) and infrared (IR) imaging with CDs

Imaging of tissue is typically difficult due light scattering in tissue and low depth penetration. The use of the NIR windows NIR-I (700-900 nm) and NIR-II (1000-1900 nm) circumvents these limitations, providing substantially decreased tissue autofluorescence and scattering, leading to better signal-to-noise ratios [196]. CDs typically have very poor absorption in the NIR/IR region, with the bulk of absorbance centred in the ultraviolet and near ultraviolet (<400 nm). Huang et al. (2013) circumvented this limitation by coupling CDs to the NIR dye ZW800. CD-ZW800 showed similar absorption peaks to ZW800 and demonstrated good stability in serum-supplemented media, suggesting longer circulation lifetime *in vivo* [61]. Geng et al.

(2018) used a different strategy to improve CD absorption in the NIR region by introducing pyrrole and graphitic structures, with N-O-CDs showed a quantum yield of 16.1% (Fig. 1.39) [197]. However, this strategy inevitably leads to sample variability as there is no way to differentiate between CDs containing introduced moieties. Tao et al. (2012) reported red-emissive CDs after oxidizing the by-products of carbon nanotubes and graphite. Although CD photoluminescence is decreased with red or NIR excitation, tissue autofluorescence is reduced even further, leading to a much higher signal-to-noise ratio [37].

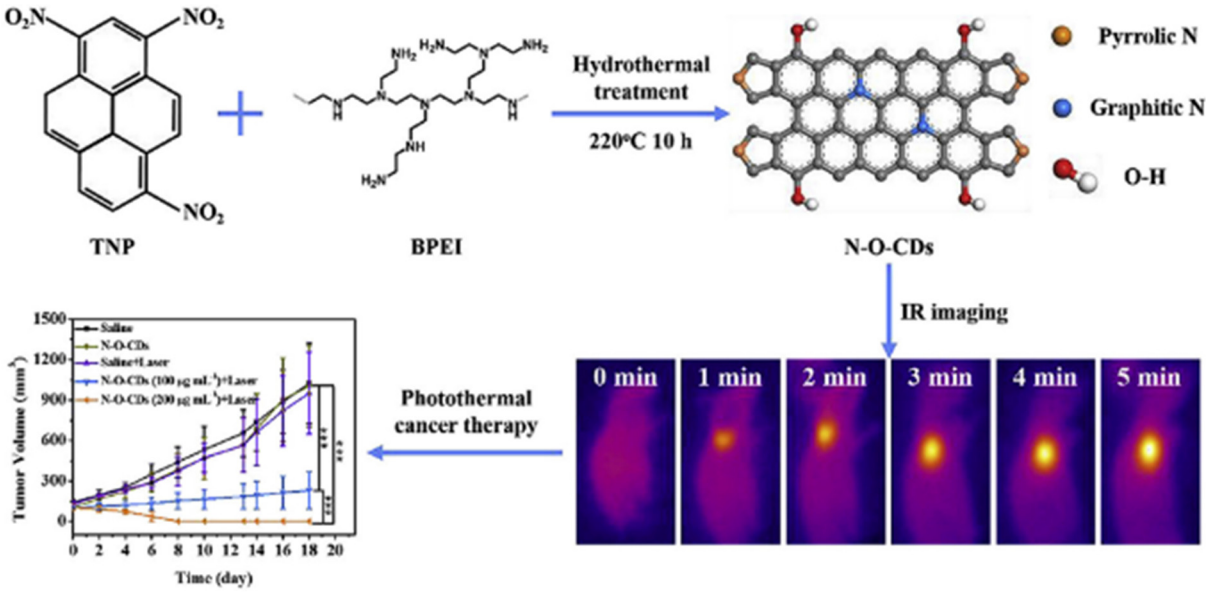

Fig. 1.39 – N-O doped CDs show strong NIR absorption due to the presence of pyrrolic and graphitic residues on surface edges. IR imaging and PPT were shown to be effective using an 808 nm laser at the absorption maxima. Reprinted from Geng et al. (2018) with permission from Elsevier [197].

Heteroatom doping significantly increases CD quantum yield

Doping with different elements has also been used to great success to increase CD quantum yield, with amine-containing compounds being routinely used in many methodologies due to its simplicity and low cost, as can be seen in Fig. 1.40. Other elements have also been utilised as dopants for these nanoparticles, such as phosphorus and bromide. Zhou et al. (2014)

demonstrated phosphorus could form surface defects on the CD surface as a result of its larger size, affecting photoluminescence. QY was shown to be highly dependent on both quinine/phosphorus bromide ratios and total reaction time. However, phosphorus-doped CDs showed reduced photostability in comparison to pristine CDs [54].

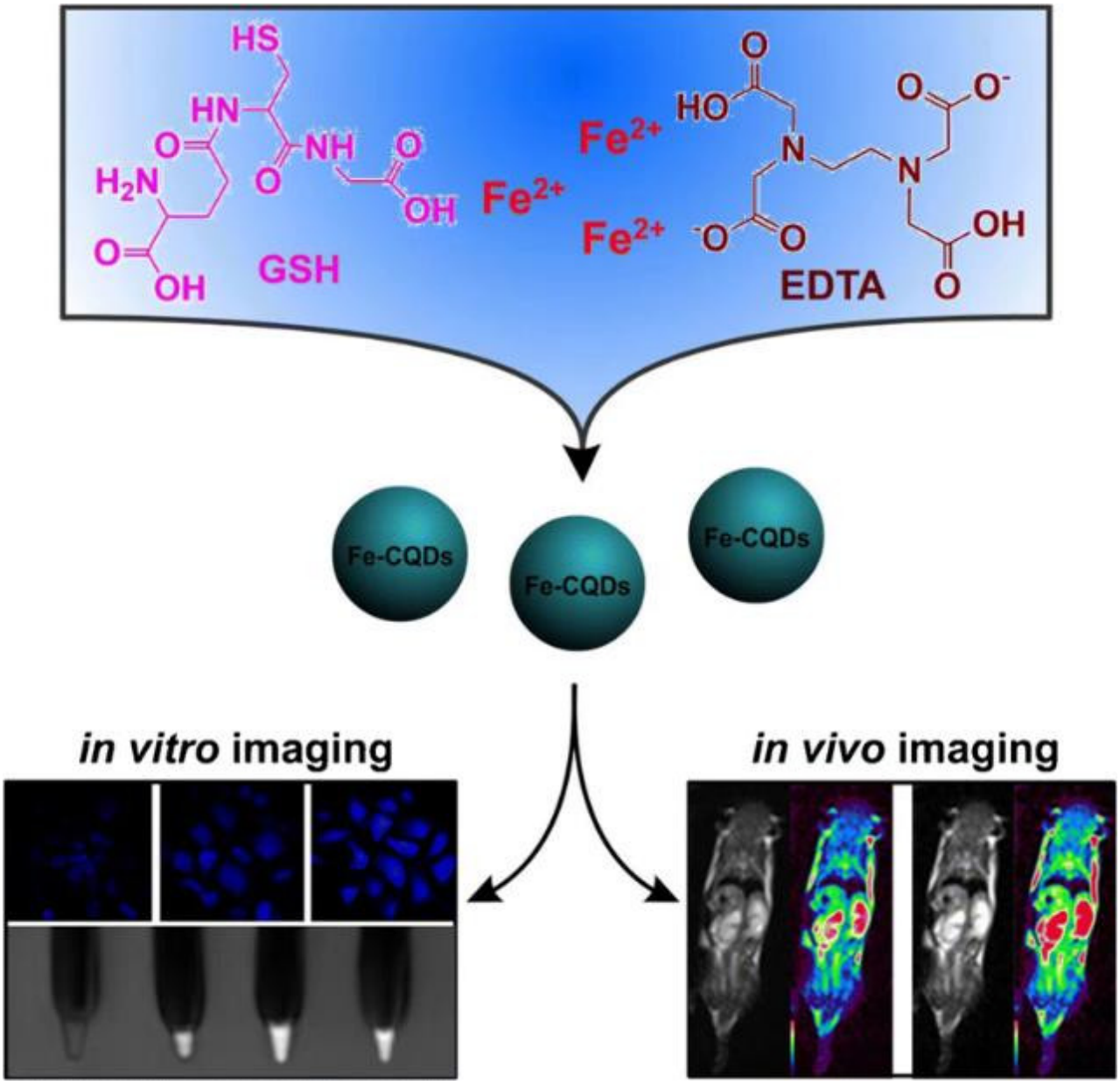

Fig. 1.40 – CDs are versatile and can be doped with complexed iron ions before synthesis. *In vitro* and *in vivo* imaging can be done due to their excellent water dispersibility and cytocompatibility. Reprinted from Huang et al. (2019) with permission from Springer Nature [198].

Likewise, Parvin and Mandal (2017) synthesized CDs with exceptionally high quantum yield (30% in green, 78% in red). P-doped CDs showed high efficiency in fluorescence microscopy and photoacoustic imaging in mice [55]. The co-doping of phosphorus and nitrogen has been linked with increased graphitization in the carbon core. Gong et al. (2015) demonstrated that this increase leads to higher red-shifted emissions as a result of more prevalent π-conjugation and lowered bandgap. XPS and FT-IR analysis confirmed the presence of phosphate functional groups on the CD surface and showed variable fluorescence emission in different pH values [199]. Nonetheless, there is no consensus on optimal doping ratios to achieve consistent increases in photoluminescence.

Photon upconversion (UC) is misattributed to CDs

The conversion of long wavelength light (NIR/IR) to short wavelength light (visible) is known as photon upconversion (UC). UC-capable nanoparticles offer numerous advantages as they take advantage of the therapeutic window in biological tissue: background fluorescence from tissue is reduced and lower light intensities are needed in comparison to two-photon excitation [200]. Although CDs have been frequently cited to be capable of UC, there are conflicting reports throughout the literature [5,42]. It is unclear how carbonaceous nanoparticles can achieve single photon upconversion and the exact mechanism has not yet been elucidated. Wen et al. (2014) determined previous experimental setups did not consider the second order diffraction from the fluorometer light source. The lack of a long pass filter would cause a false fluorescence signal as lower-wavelength light leaks and hits the sample [201]. Despite this, multiple new publications continue to state CD upconversion is possible without the use of other compounds.

Lanthanides (Ln), also known as rare earth metals, are metal ions capable of efficient UC and have been widely used as the main components in UC nanoparticles. Wu et al. (2016) did not

observe UC in Yb^{+3} and Nd^{+3}-doped CDs, though doping showed strong photoluminescence emission at 998 nm and 1068 nm, respectively. Ln-doped CDs did not show significant toxicity up to around 500 μg/ml. Interestingly, neither Yb^{+3} or Nd^{+3} affected the amorphous carbon core of CDs [202]. Chen et al. (2016) synthesised Eu^{+3}-doped CDs to improve optical properties, with Eu-CDs showing two distinct emission peaks at 460 nm and 600 nm. High resolution TEM images demonstrate CDs lack any crystal lattices [203]. Likewise, Zhang et al. (2016) found europium and terbium doping improved CD photoluminescence, showing a similar dual emission behaviour when irradiated with 360 nm light. Furthermore, they observed CD fluorescence was more resilient to pH changes in comparison to Eu^{+3} [204].

Conclusions and outlook

In this review the current trends in CDs and CD conjugates within biomedical applications including evaluation of their cytotoxicity, drug delivery, gene delivery, and bioimaging were detailed. Since their discovery in 2004, CDs have moved past from being considered newcomers to the field of carbon nanomaterials to become a highly versatile and useful component for a multitude of applications. Since then, CDs have been shown to be highly convenient nanoparticles because of their tuneable photoluminescence, cytocompatibility, and surface chemistry. There has been great progress in the development and refinement of synthesis strategies, use of alternative reagents, passivating agents, and dopants, leading to enhanced optical properties.

However, there are still many factors that have yet to be completely understood, despite great advances in understanding their photophysical properties. Reports from the literature have shown that PL and low cytotoxicity are a result of a combination of factors, from synthesis conditions to carbon precursors and passivation. Furthermore, the limitations on product yield, nonstandard purification methodologies, and variable batch reproducibility limit comparison between different CD conjugates. Nonetheless, current research has shown these nanoparticles are a viable alternative to established materials such as semiconductor quantum dots, graphene, graphene quantum dots, and metallic nanoparticles.

Biomedical applications have seen generally positive results from *in vivo* toxicological and biodistribution studies, though *in vitro* cytotoxicity studies have shown great variation. There are ongoing concerns regarding their long-term toxicity after administration, which need to be addressed before further advancement into clinical use. Nevertheless, the use of different *in vivo* models such as nematodes and zebrafish has improved our understanding on particle biodistribution, blood circulation lifetime, and renal clearance. Equally, 3D cell culture models

and CAM assay have shown the importance of conjugate evaluation prior to further *in vivo* testing as the effect of CD loading through various mechanisms such as cross-linking or host-guest chemistry on conjugate efficiency is unclear.

Conjugates have continuously demonstrated high efficiency as part of drug delivery platforms in PDT/PTT, chemotherapy, and antimicrobial applications. Recent progress has also included CDs capable of ROS production and photothermal conversion and enhanced photoluminescence. Drug loading has been shown to be possible with many standard compounds such as doxorubicin, protoporphyrin IX, and chlorin e6 through different conjugation strategies. Tailoring of surface chemistry has significantly improve, with gene delivery demonstrating better performance in comparison to the gold standards in the field because of high loading ratios and low toxicity in cationic CDs. Bioimaging with CDs as probes has seen great advances as heteroatom doping, host-guest chemistry, and synthesis methodologies have produced particles with high quantum yields and NIR/IR emission, enabling their use as platforms for theranostics.

Most studies in the field of CD conjugates have been concentrated on the synthesis of new composites and their subsequent *in vitro* evaluation. *In vivo* studies have also become widely used alongside cell culture to evaluate acute toxicity and bioimaging. This has led to the fabrication of numerous carefully designed and increasingly more complex drug delivery systems with increased therapeutic efficiency for PDT, PTT, and chemotherapy. However, very few studies have directly compared CD-drug conjugates to determine the effect of drug loading strategies on therapeutic efficiency. Likewise, conjugate evaluation has been focused on cell monolayers and murine models with limited studies carried out in other models such as cancer spheroids. Future work should focus on 1) increasing reproducibility during synthesis and conjugation and 2) improving *in vitro/in vivo* toxicological evaluation.

In the following chapter, the synthesis and drug loading of CD conjugates is discussed. Microwave reactor synthesis was selected as the fabrication route as this approach has shown consistent results and is the most widely used in the literature. PpIX was bound to CDs through two strategies: host-guest encapsulation (PpIX@CD) and amide cross-linking [PpIX-CD and (PpIX-CD)p]. Dialysis before and after crosslinking was shown to be a crucial step in sample post-processing to ensure higher product yields. Conjugates were characterized with various analytical techniques. Samples showed 34 - 48% PpIX loading efficiency and similar singlet oxygen production to PpIX for all samples. Host-guest embedding with various loading ratios showed diminishing PpIX content as initial concentration was increased. (PpIX-CD)p appeared to be the best candidate due to its high singlet oxygen production. In contrast, PpIX-CD and PpIX@CD showed increased water solubility. Results indicated newly synthesized CDs could produce a PDT effect through activation with 405 nm irradiation.

In Chapter 3, *in vitro* PDT was evaluated in a C8161 human melanoma cell line. Ultra-low fluence was selected to prevent possible PpIX photobleaching. Dark toxicity was evaluated at 1 - 100 µg/ml. Conjugates all demonstrated a 6 to 7-fold decrease in toxicity compared to PpIX. These values were used to determine the best concentration range for phototoxicity evaluation (1 - 10 µg/ml). PpIX-CD and PpIX@CD showed a 3.2 to 4.1-fold increase in photo-toxicity index (PI) at concentrations >1 µg/ml. In contrast, (PpIX-CD)p showed a significantly reduced PDT effect in all conditions. Confocal microscopy showed rapid intracellular uptake of conjugates near the nucleus. Results demonstrated an enhanced PDT effect from conjugates to the control at equal PpIX concentrations.

In Chapter 4, multicellular spheroids were used to evaluate previously obtained PDT parameters from cell monolayers. Spheroids are a 3D cell culture model capable of replicating *in vivo* tumour morphophysiological conditions such as hypoxia, tissue depth, drug resistance,

and variable diffusion rates. Previous PDT conditions were shown to be ineffective with low damage to spheroids. Hence, fluence rates (2.5 - 10 J/cm^2) and doses (1 – 10 μg/ml) were adjusted. Furthermore, fractionated light treatments were introduced to take advantage of sensitization to PDT over longer incubation periods. Viability was measured through LDH release and DNA quantification assays. Spheroids showed significant cell death and loss of sphericity after treatment. Light sheet microscopy was used to observe PDT-induced damage and determine conjugate penetration throughout spheroids. Results showed conjugates maintained equivalent PDT efficiency at relative PpIX concentrations.

Finally, Chapter 5 details the use of automated parameter extraction through computer-assisted image processing to monitor PDT in spheroids. Spheroid morphology has been previously stated to be related to viability, though the exact parameter was unclear. Results showed various parameters are relevant for different experiment stages. Spheroid variability was shown to be linked to sphericity in the days following seeding. Pre-screening individual spheroids significantly reduced variability between experimental groups. Total spheroid surface area was shown to be the most important indicators of spheroid viability. Furthermore, it was shown that this parameter could be used to screen unsuccessful PDT conditions, being capable of discerning between multiple treatment combinations.

Chapter 2 - Synthesis and characterization of CDs and CD-PS conjugates

Introduction

The previous chapter established CD-based conjugates have great potential in drug delivery for PDT. A systematic literature review identified that drug loading strategies for CD-PS conjugates have not been directly compared to determine the best approach to increase PDT efficiency. In this chapter, a systematic comparison of the efficiency of three novel CD-PS conjugates: PpIX-CD, (PpIX-CD)p, and PpIX@CD, obtained through different crosslinking strategies was undertaken.

Photodynamic therapy

Photodynamic therapy (PDT) has seen advances in recent years as an alternative cancer treatment due to its non-invasive nature, specificity and selectivity [205]. The term "PDT" describes a range of protocols based on the excitation of photosensitizers (PS) in the presence of oxygen to singlet oxygen ($^1O_2$) leading to tumour ablation [206]. PDT has been proven to be clinically effective presenting positive results in basal cell carcinoma, endobronchial lung cancer, and non-muscle invasive bladder cancer [207–209]. Highly controlled light dosimetry and rapid drug uptake maximizes the effectiveness of the treatment and prevents damage to surrounding tissue [210].

Although some have also grouped sensitizers as being first, second or third generation, this has caused confusion as to their differences (Fig. 2.1). Huang et al. (2005) stated that in many cases, newer drugs are not immediately better than previous ones due to a variety of factors [212]. Therefore, when discussing new photosensitising molecules, novelty does not equal higher efficiency. The characteristics of a good photosensitizer depend on the perspective with which we evaluate them. The clinical approach is primarily focused on various aspects related to toxicity and pharmacokinetics.

PS administration and treatment should ideally not produce any additional harmful by-products, possess an NIR/IR excitation wavelength for maximum tissue penetration, and be selectively accumulated within the target tissue (with minimal toxicity to the rest of the organism). These are among the nineteen points proposed by Allison et al. (2004) for clinically relevant guidelines in determining the usefulness of a photosensitizer [213]. In comparison, a chemistry-focused approach emphasises the importance of a high quantum yield and high singlet oxygen production efficiency, as well as low dark toxicity as key photosensitizer properties [214]. Nonetheless, both publications highlight that the most important quality of a PS is its efficient activation in tissue – an effect that is mainly related to the absorption wavelength of the photosensitizer.

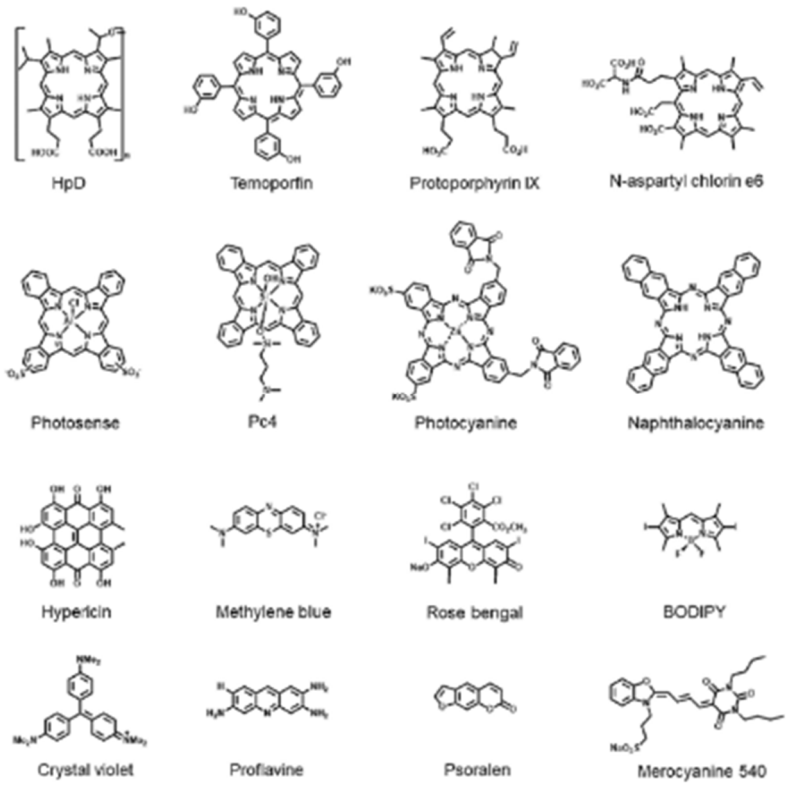

Fig. 2.1 – Porphyrins and phthalocyanines are well-known PS families. The abundance of pyrrole groups and facile modification has led to many the formation of numerous derivatives and conjugates. Reprinted from Li et al. (2018) with permission from the Royal Society of Chemistry [219].

Nanoparticle-photosensitizer conjugates have received increased interest due to several advantages such as; (i) large surface-volume ratios for increased loading efficiency, (ii) the formation of amphiphilic compounds to avoid aggregation, and (iii) the enhanced permeability and retention effect for increased accumulation in tumours due to "leaky" vasculature [215–217]. Moreover, conjugates can also function as bioimaging probes to form multifunctional theragnostics platforms through photodynamic diagnosis (PDD) [218]. Porphyrins are naturally occurring heterocyclic molecules composed of pyrrole rings connected by methylylidene bonds. These molecules are found in living organisms acting as electron and oxygen transporters or metalloenzymes through the chelation of metal ions by coordination. PS-loaded conjugates are also capable of ROS production and subsequent cancer killing effect after light exposure (Fig. 2.2).

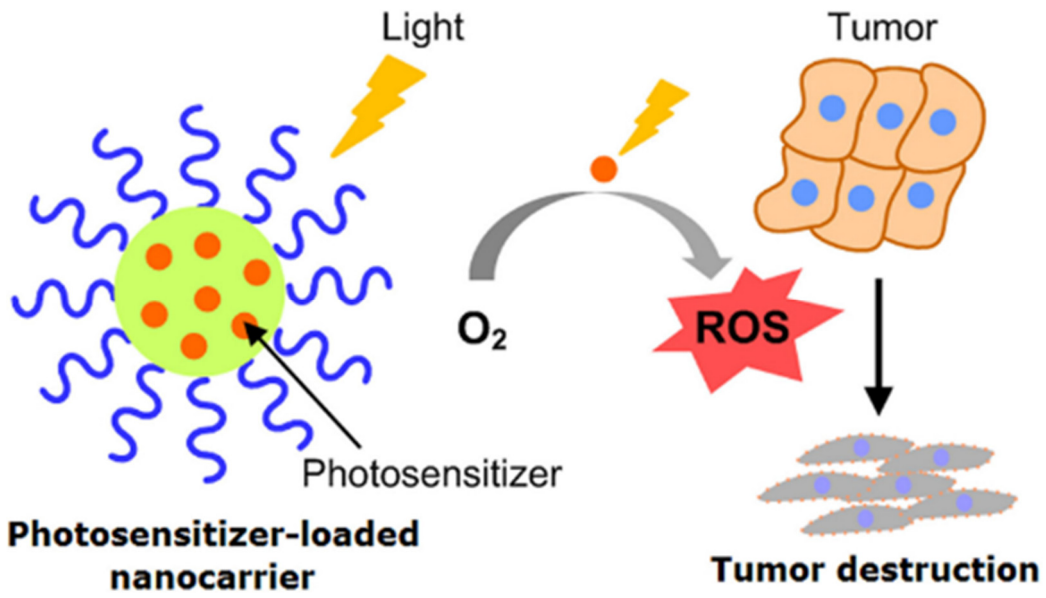

Fig. 2.2 – Schematic detailing PDT mechanism. Reactive oxygen species produced by photosensitizers lead to cell death and eventual tumour ablation. Reprinted from Hong et al. (2016) through the Creative Commons CC BY-NC-ND license [211].

Protoporphyrin IX (PpIX) is a well-characterised endogenous porphyrin photosensitizer, normally present in minor concentrations within cells as part of the heme biosynthesis pathway. Dormant cancer cells have been proven to accumulate high concentrations of PpIX and are

more susceptible to PDT [167]. However, PpIX is limited as a photosensitizer mainly due to elevated dark toxicity and rapid aggregation. This leads to decreased photoactivity as singlet oxygen production is attenuated [220,221]. Recent advances have focused on utilising carriers and chemical modifications to improve water solubility and increase cellular viability [222]. For example, Homayani *et al.* (2015) demonstrated that hydroxyl-group modification can increase the water solubility of PpIX, reducing dark toxicity and increasing cellular uptake [222].

CD conjugates as photosensitisers

CDs have shown similar success in biomedical applications in comparison to other nanomaterials such as semiconductor quantum dots, nanodiamonds, graphene, and carbon nanotubes [3,71,100,223]. Nanoparticle-based drug delivery has been shown to improve intracellular drug uptake and reduce the likelihood of cargo degradation. [97]. The rapid intracellular uptake of CDs and CD-based conjugates has been shown to be time and dose-dependent and is a combination of both passive uptake and caveolae and clathrin-mediated endocytosis [224]. Moreover, CDs can be further modified by doping with heteroatoms and surface passivation with a variety of molecules such as polyethylene glycol to achieve better photophysical properties [225]. CDs have previously been used as carriers for a wide variety of compounds, including doxorubicin, rhodamine B, dsDNA, siRNA and ciprofloxacin hydrochloride [119,176,226–228].

CDs have tuneable photoluminescence ranging across the visible spectrum which depends on their synthesis conditions, affecting quantum yield, determining excitation-dependent or independent emission, and type of photoluminescence decay [229]. *In vitro* studies demonstrate rapid intracellular uptake and do not show significant toxicity even at extremely high concentrations [53]. *In vivo* and *ex vivo* imaging in BALB/c mice show similar results

with no observable toxicity and rapid clearance from the reticuloendothelial system [69]. Furthermore, CDs have previously demonstrated comparable two-photon cross-sections to those of commercially-available quantum dots, making them highly valuable as probes for bioimaging applications [192].

Drug loading strategies for enhanced PDT

Recently, CD-PS crosslinking has recently gained research interest. CDs have extremely high surface area to volume ratios which make them ideal candidates for drug loading and cross-linking. There are several different types of crosslinking corresponding to the type of bond that is formed: physical bonds between molecules are primarily electrostatic and hydrophobic interactions, which are non-covalent and thus easily broken. In comparison, chemical linking forms covalent bonds between molecules, which provides a more rigid link and prevents their separation while increasing stability [230]. Most crosslinking methods are highly specific to functional groups and ensure correct linking orientation, preventing homodimer formation.

Carbodiimide chemistry, also known as EDC/NHS chemistry, is based on the formation of a peptide bond between a primary amine and a carboxyl. It is especially useful as there are not many compounds that are able to react with carboxyl groups. EDC (1-Ethyl-3-(3-dimethylaminopropyl) carbodiimide) is a compound that forms an o-Acylisourea ester in the presence of a carboxyl. This intermediate group is unstable in water and can suffer hydrolysis, returning it to its original state. It can also react with a primary amine to form a peptide bond, realising isourea as a secondary product. EDC is highly water-soluble and can be used by itself for crosslinking. The use of NHS (N-Hydroxysuccinimide) or sulfo-NHS (N-hydroxysulfosuccinimide) results in a stable ester that can resist drying and is reactive to amides. This series of reactions are widely used in crosslinking proteins, nanoparticles and other molecules [231]. Photosensitizers such as chlorin e6, Rose Bengal and PpIX have been

previously covalently linked through carbodiimide chemistry, the latter of which showed a PDT effect under two-photon excitation [144,153,232]. Similarly, recent advances have shown embedded photosensitizers are capable of singlet oxygen production while embedded on nanoparticles [148,150].

CD formation and synthesis

The process by which carbon dots are formed is a combination of carbonization and nucleation. Dissolved molecules in the solution become rapidly oxidized and decompose, with nucleation beginning simultaneously [21]. Fu et al. (2015) developed a model using three different aromatic compounds (anthracene, pyrene and perlyene) within a poly (methyl methacrylate) matrix to mimic the optical properties found in carbon quantum dots. The results demonstrated that absorbance was influenced by the molar percentage of each PAH, indicating that the amorphous carbon core also increases photoluminescence as surface defects were introduced [233]. Absorbance changes after CD formation can be easily seen, as the solution passes from a transparent liquid to shades of pale yellow, up to black [234]. There is also a distinct odour that is likely due to the formation of polycyclic aromatic hydrocarbons (PAH) within the solution. These compounds are formed during incomplete combustion and have multiple benzene rings [235].

Synthesis routes have advanced substantially from the initial arc-discharge reaction that led to their discovery. CDs can be fabricated through both top-down and bottom-up approaches, as can be seen in Fig. 2.3. These include laser ablation [237], microwave-assisted pyrolysis [238], combustion [239], arc-discharge [1], solid-state carbonization [240], electrochemical oxidation [241], and acid reflux [242], among others. The use of a one-pot reaction is beneficial as the cost-efficiency is generally higher; production yields can be increased with less quantity of reagents and purification can be achieved with less intermediate phases. The production of CDs

can be stated to be a completely “green synthesis” methodology, if the particles are produced from biomatter or simple carbohydrates. Furthermore, most synthesis protocols do not use additional solvents or contaminating agents such as heavy metals [243].

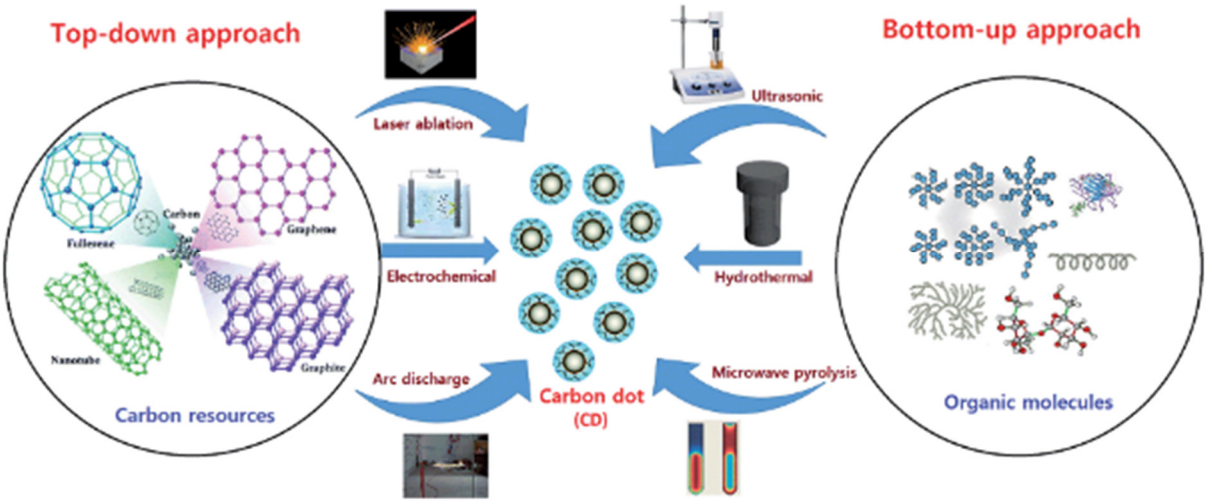

Fig. 2.3 – CD synthesis is highly versatile. Fabrication of samples can be top-down: produced from a pre-existing structure such as carbon allotropes, or bottom-up: based on the pyrolysis of organic compounds. Reprinted from De et al. (2017) with permission from the Royal Society of Chemistry [236].

It has been shown that each fabrication method influences physical and optical properties of the nanoparticles, including particle size, surface functionality and photoluminescence. Deionised water is the most common aqueous medium for CD synthesis and typically yields particles with negative zeta potential and high hydrophilicity. On the other hand, hydrophobic CDs have been reported by means of using different aqueous media such as ethanol [244] and dimethylformamide [245]. Ionic liquids have also been used as precursors to simultaneously fabricate hydrophilic and hydrophobic CDs in a one-pot reaction [246].

Microwave synthesis, also known as microwave chemistry, is the use of microwave radiation to produce a chemical reaction and has been an invaluable research tool for the synthesis of new compounds. The use of microwaves has several advantages over other related CQD synthesis methods. The heating by microwaves does not depend on thermal conductivity, leading to a variety of thermochemical reactions caused by differential absorption of

microwaves and variable dielectric heating rates [247].

Although reactions can take place within commercial microwaves, specialised reactors have been shown to yield much better results for nanoparticle synthesis. There are several additional disadvantages to utilizing commercial microwave ovens. This is mainly due to the variability that is caused by the microwave itself, as it was not designed to reliably reproduce heating conditions. Aside from external modifications, there is no method of dependable measurement of temperature and pressure. Microwaves are also randomly directed within the equipment, resulting in uneven heating of the solution and localized “hot-spots” [248]. Finally, the lack of a cooling mechanism results in the shutdown of the machine, preventing lengthy reactions as the equipment overheats. These conditions severely limit the usefulness of a domestic microwave, and as such it has been mostly displaced by specialized microwave synthesizers.

Microwave reactors can conduct organic and inorganic synthesis in a highly controlled environment, increasing experimental reproducibility. The high pressure and continuous stirring of the solution during the reaction, combined with the instantaneous and homogeneous temperature increase results in more reproducible reactions compared to the uneven heating and low temperature thresholds found in commercial equipment. This aspect becomes more important as the cost of the materials used increases, as is the case with lanthanide-doped nanoparticles. However, there are limitations to the use of microwave reactors. The most notable is the relatively smaller reaction volumes that must be used. Reaction vessels for microwave reactors are typically in the 5 – 25 ml range as higher volumes are difficult to manage because of the pressure within [249]. Thus, microwave-assisted pyrolysis was selected out of the possible fabrication routes for its ease of access, low cost, adaptability, and reliability. Additionally, hydrothermal synthesis was evaluated as a possible synthesis route for increasing product yield per reaction. Fig. 2.4 shows a general scheme for CD conjugate synthesis.

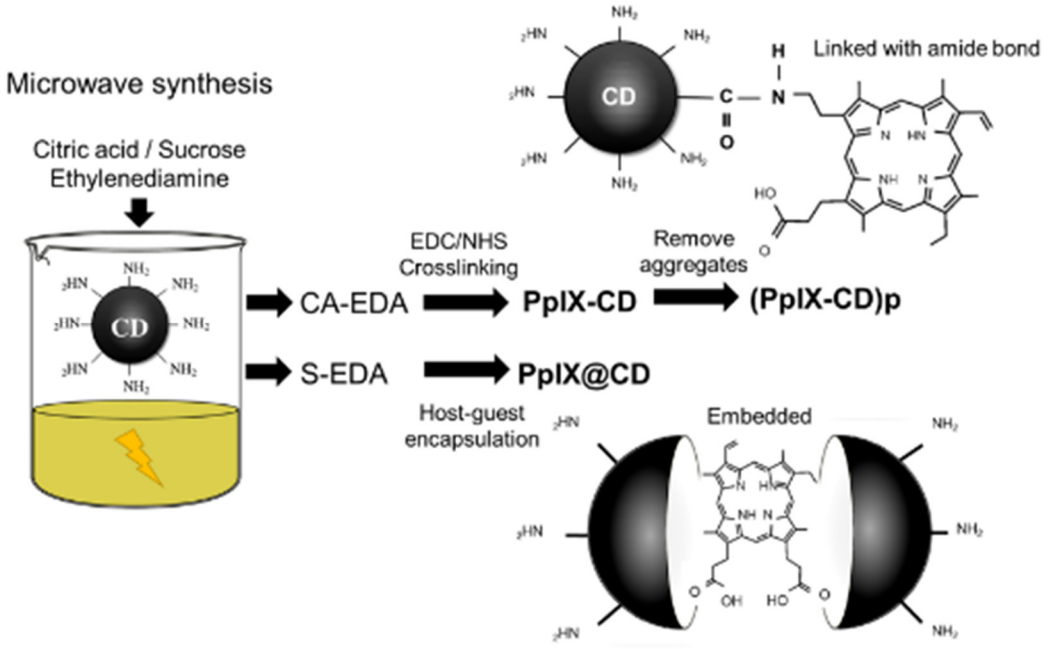

Fig. 2.4 – CD conjugates were synthesised with two distinct loading strategies. Host-guest encapsulated (PpIX@CD) samples were produced in a one-pot reaction. CA-EDA CDs were used to produce amide bond-linked (PpIX-CD and (PpIX-CD)p) conjugates. S-EDA CDs were embedded with PpIX in a one-pot encapsulation step.

Aim: Fabricate carbon dot-protoporphyrin IX conjugates capable of efficient singlet oxygen production.

Objectives:

- Determine the best synthesis route for obtaining nitrogen-doped CDs with high yield and reliability.
- Select CD samples based on strongest photoluminescence and advantageous surface chemistry for crosslinking using primary amine groups ($-NH_2$).
- Improve amide crosslinking and host-guest encapsulation of PpIX with CDs.
- Assess conjugate photophysical properties including singlet oxygen production and drug loading efficiency of conjugates.

Experimental

Materials

In the following section, all chemicals were obtained from Sigma Aldrich, UK unless stated otherwise. The vessels used for measurement and reactions were of inert material. In all synthesis routes, CDs were prepared using sucrose or citric acid as a primary carbon source and ethylenediamine as a passivating agent and nitrogen source. Varying passivating agent/carbon source ratios (w/w) were tested. All reagents were dissolved prior to heating in deionised water at room temperature.

Citric acid monohydrate, sucrose, ethylenediamine, protoporphyrin IX, sodium chloride, resazurin sodium salt, (N-(3-Dimethylaminopropyl)-N'-ethylcarbodiimide), N-Hydroxysuccinimide, formaldehyde, phenalenone, 2-(N-Morpholino) ethanesulfonic acid, acetone, dimethyl sulfoxide, 2-mercaptoethanol and N,N-dimethylformamide were acquired from Sigma Aldrich (United Kingdom). Dulbecco's Modified Eagle's Medium (DMEM, high glucose), Dulbecco's Modified Eagle's Medium (DMEM, high glucose, without phenol red), foetal bovine serum (FBS), phosphate buffer saline (PBS), and trypsin – ethylenediaminetetraacetic acid solution were obtained from Thermo Fisher (United Kingdom). Syringe filters with a 0.2 μm pore size were acquired from Sarstedt (United Kingdom). 1 kDa molecular weight cut-off (MWCO), 6.4 ml/cm dialysis tubing was acquired from Spectrum Labs (United States of America). All chemicals were used as received unless stated otherwise. Deionized water was used for all buffers and samples in experiments. Septa steel ring caps and 35 ml glass reaction vessels were obtained from CEM Corporation (United Kingdom).

Carbon dot synthesis

Domestic microwave synthesis

A Daewoo KOR-6L65 domestic microwave (700 W maximum power) was used to fabricate carbon dots. The carbon source and passivating agent were mixed in a 100 ml deionised water in a glass beaker. This solution was placed in magnetic stirring until no more powder could dissolve in the aqueous phase. The beaker was then transferred to the microwave and heated for 3,5, and 10 minutes until a visible colour change was observed. CDs were moved using safety gloves and allowed to cool until reaching room temperature.

Microwave reactor synthesis

CA-EDA CDs were synthesized utilising 5 g of citric acid and 1.25 g of EDA dissolved in 100 ml of deionized water and stirred until no visible precipitate remained. This process was repeated for S-EDA CDs with 5 g of sucrose and 1.25 g EDA. A CEM Discover SP microwave reactor was used to heat the precursor solutions for 5 minutes at constant 150°C (200 W maximum power and 17 bar threshold). The resulting yellow-coloured solution was cooled to room temperature using nitrogen and centrifuged at 5000 rotations per minute (rpm) for 30 minutes to remove debris from carbonization.

Host-guest embedding

Host-guest encapsulated CDs were synthesised through this method. All samples were obtained by adding an additional reagent to the carbon and nitrogen source mixtures, typically in ≥1% w/w ratios.

PpIX-based conjugates (PpIX@CD) were fabricated by adding 50 mg PpIX to the previously mentioned sucrose solution. Additional stirring was used to properly mix all components before pyrolysis. Reaction parameters were also adjusted to high stirring speed.

Dimethylformamide (DMF) was used as a solvent instead of water to produce PpIX@CD-DMF, synthesized by mixing 5 g of sucrose, 1.25 g EDA, 75 ml deionised water and 75 ml DMF. Additionally, the quantity of PpIX was adjusted to produce various conjugates at different w/w ratios (0.1 – 2%). Likewise, a variety of compounds were tested for host-guest embedding in addition to PpIX: heparin, Nile blue, and naphthol green. These were added in the same ratios as PpIX and were pyrolysed with the standard parameters.

Hydrothermal synthesis

CDs were synthesised using a Series 4760 300 ml general purpose non-stirred pressure vessel (Parr Instrument Company, United States) fitted with a thermocouple (part no. A472E). In summary, 5 g of citric acid or sucrose were added to 1.25 g ethylenediamine and dissolved in 100 ml deionised water. The solutions were placed in glass jars for transport. Synthesis was carried out by heating the vessel with an isomantle up to 140 – 200 °C for 6 hours. The solutions were left to cool until reaching room temperature.

Sample processing

The solutions were centrifuged at 2000 rpm for 10 minutes to eliminate remaining insoluble ashes from the water. This step was repeated as many times as necessary for each solution. The CD-containing liquid was dialysed against deionised water using a pre-wetted Spectra/Por 6 dialysis tubing made from regenerated cellulose (Spectrum Labs, United States of America). The membrane has a 1 kDa molecular weight cut off (MWCO) and is capable of carrying up to 6.4 ml/cm of liquid. The dialysis membrane was stored in 0.05% sodium azide solution when not in use.

A 2L or greater glass beaker was filled with deionised water and placed under the lowest possible magnetic stirring speed (200 rpm). Around 15 – 20 cm of tubing was used taken and fitted with clips to prevent sample leaking. A glass pipette was used to carefully transfer the

CD solution to the membrane. Deionised water was replaced every 2 hours or when an appreciable colour change was observed. In total, all samples were dialysed for 48 hours. Afterwards the solutions were transferred to plastic containers and placed in storage at -80° C.

A Labconco Triad freeze-drying system removed the remaining water, using the following parameters: -10°C shelf temperature, -60°C collector temperature, 0.1 mbar internal vacuum pressure, 0.5 degrees per minute, 48-hour main drying step. Each solution was frozen in 20 ml portions to maximize surface area and enhance sublimation. An additional drying step was performed, with the equipment slowly equalising the samples to room temperature. The powder samples were collected and weighed prior to storage at -20 °C. Silica gel packets were used as an additional desiccant for stored powders at room temperature.

Amide crosslinking

Standard protocol

The standard protocol for amide crosslinking is used mainly with proteins. Briefly, 1 mg/mL PpIX was dissolved in 1 mL 0.1 M 4-morpholinoethanesulfonic acid (MES) at pH 4.5-5 and thoroughly mixed. 0.4 mg (1-ethyl-3-(3-dimethylamino) propyl carbodiimide, hydrochloride (EDC) and 0.6 mg N-hydroxysuccinimide (NHS) were added to the solution and left to react for 15 minutes in the dark. EDC was quenched with 1.2 µl 2-mercaptoethanol. Subsequently, 1 ml of a 1 mg/mL solution of CDs were added and allowed to react at room temperature for 8 hours. The reaction was quenched with hydroxylamine and the conjugates were recovered via dialysis.

Modified crosslinking protocol

The following protocol for amide crosslinking was adapted from Yildiz et al. (2010) and Fowley et al. (2013). [144,250] All containers were protected from light to prevent bleaching

as PpIX is a light-sensitive compound. 100 mg of PpIX was added to 20 ml dimethylformamide (DMF) and placed in stirring (200 rpm) until completely dissolved. Afterwards, 25 mg EDC (6.25 mM) and 50 mg NHS (21.72 mM) were added to the solution, which was left stirring for 30 minutes. 100 mg CDs (citric acid / ethylenediamine) were added to 20 ml deionised water, stirred until completely dissolved, and added to the PpIX solution. The solution was left stirring overnight and transferred to a separate beaker. The same processing procedure was used for conjugates, with centrifugation removing insoluble PpIX and dialysis removing excess reagents and waste. After centrifugation, the pellet was suspended in deionised water and considered a separate sample. Samples were freeze-dried and stored for further use.

Characterisation

Ultraviolet-Visible (UV-Vis) spectroscopy

UV-Vis spectra were obtained using a Varian Cary 50 spectrophotometer (Cary Instruments, United States). Conjugates were diluted in deionised water to 5 µg/ml prior to measurement and subjected to ultrasonic processing to break up aggregates. The equipment was calibrated before each use according to the manual and the same deionised water was used as a blank for the measurements. A total of 2.5 ml of diluted conjugate was placed within a disposable polystyrene cuvettes of 4.5 ml volume and 10 mm path length (Fisher Scientific, United Kingdom). Absorbance was measured in the range of 250 – 750 nm.

Fluorescence spectroscopy

A Fluoromax 4 spectrofluorometer (Horiba Ltd., Japan) was used to obtain fluorescence spectra from samples. Conjugates were diluted as previously stated. Deionised water was used to calibrate the equipment prior to use. A quartz cuvette (3.5 ml volume and 10 mm path length) was filled with 3 ml of solution. Fluorescence was measured in the range of 350 – 750 nm with various excitation wavelengths.

PpIX content was estimated according to a previously established method by Gunter et al. [251]. In summary, PpIX was diluted to 0.4, 0.8, and 1.6 µg/ml solutions in deionised water. The emission of the solution was measured (λ_{ex} = 400 nm, λ_{em} = 658 nm) and fitted using linear regression. CD emission at λ_{ex} = 400 nm was subtracted from all samples to estimate the PpIX content of conjugates.

Fourier-transform infrared spectroscopy (FTIR)

Infrared spectra were obtained with a Nicolet iS50R FT-IR in photoacoustic mode. Powdered samples were carefully placed onto the crystal and pressed firmly to ensure contact in the sample holder. Spectra were obtained as either survey (16 measurements) or complete (512 measurements) in the range of 4000 – 450 cm^{-1}. Samples were recovered for further use and stored as detailed previously.

Transmission electron microscopy (TEM)

A Tecnai G2 Spirit transmission electron microscope (FEI Company, United States) was used to obtain images. Conjugates were diluted as previously detailed, with aggregates being removed with a UP50H ultrasonic probe (Hielscher Ultrasonics GmbH, Germany) prior to imaging. Using a micropipette, 10 µl drops of conjugates dilutions were placed onto copper coated TEM grids (SPI Supplies, United States) and left to dry at room temperature for 1 minute. Images were obtained magnifications ranging from 18,500 to 68,000×.

Singlet oxygen generation

This method was replicated from a previous paper by McKenzie et al. (2017) [252]. Phenalenone was used as a reference compound to indicate 95% singlet oxygen generation. Conjugates were dissolved in DMF and subsequently diluted to an absorbance value of 0.1 (± 0.01) at 355 nm. A Q-SW Nd:YAG 355 nm laser (Ls-1231M LOTISII 2006 model) was used to irradiate the samples with 8 ns pulses with 50, 100, and 200 mJ. This was repeated 4 times

per power and solution to generate an average singlet oxygen decay signal. An InGaAs photodiode 3 mm active area (J22D-M204-R03M- 60-1.7, Judson Technologies, United States) coupled with a digital oscilloscope (TDS 3032B Tektronix, United States) and a high-contrast bandpass filter fitted on the front of the detector (1277 nm centre wavelength, 28 nm FWHM, custom-made by Izovac, Belarus) were used to detect the decay of singlet oxygen ($^1O_2$) to triplet oxygen ($^3O_2$). The corrected initial amplitudes were obtained with the following equation:

$$Corrected\ initial\ amplitude = \frac{Initial\ amplitude}{1 \times 10^{-OD}}$$

Subsequently, singlet oxygen generation was calculated with the corrected initial amplitudes for all samples and reference with the following equation:

$$Singlet\ oxygen\ generation = \frac{Corrected\ PS\ initial\ amplitude}{Corrected\ reference\ initial\ amplitude} \times 100$$

X-ray photoelectron spectroscopy (XPS)

X-ray photoelectron spectroscopy (XPS) analysis was carried out with a monochromated Al-kα X-ray source, two analysis points per sample and a total scan area of 700 x 300 μm using an Axis Ultra DLD system (Kratos Analytical, United Kingdom). 5 mg of conjugate powder samples were mounted on between indium foil and a paper label to mitigate the risk of differential charging. Survey scans were collected in the range of 1200 to 0 eV binding energy (160 eV pass energy, 1 eV intervals, and 300 seconds per sweep – with 4 sweeps collected). High-resolution C 1s spectra were collected at 20 eV pass energy and 0.1 eV intervals. The influence of indium foil on each sample was removed considering a surface composition of 26.8 at% O, 19.4 at% In, and 53.8 at% C.

Thermogravimetric analysis (TGA)

Sample analysis was carried out using a Q50 analyser (TA Instruments). Briefly, approximately 1 mg of sample was placed on a platinum sample holder, which was cleaned with acetone. CDs and conjugates were heated at 10 °C/min from room temperature until reaching 1000 °C. After each run, the sample holder was cooled, cleaned, and set up for the next analysis.

Results and discussion

Domestic microwave and hydrothermal synthesis

Synthesis conditions were not suitable using the domestic microwave

CDs were first synthesised using a domestic microwave to pyrolyze carbon-containing compounds dissolved in water at maximum power for 1 – 10 minutes. A variety of carbon sources were selected for CD synthesis from those previously used in the literature [55,149,253] (Table 2.1). While sucrose (S) and citric acid (CA) have high solubility in water, chitosan required an acetic acid solution and additional mixing time. The solutions changed colour during pyrolysis, from pale yellow to dark black with an oil-like residue. This colour depends on factors such as the amount of precursor within the solution, the type of carbon source, reaction, and heating rate. Sucrose and citric acid samples showed effective decomposition at 3 and 5 minutes, producing amber to black CD suspensions. Solutions containing chitosan were more difficult to handle and produced significantly more char than CA and sucrose samples. The solution may smell sweet due to formation of compounds as carbohydrates undergo caramelization and the Maillard reaction [254], or become burnt due to carbonization [255].

Table 2.1 - Compounds used for CD synthesis

Compound	Category	Type	Molecular weight	Molecular formula	Melting point
Sucrose	Carbon source	Disaccharide	342.30 g/mol	$C_{12}H_{22}O_{11}$	N/A
Citric acid		Organic acid	210.04 g/mol	$C_6H_8O_7$	~ 153 °C
Ethylenediamine	Passivating agent	Organic compound	60.10 g/mol	$C_2H_8N_2$	8 °C
Polyethylenimine		Branched polymer	43.04 g/mol	$(C_2H_5N)_n$	59-61 °C
Poly(ethylene) glycol		Polyether oligomer	380 - 480 g/mol	$C_{2n}H_{4n}+2O_{n+1}$,	4-8 °C
Protoporphyrin IX	Cargo	Porphyrin	562.66 g/mol	$C_{34}H_{34}N_4O_4$	>350 °C

Reaction times greater than 5 minutes showed a rapid evaporation of the water and eventual char formation. Likewise, samples with over 5 grams total of combined reagents rapidly formed aggregates which coalesced at the bottom of the beaker. Char formation could be slightly decreased as the concentration of carbon source was adjusted, though it did not completely prevent their appearance. The solution colour was noticeably lighter as less total mass was used. Furthermore, the handling of the glassware was difficult due to its rapid heating and spillage of solution, even after adjusting settings in the microwave.

Hydrothermal synthesis was affected by char formation

Hydrothermal synthesis allowed much larger volumes to be processed at once in comparison to domestic microwave, with a maximum of around 250 ml in comparison to 50 ml. Although the use of a closed vessel allowed higher temperatures and constant monitoring, there were still issues with this method. Fig. 2.5 shows char formation could not be avoided as there was no internal stirring mechanism and the cleaning required several days as this residue was not easily

removed. Therefore, pyrolysis with domestic microwave and via hydrothermal treatment proved inefficient due to the lack of control over experimental parameters and low product yield. Synthesis through this method limits reaction efficiency and prevents the use of solvents other than water. Nonetheless, CA and sucrose showed positive results in comparison to chitosan and were selected to continue with microwave reactor synthesis.

Fig. 2.5 – Samples produced through domestic microwave synthesis. CD samples obtained by domestic microwave-assisted pyrolysis of sucrose and PEG-400. The colour change can be observed from the precursor solution (left) to CD solutions. Char formation after carbonization can be seen at the bottom of the beaker (right).

Microwave reactor synthesis

CD precursor solutions were pyrolysed using a microwave reactor to produce aqueous CD suspensions. Although CDs may be obtained from the pyrolysis of any organic matter, the additional processing steps required to remove contaminants led to the use of laboratory-grade reagents [256]. Microwave-assisted pyrolysis was selected as the synthesis route because of its adaptability, ease of use, reproducibility, and rapid reaction time, shown in Fig. 2.6. In comparison, other protocols like hydrothermal synthesis or combustion are more difficult to standardize. The microwave reactor could not maintain a constant temperature over 200°C

without surpassing the designated internal pressure safety threshold of 17 bar using the maximum volume of 40 mL CD precursor solution. Temperatures under 120°C did not produce a noticeable colour change in the solutions.

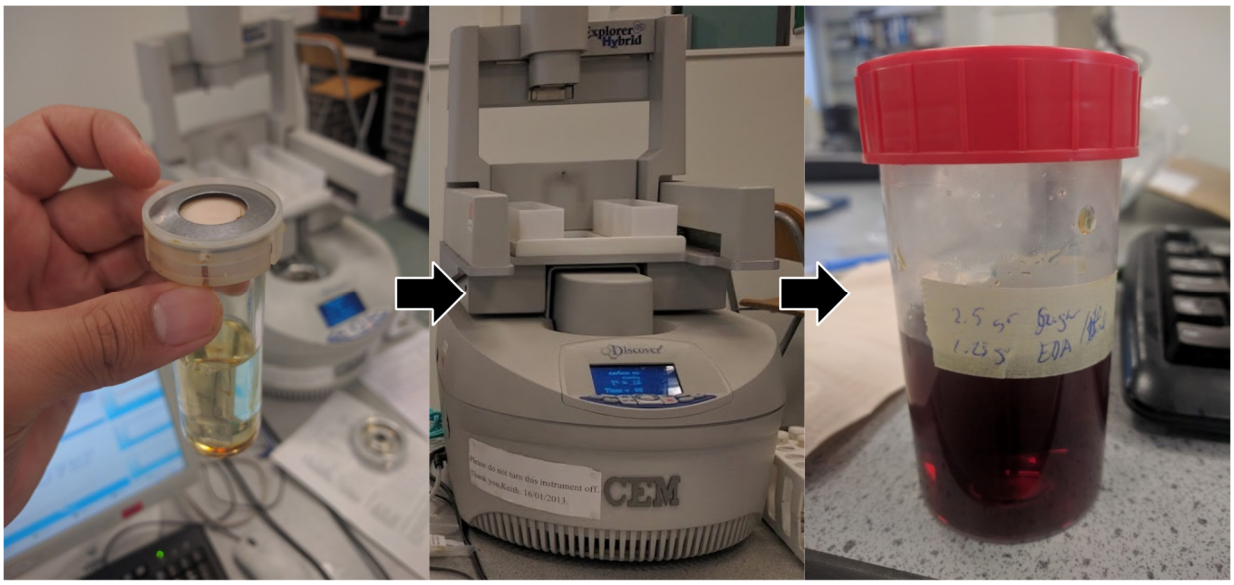

Fig. 2.6 – Microwave reactor synthesis setup. Precursor solution is placed within vessel with metal-reinforced cap (left). The solution is pyrolysed with the Discover SP microwave reactor setup (middle) and recovered after cooling (right).

The final reaction temperature (150 °C) and time (5 minutes) was chosen as it produced the best product yield, and has previously been shown to be adequate for rapid CD synthesis with citric acid as a molecular precursor [257]. A minimal amount of char was produced after the reaction as stirring within the vessel ensured homogeneous heating. The carbon source concentration was further adjusted from 0.25 g/ml to <0.1 g/ml. As was previously observed, the increase of reaction time and temperature led to a darker solution colour and formation of aggregates. Samples without constant stirring rapidly produced aggregates and vessel overheating. In total, 6 samples were obtained, which are detailed in Table 2.2.

Table 2.2. Samples synthesised via microwave reactor

Sample	Carbon source	Passivating agent
CA-EDA	Citric acid	EDA
CA-PEI		PEI
CA-PEG		PEG-400
S-EDA	Sucrose	EDA
S-PEI		PEI
S-PEG		PEG

Optimisation of synthesis using various carbon-containing compounds

CDs were synthesized utilizing microwave-assisted pyrolysis of a carbon source (citric acid or sucrose) and a passivating agent (PEG_{400}, PEI, or EDA). PEG has been shown to effectively passivate CDs for biomedical applications due to its non-toxicity and low immunogenicity. However, it has also been shown to act as a carbon source for CD formation due to its thermal decomposition at 120°C [258]. PEI and EDA also undergo similar processes during carbonization and become part of the amorphous carbon core. However, their main advantage is the enhancement of photoluminescence through nitrogen doping, which introduces additional surface defects. Furthermore, nitrogen-doped CDs possess available primary amine functional groups which can be used in amide cross-linking. The best reaction conditions for product yield and photoluminescence were determined to be 150°C and 5 minutes respectively to prevent excessive formation of aggregates. This methodology was utilized to produce CA-EDA (citric acid-based) and S-EDA (sucrose-based) CDs.

Host-guest embedding PpIX within CDs

Host-guest embedding has been shown to effectively encapsulate a variety of molecules within CDs, such as NIR dyes and photosensitisers [145,148]. The mechanism of encapsulation is thought to begin after initial carbon precursor carbonization. CD synthesis has been shown to be caused by the aggregation of furfural derivatives and polycyclic aromatic hydrocarbons from the decomposition of the various carbon sources [259]. The nucleation of these compounds leads to the formation of an amorphous carbon core around several guest molecules, effectively trapping them. Fig. 2.7 shows the effect of changing PpIX wt% during one-pot synthesis.

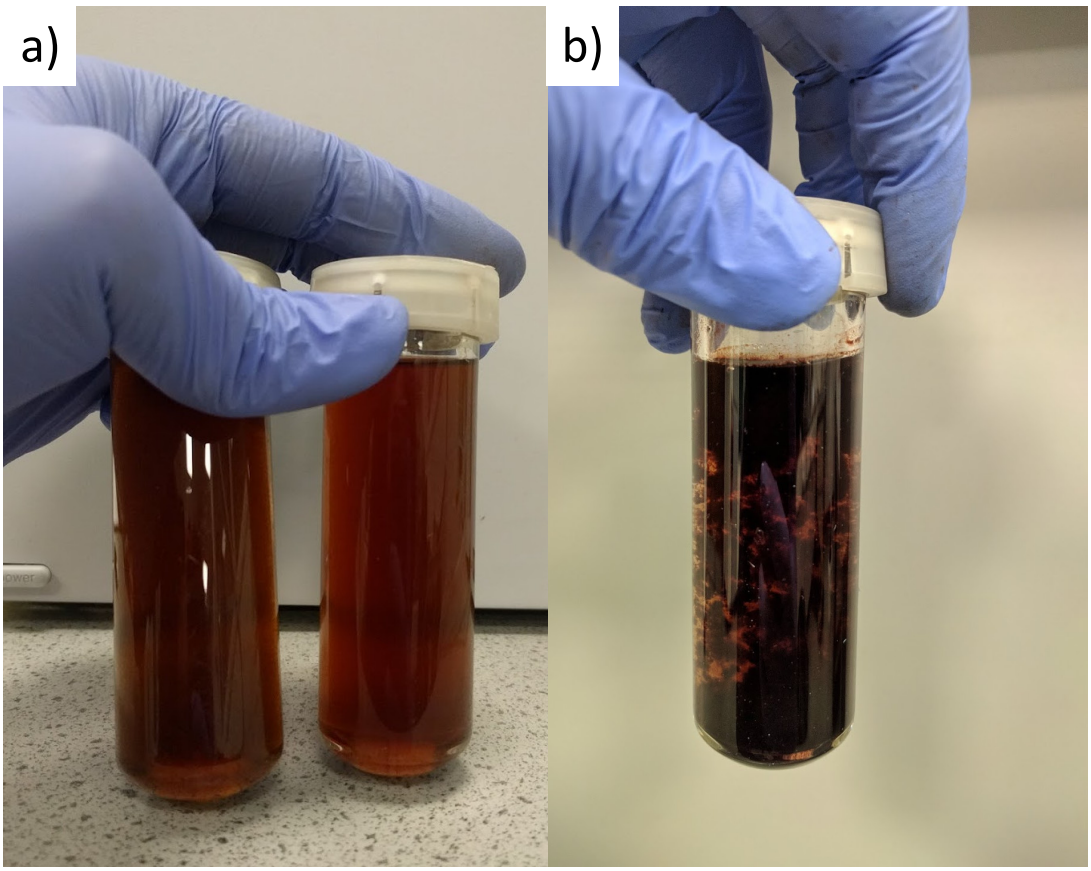

Fig. 2.7 – PpIX@CD samples change according to wt%. Lower percentages such as 0.5 and 1% (a) showing decreased aggregate formation compared to 2% (b).

Initial experiments led to the formation of large ash-like aggregates during the carbonization of citric acid and sucrose. These ashes decreased in quantity as temperature, time, and carbon source quantity were optimised. In particular, the adjustment of the initial carbon source concentration and continuous stirring the solution throughout the process ensured minimal char formation. Nonetheless, it is difficult to avoid precipitate formation in embedded CDs during microwave synthesis, as has been previously reported in the literature [148]. Though this fraction can be removed through centrifugation or chromatography, a large quantity of the guest molecule is lost after synthesis. Fig. 2.8 shows variations in colour with increasing PpIX wt% after synthesis and dialysis.

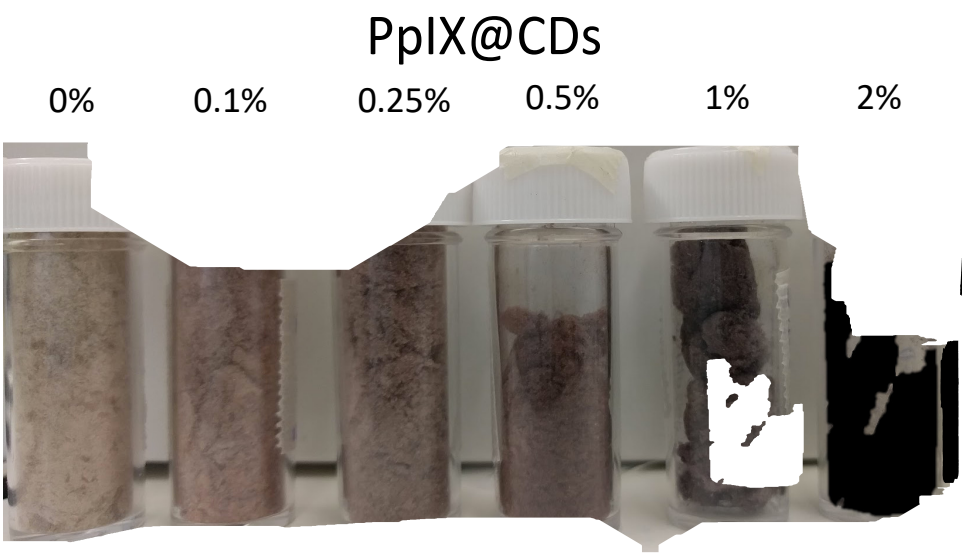

Fig. 2.8 – Freeze-dried PpIX@CD conjugates. A noticeable colour change can be seen as PpIX wt% increases.

Thermal degradation limits host-guest embedding in CDs

However, there is a key limitation in host-guest embedding with CDs that limits its versatility in comparison to crosslinking or other noncovalent interactions: the guest molecule must have a thermal stability higher than the reaction temperature for CD synthesis. Heat-sensitive molecules such as peptides, nucleic acids, or proteins cannot withstand the heat and would eventually be pyrolysed, acting as a secondary carbon source. PpIX has greater thermal

stability in comparison to the other reagents used for CD synthesis (citric acid or sucrose, ethylenediamine), ensuring only sucrose-based particles are formed [260,261]. This is expanded upon in the section detailing TGA results.

Amide crosslinking

Refining crosslinking protocol improved product yield

EDC-NHS cross-linking ensures the directional cross-linking of CDs to PpIX and avoid the formation of dimers. The standard protocol is that of protein cross-linking with an activation buffer for the component with carboxyl groups (0.1 M MES, 0.5 M sodium chloride in deionised water) at pH 6. However, PpIX has very low solubility in water and readily aggregated even at low concentrations (<50 μg/ml). Yildiz *et al.* (2010) fabricated a similar conjugate using a 1:1 DMSO/water solution to improve compound solubility prior to cross-linking [250]. Various water-miscible solvents for PpIX were tested to improve crosslinking efficiency, including acetone, DMSO, and DMF. The choice of solvent was limited by CD solubility and compatibility with the dialysis membrane. After several trails, DMF was determined to be the most suitable solvent for PpIX. Interestingly, MES buffer did not significantly improve PpIX loading in comparison to a solution containing only EDC and NHS. The addition of excess EDC (>6.25 mM) and NHS (>21.72 mM) did not show significant changes to conjugate yield.

After crosslinking, the solution was left to stand at room temperature to observe precipitation. This led to the separation of the less soluble fraction, named (PpIX-CD)p, from PpIX-CD, which can be clearly seen in Fig. 2.9. The remaining aggregates were removed after increasing centrifugation to 20 minutes and 12,000 rpm. (PpIX-CD)p showed significantly reduced solubility in water compared to both PpIX-CD and PpIX@CD but remained slightly better than free PpIX.

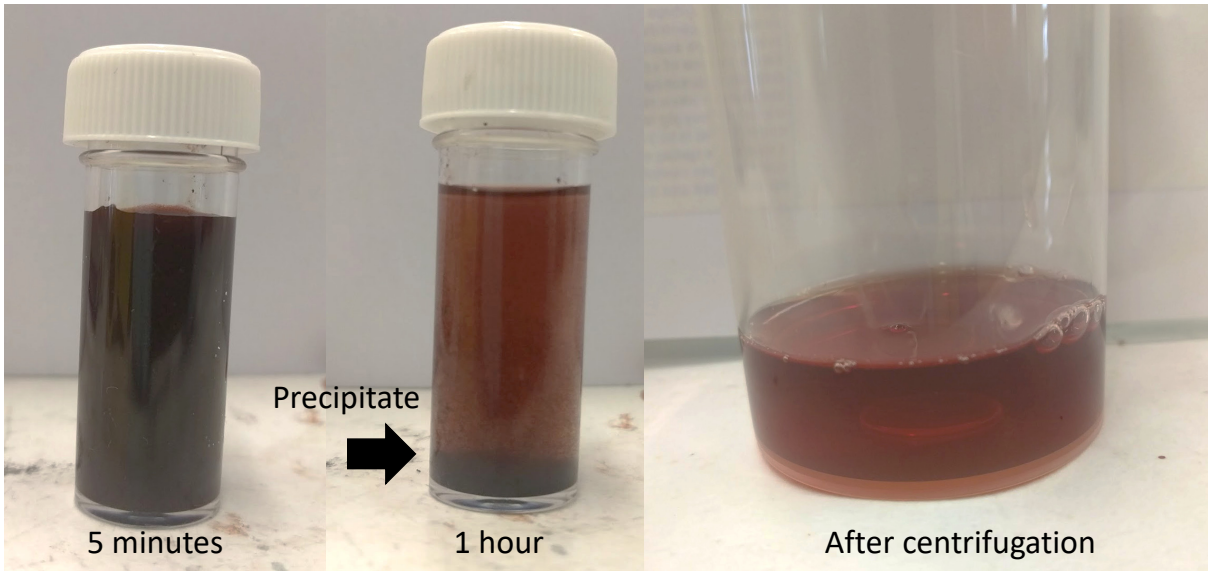

Fig. 2.9 – Crosslinked conjugates are separated by centrifugation. The solution gradually separated into two fractions: PpIX-CD and (PpIX-CD)p.

EDC-NHS linking has also been used to bind multiple molecules to CDs simultaneously. Zheng et al. (2016) demonstrated efficient PDT with a carbon nitride (C_3N_4)-based multifunctional nanocomposite (PCCN) consisting of CDs, Arg-Gly-Asp (RGD) motif, and PpIX. PCCN demonstrated water-splitting ability to produce singlet oxygen production while in a state of hypoxia with a PpIX content of 9.6% [158]. Despite decreasing total loaded PpIX in comparison to the previously described conjugates, it has the advantage of cell-specific targeting which could enhance their PDT efficiency.

EDC/NHS crosslinking is a better alternative due to water solubility

Incorrect crosslinking results in random coupling between molecules and leads to the formation of large aggregates, as dimers and eventually polymers begin to form. These less-soluble particles can significantly decrease treatment efficiency and generally present diminished photoluminescence due to self-quenching [262]. Hua et al. (2017) reported CDs could be covalently bound to PpIX [263]. They utilised the DCC/HOBt (dicyclohexylcarbodiimide/1-hydroxybenzotriazole) coupling strategy, also known as Steglich esterification. Cellular uptake

and decreased toxicity prior to photoactivation were observed. Interestingly, these conjugates presented a similar size (25.2 ± 5.7 nm) to that of PpIX-CD (25 ± 10 nm) but showed a lower PpIX loading efficiency of 23.3% in comparison to 43.3% (PpIX-CD) and 35.59% (PpIX@CD). Furthermore, they reported an intrinsic nucleolus-targeting capability better than the only commercially-available dye SYTO RNASelect [264]. These particles have also been used to conjugate photosensitizer Rose Bengal and the mitochondria targeting moiety triphenylphosphonium with CDs [154,265]. This reaction is widely known and extensively used in the pharmaceutical industry. DCC/HOBt benefits from the lack of hydrolysis during the reaction and lower total cost compared to EDC [266].

However, the choice of DCC/HOBt over EDC/NHS linking was unexpected as the former is not completely suitable for use with CDs. DCC and EDC are zero-length crosslinkers, meaning they form direct interactions between molecules through binding [267]. Although DCC has an extraordinarily high activation efficiency, it is limited by almost non-existent water solubility and formation of dicyclohexylurea after linking, requiring additional filtration steps to remove it from the solution. [268]. CDs are typically not soluble in organic solvents, which are required for DCC crosslinking. Furthermore, EDC is highly water soluble and its reaction by-product urea can be easily removed through dialysis [269]. Therefore, DCC is the less desirable choice for carbodiimide-based crosslinking of CDs in comparison to EDC.

In summary, three samples containing PpIX were obtained, as detailed in Fig. 2.10. CA-EDA CDs were used to crosslink PpIX using EDC/NHS chemistry, forming PpIX-CD (soluble fraction) and (PpIX-CD)p (insoluble fraction). PpIX@CD was synthesized using a one-pot reaction with sucrose, EDA, and PpIX.

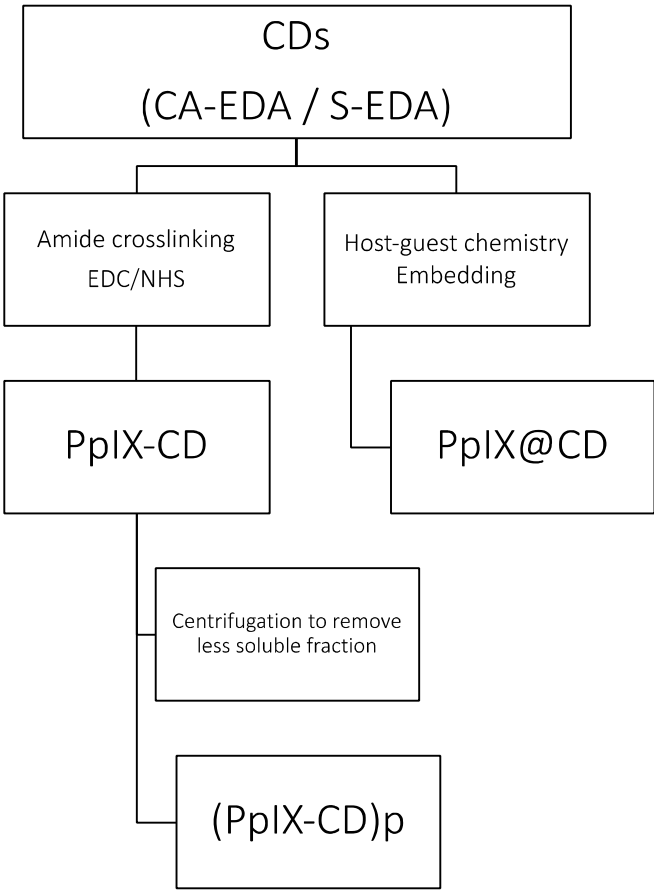

Fig. 2.10 – Schematic detailing newly synthesized PpIX-loaded conjugates.

Sample processing

Purification was carried out in several steps throughout synthesis and cross-linking. The use of centrifugation at 10,000 rpm successfully removed the largest aggregates. Generally, samples with higher quantities of sucrose, citric acid, and PpIX required additional rounds of centrifugation. Likewise, initial experiments showed greater precipitate formation as reaction times were increased.

Dialysis was a crucial part of sample post-processing

Dialysis removed remaining compounds from synthesis and cross-linking such as polycyclic aromatic compounds, buffer salts, and unbound PpIX [233]. As was observed with centrifugation, samples fabricated with greater amounts of carbon precursors or PpIX required additional time from 24 to 96 hours. These samples required additional water changes during the initial process as contaminants rapidly passed through the membrane, seen as a noticeably colour change in Fig. 2.11.

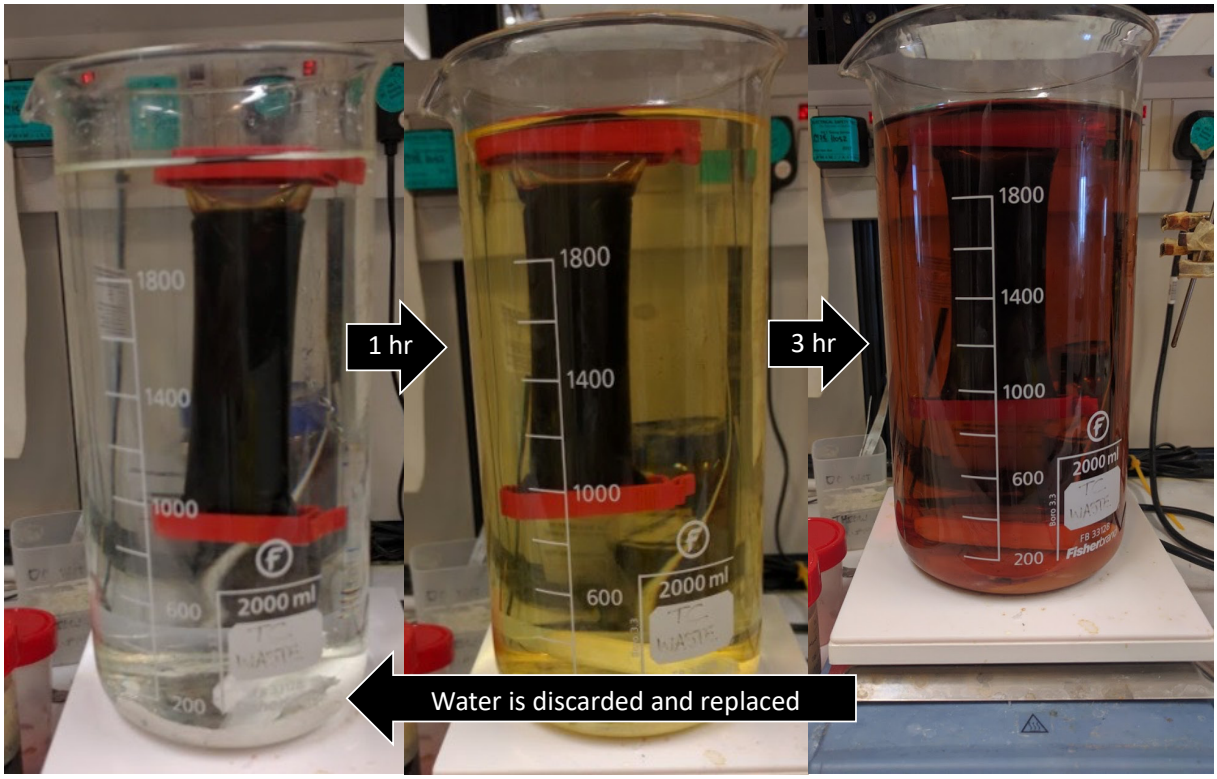

Fig. 2.11 – Dialysis was repeated to remove contaminants. The process was repeated until no colour change could be observed. Water was changed regularly to speed up contaminant removal. Approximately 50 ml of CD solution could be processed per container.

Freeze-drying was affected by impurities within samples

Freeze-drying produced a reddish to black powder which was subsequently weighed and stored in a dry environment away from light until used. Dialysis was found to be a necessary processing step for CD conjugate synthesis as particle recovery was impossible without its use,

resulting in a black sticky residue which was unable to be completely dried into powder form, seen in Fig. 2.12. In contrast, CD suspensions could be directly transferred after dialysis and successfully freeze-dried, resulting in a flaky powder being recovered, seen in Fig. 2.13.

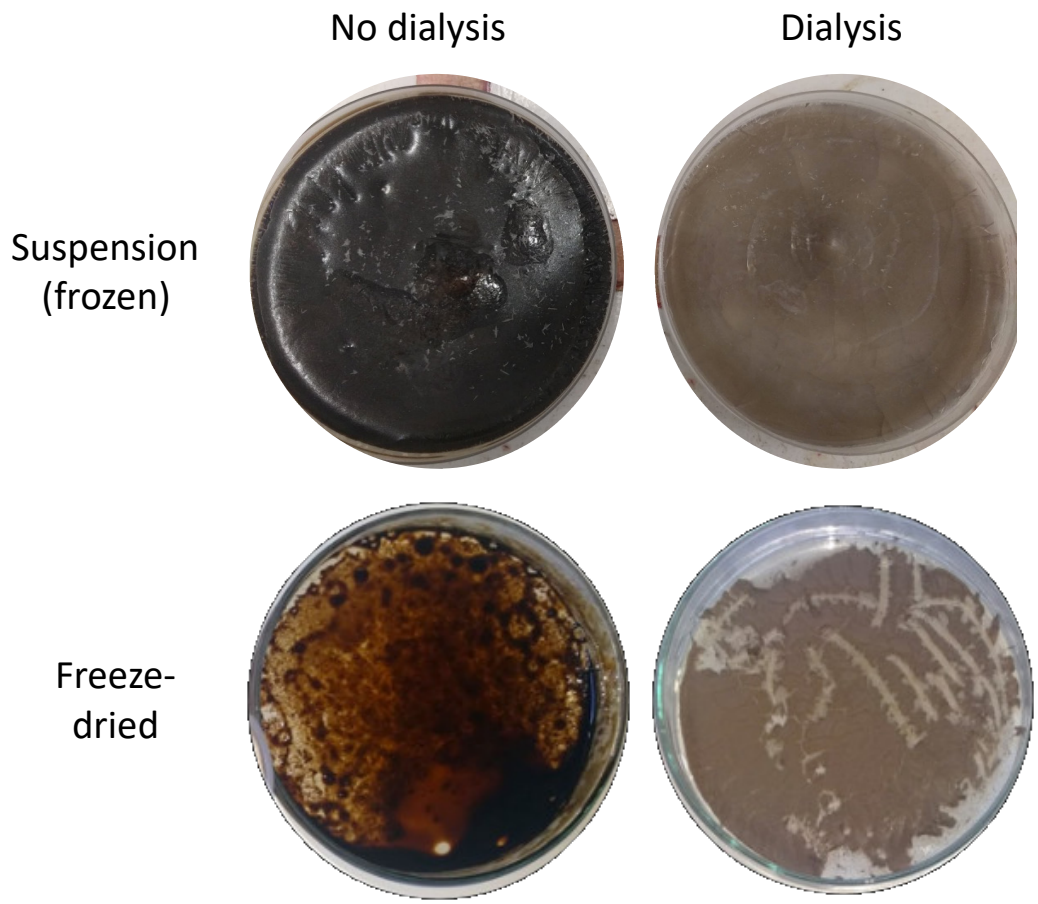

Fig 2.12 – Dialysis significantly changes product quality. The repetition of this process successfully removed most contaminants from the suspension and prevented sample rehydration after freeze-drying.

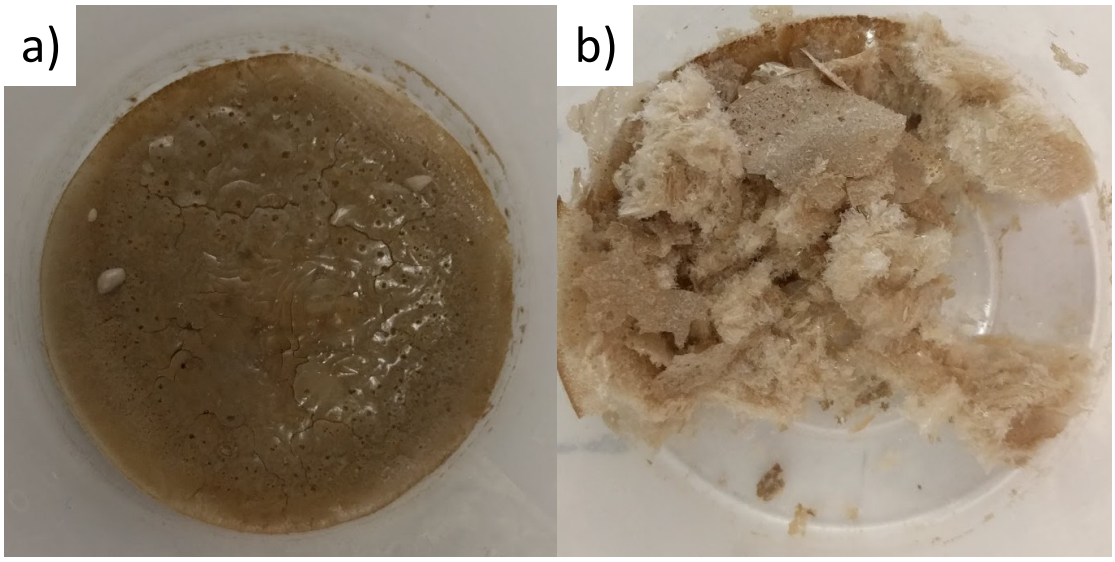

Fig. 2.13 – Sequential rounds of freeze-drying ensured complete removal of residual water. CDs were recovered and stored to prevent rehydration due to ambient moisture.

In summary, CDs were synthesized using microwave-assisted pyrolysis of citric acid or sucrose and ethylenediamine. The photosensitising drug PpIX was loaded onto CDs through amide crosslinking, producing two separate components: PpIX-CD and (PpIX-CD)p. Likewise, host-guest chemistry led to the synthesis of PpIX@CD with varying amounts of embedded porphyrin in a one-pot reaction. Conjugates showed increased solubility in water compared to PpIX due to the high hydrophilicity of CDs, seen in Fig. 2.14.

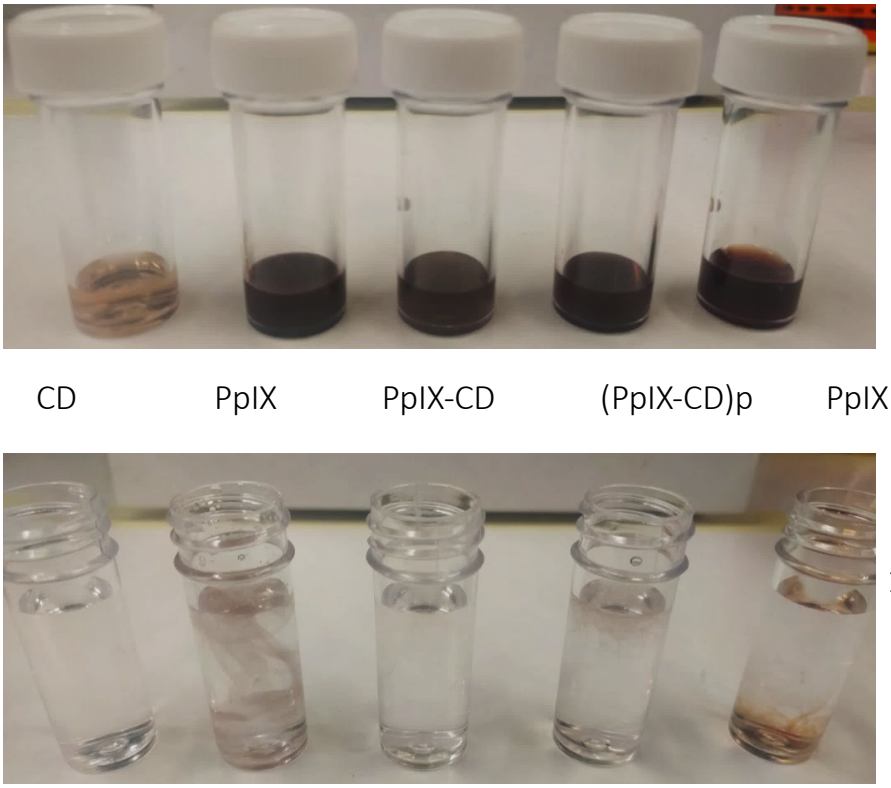

Fig. 2.14 – PpIX conjugates show variable dispersibility in water. After initial addition to solution, PpIX@CD and (PpIX-CD)p remained suspended and remained as such until mixed. PpIX-CD readily formed a slightly reddish suspension without observable precipitation.

Characterisation

Photoluminescence (PL) spectroscopy

Synthesised samples were first analysed using FL spectroscopy to determine their emission spectra. Fluorescence was measured in the range of near ultraviolet and visible light spectra (λ_{ex} = 300 - 500 nm) to match the typical absorbance maxima found in CDs. Emissions were detected in the range of 390 – 750 nm for all samples.

CD samples showed clear variations in photoluminescence, mostly based around the passivating agent that was used alongside the carbon source. Citric acid (CA) CDs showed higher emissions in comparison to sucrose-based CDs. Most samples showed high PL values in the range of 350 – 375 nm. PEG-coated CDs exhibited significantly reduced emissions across all wavelengths. These differences are much more apparent at lower excitation wavelengths, particularly 300 nm (Fig. 2.15). In comparison, PEI and EDA passivated CDs showed similar values regardless of excitation. PL increase is likely caused by the integration of nitrogen within CDs during one-step synthesis. Heteroatom doping has been shown to be an effective method for increasing CD emission and can be achieved using a nitrogen-rich carbon source or passivating agent during synthesis [38]. Nitrogen doping produced favourable results, yielding particles with enhanced photoluminescence in the desired excitation wavelengths for use with PpIX.

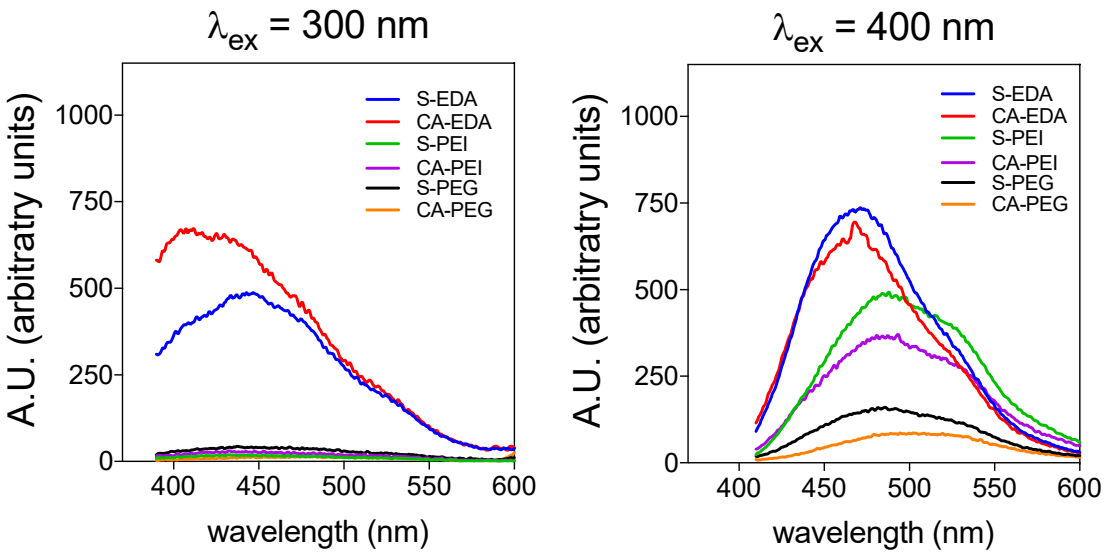

Fig. 2.15 – Comparison of emission at 300 and 400 nm excitation with various molecules used for passivation. EDA-coated CDs demonstrated significantly higher photoluminescence at both 300 and 400 nm excitation compared to PEG and PEI.

Interestingly, all samples show a combination of excitation dependent and independent photoluminescence. Excitation-independent behaviour in CDs has been observed with excitation wavelengths in the UV (around 280 - 380 nm) [270]. However, most reported CDs display excitation-dependent emission, where higher excitation wavelengths cause slight spectral shifts. Multicolour fluorescence could also be achieved by optimising the solvent and pH [271]. Nonetheless, all synthesized samples have a similar range of photoluminescence, rising from approximately 400 nm and dropping at 600 nm (Fig. 2.16).

In theory, further improvement of synthesis conditions could lead to red-shifted emission and increased quantum yield. Preliminary evaluation of newly synthesized samples using PL spectroscopy indicated that the use of ethylenediamine produced the best and most consistent results that could overlap with PpIX absorbance maxima (405 nm). Therefore, S-EDA and C-EDA CDs were selected for use in PpIX crosslinking.

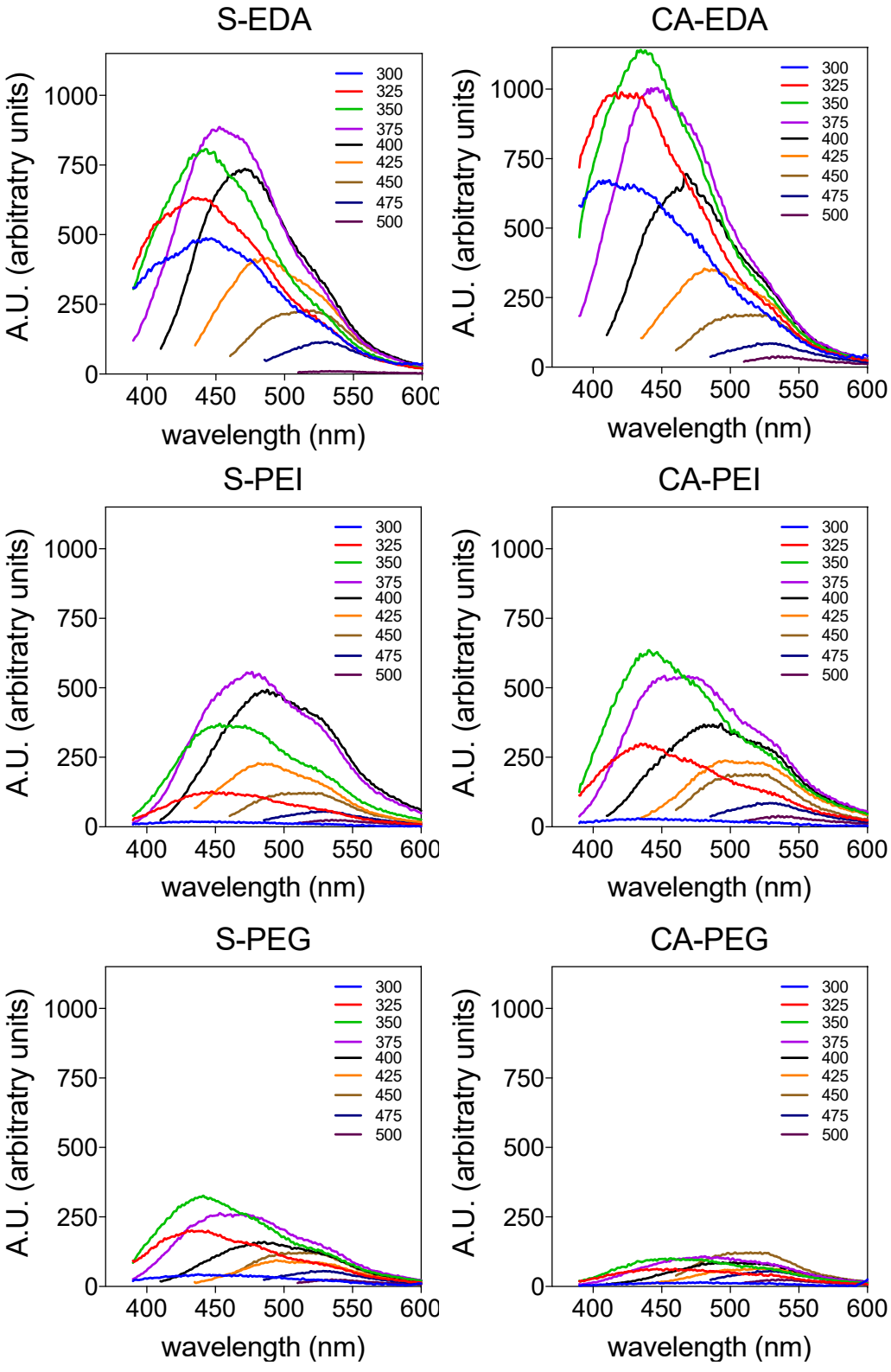

Fig 2.16 – Fluorescence spectra of synthesized CD samples from various carbon sources using excitation wavelengths ranging from 300-500 nm. PEG-coated samples showed drastically reduced photoluminescence in comparison to amine-rich PEI and EDA.

Photoluminescence at 405 nm excitation is needed for in vitro tests

Fluorescence for PS conjugates was measured by matching the maximum excitation wavelength to the LED used for *in vitro* tests (λ_{ex} = 405 nm), shown in Fig. 2.17. PpIX@CD was compared to S-EDA CDs while PpIX@CD and (PpIX-CD)p were compared to CA-EDA CDs. Fluorescence spectra demonstrate a dual emission behaviour from all conjugates. CD-related emissions are attenuated in conjugates, while PpIX-related emission peaks >600 nm are very similar between all samples. (PpIX-CD)p showed greatly reduced fluorescence to all samples in the range of 420 – 550 nm. PpIX loading in conjugates showed various ratios: PpIX-CD (41%), (PpIX-CD)p (34%), and PpIX@CD (48%).

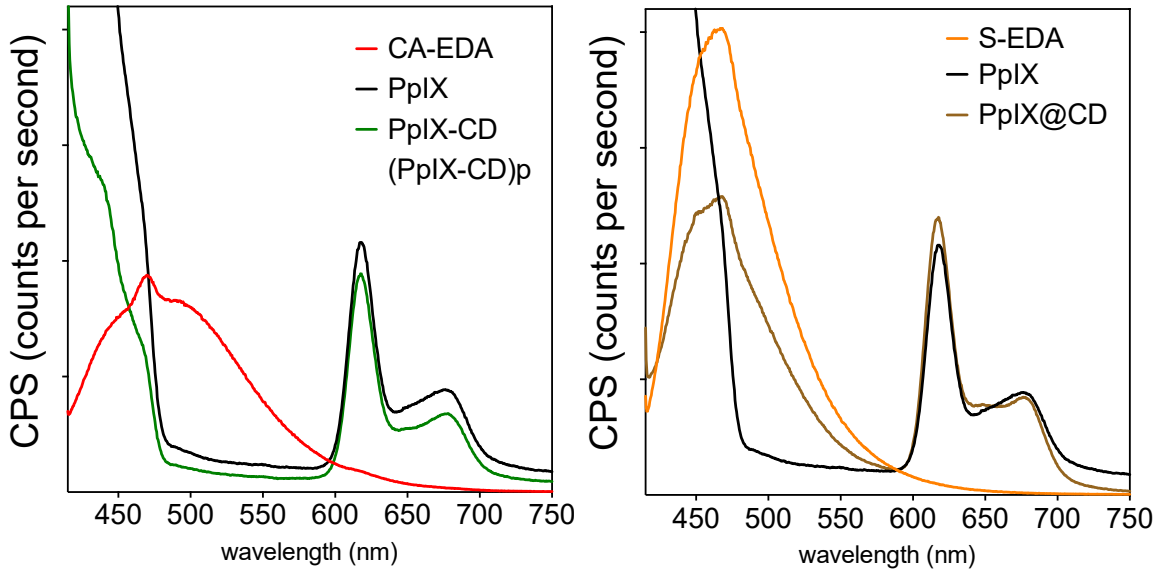

Fig. 2.17 – Fluorescence spectra of conjugates separated by CD subtype.

A dual emission behaviour was observed in all conjugates with intense and broad emissions at the 420-520 nm range similar to CD samples in literature [272]. Drug loading through both amide cross-linking and embedding directly reduced CD fluorescence. However, S-EDA CDs (within PpIX@CD) did not show the same decrease of photoluminescence after PpIX loading compared to PpIX-CD and (PpIX-CD)p. It is likely that porphyrin embedding increases the

prevalence of surface defects, which have been shown to enhance CD-based photoluminescence [273]. Nonetheless, all samples show a reduction of photoluminescence. This is likely caused by quenching of CD-based emissions through conjugate aggregation and obstruction of surface defects, which have been reported to heavily contribute to CD photoluminescence [274]. In particular, (PpIX-CD)p exhibited a near complete depletion of CD-related emissions. However, porphyrin-associated peaks to not seem to be greatly affected by either embedding or amide cross-linking at its emission peaks at 617 and 677 nm. This is possibly due to its outer location within the conjugate as PpIX binds to the CD surface through its carboxyl group. Additionally, the use of a DMF/water mixture during PpIX@CD synthesis could also have cause a change in emission.

Conjugates show variable PpIX content

PpIX loading was calculated as stated in the literature by using a calibration curve with diluted porphyrin in its linear range (0.4 – 1.6 μg/ml), seen in Fig. 2.18. PpIX content was estimated by comparing the relative intensities of the 658 nm peak while exciting the solution at λ_{ex} = 404 nm of PpIX [251]. CD fluorescence from both CA-EDA and S-EDA was subtracted from each conjugate to estimate drug loading. Through these observations, the total quantity of PpIX that could be introduced efficiently with host-guest embedding in CDs without precipitate formation is approximately 1 wt%. In comparison, previously reported Nile Blue embedded in PEG-based CDs used a 1:10 weight ratio and exhibited a higher degree of aggregate formation. This required centrifugation at 20,000 g and the use of an aqueous gel separation column to recover the sample [275].

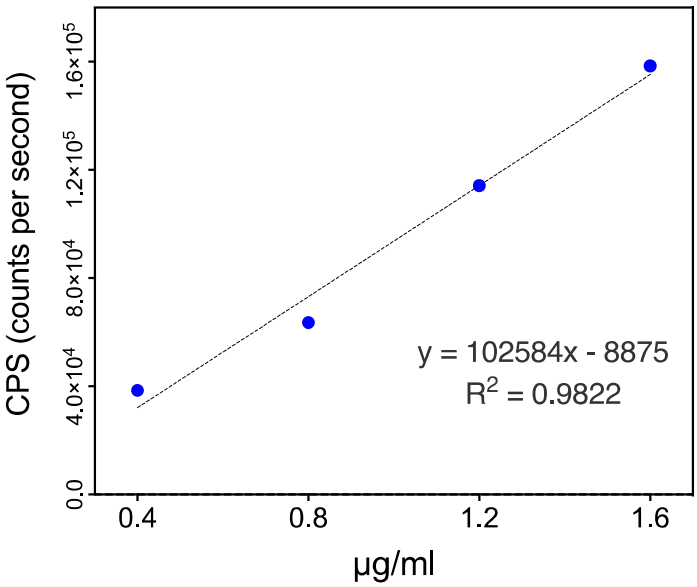

Sample	PpIX %
PpIX	100
PpIX-CD	41
(PpIX-CD)p	34
PpIX@CD	48
CDs (CA-EDA/S-EDA)	0

Fig. 2.18 – Loading in conjugates was calculated using a PpIX calibration curve. The curve was based on PpIX fluorescence at the absorbance maximum (λ_{max} = 405 nm). Conjugates were diluted and compared to estimate PpIX content.

Host-guest embedded samples showed significant variation. As expected, increasing porphyrin wt% in the precursor solution led to gradual increases in final PpIX content from 0.1 to 1 wt%, shown in Fig. 2.19. Intriguingly, samples doped with 2 wt% PpIX did not follow this trend, showing lower loading efficiency in comparison to 1 wt%. It is possible that the reaction time used for PpIX@CD synthesis was not enough to pyrolyse all available sucrose and EDA, causing only partial encapsulation of all available porphyrin. Reaction times for microwave synthesis are extremely varied and have been evaluated up to a total length of 30 minutes [276]. Nonetheless, it is highly likely that the precipitate formed during PpIX@CD 2% synthesis corresponds to unbound PpIX. Thus, PpIX@CD (1 wt%) was selected to be used in all further studies due to its high PpIX content.

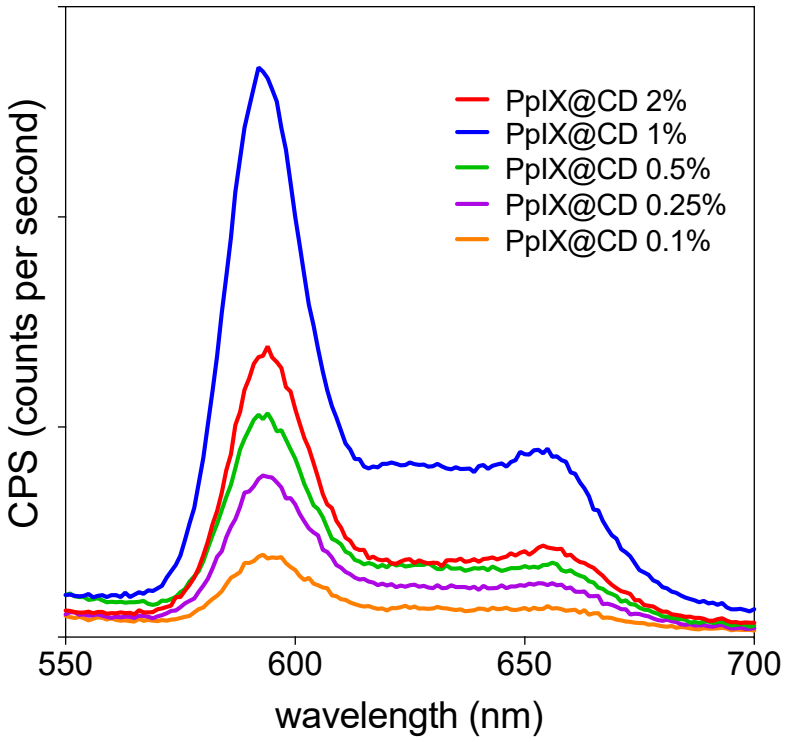

Initial wt%	PpIX %
2	24
1	48
0.5	18
0.25	14
0.1	8

Fig. 2.19 – Fluorescence spectra of PpIX host-guest encapsulated conjugates. All samples show fluorescence corresponding to the characteristic emission bands. PpIX loading efficiency was calculated as previously detailed.

Ultraviolet-visible spectroscopy (UV-Vis)

Absorbance and fluorescence spectra were obtained utilising conjugates suspended in PBS at pH 7. CDs typically have a strong and broad absorption in the ultraviolet region, followed by a constant decrease as excitation wavelength increases [277]. In general, absorption below 375 nm has been attributed to π–π* transitions of the carbon dot surface, mainly from C=C and C=N bonds [278]. Nonetheless, conjugate absorbance was dominated by PpIX with a high absorption band at approximately 405 nm, followed by a small peak at 500 nm. PpIX-CD and (PpIX-CD)p showed similar absorbance while PpIX@CD showed a 40% decrease at equal concentrations.

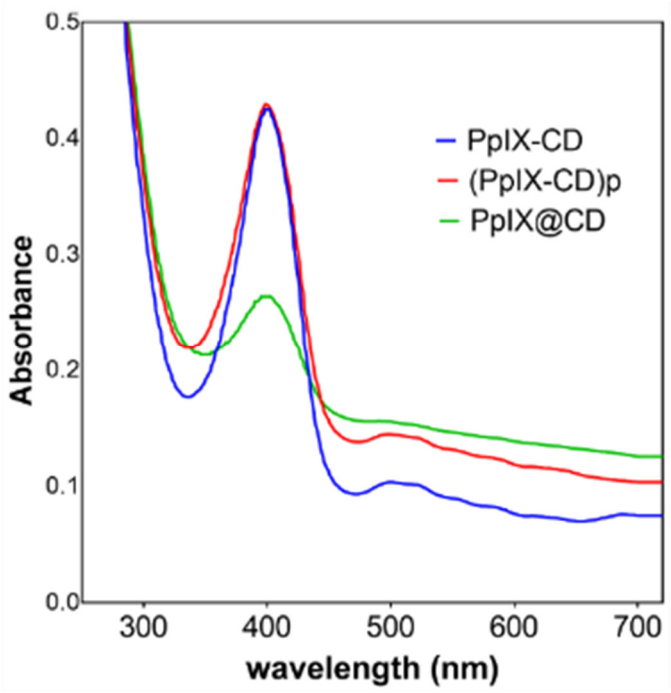

Fig. 2.20 – Absorbance spectra of PpIX, PpIX-CD, (PpIX-CD)p and PpIX@CD in water.

Fourier transform infrared spectroscopy (FT-IR)

Infrared spectra obtained from PpIX and PpIX-CD were found to be nearly identical. Similarly, this was observed between CA-EDA, S-EDA CDs, (PpIX-CD)p and PpIX@CD. FT-IR spectroscopy was used to evaluate conjugate surface chemistry in the range of 4000-700 cm^{-1}. CA-EDA CDs were found to be very similar to S-EDA CDs, likely due to the similarity of their carbon sources. Conjugates were divided as previously mentioned in two groups based on their similarities to CDs or PpIX. The assignment of peaks was carried out by comparing IR spectra to those found in the literature for CD samples (Table 2.3).

Peaks attributed to C-C stretching at 1680cm^{-1} can be seen in all samples. However, the small 1720 cm^{-1} peak corresponding to C=O stretching and the broad -OH peak at around 3000 cm^{-1} were not observed in PpIX-CD and PpIX (Fig. 2.21). In comparison, these peaks were seen in all other samples including PpIX@CD and (PpIX-CD)p (Fig. 2.22). The characteristic amide band can be observed in CD, (PpIX-CD)p and PpIX@CD around 1570 cm^{-1} and is absent in

PpIX-CD. Peaks in the range of 1395-1216 cm^{1} can be ascribed to C=C, C=N, and C=C-O respectively. The small sharp peaks at 1075 and 1059 cm^{-1} can be seen in samples corresponding to C-O and C-H groups. The reduction of available amine functional groups during amide cross-linking is likely the cause for variation between spectra. These slight variations between samples can be observed particularly in the distinctive amide I peak at ~1570 cm^{-1}. The change in the availability of primary amines can also be seen in the region of 918-625 cm^{-1} which has been previously linked to N-H wag in carbon dots [195]. Samples show a small amount of water in the 3000 cm^{-1} region, which corresponds to -OH. This broad peak shows some absorbed humidity is present in all samples regardless of freeze-drying (Fig. 2.23).

Table 2.3. FT-IR peak assignation. Table with assigned FT-IR peaks in conjugates in the range of 2000 - 700 cm-1.

Peak (cm^{-1})	**Assignment**	**Reference**
1720	C=O stretching	Sellitti et al. (1990) [279]
1680	C=C stretch	Lei et al. (2016) [280]
1570	N-H bending	Liu et al. (2016) [281]
1395	O-H/C-N	Lei et al. (2016) [280]
1338	C=N	Liu et al. (2016) [281]
1216	C=C-O	Liu et al. (2016) [281]
1075	C-O	Liu et al. (2016) [281]
1059	C-H bending	Sellitti et al. (1990) [279]
918 - 625	N-H wag	Meiling et al. (2016) [195]

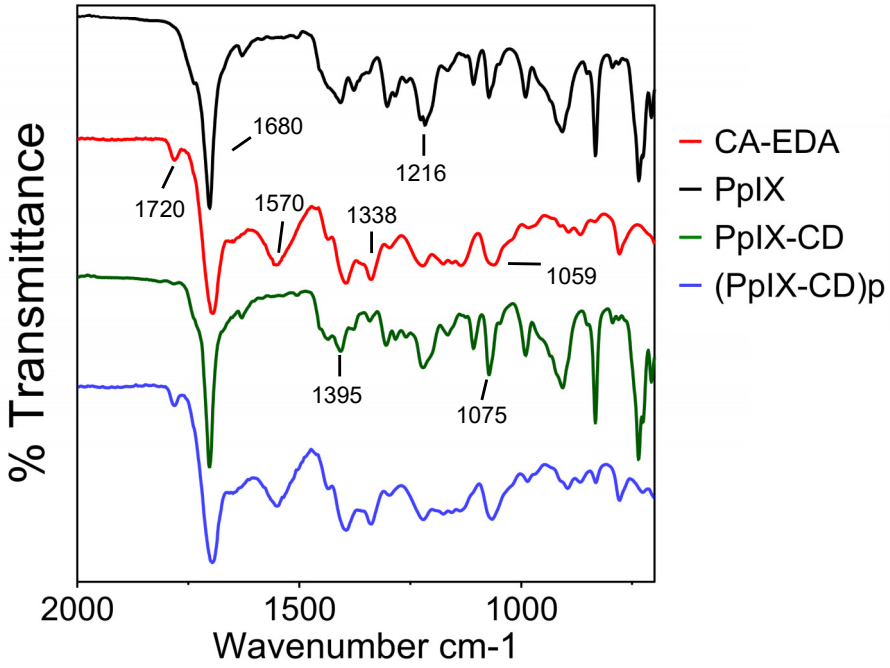

Fig. 2.21 – FT-IR spectra comparing surface chemistry of CA-EDA samples. The characteristic amine band (N-H) does not appear in PpIX-CD, indicating complete crosslinking using EDC/NHS.

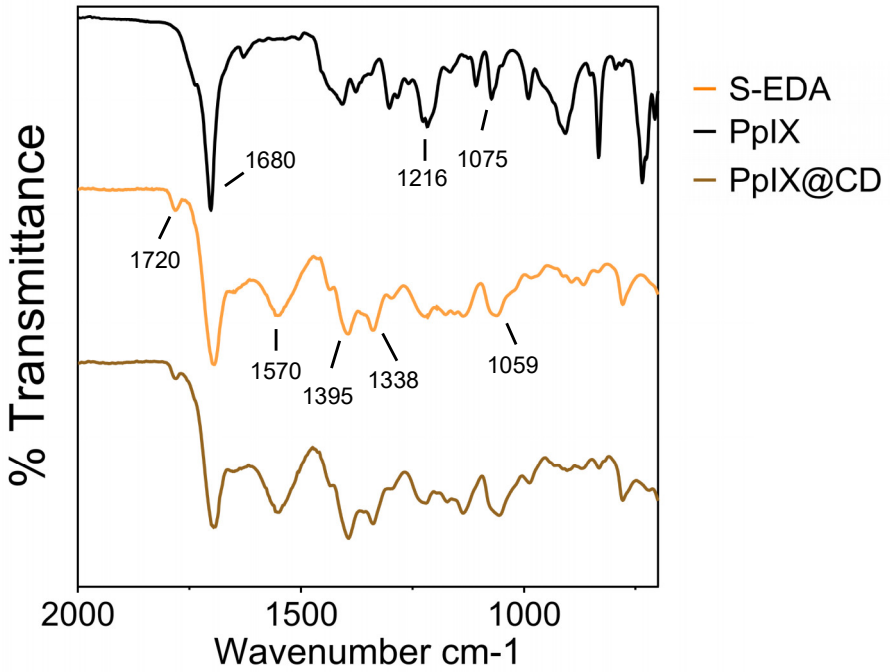

Fig. 2.22 – FT-IR spectra comparing surface chemistry of S-EDA sample PpIX@CD. Amine groups are available as PpIX was noncovalently bound through host-guest chemistry.

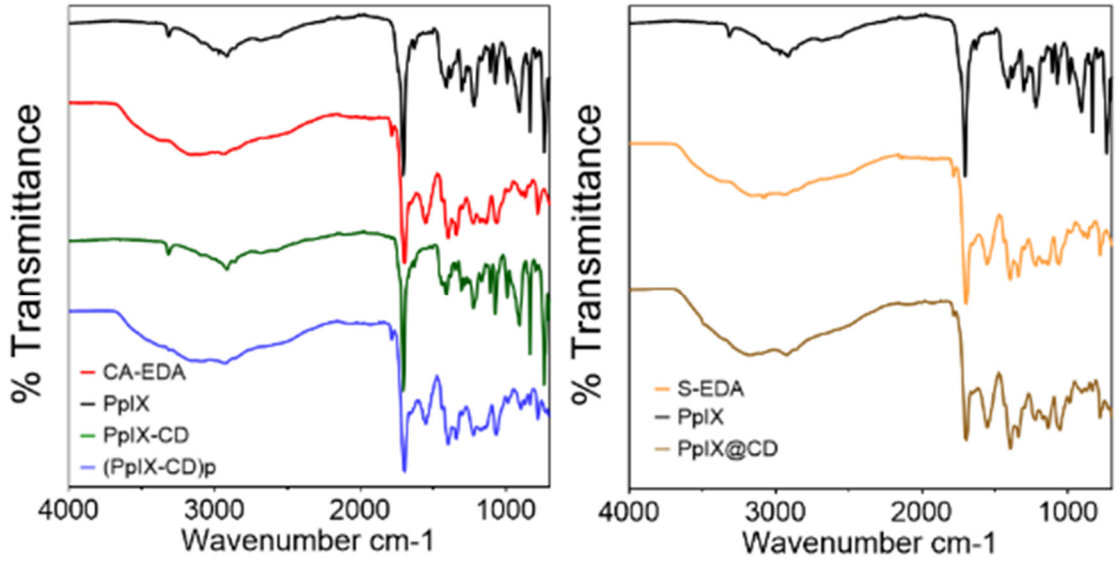

Fig. 2.23 – Full FT-IR spectra of CA-EDA and S-EDA conjugates.

Changing PpIX% for embedded samples did not change surface chemistry

PpIX@CD samples did not show a significant difference in surface chemistry between each other, as can be observed in Fig. 2.24. The C-C stretch at 1680 cm^{-1} could be seen in all samples, whereas the opposite was seen with the C-H band at 1059 cm^{-1}, which increased at 0.1, 0.25 and 2 wt%. Primary amines appear to be more available in these samples, as can be seen in the region of 918-625 cm^{-1}, which was mentioned previously. However, the characteristic amide band at 1570 cm^{-1} can be seen in all samples with similar intensity, indicating the presence of nitrogen on the surface.

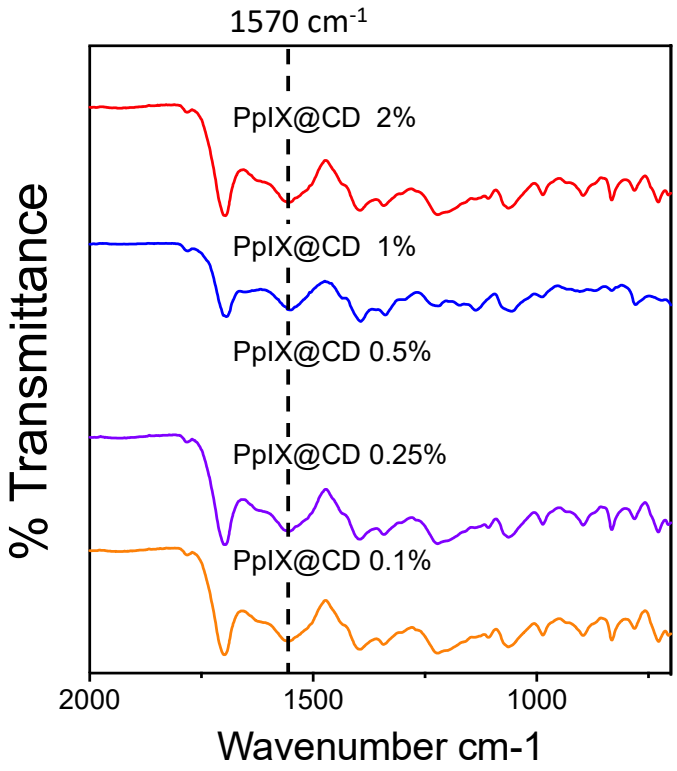

Fig. 2.24 – FT-IR spectra comparing surface chemistry of PpIX host-guest encapsulated samples.

Transmission electron microscopy (TEM)

Transmission electron microscopy (TEM) revealed a quasispherical particle morphology for all CD and conjugate samples, with CDs being observed as small aggregates (Fig. 2.25). with an average diameter of 25 ± 10 nm (PpIX-CD) and 17 ± 6 nm (PpIX@CD). (PpIX-CD)p exhibited a highly variable particle size range of 15 – 100 nm. Conjugates displayed an irregular quasispherical morphology, with aggregates forming regardless of the concentration and sample grid-loading combination that was tested. CA-EDA and S-EDA CDs showed an average particle size below 10 nm and a more defined spherical morphology. Finally, PpIX coalesced into well-defined geometric structures with sizes greater than 100 nm in diameter.

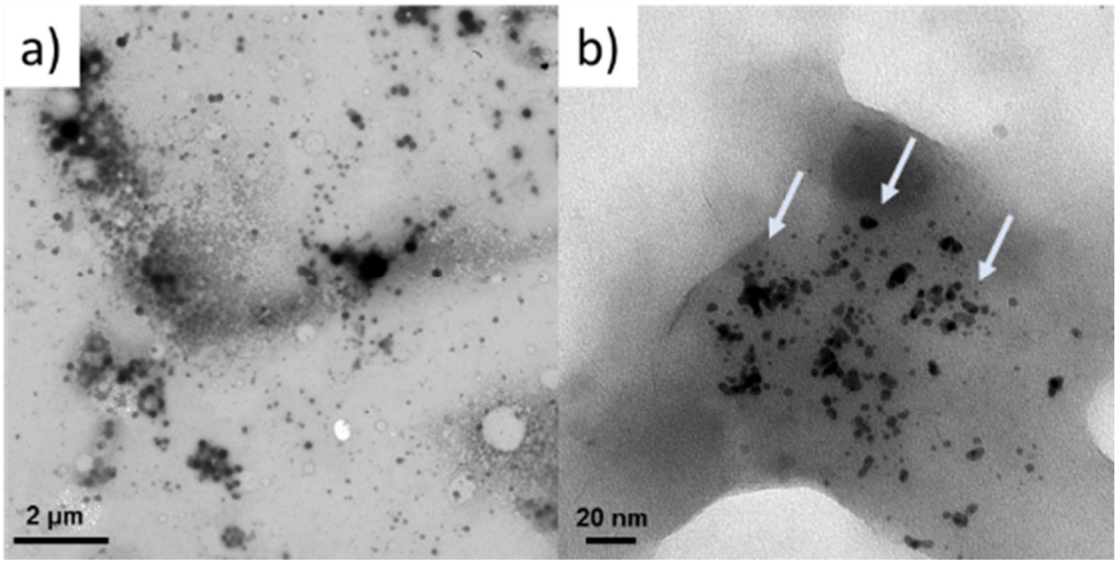

Fig. 2.25 – CDs form small aggregates in water suspension. TEM images of CDs at 690× (a) and 68,000× (b). CDs form small aggregates (<200 nm) at higher concentration (a). Individual particles can be seen after diluting stock solutions and sonicating samples (b).

TEM images demonstrate a size and morphology variation between conjugates, which could be caused by the synthesis strategy and influences particle solubility. This can be seen with particle aggregation for various samples in Fig. 2.26. PpIX-CD was fabricated in a controlled and directed cross-linking reaction utilising purified CA-EDA CDs and PpIX. Results show PpIX-CD and PpIX@CD form reduced aggregates under 200 nm in size while both (PpIX-CD)p and PpIX quickly form aggregates. Conjugates show reduced solubility in water in comparison to base CDs but are more soluble than PpIX in concentrations below 25 µg/ml. Solutions with conjugates show slight precipitation after several hours of ultrasonic processing. Additionally, (PpIX-CD)p was determined to be the most heterogeneous sample due to its wide size distribution.

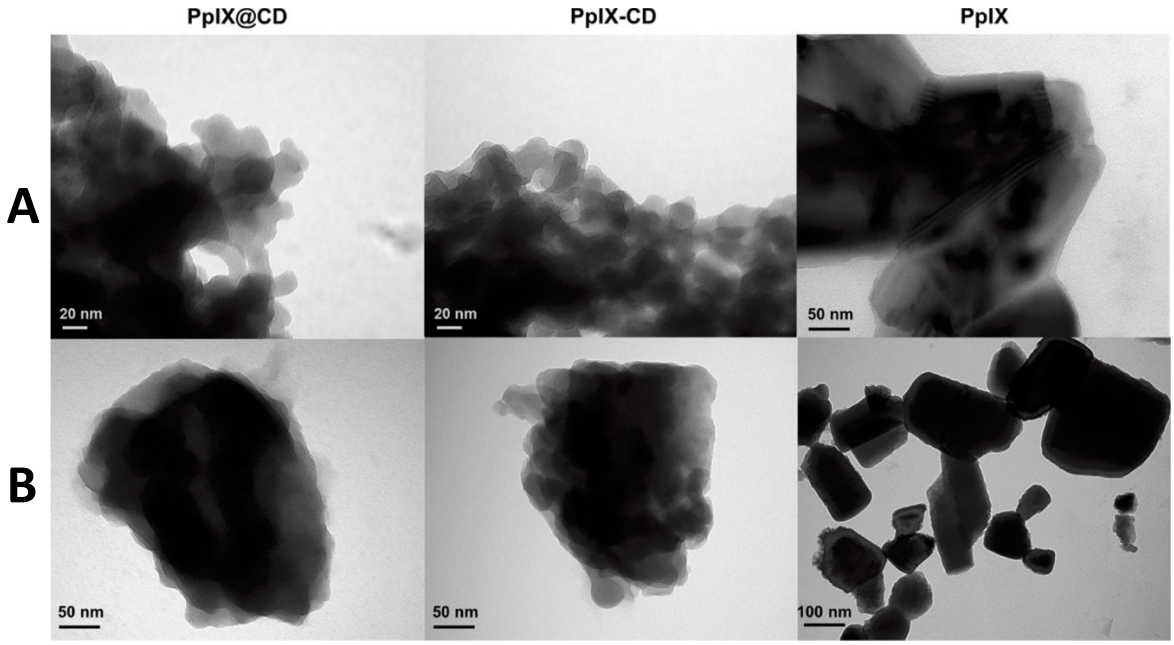

Fig. 2.26 – CD-PS conjugates show decreased aggregation in water. TEM images of conjugates at 30,000× (A) and 68,000× (B). Conjugates show irregular morphology and less aggregation in comparison to PpIX (30,000× and 18,500×).

Host-guest embedding relied on the one-pot synthesis of PpIX@CD which produced slightly larger aggregates, with some variations which can be seen in Fig. 2.27. CD nucleation and growth is altered by various synthesis conditions, such as temperature and type of carbon source. This could be further affected by the use of hydrophobic compounds and may have led to greater size variation in PpIX@CD compared to PpIX-CD [282]. Therefore, host-guest embedding appears to be a less reliable and reproducible strategy for drug loading in CDs in comparison to amide cross-linking.

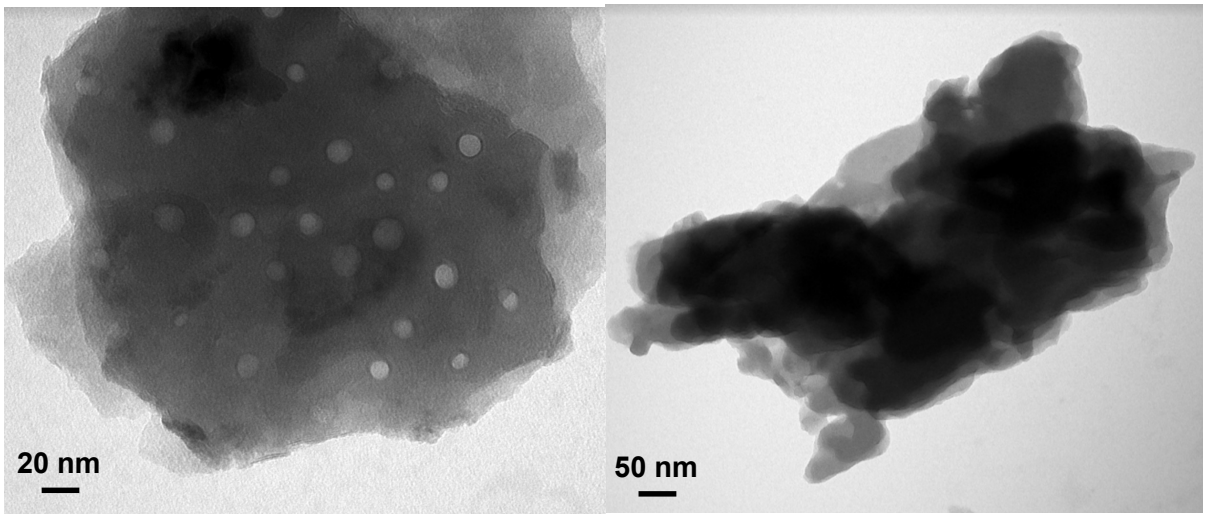

Fig. 2.27 – PpIX-loaded CDs can form aggregates depending on synthesis conditions. PpIX@CD formed some separate porous nanoparticles, seen at 49,000× (right). PpIX-CD aggregates caused by dimerization could be seen at 49,000× (right).

Aggregates could be seen in all samples regardless of conjugation strategy or PpIX concentration. Imaging of PpIX@CD showed the presence of a minute amount of porous particles, which have been previously reported in the literature [135]. These structures are approximately ten times larger than the previously observed PpIX@CD conjugates. PpIX@CD also showed the formation of self-assembled nanostructures after the sample dried on the TEM grid, which can be seen in Fig. 2.28. These tubular structures are likely caused by hydrophobic interactions, formed through π–π stacking of the internal pyrrole rings found within PpIX. Similarly, PpIX-CD showed the formation of aggregates of approximately 250 – 400 nm in

size, which could be formed as multiple CDs and PpIX molecules are bound through amide bonds.

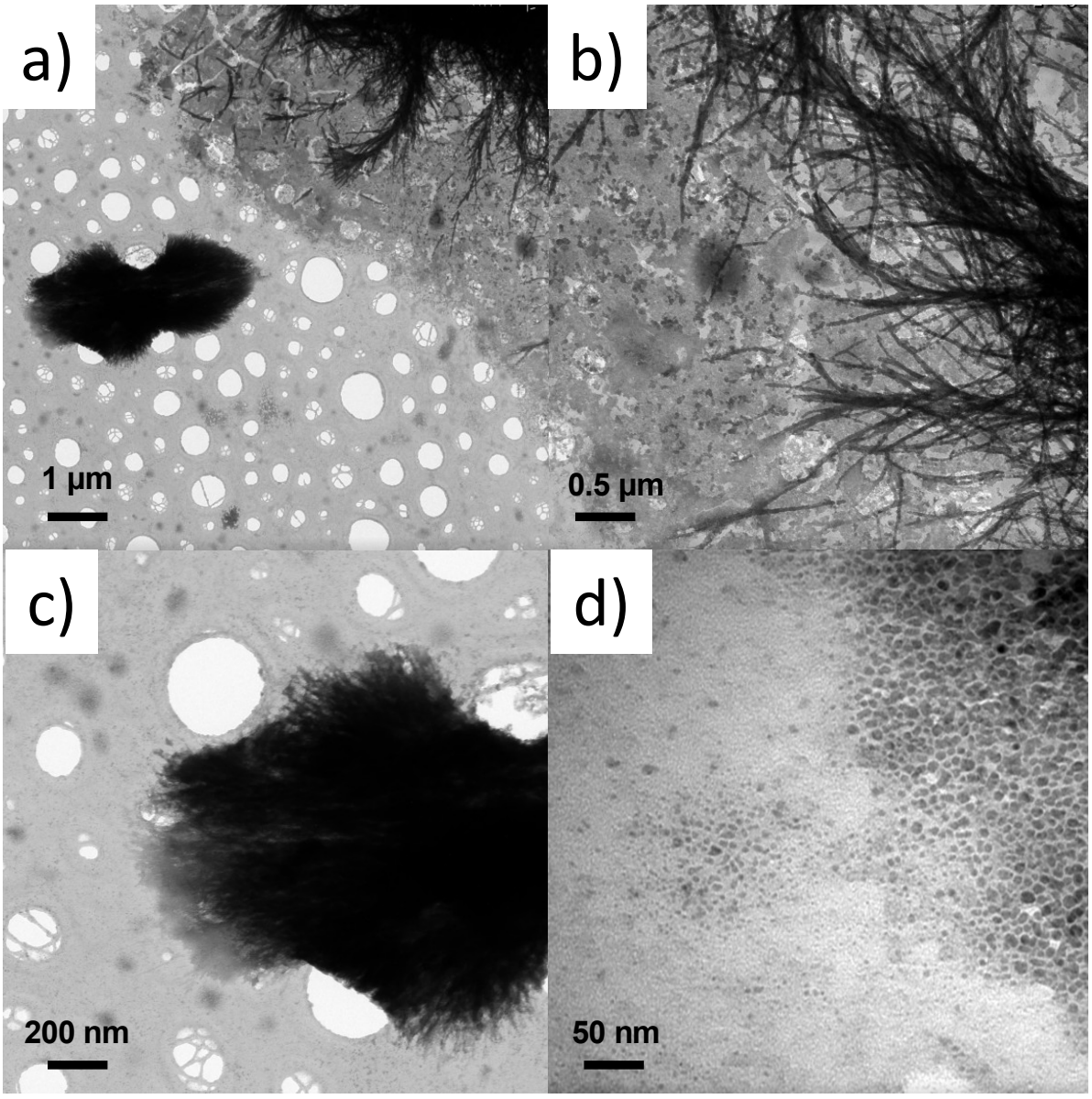

Fig. 2.28 – PpIX@CD self-assembles at higher concentrations. TEM images of PpIX@CD show tendril-like structures forming from aggregates, with individual particles becoming clearer at higher magnifications.

Finally, (PpIX-CD)p readily aggregated in water in all concentrations (0.1 – 10 µg/ml) and after processing the solution with an ultrasonic probe. The formation of these aggregates is likely the cause of its low photoluminescence due to rapid quenching. It is likely these

aggregates contain a high concentration of PpIX as they are similar in appearance with more defined edges instead of an amorphous form, shown in Fig. 2.29.

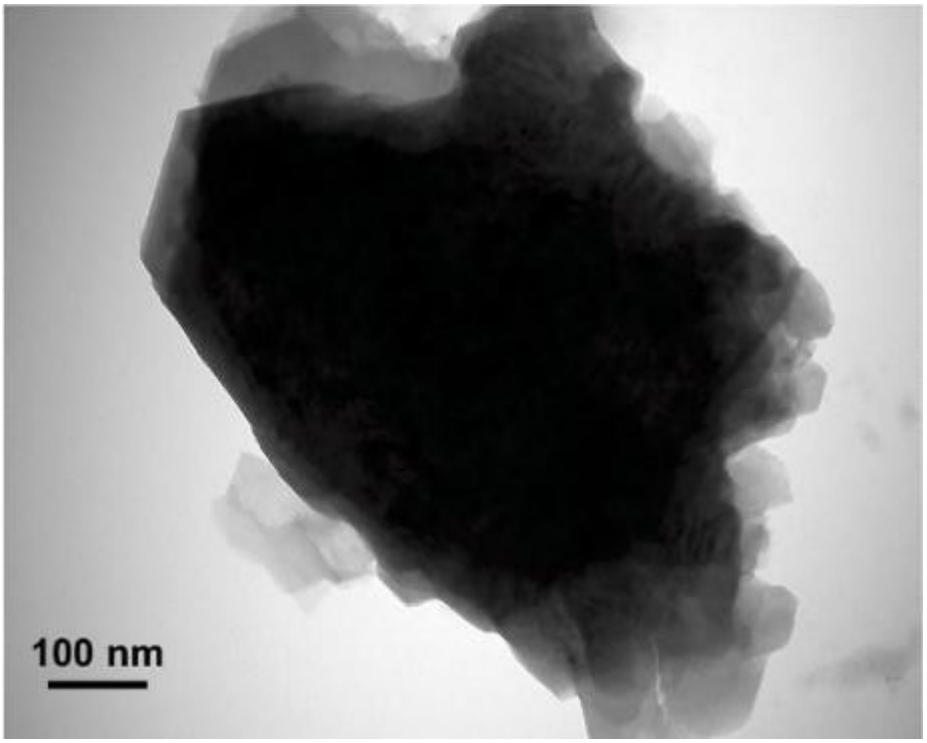

Fig. 2.29 – (PpIX-CD)p rapidly forms large aggregates in water. TEM image at 18,500X, individual particles can be observed around the edges of the aggregate.

Singlet oxygen generation confirms PpIX loading and potential use for PDT

Singlet oxygen production was determined by the time-resolved measurement of its characteristic luminescence at 1270 nm. Samples were excited utilising a 355 nm Nd:YAG laser at 50, 100, and 200 mJ (Fig. 2.30). Phenalenone (PH) in DMF was used as a standard indicating 100% singlet oxygen production. PpIX was determined to produce an average of 92.18% singlet oxygen. $^1O_2$ production in conjugates was also calculated with values of 63.79% (PpIX-CD), 77.10% (PpIX-CD)p and 51.62% PpIX@CD.

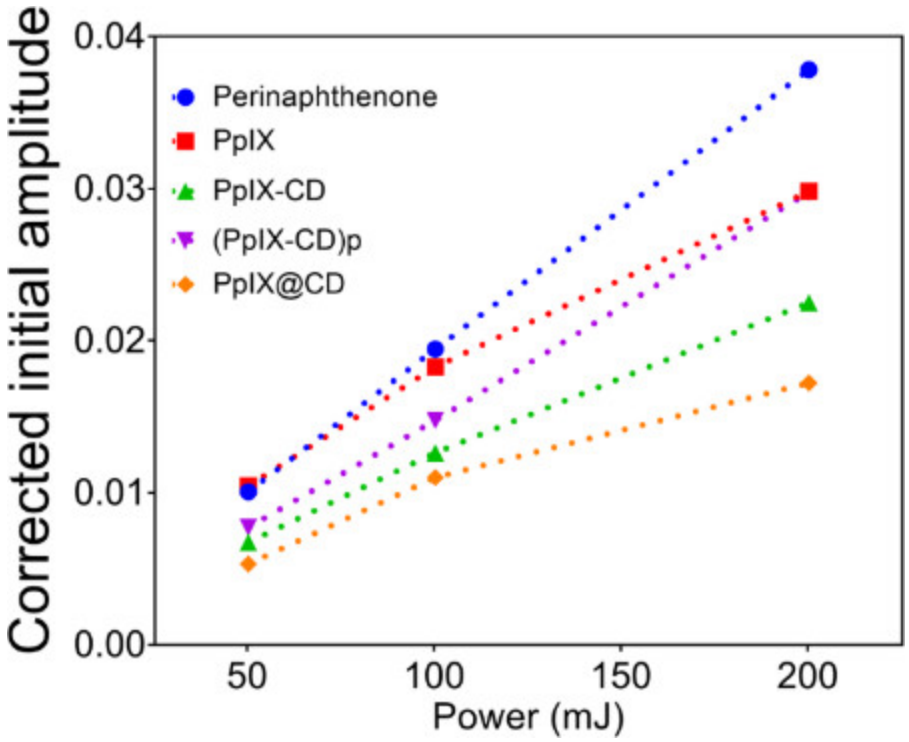

Fig. 2.30 – Singlet oxygen yield of conjugates in DMF. Corrected initial amplitude of lifetime generated singlet oxygen against the power of a 355 nm Nd:YAG laser to calculate singlet oxygen yield of each sample. Phenalenone was used as a control for 95% production.

Singlet oxygen ($^1O_2$) production alone initially indicates (PpIX-CD)p is the best conjugate for PDT, while PpIX-CD and PpIX@CD appear to have reduced efficiency. However, this is because DMF was required for the measurement. $^1O_2$ yield was likely affected by the increased solubility of (PpIX-CD)p in organic solvents, as this conjugate readily aggregates in water. Nonetheless, we observed all the samples showed decreased singlet oxygen emission in comparison to PpIX. Our results indicate fluorescence emission intensity of the conjugates cannot be directly linked to singlet oxygen yield.

X-ray photoelectron spectroscopy (XPS)

XPS analysis with survey and high resolution C1s scans determined conjugates have little to no difference in surface composition with PpIX (Table 2.4). Carbon dot compositions are very similar between CA-EDA and S-EDA samples, with only slight variations in C and O. The

pure PpIX sample is close to what is expected given its chemical formula ($C_{34}H_{34}N_4O_4$). If hydrogens in this sample are neglected, it has concentration values of 82.6 at% C, 8.2 at% N and 9.0 at% O, as seen in Table 2.4 as compared to 81% C, and 9.5% N and O theoretically. In comparison, CD conjugates demonstrate small increases in oxygen. The high resolution C1s spectra peak positions are given relative to C-C/C-H being at ~285.0 eV, and it is assumed the lowest carbon peak position is C-C/C-H as no carbides were expected in these samples. There was no distinction in peak position between both C-C and C=C type bonds and are therefore expected to be the major peak.

Table 2.4. Surface composition (atomic%) of PpIX and CD-conjugates.

Sample	C	O	N	Na	Cl
CA-EDA	56.7	37.4	5.8	<0.1	0.1
S-EDA	59.1	35.4	5.4	<0.1	0.1
PpIX	82.6	9.0	8.2	<0.1	0.2
PpIX-CD	81.6	9.6	8.6	<0.1	0.2
(PpIX-CD)p	76.4	13.5	9.7	<0.1	0.4
PpIX@CD	82.1	9.4	8.3	<0.1	0.2

XPS analysis demonstrated there is little to no variation in the carbon envelopes of conjugates and PpIX. C=C bonds seen in the high resolution C1s spectra could present π-π* transitions, which could lead to small intensities at higher binding energies but should not be considered true XPS peaks. We observed that the C-N environment is the major component and is seen at

a higher binding energy and slightly reduced peak positions. This is possibly due to the influence of carbons attached to nitrogen in PpIX and conjugates as it contains a porphyrin core with a tetrapyrrole macrocycle, giving it an aromatic nature [283].

Thermogravimetric analysis (TGA)

TGA analysis showed a clear difference between CDs and PpIX conjugates, seen in Fig. 2.31. The thermal desorption of water physically adsorbed on the samples caused a slight weight loss at temperatures lower than 120°C, which is consistent with previous reports [284]. CDs showed a slight drop in mass as thermal stability until approximately 188°C – slightly above the thermal decomposition temperatures of citric acid (176°C) and sucrose (185°C), respectively [260,285]. The weight loss continued as external oxygen-containing functional groups were oxidized at temperatures in the range of 200 - 500°C. In contrast, PpIX showed great thermal stability up to approximately 300°C, which is well past the CD synthesis temperature of 150°C. The majority of PpIX molecular mass is based on its pyrrole ring which begins thermal decomposition around 340-450°C as evidenced by TGA analysis. Although there is a slight mass reduction from 26-360°C, this has been mainly linked to the breaking of reactive bonds outside the ring [261]. Therefore, it is highly likely host-guest embedding does not significantly alter PpIX structure and functionality during microwave-assisted synthesis.

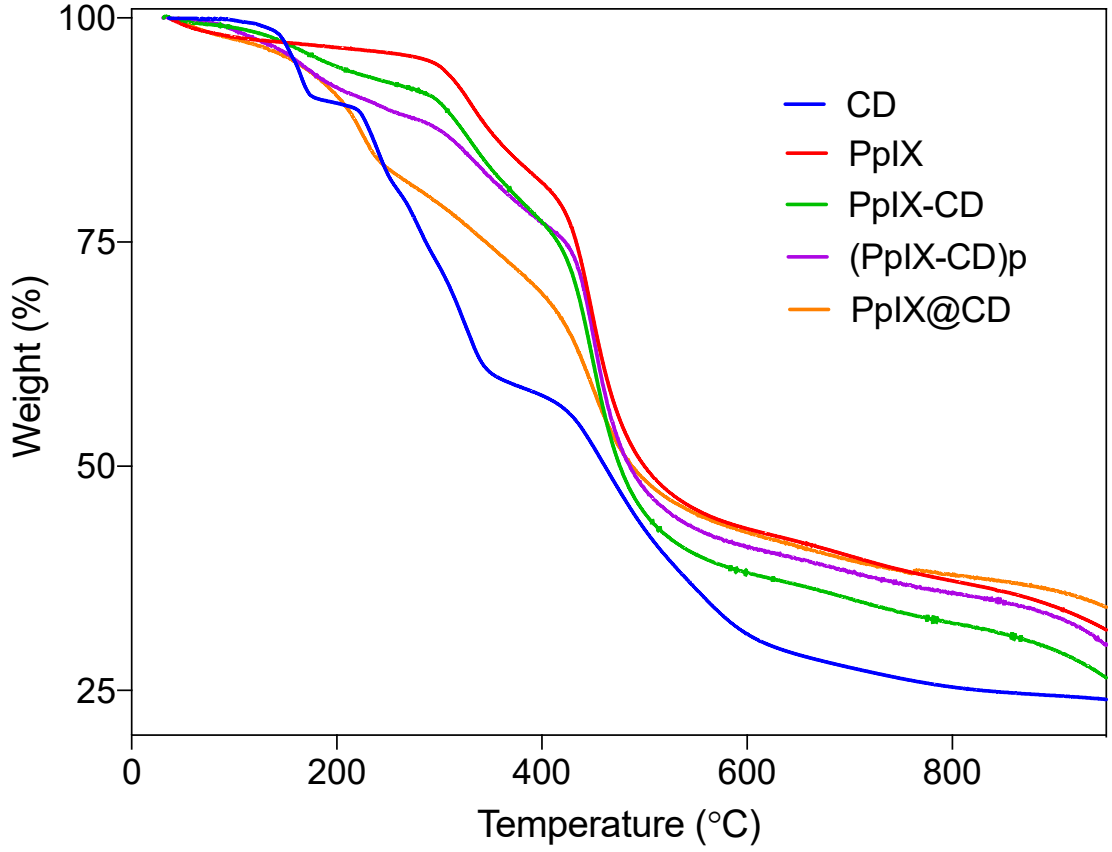

Fig. 2.31 – PpIX loading increases CD thermal stability. TGA demonstrates CDs decompose at lower temperatures compared to PpIX and its conjugates.

Conjugates showed increased thermal stability due to PpIX loading and exhibited similar thermal decomposition. PpIX-CD and (PpIX-CD)p showed similar behaviour to PpIX, with mass loss at 345 and 450°C. Additionally, there is a slight reduction in mass around 230°C. In contrast, PpIX@CD does not show significant mass loss at 345°C, instead showing two clear peaks at 232 and 460°C. The first is likely related to the oxidation of CD surface groups, which are exposed in PpIX@CD, while crosslinked conjugates are completely bound with PpIX. The second peak corresponds to the degradation of the pyrrole ring of PpIX embedded on the CD surface. These variations in weight loss (% loss per °C) can be observed in Fig. 2.32.

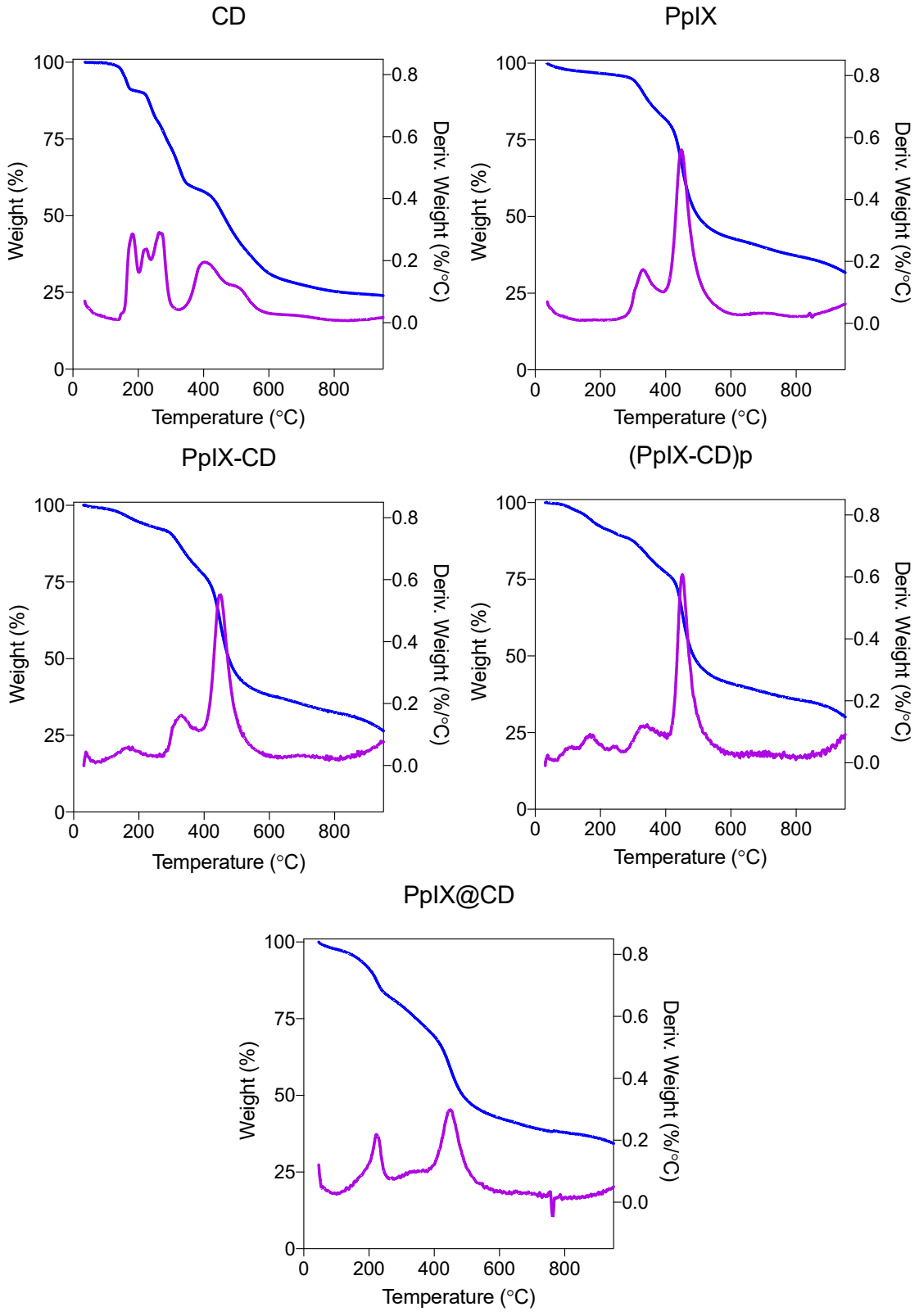

Fig. 2.32 – TGA of CDs and drug loaded conjugates. Conjugates show slight variation from PpIX. PpIX@CD showed increased weight loss around 200 °C.

Conclusion

In summary, CDs were fabricated with citric acid or sucrose as carbon sources and ethylenediamine as a passivating agent. Microwave synthesis showed higher product yield and better control over parameters in comparison to domestic microwave or hydrothermal synthesis. However, small reaction volumes are a limiting factor in CD synthesis through this method. The comparison of various carbon sources and passivating agents led to the selection of citric acid, sucrose, and EDA for CD production. Dialysis was shown to be a crucial part of sample post-processing as freeze-drying is unsuccessful without it.

Afterwards, PpIX was successfully loaded in carbon dots to form drug-loaded conjugates using two different strategies. Host-guest encapsulation of PpIX in various wt% with a one-pot reaction produced composites with varying PpIX content. A total of 1 wt% led to the highest drug loading, which was named PpIX@CD. Likewise, amide crosslinking was used to synthesize PpIX-CD through a modified protocol. The less soluble fraction of (PpIX-CD)p was recovered after centrifugation. Host-guest embedding was shown to be a viable and cost-effective alternative to carbodiimide crosslinking for loading PpIX. Nonetheless, sample variability requires the optimization of synthesis conditions as a limit for drug loading could be observed after changing initial drug weight percentage. Similarly, EDC/NHS crosslinking showed greater variability as a separate fraction of conjugates were obtained following processing with dialysis and centrifugation.

Particles were shown to increase in size and behave similarly to PpIX as seen with TGA and FT-IR evaluation. TEM showed conjugates aggregate less than PpIX but are still less hydrophilic than CDs. PpIX loading in carbon dot conjugates reduced CD-attributed photoluminescence and singlet oxygen generation in all conjugates regardless of drug loading percentage after excitation with 405 nm light. Although this suggests PDT is possible with all

three conjugates (PpIX-CD, (PpIX-CD)p and PpIX@CD), characterisation alone is not sufficient to determine which sample is the best suited for *in vitro* PDT. Interestingly, results suggest host-guest encapsulated samples are a better alternative to crosslinked CD conjugates. These observations will be taken forward in the next chapter as *in vitro* evaluation may show possible differences between samples and treatment conditions to determine the best performing PpIX-containing sample.

Chapter 3 – Phototoxicity and bioimaging of conjugates in cell monolayers

Introduction

In the previous chapter, there was a brief introduction on photodynamic therapy (PDT) and the usefulness of nanoparticle-drug conjugates. PpIX-loaded CDs were shown to be capable of singlet oxygen production and increased water solubility. The next step requires the biological evaluation of PDT using cell culture; cytotoxicity evaluation of new photosensitising compounds is a necessary step to assess variations in treatment efficacy. *In vitro* evaluation of cytotoxicity is typically carried out using an assay to measure metabolic activity, which is often defined as the number of "healthy" cells in a sample. The commercially-available assays MTT (3-(4,5-dimethylthiazol-2-yl)-2,5-diphenyltetrazolium bromide and resazurin (also known as Alamar Blue) are examples of well-known and established methods for estimating cytotoxicity in cell monolayers [286].

PDT can cause cell death through both apoptosis and necrosis in cancerous tissue, inflicting damage to proteins, DNA, and lipids [287–289]. Necrosis is more common with high drug concentrations due to PS dark toxicity, apoptosis is generally preferred as there is no cellular ablation and release of factors such as cytokines, which affect healthy surrounding cells [290]. Treatment efficiency can vary depending on many factors, including lesion type, size, and location. Additionally, PS effectiveness is variable, fluctuating according to its concentration and localization within the tissue. ROS generation is highly influenced by the concentration of oxygen in the tumour microenvironment. This limits PDT effectiveness on hypoxic tissue and tumours located below the tissue penetration depth of the light [206].

Fluorescence-based microscopy techniques have also been used to determine photosensitiser uptake and intracellular localisation. In particular, confocal laser scanning microscopy (CLSM)

is a tool with high sensitivity which can be used to observe nanoparticles with micrometre resolution. The use of multiple filters and laser lines, including two-photon excitation, enables the acquisition of three-dimensional imaging through optical sectioning [291].

In the following chapter, the evaluation of cytotoxicity and bioimaging capabilities of CDs and PpIX conjugates will be discussed. Fig. 3.1 shows a summary of the synthesised PpIX-containing samples from Chapter 2.

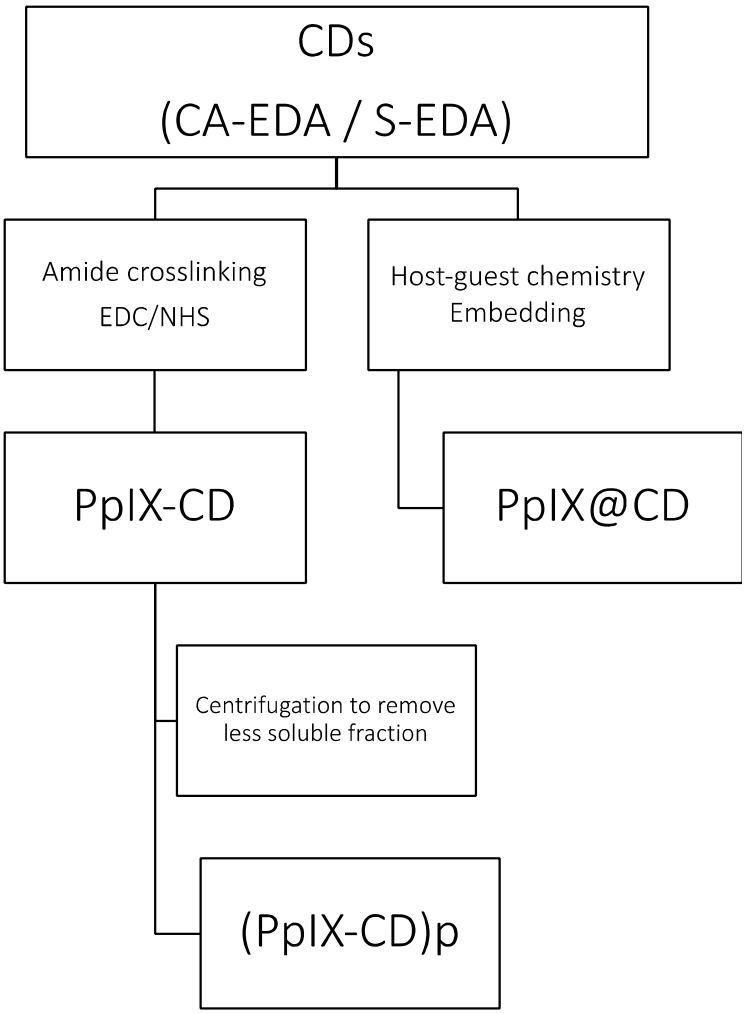

Fig. 3.1 – Schematic detailing conjugates used for *in vitro* PDT. PpIX-CD and (PpIX-CD)p were fabricated through amide crosslinking. The latter corresponds to the insoluble (precipitate) fraction separated from PpIX-CD after centrifugation. PpIX@CD was obtained using a one-pot reaction.

Aims: Demonstrate differences in cytotoxicity and PDT efficiency of PpIX-loaded conjugates and PpIX using a metastatic human cancer cell line.

Objectives:

- Determine maximum *in vitro* concentration for conjugates based on dark toxicity (LC50).
- Evaluate the effects of light dose and conjugate concentration on *in vitro* PDT.
- Examine conjugate intracellular uptake and localisation using microscopy.

Experimental

In the following section, all chemicals were obtained from Fisher Scientific, UK unless stated otherwise.

Materials

Protoporphyrin IX, resazurin sodium salt, and dimethyl sulfoxide were acquired from Sigma Aldrich (United Kingdom). Dulbecco's Modified Eagle's Medium (DMEM, high glucose), Dulbecco's Modified Eagle's Medium (DMEM, high glucose, without phenol red), phosphate buffer saline (PBS), 4′,6-diamidino-2-phenylindole. (DAPI), and trypsin–ethylenediaminetetraacetic acid (EDTA) solution were obtained from Thermo Fisher (United Kingdom). Syringe filters with a 0.2 µm pore size were acquired from Sarstedt (United Kingdom). All chemicals were used as received unless stated otherwise. Deionized water was used for all buffers and samples in experiments. Septa steel ring caps and 35 ml glass reaction vessels were obtained from CEM Corporation (United Kingdom).

2D cell culture – monolayer

Cell culture

Conjugates were diluted in sterile deionised water at a concentration of 1 mg/ml to make a stock solution. Standard cell culture media DMEM (Dulbecco's Modified Eagle Media) was used to make working solutions at various concentrations. An ultrasonic probe was used to break up aggregates in the stock solution before mixing via vortex. The conjugate-supplemented media was covered with aluminium foil and stored at 4°C for further use.

Cells were donated by Dr. Helen Bryant from the Medical School, University of Sheffield. The cell lines C8161 (human melanoma) and U2-OS (human osteosarcoma) were cultured in

standard conditions (37°C, 5% CO_2) using DMEM with 10% foetal calf serum (FCS) (Lonza, United Kingdom), 1% penicillin-streptomycin, and 1% glutamine. Each plate was passaged after reaching ~90% confluence. C8161 is a human cutaneous amelanotic melanoma cell line which has been shown to be highly aggressive, invasive, and metastatic, making it an ideal model for PDT [292]. U2-OS is a human osteosarcoma cell line, ideal for microscopy due to their large size.

Evaluation of cytotoxicity

Nanoparticle-supplemented DMEM was prepared utilising a stock solution (1 mg/ml) of each conjugate, at concentrations from 1–100 μg/ml. Full media with serum was used to make all conjugate dilutions. Solutions were subjected to ultrasonic processing with a Hieschler UP50H ultrasonic probe, with filter sterilisation prior to use in cell culture. Dilutions were stored at 4°C until used.

Growth media was prepared utilising phenol red-free DMEM with the following: 10% foetal calf serum, 1% antibiotics (penicillin and streptomycin) and 1% glutamine. C8161 melanoma cells were used from passage 10 to 20 and were cultured in a T75 plate 5% CO_2 at 37°C, until reaching approximately 90% confluence. Cells were detached using 0.25% Trypsin-EDTA. Afterwards, cells were diluted to 6×10^4 cells/ml; each well of a 96-well plate was seeded with 100 μl of cell suspension and placed in the incubator overnight to allow attachment.

Dark toxicity

Growth medium was replaced with 100 μl of conjugate dilutions (1–100 μg/ml) and DMEM was added to untreated cells to act as a control. The plates were covered with aluminium foil and returned to the incubator for 3 hours. Each well was washed with PBS and fresh media was added, with plates remaining in the incubator for an additional 18 hours (totalling 24

hours). After incubation, each well was washed with PBS and 200 µl growth media was replaced prior to the metabolic activity assay.

Light-activated toxicity

Growth medium was replaced with 100 µl of conjugate dilutions (1–10 µg/ml) and DMEM was added to untreated cells to act as a control. Cells were returned to the incubator for 3 hours to allow particle uptake. Afterwards, all wells were washed using PBS and 200 µl phenol red-free media was added. A M405L2 ThorLabs mounted LED with a collimator adapter (405 nm, 2.76 mW/cm^2) was used to induce light-activated toxicity. Cells were placed under illumination for 3 minutes and subsequently returned to the incubator. Metabolic activity measurements were taken at 24, 48 and 72-hour time points (post light activation).

Metabolic activity assay

A 1 mM resazurin solution was prepared by dissolving 25.18 mg of resazurin sodium salt in 100 ml sterile PBS. The solution was filter sterilized using a 0.2 µm syringe filter. 100 µl of media was taken from each well and transferred to a new plate. Metabolic activity was assessed by adding 20 µl to each well. The plates were read using a Biotek ELx808 Microplate Reader at 570/585 nm with a sensitivity of 50. Conjugate LD50 values were obtained and converted into PpIX-adjusted concentrations (µM) based on the previous estimated PpIX content of each sample.

Confocal light scanning microscopy

Fluorescence images were obtained using a Zeiss LSM510 Meta confocal microscope fitted with a two-photon Ti-Sapphire laser. U2-OS cells were seeded in six-well tissue culture plates at a density of 1×10^5 cells per well. Cells were placed in the incubator for 2 hours to allow cell attachment. A 1 µg/ml solution of each conjugate was prepared. Wells were washed with

PBS and growth media was replaced with 2 ml of conjugate solution. The plate was returned to the incubator for 30 minutes. Immediately afterwards the wells were washed with PBS and fixed using 3.7% formaldehyde and 300 nM 4′,6-diamidino-2-phenylindole. (DAPI).

Image acquisition.

Images were obtained using 488 nm (15%), 543 nm (15%) and 800 nm (6.5%) laser lines. Confocal laser scanning microscopy was performed using an Achroplan 40×/0.75 N.A. water immersion objective. Z-stacks were defined as a 210.4 ×210.4 × 7.2 µm area with a pixel time of 51.2 µs.

Statistical analysis

Experiments carried out with three independent repeats in triplicates (N = 3, n = 3) and results were normalized using untreated controls. Statistical analysis was carried out using GraphPad Prism version 7.04. A normality test was performed on each data set to confirm the use of ANOVA. The comparison of metabolic activity was evaluated by 2-way ANOVA analysis with Dunnett's test for multiple comparisons, with adjusted *P* values < 0.05 considered statistically significant. Data was presented as means ± SEM (standard error of the mean). Charts include symbols representing adjusted *P* values, which are shown below.

Table 3.1 – List of symbols used to represent significance

P value	***Symbol***
>0.05	ns (non-significant)
<0.05	*
<0.01	**
<0.001	***
<0.0001	****

Results and discussion

Considerations for using PpIX-loaded CD conjugates for PDT in cell culture

It has been previously established that colloidal stability of nanoparticle suspensions depends on a multitude of factors including concentration and hydrophilicity. The addition of serum further complicates this by causing nanoparticle-protein interactions and changing sedimentation rates. Additionally, spatial distribution of nanoparticles is affected by the administration route, which can lead to drastically different experimental outcomes [35]. DMEM-conjugate solutions over 10 μg/ml exhibited a distinct colour change from golden yellow to increasingly darker shades of red with the addition of both PpIX and conjugates. Sedimentation was apparent for all conjugate samples over 50 μg/ml, while CDs did not show observable aggregation even while at concentrations > 1 mg/ml. The use of ultrasonic processing effectively removed aggregates prior to their addition to cells.

Two separate parameters were chosen for the evaluation of conjugate cytotoxicity: dark toxicity (inherent toxicity of the particles prior to light exposure) and light-activated toxicity. The average lethal concentration at which metabolic activity is reduced by 50% (LD50) was estimated using these concentrations. The photo-toxicity index (PI) was also calculated to make direct comparisons between conjugates and PpIX. PI links dark and light-activated toxicity – higher PI values indicate greater efficiency with lower photoactivation LD50 and increased dark toxicity resistance to PS.

Dark toxicity evaluation

Carbon dots and PpIX show significantly different dark toxicity values

CA-EDA and S-EDA CDs were used as controls for CD-induced toxicity and showed good cytocompatibility, with >80% metabolic activity even at concentrations of 100 - 250 μg/ml at

24 hours, which can be seen in Fig. 3.2. These values are similar to those previously reported by Hill et al. (2016) and Xu et al. (2016) for nitrogen-doped CDs (N-CDs) fabricated through microwave pyrolysis [39,43]. Surface charge and functional groups are a determining factor in CD cytocompatibility: pristine (negative) and PEG-coated (neutral) particles having higher LD50 values in comparison to amine (positive) CDs [51].

However, N-CDs have been shown to have increased photoluminescence in comparison to non-passivated samples and benefit from the availability of primary amine groups for crosslinking [55]. In contrast to CDs, PpIX showed significant toxicity at concentrations over 2.5 µg/ml and an LD50 of ~14.6 µg/ml, which is similar to the literature [293]. Previous studies have shown that the overexpression of ATP-binding cassette transporter ABCB6, involved in the regulation of porphyrin synthesis, is a key factor in PpIX accumulation within cancer cells [294].

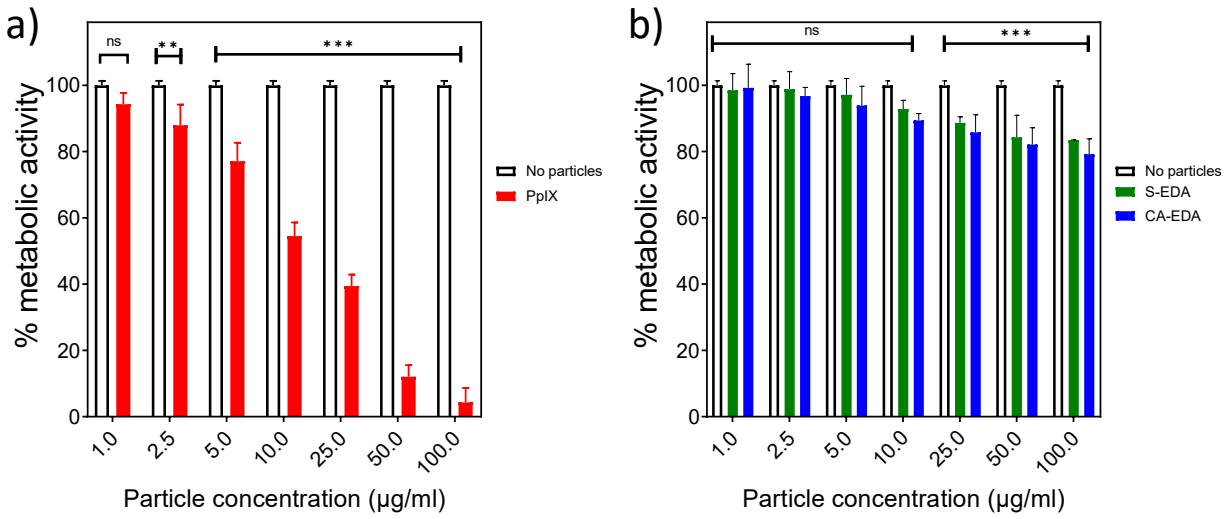

Fig. 3.2 – CDs and PpIX have significantly different effects on metabolic activity due to dark toxicity. PpIX shows a sharp drop in viability after 10 µg/ml (a). In comparison, CD cytocompatibility can be clearly seen, with cells maintaining high metabolic activity (>80%) at ultrahigh concentrations of 100 µg/ml (b). All samples were compared to the negative control to determine differences at each concentration. (N=3, n=3)

Conjugate toxicity varies according to crosslinking strategy

PpIX-loaded particles showed a similar decrease in metabolic activity after incubation, as was observed with PpIX in Fig. 3.3. PpIX@CD showed slightly higher dark toxicity than crosslinked samples at lower concentrations. Nonetheless, total dark toxicity was improved significantly as LD50 concentrations increased approximately 6-fold higher than free PpIX regardless of loading strategy. PpIX-CD and (PpIX-CD)p showed significant difference to PpIX after 5 µg/ml, while PpIX@CD showed a slightly lower improvement at 10 µg/ml. Interestingly, (PpIX-CD)p demonstrated the lowest dark toxicity of all samples (~100.5 µg/ml). Fig. 3.4 shows all samples together, with CDs and PpIX-loaded CDs displaying a significantly higher metabolic activity than PpIX at concentrations >10 µg/ml.

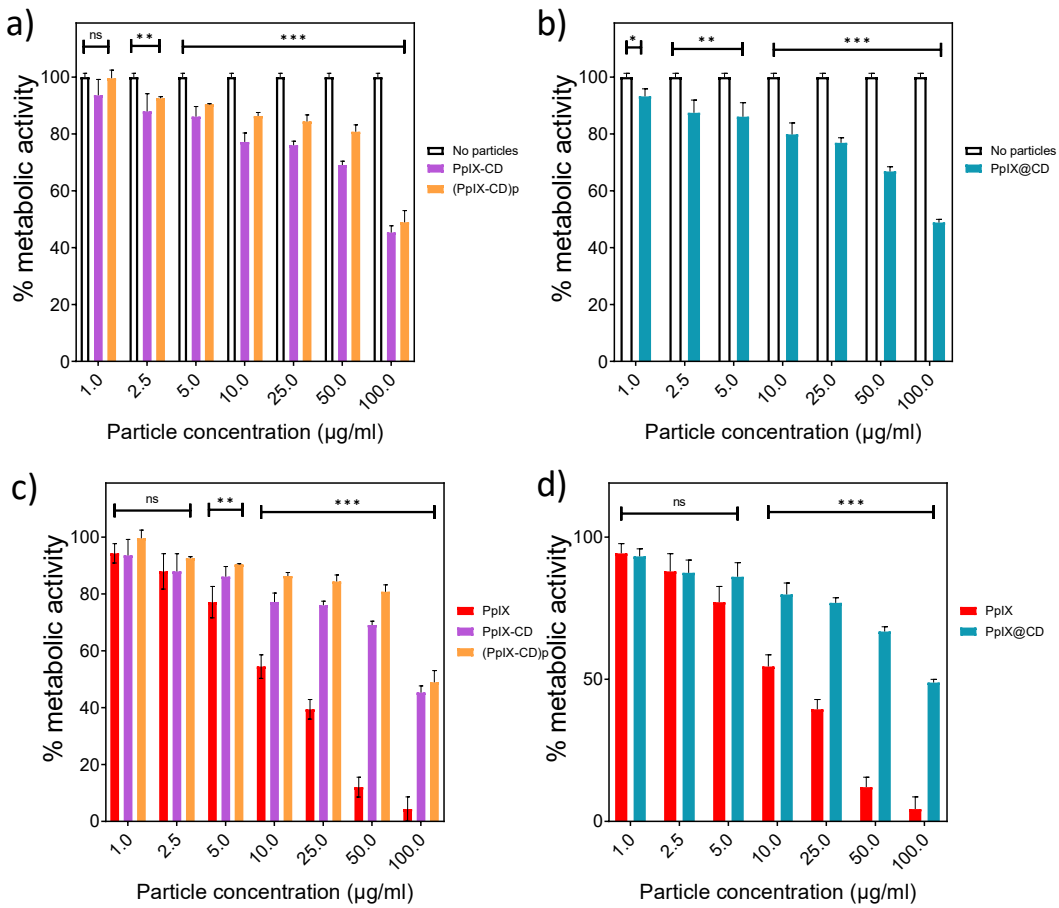

Fig. 3.3 – Conjugates show significantly improved cytocompatibility in comparison to PpIX. The improvement was observed regardless of crosslinking strategy. PpIX@CD was slightly more toxic than PpIX-CD or (PpIX-CD)p at lower concentrations (<5 µg/ml). Each conjugate was compared to the positive control PpIX. (N=3, n=3)

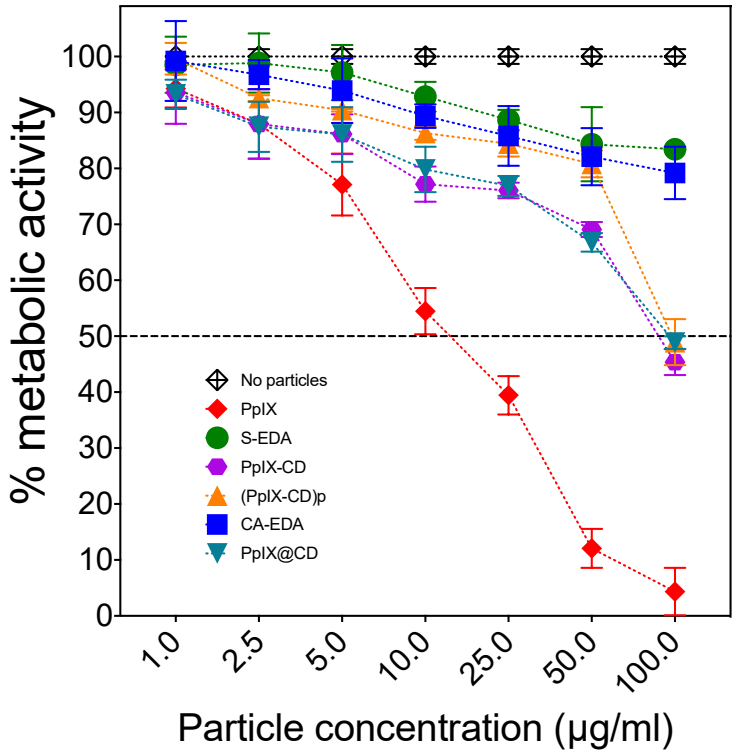

Fig. 3.4 – CDs and conjugates have lower dark toxicity than PpIX. PpIX-CD and PpIX@CD show similar drops in metabolic activity with increasing concentrations. (PpIX-CD)p appears to be the most cytocompatible conjugate, closely mirroring CA-EDA until around 50 µg/ml. (N=3, n=3)

PpIX-adjustment of conjugate concentrations reveals differences between samples

Conjugates were previously shown to have varying amounts of loaded PpIX, with PpIX@CD (48%) and PpIX-CD (41%) having greater loading efficiency than (PpIX-CD)p (34%). These values were used to adjust concentrations from "Particle (ug/ml)" to "PpIX (µg/ml)", which can better reflect the changes in dark toxicity, seen in Fig. 3.5. Adjusted LD50 values showed a 3-fold increase in comparison to the drug alone. Interestingly, PpIX@CD exhibited the highest LD50 of all samples while containing the highest PpIX concentration at 80.8 µM PpIX-adjusted (95.4 µg/ml), compared to PpIX-CD (64 µM PpIX-adjusted, 88.5 µg/ml) and (PpIX-CD)p (60.3 µM PpIX-adjusted, 100.5 µg/ml).

Nanoparticle toxicity may be influenced by solubility in an aqueous environment, incubation time, and cell type. The hydrophobic nature of PpIX, with approximately 1 µg/ml solubility in

water, is the likely cause of toxicity as it readily aggregates [295]. The decrease in dark toxicity of CD-based conjugates is likely a combination of more innocuous intracellular localization and decreased formation of aggregates after uptake due to the presence of crosslinked nanoparticles. In summary, dark toxicity was uniformly improved in PpIX-loaded conjugates and concentrations of 0.5 – 10 µg/ml were selected for further evaluation of phototoxicity.

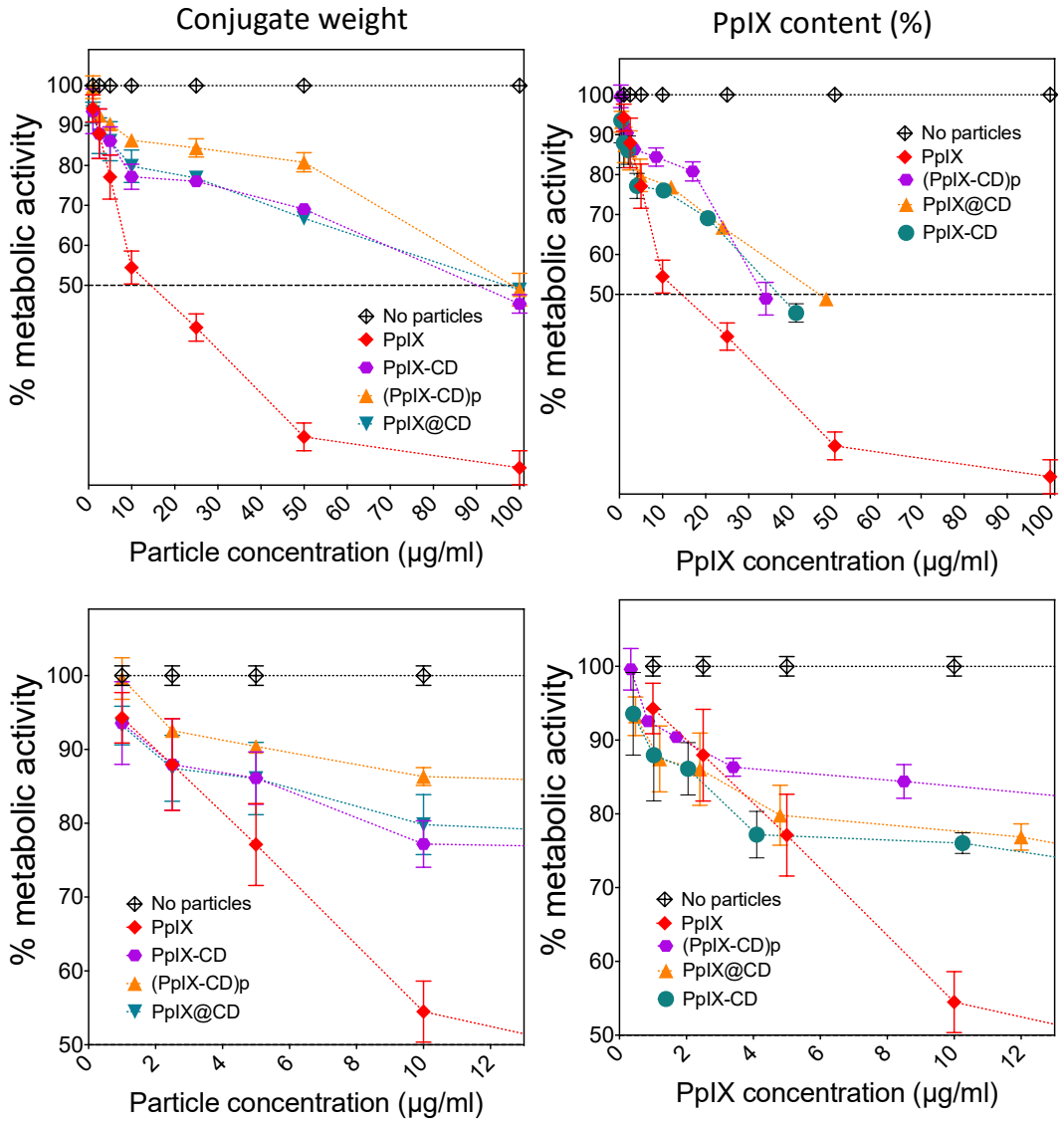

Fig. 3.5 – PpIX-adjusted concentrations show improved cytocompatibility in conjugates. Samples demonstrated decreased dark toxicity after changing values to %PpIX (µg/ml). Conjugates showed a similar drop in metabolic activity to PpIX until 4 – 5 µg/ml.

Light-activated toxicity

Selection of light source for PDT

Previously, conjugates were shown to have an absorbance maximum around 400 nm, with a dual emission behaviour stemming from both CDs and loaded PpIX. Singlet oxygen generation was also previously demonstrated to be possible after excitation with an Nd:YAG 355 nm laser. There were two available options for activating PpIX: a laser (Vortran Stradus 405 nm) and a ThorLabs 405 nm mounted LED. The use of a laser allows control over laser power (up to maximum 200 mW) with a small spot size of approximately 0.25 – 0.36 cm^2. However, maintaining irradiation at a constant rate was difficult and only one well from a 96-well plate can be treated at a time. In comparison, the mounted LED has lower maximum power output, but can easily irradiate a much larger area without causing damage to adjacent tissue through heat. LEDs have also been used individually or within arrays to treat patients clinically [296]. Although LED output is low (2.76 mW/cm^2) it is sufficient to deliver ultralow PDT doses which have been reported previously [297]. Furthermore, low irradiance has been shown to be beneficial, as photobleaching is significantly diminished below 5 mW/cm^2 [298].

Determination of maximum LED spot size for consistent photoactivation

An initial photoactivation test was carried out to determine the maximum area in which light exposure produces consistent cell death (Fig. 3.6). Outer wells were excluded from all experiments as they serve as evaporation barriers for the inner wells, leading to variable cell growth and inconsistent results. Cells treated with solution of 2.5 μg/ml PpIX showed drastically reduced metabolic activity after light activation for 3 minutes depending on LED height. Wells within the LED spot showed significantly reduced metabolic activity, with values under 45%. In comparison, wells located on the edge of the light spot exhibited uneven results.

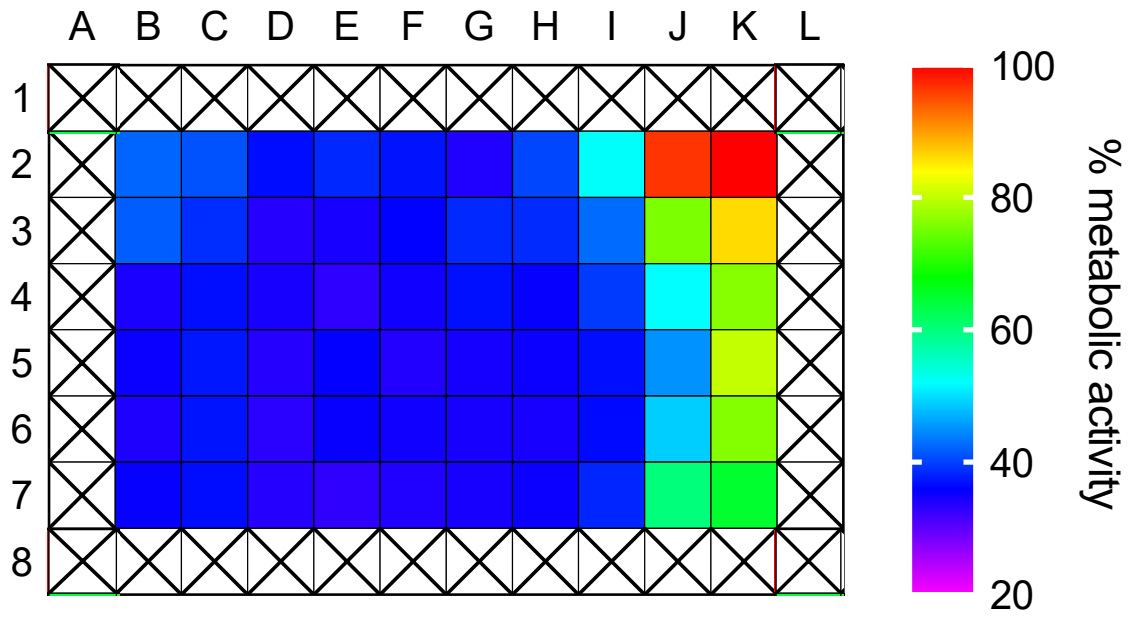

Fig. 3.6 – Heatmap indicating variation in phototoxicity. The position of the LED spot was adjusted to cover most of the 96 well plate. Wells on the top right corner show a reduced PDT effect due to insufficient light exposure. Outer rows and columns were not used as media evaporation causes variance in cell growth.

The duration of light toxicity was evaluated at 1, 2, and 3 minutes total light exposure (1- and 2-minute exposure shown in Fig. 3.7). PpIX and conjugates showed significant light toxicity at all concentrations and mostly did not show variation among each other. Initial results show PpIX-loaded CDs can produce an equivalent PDT effect to PpIX *in vitro*. Additionally, both PpIX-CD and PpIX@CD showed good photostability during singlet oxygen generation testing. This indicates longer timescales or repeated light treatments could be possible without inducing bleaching. Further phototoxicity evaluation used 3-minute light exposure due to the greater reduction in metabolic activity.

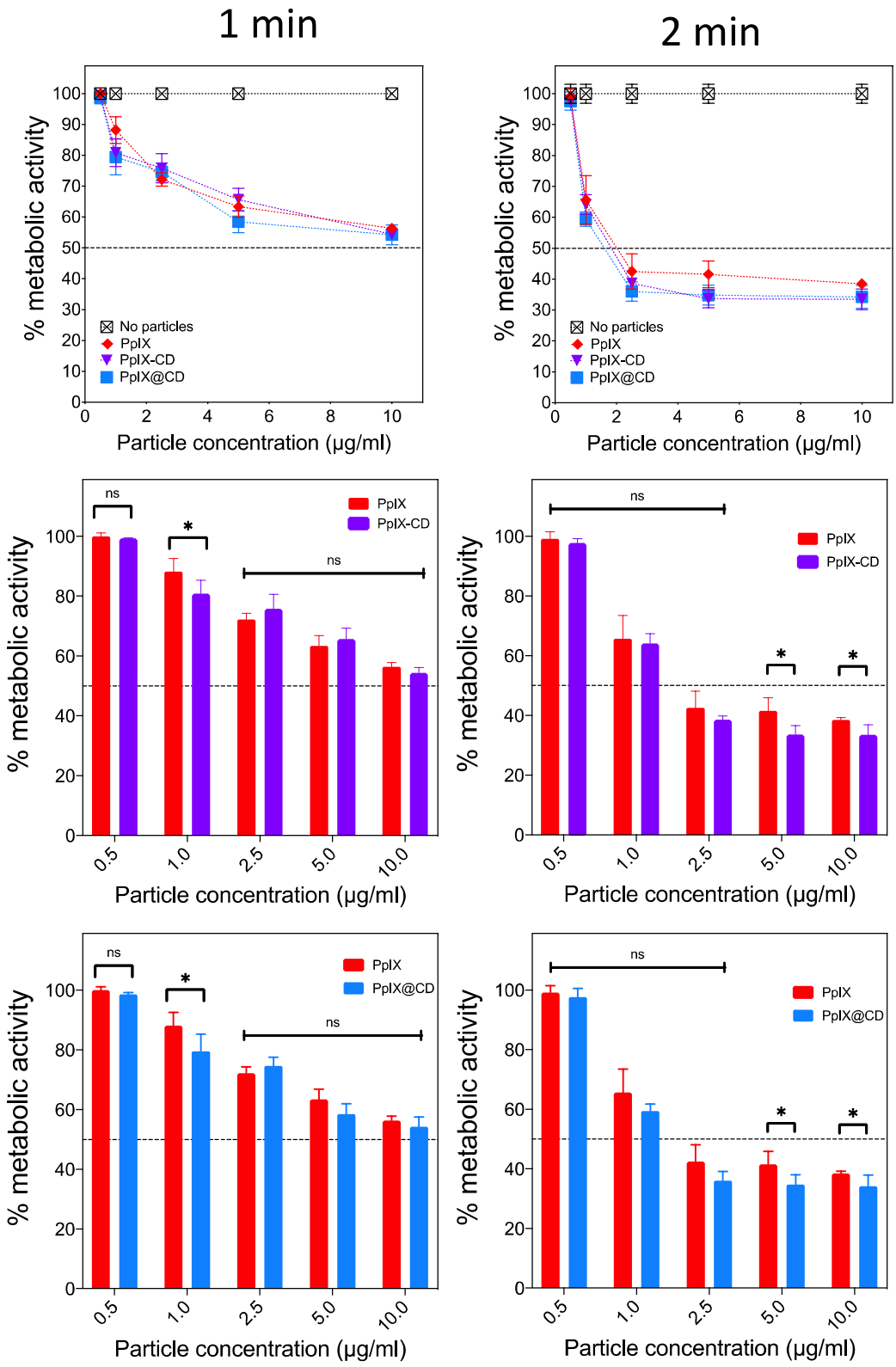

Fig. 3.7 – Phototoxicity varies according to total light exposure duration. A 2-fold increase in light exposure duration leads to increased variability at higher conjugate concentrations. Each conjugate was compared to the positive control PpIX. (N=3, n=3)

Calculation of fluence enables comparison with previously published work

Fluence, also known as radiant exposure, is the total energy output by a light source in a defined area, expressed as J/cm^2. Together with irradiance, which is expressed in W/cm^2, it is possible to compare multiple light activation methodologies. Total light exposure (H_e) is calculated by the following equation:

$$H_e = \frac{\delta Q_e}{\partial A} = \int_0^t E_e(t)\, dt$$

In which Q_e is the radiant energy, A is the area, E_e corresponds to the irradiance, and t is the time of exposure to irradiation [299]. The total power output was estimated to be 2.76 mW/cm^2 by considering the spot size diameter and maximum power output from the LED as was previously set with the driver. This value was close to the average irradiance indicated by the manufacturer (2.46 mW/cm^2). Thus, a 3-minute period of light exposure is estimated to be 0.49 J/cm^2, which is a very low light dose for PDT. Kah et al. (2008) used a similarly low light dose 1.44 J/cm^2 (LED irradiance 4 mW/cm^2) with gold nanoshells for *in vitro* PDT, showing cell monolayers are susceptible to phototoxicity with low irradiance [300].

Increased irradiance can be achieved through a variety of means. The most common method is the use of lasers, high-powered LEDs or LED arrays and was previously sought after to produce an enhanced PDT effect. However, greater irradiance and fluence values have been shown to cause significant problems. Photobleaching becomes much more likely as light intensity increases and has been shown to be an oxygen-dependent process in PpIX [301]. The bleaching dose for PpIX was estimated to range between 1.8 – 3.5 J/cm^2 at an irradiance of 5 mW/cm^2. Robinson et al. (1998) determined that exposure for >1000 seconds reduced PpIX fluorescence by over 90% [298]. Additionally, high fluence leads to rapid oxygen depletion within the target area. This reduces PDT efficiency as tumours are commonly within a hypoxic

microenvironment [302]. Low fluence PDT (< 25 J/cm^2) has gained interest as a method for bypassing these aforementioned issues and has shown positive results clinically [303]. Ericson et al. (2005) showed a significant improvement in treatment outcome as irradiance was adjusted from 75 mW/cm^2 to 30 mW/cm^2 [304]. This highlights the importance of PDT parameter screening when selecting different conditions for treatment.

CDs are not capable of producing a significant PDT effect

Pre-mixed nanoparticle suspensions were sonicated and vortexed to remove any aggregates that formed during storage. CA-EDA and S-EDA CDs were also used to determine if CDs alone contribute to cell death after light irradiation. Yi et al. (2017) previously reported N-doped CDs (N-CDs) capable of singlet oxygen generation due to contributions from surface defects [305]. However, results indicate both control samples (CA-EDA / S-EDA) do not significantly affect metabolic activity, with equal results regardless of light irradiation duration and intensity. This difference could be due to the difference in synthesis conditions. N-CDs were synthesized through the solvothermal processing of anthracite in DMF, leading to particles with very low oxygen content. While singlet oxygen generation from CDs may be capable of enhancing the PDT effect, water solubility is likely to be affected.

PpIX and conjugates show variable efficiency during photoactivation

Light activated toxicity of conjugates demonstrated similar LD50 values between PpIX, PpIX-CD and PpIX@CD, seen in Fig. 3.8. In contrast, (PpIX-CD)p showed a significant difference from all other samples with a reduced PDT effect at concentrations over 2.5 μg/ml. (PpIX-CD)p had previously shown a high singlet oxygen yield in DMF but failed to produce a significant phototoxic effect in comparison to the control. This diminished water solubility in comparison to PpIX-CD may be caused by the formation of multiple covalent bonds during cross-linking leading to self-quenching. As a result, it showed drastically reduced efficiency

compared to other PpIX-conjugates with a LD50 of 7.2 µg/ml. (PpIX-CD)p has also previously shown high particle size dispersion, further reducing its value as a photosensitizer.

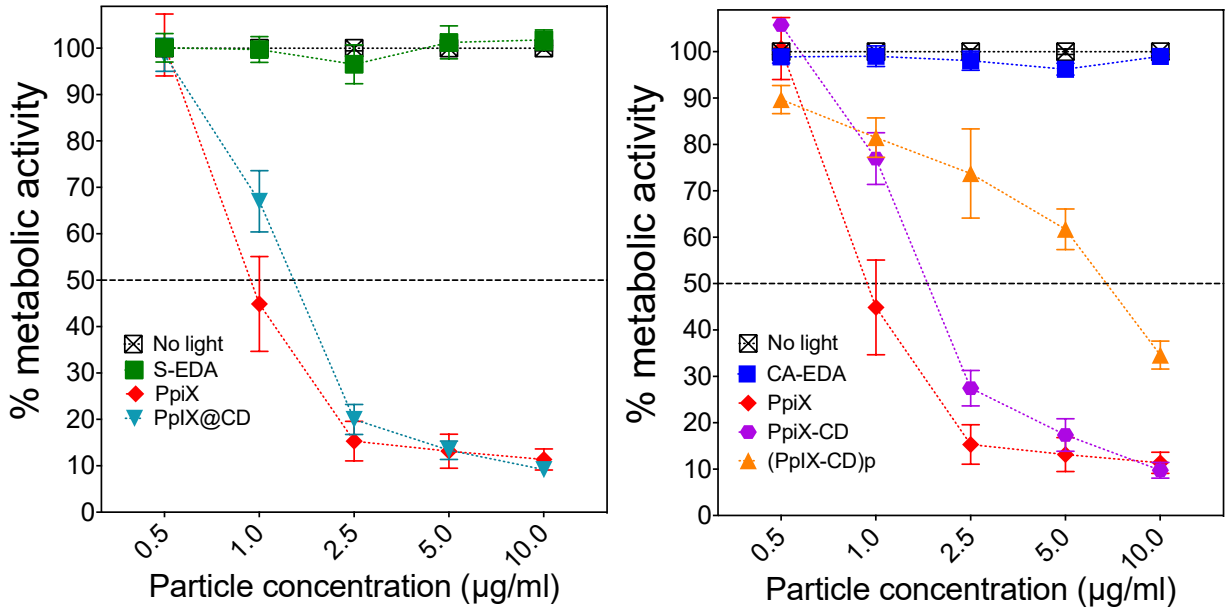

Fig. 3.8 – Light-activated toxicity of CA-EDA conjugates (3-minute light exposure, 24-hour post light). (PpIX-CD) showed markedly diminished PDT efficiency in comparison to other samples. PpIX-CD and PpIX@CD showed equal performance to PpIX at concentrations >1 µg/ml ($p < 0.05$). (N=3, n=3)

PpIX-CD and PpIX@CD demonstrated significant difference from PpIX ≤ 1 µg/ml (24 hours) but did not show a significant difference at concentrations of > 2.5 µg/ml in any time point. Results suggest conjugates are capable of an enhanced PDT effect compared to PpIX, though the exact mechanism is unclear. Fowley et al. (2013) first reported the formation of a PpIX and CD conjugate with a Förster resonance energy transfer (FRET) mechanism for enhanced PDT, where dark toxicity was reduced as a result of improved PpIX dispersibility in aqueous media. Furthermore, single and two-photon activation of the conjugates was shown to effectively induce phototoxicity [144]. Therefore, it is possible an enhanced PDT effect could be produced by PpIX-CD and PpIX@CD due to the same FRET mechanism, using either a lower wavelength for CD excitation or via two-photon irradiation. Two-photon (2P) PDT is a highly promising future trend for photosensitiser-focused research and is capable of a selective highly

targeted treatment for a wide variety of conditions such as brain tumours and other deep-seated cancers, while limiting damage to surrounding healthy tissue. However, it is limited by an extremely small area due to the energy constraints of high-powered lasers. Although two-photon photosensitisers have been successfully fabricated and evaluated *in vitro*, a considerable improvement is expected using vectors such as CDs for more efficient intracellular localisation.

Cell monolayers slowly recover from PDT treatments at all concentrations

Cell cultures were monitored for an additional 48 and 72 hours post light exposure. Metabolic activity *in vitro* shows a slight recovery at both time points regardless of conjugate type or concentration, which can be seen in the Fig. 3.9 and tables A4.1, A4.2 (Chapter 4 Annex). PpIX-CD and PpIX@CD followed the same pattern as PpIX >1 μg/ml at all time points, with a sharp drop at 24 hours. In contrast, (PpIX-CD)p continuously exhibited decreased phototoxicity at all concentrations with high variability, particularly at 72 hours. This variation could be caused by cellular response to various sub-lethal concentrations of PSs and light treatments. Charara et al. (2017) showed lipophilicity was a key factor in ongoing toxicity even after irradiation, with porphyrin-based PS suppressing the metabolism and proliferation of MCF-7 cells [306]. However, it is possible that this same mechanism also influences dark toxicity for these compounds.

There are post-illumination effects that lead to cell death after sustained damage by singlet oxygen production. Direct damage to organelles includes cytochrome C release and B-cell lymphoma 2 (Bcl-2) damage, both of which are involved in the mitochondrial pathway of apoptosis [307]. Tumour necrosis factor receptor (TNFR), mitogen-activated protein kinases (MAPK), and nuclear factor Kappa-B (NF-κB) both play key roles in apoptosis signalling within cells affected by PDT. In comparison to the ordered cell death seen in apoptosis, necrosis is a faster and more chaotic form of cell death caused by physical or chemical damage.

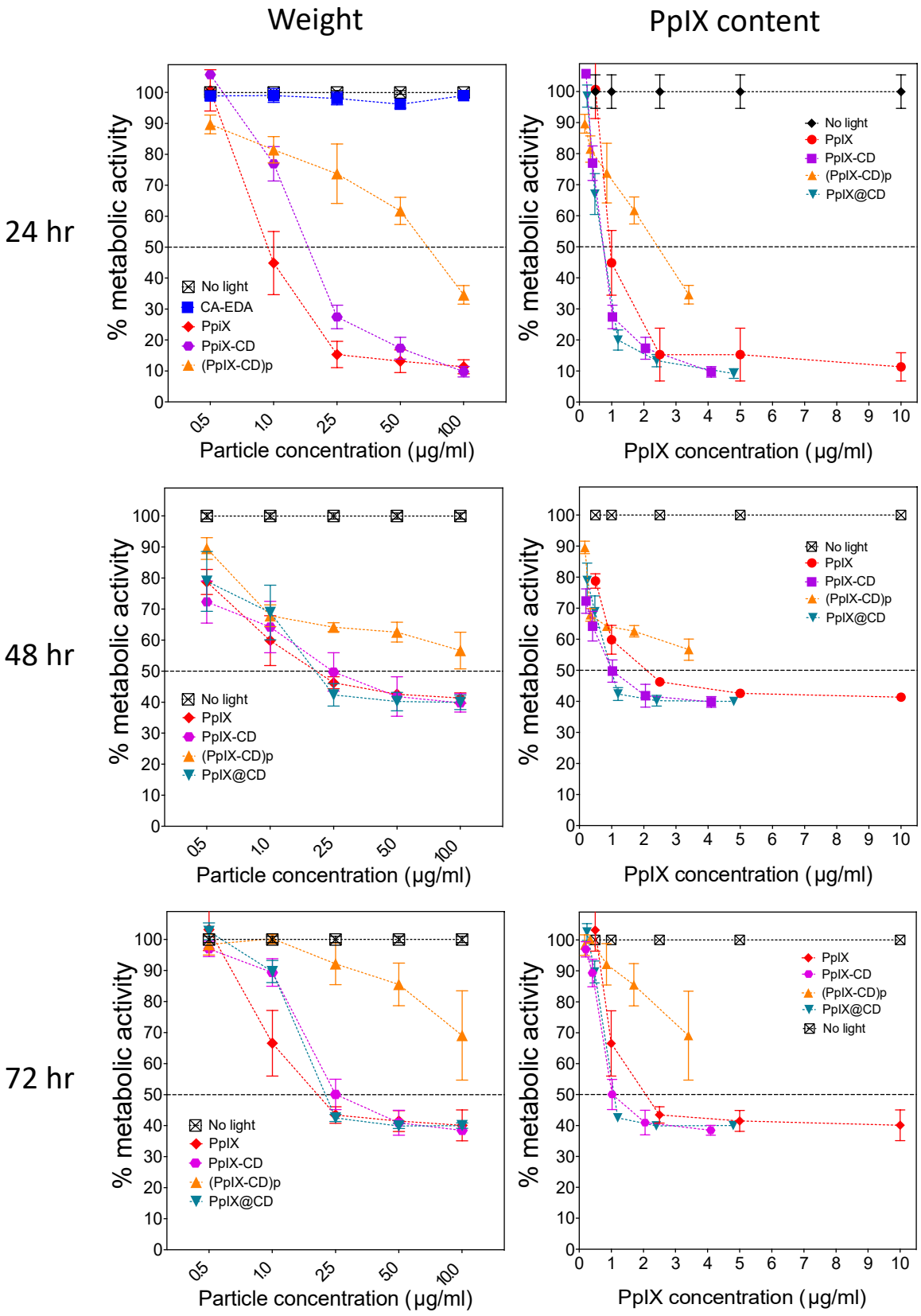

Fig. 3.9 – Light-activated toxicity of CA-EDA conjugates varies after PDT. 3 minutes of light exposure reduces metabolic activity by over 75% after 24 hours of treatment, but slowly recovers over a 72-hour period. (N=3, n=3)

PDT-induced damage induces apoptosis through interaction with cellular components

The exact mechanism of cell death in PDT varies according to a variety of factors including subcellular localization of the PS, light dose, oxygen concentration, and cell type [308]. However, most research agrees that high dose PDT, which includes high PS concentrations, high fluence rates, or both, tend towards necrosis. Likewise, reducing PS concentrations and fluence rates appears to guide cells towards apoptosis [309].

The intracellular localization of conjugates may also benefit the action mechanism of singlet oxygen. The intracellular accumulation of PpIX in mitochondria has been previously reported based on its uptake by binding to a mitochondrial translocator protein involved in the heme biosynthesis pathway [310]. Additionally, porphyrins have been shown to inhibit several important mitochondrial enzymes leading to the inhibition of oxidative phosphorylation [311]. PpIX-based conjugates appear to follow these previously described interactions, with the advantage of slightly increased water solubility due to the presence of CDs. However, the mechanism of cell death after photoactivation of CD-PpIX conjugates is still unclear. PpIX-induced cell death has been shown to be p53-dependent and independent; Zawacka-Pankau et al. (2007) proposed PpIX sensitizes cancer cells making them susceptible to PDT and disrupting proliferation through the destabilization of the HDM2-p53 complex in the mitochondria [312]. The previous results suggest that the variation of incubation time before light exposure may also influence phototoxicity.

Additionally, results suggest singlet oxygen generation may not be directly linked to increased phototoxicity for CD conjugates, as it was previously shown that these values were equal or below those obtained from PpIX. Interestingly, PpIX-CD and PpIX@CD only showed slight differences in efficacy versus PpIX at all timepoints (Fig. 3.10). This indicates both loading strategies are highly efficient methods for improving PDT outcome *in vitro*.

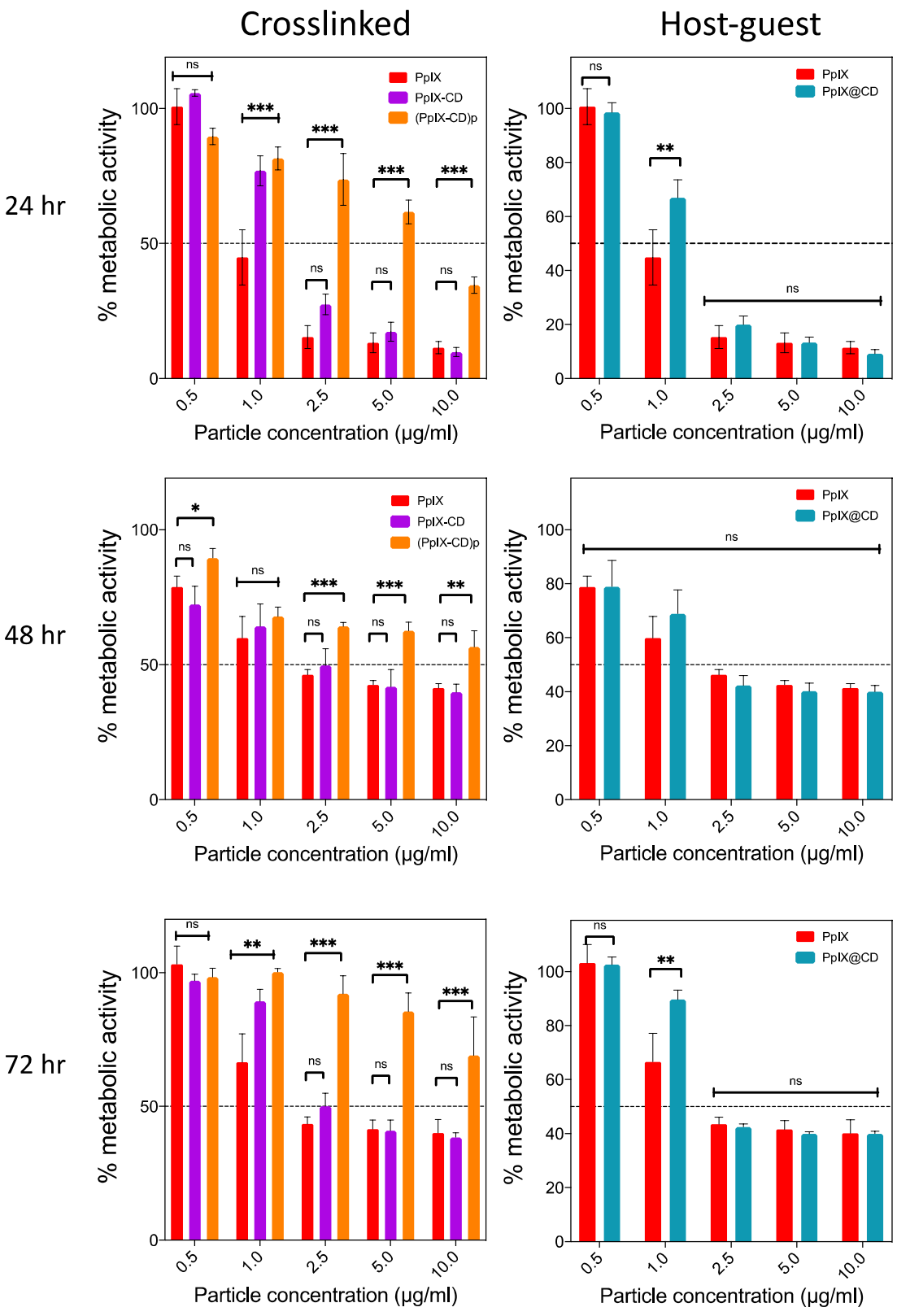

Fig. 3.10 – PpIX-CD and PpIX@CD show similar PDT efficiency to PpIX at concentrations >1 µg/ml. In contrast, (PpIX-CD)p shows a constant difference at all timepoints with concentrations >1 µg/ml. Each comparison was made between the control (PpIX) and conjugates. (N=3, n=3)

Photo-toxicity index is significantly increased in PpIX-CD and PpIX@CD

Photo-toxicity index (PI), also known as photocytotoxicity index, is a ratio used to compare the effectiveness of photosensitisers. This value is calculated by dividing the LD50 of dark toxicity by the LD50 of light toxicity [252]. PpIX-CD and PpIX@CD PI values were improved significantly from 14.6 to 46.6 and 59.6 respectively compared to free PpIX, representing a 2.8 and 3.5-fold increase, seen in Table 3.2. In contrast, (PpIX-CD)p showed slightly reduced PI due to its poor phototoxicity but high cytocompatibility compared to PpIX. Therefore, PDT efficiency was improved due to the decreased dark toxicity of conjugates. This result highlights the importance of photosensitiser cytotoxicity and solubility in PDT effectiveness.

Table 3.2. PpIX-CD conjugates improve PDT efficiency.

PPIX %	**Singlet Oxygen**		**Dark**		**Light**		**PI**
	Sample	O_2^1 Yield	LC_{50} µg/ml	LC_{50} PpIX (µM)	LC_{50} µg/ml	LC_{50} PpIX (µM)	
0	CA-EDA	0	>100	N/A	N/A	N/A	N/A
0	S-EDA	0	>100	N/A	N/A	N/A	N/A
100	PpIX	92.2	14.6	25.8	1.0	1.0	14.6
43.10	PpIX-CD	63.8	88.6	67.3	1.9	1.9	46.6
53.13	(PpIX-CD)p	77.1	100.5	99.5	7.2	7.2	13.9
35.59	PpIX@CD	51.6	95.4	59.9	1.6	1.3	59.6

Confocal scanning laser microscopy (CSLM)

Confocal laser scanning microscopy (CSLM) was used to observe PpIX-CD and PpIX@CD uptake and distribution in osteosarcoma cells (U2-OS). Conjugates were premixed and added to cells for incubation for 3 hours.

CDs can be used as nonspecific bioimaging probes

CDs showed extremely rapid uptake and fluorescence at all concentrations (1 – 250 μg/ml). Fluorescence was observed along the cytoplasm, which is commonly seen in CDs [313]. Interestingly, small aggregates can be seen above the cell nuclei. This suggests both CA-EDA and S-EDA have a slight affinity for the nucleus in comparison to another subcellular localisation. While organelle targeting CDs have been previously reported, results do not indicate any other specific binding [314]. CDs were also shown to be capable of weak two-photon absorption alongside DAPI. However, intensity was diminished possibly due to particle self-quenching and aggregation.

PpIX-loaded conjugates show similarities to PpIX intracellular localisation

CSLM imaging of PpIX, PpIX-CD and PpIX@CD demonstrated similar behaviour as bioimaging probes and are mostly distributed along the cytoplasm, with strong emission at 543 nm excitation. Fig. 3.11 shows of PpIX and drug-loaded conjugates distributed along the centre of cells. In contrast to CDs, these samples did not form aggregates on the nucleus, instead remaining on its periphery. Cancer cells have been shown to have increased mitochondria in the perinuclear area, which is consistent with our observations [61]. Z-stacks showed both CDs and conjugates did not penetrate within the nuclei, while PpIX, did not show a specific subcellular localisation.

There are small differences between the samples; PpIX-CD appears to have slightly more aggregates in comparison to PpIX@CD. However, the latter shows weaker fluorescence emission at 488 nm. Interestingly, this is also observed with 543 nm excitation, despite its higher drug content. This could be caused by the obstruction of surface defects during PpIX encapsulation. Nonetheless, conjugate concentration appears to be higher near the nucleus for PpIX-CD and PpIX@CD (Fig. 3.12). Additionally, rapid uptake of all conjugate samples was observed at various concentrations and time points.

Unsurprisingly, (PpIX-CD)p has a noticeably decreased fluorescence intensity in comparison to all other samples, which can be seen with its sharply decreased emission at 488 and 543 nm. This signal reduction could be caused by multiple factors. It was previously observed that (PpIX-CD)p rapidly aggregates due to its poor water solubility. This has been shown to cause quenching as carbon dots and PpIX [220,315]. These results indicate PpIX-CD and PpIX@CD can act as high-contrast imaging probes without decreasing therapeutic efficiency for theragnostics applications.

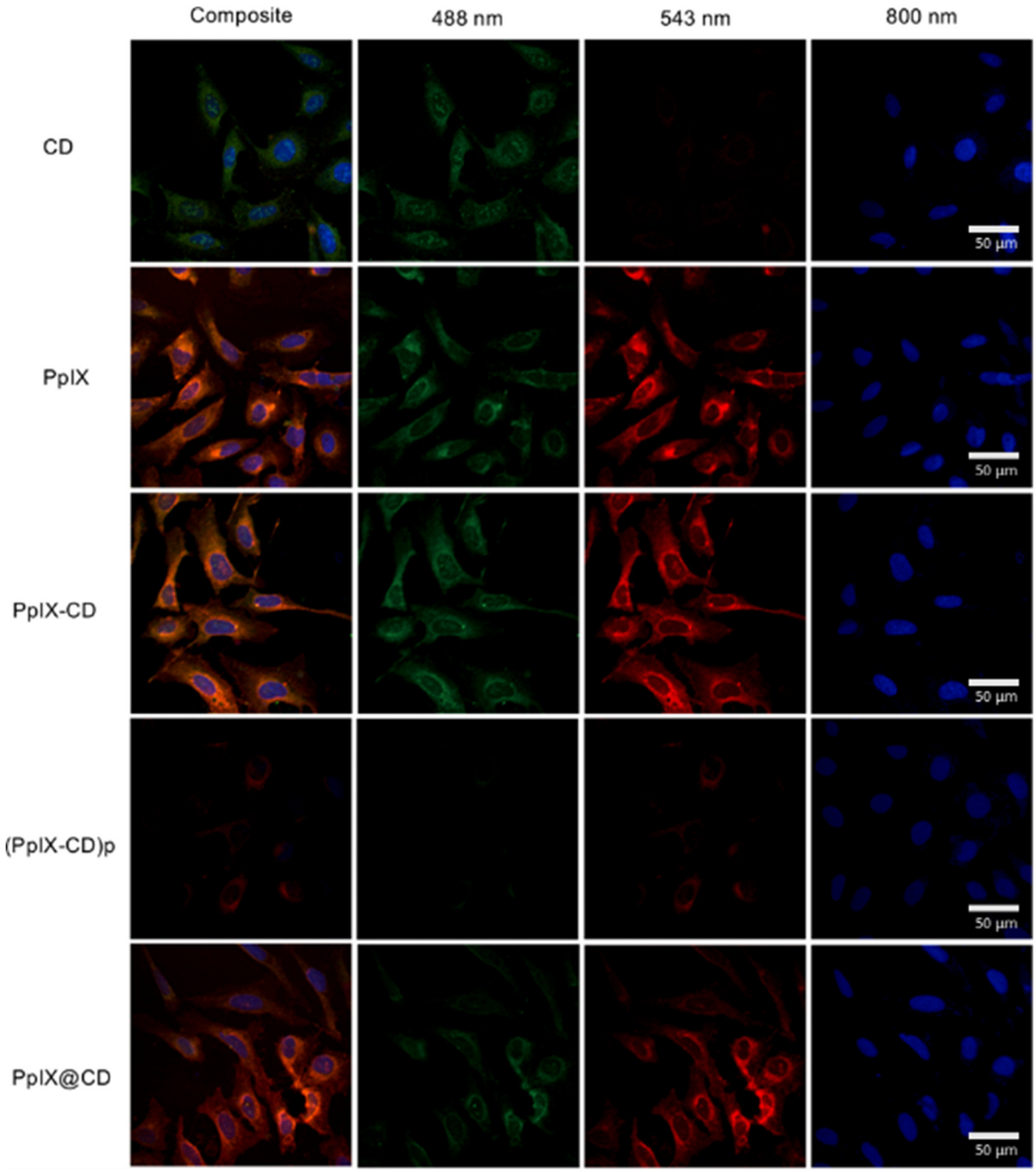

Fig. 3.11 – CD-PS conjugates can be used as probes for fluorescence imaging. CSLM images of U2-OS osteosarcoma. PpIX-CD and PpIX@CD have similar emissions to both CDs and PpIX, while (PpIX-CD)p has greatly decreased fluorescence emission. Conjugates appear to aggregate near the nuclei.

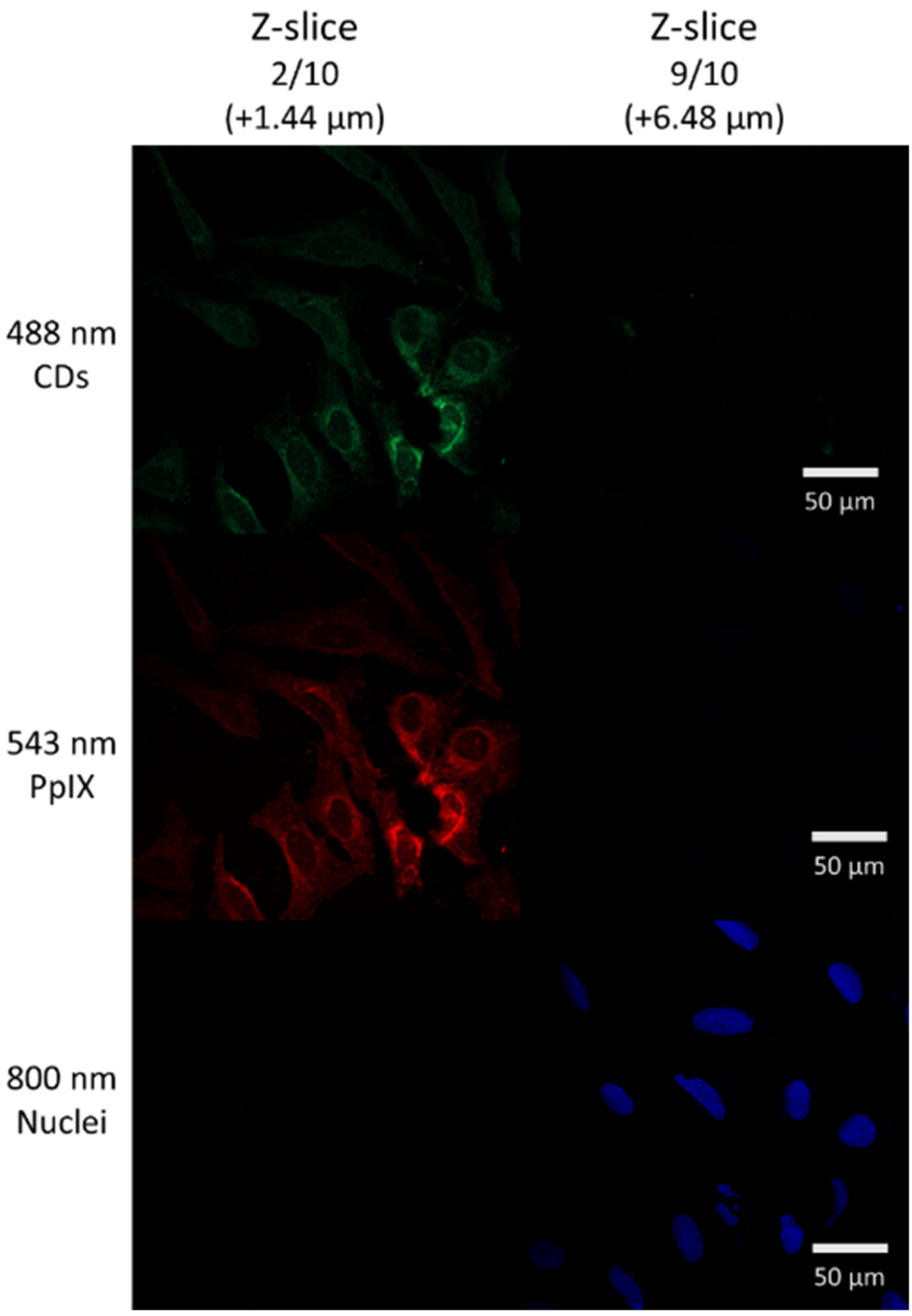

Fig. 3.12 – CD-PS conjugates show non-specific intracellular localisation. CSLM of conjugates show accumulation in the perinuclear area and cytosol. Both PpIX@CD and PpIX-CD (not shown) particles did not penetrate within the nucleus, which can be seen through the comparison of z-slices. Lower z-slices (left) do not show brightness with DAPI staining while CD and PpIX fluorescence is high. Conversely, higher z-slices (right) clearly show cell nuclei with no overlapping signal from 488 or 543 nm.

Conclusion

The evaluation of cytotoxicity is a crucial component of research into new nanomaterials. PDT and other similar biomedical applications require compounds that are simultaneously highly efficient and biocompatible. Conjugation with nanoparticles as carriers has been used to improve drug solubility and enhance their therapeutic effect. Previously, characterisation showed similarities between conjugates and PpIX in surface chemistry, but improved stability in water.

Dark toxicity was evaluated to determine the inherent cytocompatibility of nanoparticles in cells. CDs showed high cytocompatibility *in vitro* at concentrations up to 250 μg/ml with minimal variations between samples (CA-EDA and S-EDA). PpIX-containing CDs showed a 2.2 to 3.7-fold decrease in dark toxicity compared to PpIX. Interestingly, (PpIX-CD)p showed the highest LD50 (100.5 μM PpIX) compared to PpIX-CD (88.5 μM PpIX)and PpIX@CD (95.4 μM PpIX).

Light-activated toxicity was evaluated to determine differences between conjugates. PpIX-CD and PpIX@CD showed equivalent light-induced toxicity to PpIX in concentrations >1 μg/ml, leading to a 3.2 to 4.1-fold increase in photo-toxicity index (PI). These results demonstrated host-guest encapsulated PpIX@CD and carbodiimide-linked PpIX-CD conjugates produce similar PDT effect to that of PpIX with a lower drug concentration, increasing the therapeutic window of the compound. In contrast, (PpIX-CD)p showed decreased phototoxicity in comparison to PpIX. Further monitoring of cells revealed post-illumination suppression of proliferation at 48- and 72-hours post exposure.

Confocal light scanning microscopy demonstrated rapid intracellular uptake and accumulation of conjugates. CDs were rapidly taken up by cells and remained within the cytoplasm, forming

small aggregates within the nuclei. In contrast, PpIX-loaded particles were located within the periphery of the cell nucleus, suggesting accumulation near mitochondria. PpIX-CD and PpIX@CD showed strong photoluminescence at low concentrations (1 μg/ml) similar to both PpIX and CDs. In contrast, (PpIX-CD)p showed rapid quenching and low photoluminescence.

CD-based conjugates have great potential in biomedical applications as carriers in PDT, as well as biomedical applications related to theragnostics, drug delivery, and bioimaging. Nonetheless, there is a need for further biological evaluation of photosensitiser-drug conjugates.

Chapter 4 – Phototoxicity and bioimaging of CD-PpIX conjugates in a cancer spheroid cell model

Introduction

Clinically, solid tumours grow in varied locations within the body, occupying a three-dimensional (3D) space in which characteristic conditions such as hypoxia, drug resistance, and dormancy appear [316]. The complex interaction between tissue oxygenation, vascularisation, light absorption, and drug biodistribution makes selecting ranges for PDT parameters difficult. Thus, animal models are often used early in the translational process. However, the testing these novel agents/formulations is more complex than for many non-light activated small molecules by the requirement for light and oxygen for activity, hence the need custom models to study PDT.

Currently, *in vivo* tumour xenograft mouse models are the gold standard for PDT evaluation, with PS being administered by subcutaneous injection or topical application, shown in Fig. 4.1. Human tumour xenografts have also been explored for PS evaluation but are susceptible to infections [317]. Although *in vivo* models have been widely successful, they are limited by high costs and strict regulatory controls. The evaluation of multiple PDT parameters and treatment combinations becomes increasingly more difficult due to the number of animals required. Thus, there is an urgent need for better models of PDT for PS evaluation prior to *in vivo* testing.

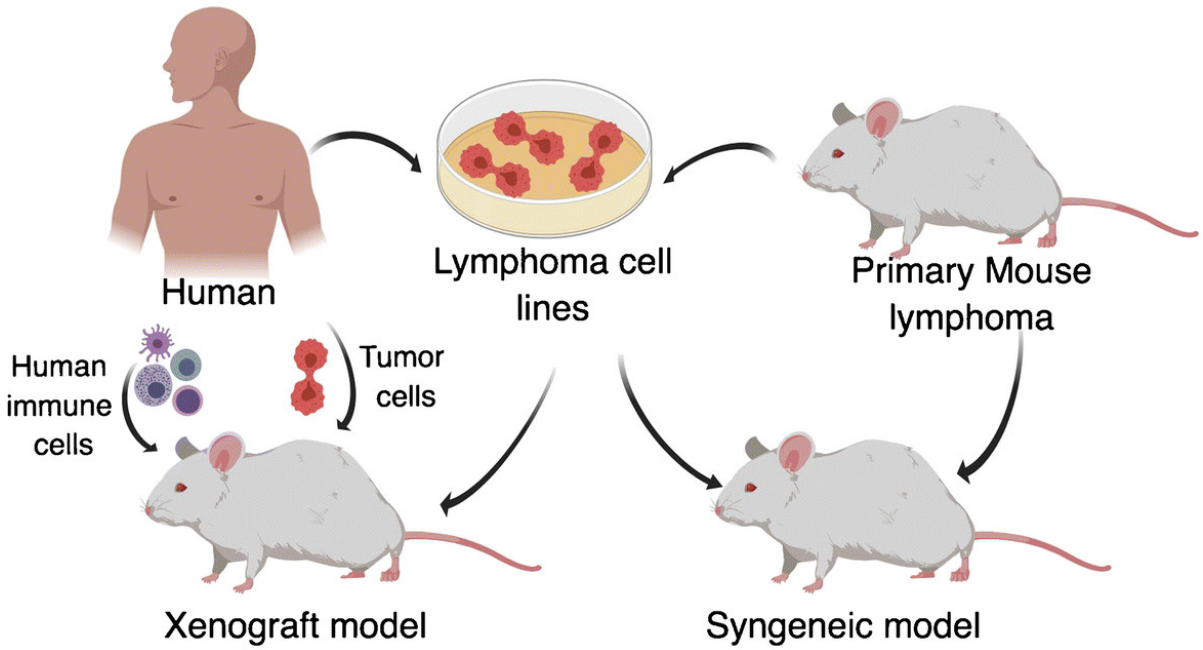

Fig. 4.1 – *In vivo* mouse models are the current gold standard for cancer drug testing. Typically, there are two distinct approaches: human xenografts make use of cancer cell lines, while syngeneic models use allografts from immortalised mouse cancerous tissue. Adapted from Noble and Mishra (2019) with permission from Springer Nature [318].

In comparison, traditional cell culture using cell monolayers (2D) cannot accurately replicate these conditions *in vitro* due to vastly different diffusion rates and cell-cell in 3D versus 2D [319]. The recreation of tumour microenvironment and tissue architecture is key to understand tumour biology and develop new strategies for treatment. There are various models used for this purpose, which include organotypic tissue cultures from patients [320], scaffolds for tissue engineering [321], organoids [322], and spheroids [323].

Multicellular tumour spheroids (MCTS) are a well-known 3D cell model which resemble tumours morphologically and biologically. Spheroids can be grown using a variety of immortalised cell lines or patient-derived tissue samples [324]. Their growth can be stimulated by preventing cells from attaching to a suitable surface, which promotes the formation of cell-cell interactions, production of extracellular matrix, and compaction. In turn, this leads to the formation of biologically relevant zones: an outer layer with rapidly proliferating cells, an

intermediate layer with cells in a state of quiescence, and an inner necrotic layer caused by hypoxia and nutrient deficiency (Fig. 4.2) [325]. Spheroids have demonstrated higher drug resistance in comparison to cell monolayers as there are more barriers for delivery such as binding to the extracellular matrix, membrane proteins, cell membranes, or cell-cell junctions [326]. PDT is particularly limited by the availability of oxygen diffused within the cell microenvironment. Furthermore, hypoxic inner regions lead to inefficient diffusion and the development of necrotic cores, which have also been shown to influence drug response [327]. Nonetheless, spheroids have seen increasingly more research interest in the area of PDT. Their innate properties, ease of production, and similarities to *in vivo* tumours makes them ideal for PDT parameter screening in comparison to cell monolayers [328].

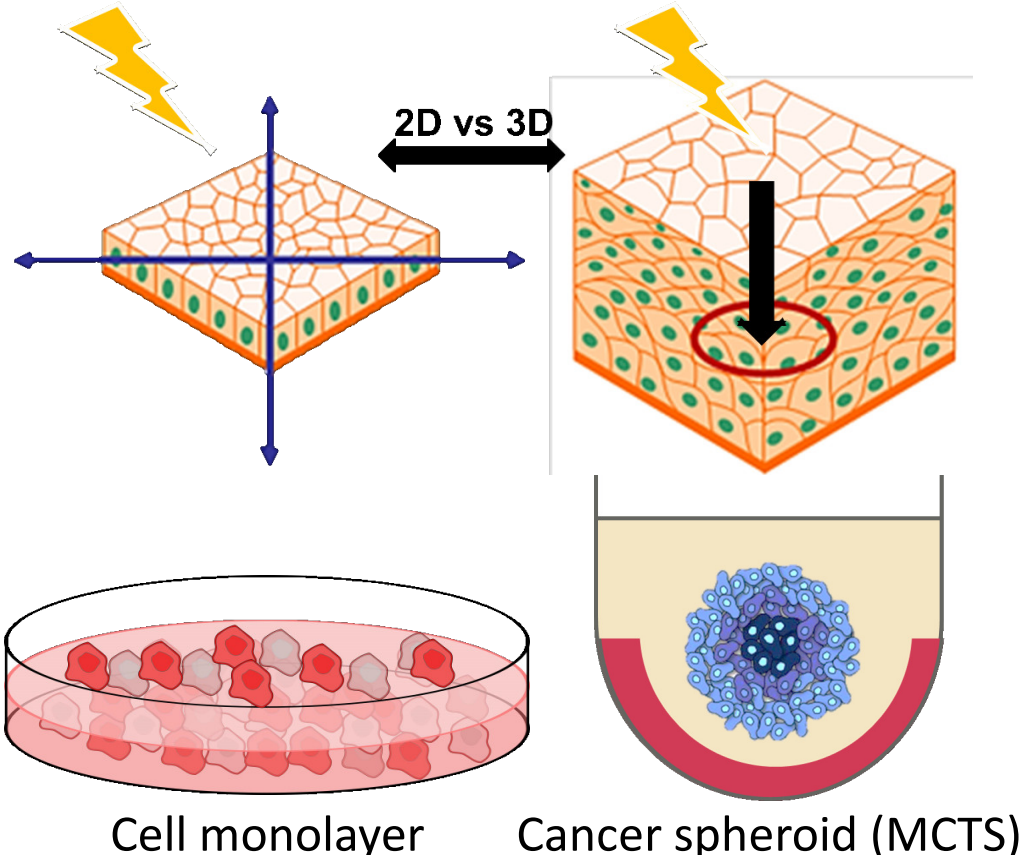

Fig. 4.2 – 3D cell culture models improve the relevance of *in vitro* drug evaluation. Cancer spheroids can replicate relevant morphophysiological characteristics of *in vivo* tumours like hypoxia and increased drug resistance. They have also been widely used in high-throughput screening and are easily produced with inexpensive reagents. Nonetheless, their single cell line lineage and inability of long-term culture limit their usefulness in comparison of organoids.

However, standardisation of spheroid culture is difficult, mainly due to variability during initial stages of growth. The method of preventing cell adhesion influences heterogeneity in spheroids grown in identical conditions. Spheroid size is also directly linked to drug resistance, with larger (500 μm) spheroids showing up to a 22-fold increase difference compared to cell monolayers with PDT. Spheroids >250 μm showed a 40-50% decrease in drug uptake, while 100 μm spheroids did not show a significant difference from cell monolayers during exponential or plateau growth phases [329]. Therefore, identifying an appropriate phase of spheroid development is crucial for evaluating drug phototoxicity. Fig. 4.3 shows a summary of previously used PpIX-containing conjugates used for *in vitro* PDT in Chapter 3.

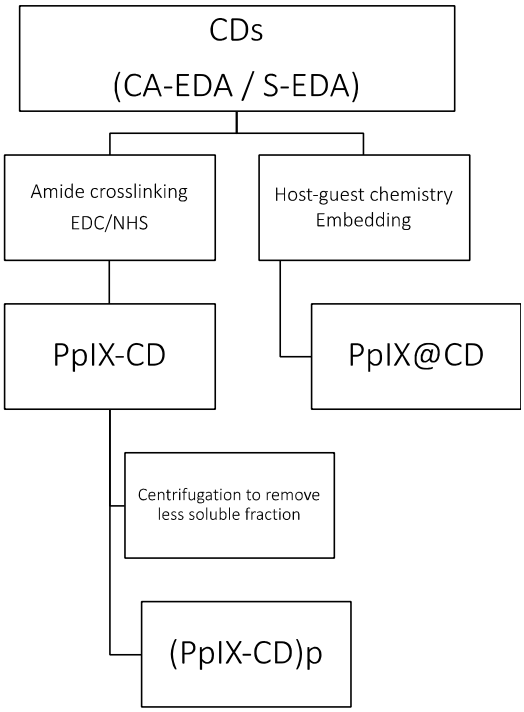

Fig. 4.3 – Schematic detailing conjugates used for *in vitro* PDT. PpIX-CD and (PpIX-CD)p were fabricated through amide crosslinking. The latter corresponds to the insoluble (precipitate) fraction separated from PpIX-CD after centrifugation. PpIX@CD was obtained using a one-pot reaction.

Aim: Screen treatment combinations to determine best parameters for low fluence PDT using multicellular cancer spheroids.

Objectives:

- Select a time point during spheroid growth for PDT evaluation based on growth kinetics.
- Determine *in vitro* PDT parameters for spheroids based on previously measured LC50 concentrations and light doses.
- Evaluate the effect of light fractionation (sequential light exposures) on spheroid damage.
- Examine PDT-induced morphological changes in spheroids using light sheet fluorescence microscopy (LSFM) and scanning electron microscopy (SEM).

Experimental

All reagents were used as received unless stated otherwise. Deionized water was used for all buffers and samples in experiments.

Materials

2-hydroxyethylagarose, formaldehyde, and dimethyl sulfoxide (DMSO) were acquired from Sigma Aldrich (United Kingdom). Dulbecco's modified Eagle's medium (DMEM, high glucose), Dulbecco's modified Eagle's medium (DMEM, high glucose, without phenol red), foetal bovine serum (FBS), Quant-iT Picogreen dsDNA quantification kit, Pierce LDH cytotoxicity assay kit, LIVE/DEAD Viability/Cytotoxicity Kit for mammalian cells, and trypsin-EDTA were obtained from Thermo Fisher (United Kingdom). Syringe filters with a 0.2 μm pore size were acquired from Sarstedt (United Kingdom). 1 KDa MWCO, 6.4 ml/cm dialysis tubing was acquired from Spectrum Labs (United States of America).

Sample preparation

CD-PS conjugates were prepared according to a previously described protocol [330]. CDs were synthesized via the microwave pyrolysis citric acid or sucrose, with ethylenediamine as a passivating agent and PpIX for host-guest embedded conjugates. Amide cross-linking was used to bind CDs and PpIX. Conjugates were further processed utilising centrifugation and dialysis to remove excess reagents and waste products.

Multicellular tumour spheroid (MCTS) culture

Cells were donated by Dr. Helen Bryant from the Medical School, University of Sheffield. The cell lines C8161 (human melanoma) were cultured in phenol red-free DMEM with 10% foetal calf serum, 1% penicillin and streptomycin, and 1% L-glutamine. Cells were cultured in a T75

plate at 37°C, 5% CO_2 until around 80% confluence. Multicellular tumour spheroids were produced utilising agar coating to prevent cell adhesion. A 1.5% agarose solution was prepared with 2-hydroxyethylagarose and standard cell culture media (DMEM). This solution was sterilised by autoclave and stored at 4°C. Agar-coated plates were prepared by adding 100 µl of the agarose solution into each well and left to set at room temperature for at least 1 hour. Plates were seeded with 100 µl phenol red-free media containing 6 x 10^3 cells per well and returned to the incubator until spheroids reached approximately 500 µm diameter. Growth media was changed every third day by adding 100 µl to each well and removing an equal volume.

Photoactivation with multicellular tumour spheroids

Spheroids were subjected to single and double light exposure periods with a mounted LED. Conjugates were subjected to ultrasonic processing with a Hieschler UP50H ultrasonic probe prior to the dilution to remove aggregates and dissolved in phenol red-free media at a concentration of 50 µg/ml, being kept refrigerated until used. Stock solutions were placed in an ultrasonic water bath for 15 minutes at 37°C. Spheroids were treated using conjugate dilutions to achieve concentrations of 1, 5, and 10 µg/ml in a 200 µl volume. The plates were then returned to the incubator for 2 hours to allow uptake.

A M405L2 ThorLabs mounted LED with a collimator adapter (405 nm, 2.76 mW/cm^2) was used to induce light-activated toxicity. Single exposure samples were placed under illumination for 15, 30, and 60 minutes and subsequently returned to the incubator, corresponding to 2.5, 5, and 10 J/cm^2. Sequential light exposure was carried out for spheroids on Day 2. LDH release and DNA quantification were measured at 24, 48 and 72-hour time points (post light activation).

LDH release assay

LDH (lactate dehydrogenase) is an enzyme present in all cells which is used as a marker for plasma membrane damage. Adverse conditions cause enzyme leakage, which can be quantified colorimetrically as a red-coloured formazan product is formed when adding a tetrazolium salt. This is a rapid and inexpensive assay which can differentiate between growth inhibition and cell death [331]. While resazurin reduction is a useful tool for determining metabolic activity, determination of spheroid viability is more useful for PDT evaluation.

LDH release was measured in all samples by collecting 50 µl of media and transferring it to a 96-well plate. Spheroids with no conjugates and equal irradiation times were used as negative controls for spontaneous LDH release. The positive control was carried out by incubating spheroids with TE buffer (10 mM Tris-HCl, 1 mM EDTA, pH 7.5) for 45 minutes. An additional four freeze-thaw cycles were used to ensure membrane disruption and indicate maximum LDH release. Subsequently, 50 µl LDH working solution was added to each well and covered to avoid contact with light. Plates were incubated for 30 minutes and 50 µl LDH stop solution was added to finalise the reaction. Absorbance for each well was read at 490 nm (LDH) and 680 nm (background) with a with a fluorescence plate reader (Biotek Instruments ELx800). Viability was calculated with the following formula:

$$\%Cytotoxicity = \frac{(Sample\ LDH\ release - Spontaneous\ LDH\ release)}{(Maximum\ LDH\ release - Spontaneous\ LDH\ release)} \times 100$$

$$\%Viability = \%Cytotoxicity_{Control} - \%Cytotoxicity_{Sample}$$

dsDNA quantification (PicoGreen) assay

Changes in cell growth are typically measured using metabolic activity assays such as MTT or resazurin reduction. However, they may not always accurately represent actual cell numbers,

leading to discrepancies between assays. In comparison, dsDNA quantification can provide a much more precise measurement that is independent of intracellular conditions. PicoGreen is a dye which increases its fluorescence after binding with DNA and can be easily quantified using a microplate reader. It is also well-suited for spheroid analysis as it does not suffer from false readings due to high ECM content. However, samples require complete lysis to release all dsDNA for measurement.

Picogreen working solution was prepared by dissolving the reagent in TE buffer (10 mM Tris-HCl, 1 mM EDTA, pH 7.5) according to the instructions from the manufacturer. Spheroids were removed from each well and placed in a 96-well plate and carefully washed three times with 50 µl sterile PBS to remove cellular debris. Cell lysis was performed by adding 50 µl TE buffer to each well and freeze-thawed four times. An equivalent volume of 100 µl Picogreen working solution was added. Plates were covered from light and incubated for 10 minutes at room temperature. Fluorescence was read at 485 nm excitation and 528 nm emission with a fluorescence plate reader (Biotek Instruments FLx800). A blank was prepared by adding deionised water and Picogreen in equal volumes.

Live/dead Staining

Cells were stained with 2 µM calcein AM and 4 µM ethidium homodimer-1 to differentiate live and dead cells. Staining solutions were prepared on the day of use to avoid the spontaneous hydrolysis of calcein AM due to moisture. Spheroids were moved to new wells and gently washed with PBS before adding 100 µl of staining solution. The plates were left at room temperature for 45 minutes before washing with PBS and storing at 4°C.

Microscopy

Light microscopy

Images were obtained using an AE2000 inverted light microscope (Motic, United States) fitted with a Moticam 2.0 camera (2 MP) and a 4x objective. Images were obtained before and after clearing cellular debris from each well. White balance was used increase spheroid contrast against the background.

Light sheet fluorescence microscopy (LSFM)

Spheroids were embedded in 1% 2-hydroxyethyl agarose prior to imaging. LSFM was carried out with a Zeiss Z.1 light sheet microscope (Zeiss, United Kingdom) fitted with a W Plan-Apochromat 10x objective. Images were obtained as Z-stacks with a 1.8 µm slice interval and a size of 878.09 µm × 878.09 µm. Light sheet thickness was adjusted to 6.4 µm and the pixel size was 0.46 µm. Image processing was carried out using Zeiss ZEN 2014 SP1 software version 9.2.0.0 and ImageJ.

PpIX uptake quantification

PpIX uptake within MCTS was confirmed through fluorescence based on its emission at 633 nm after excitation with the 405 nm laser line. Additionally, a separate control to measure background fluorescence was prepared by adding growth media instead of nanoparticle suspension. The innermost section of each spheroid was taken to estimate total PpIX uptake.

Live/dead microscopy

The equipment was set up with the following: a 405/488/561/640 nm laser blocking filter, an SBS 560 nm long pass filter. Images were captured simultaneously: Calcein AM (live, 505-545 nm bandpass filter) and ethidium homodimer-1 (dead, 660 nm long pass filter). A 448 nm laser was used at 0.6% power with 119.85 ms exposure time. Each spheroid was imaged at 0,

120, and 240 degrees with the same parameters.

Drug uptake analysis

After a 3-hour uptake period, samples were fixed with 3.7% paraformaldehyde overnight and kept at 4°C until used. The equipment was set up with the following: a 405/488/561/640 nm laser blocking filter, an SBS 560 nm long pass filter. A 405 nm laser (5% power and 199.7 µs exposure time) was used to acquire images. Fluorescence intensity was measured within the middlemost section of the spheroid as determined by Z-stacks (2 µm interval).

Scanning electron microscopy (SEM)

Spheroids fixed in 3.7% paraformaldehyde were washed twice in PBS at intervals of 10 minutes. Afterwards, they were fixed a second time in 1% aqueous osmium tetroxide for 1 hour at room temperature before undergoing two more PBS washes. Samples were exposed to an ethanol series at room temperature at 15-minute intervals (75%, 95%, 100%, 100% dried over anhydrous copper sulphate). Each sample was placed in 50/50 mixture of 100% ethanol / 100% hexamethyldisilazane for 30 minutes, followed by 30 minutes in 100% hexamethyldisilazane. Spheroids were air-dried overnight in a fume-hood and coated with gold in an Edwards S150B sputter coater. SEM micrographs were obtained using TESCAN Vega 3 LMU Scanning Electron Microscope at an accelerating voltage of 20 kV.

Statistical analysis

Experiments carried out with three independent repeats in triplicates (N=3, n=6) and results were normalized using untreated controls. Statistical analysis was carried out using GraphPad Prism version 8.3.0. A normality test was performed on each data set to confirm the use of ANOVA. The comparison of metabolic activity was evaluated by 2-way ANOVA analysis with Dunnett's test for multiple comparisons, with adjusted P values < 0.05 considered

statistically significant. Data was presented as means ± SEM (standard error of the mean). Charts include symbols representing adjusted *P* values, which are shown below.

Table 4.1 – List of symbols used to represent statistical significance.

P value	***Symbol***
>0.05	ns (non-significant)
<0.05	*
<0.01	**
<0.001	***
<0.0001	****

Results and Discussion

Spheroid culture

Selection of spheroid culture system

Spheroids can be formed by covering tissue culture plates with a material which prevents specific and unspecific cell attachment. Although there are other alternative methods for spheroid production such as hanging drop and rotating vessels, the use of non-adherent surfaces does not require additional equipment and can be adapted for use with biological assays. However, there is no effective control of spheroid size and variations are common between plates, even considering the use of ultra-low attachment microplates.

The agar coating method with 2-hydroxyethylagarose has been previously used to successfully produce MCTS from various cell lines, such as NCI-ADR-RES (ovarian adenocarcinoma) and HUH7 (hepatocellular carcinoma) [84,332]. This is a simple, low-cost, and reliable method for cultivating spheroids which makes use of agarose dissolved in serum-free media. A total of 100 µl agar allowed cells to remain in suspension and form three-dimensional aggregates, leaving approximately 100 µl extra volume for growth media.

Spheroid growth kinetics can be used to select the best time point for experiments

First, a preliminary study was carried out to determine the growth kinetics of C8161 with different cell seeding densities. MCTS can begin forming with as low as 100 cells per well and quickly develop different zones. Spheroids under 200 µm typically have proliferating and quiescent cells, while those around 300 µm begin to show signs of hypoxia in their centres. Furthermore, the diffusion limit of molecules such as oxygen is 150 – 200 µm, leading to the formation of a necrotic core in spheroids larger than 500 µm after several days [333].

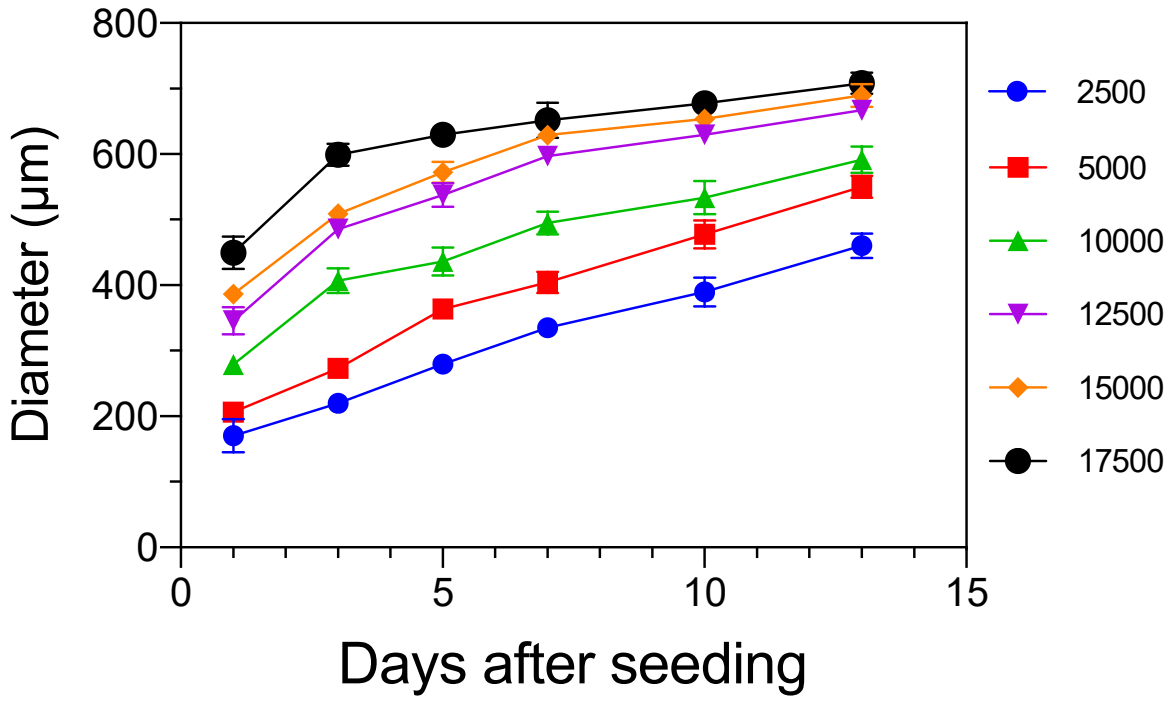

Fig. 4.4 – Spheroid growth kinetics based on initial seeding density. Diameter was measured using images taken with an AE2000 inverted light microscope and ImageJ. Growth reached a slowed after spheroids passed 600 µm.

The manipulation of low cell densities for spheroid formation is challenging as there is an increasingly greater variation in diameter and the experiment time greatly increases. A seeding density of 12,500 cells per well was selected as it continued growth until slowing after day 13 post-seeding (Fig. 4.4). A key advantage of large spheroids (>500 µm) have been shown to have a high degree of similarity to murine xenografts in cell cycle and apoptosis [334]. They have also shown increased drug resistance in comparison to smaller aggregates (<300 µm), likely due to a combination of necrosis and hypoxia [335].

In the following experiments, a series of morphometric parameters were acquired using automatic image processing software (AnaSP). Spheroids were preselected before PDT based on their sphericity, ensuring drug uptake and diffusion variations are minimised. This methodology will be expanded upon in Chapter 6.

Assays for estimating of drug-induced toxicity vary in 3D cell models

MCTS are compatible with many of the commonly used cytotoxicity assays for monolayers, including MTT and resazurin reduction. The combination of multiple assays can be used to elucidate more information regarding treatment effectiveness. However, there are key limitations to their use with spheroids. These assays are indirect measurements of cell viability which are affected by variables such as cell culture conditions, incubation time, and lack of supplied standards, which need to be standardised previously. Nonetheless, they are widely used as initial tests for nanoparticle cytotoxicity evaluations. This has led to increasingly greater discrepancies as the estimation of cell proliferation after exposure to unknown compounds is not optimal [336].

However, it has been shown that the higher cell density within 3D cell models, including cancer spheroids, results in great inconsistencies in comparison to traditional cell monolayers. Firstly, metabolism drastically changes in spheroids, particularly due to cell-cell interactions and the presence of cell layers (proliferating, quiescent, and necrotic). In comparison to cell monolayers, which keep expanding until they take up all available space, spheroids typically reach a maximum size and maintaining their state for several days before dying. Secondly, the diffusion of reagents through a 3D environment is inconsistent and leads to poor reproducibility. Therefore, the selection of an appropriate assay is essential to evaluate MCTS drug response [337].

LDH release was chosen to monitor the relative damage to cell membranes in each spheroid. While other assays such as MTT or ATP quantification are well-known and low-cost, repeated measurements are impossible as spheroid disruption is required to analyse the contents. Alamar blue (resazurin reduction) assay can be used without affecting the sample but is difficult to standardise as spheroids are suspended on agar, which absorbs part of the solution and is

difficult to wash away. In contrast, the LDH assay only requires a small aliquot of growth media to analyse each sample, reducing the risk of spheroid disruption as samples which have been heavily damaged by PDT are often very structurally weak and readily break apart if not handled carefully.

DNA quantification is another parameter which can be compared when evaluating PDT effect and its subsequent cytotoxicity. However, it is heavily reliant on complete cell membrane disruption in order to accurately quantify total DNA in each sample. Although the manufacturer's guidelines suggested the use of a lysis buffer (TE, Tris-EDTA), it was observed that it was not enough to cause total spheroid disruption even after incubation for 4 hours. Therefore, the protocol was changed to use TE buffer in combination with a total of 4 freeze-thaw cycles, ensuring each sample was completely lysed prior to analysis.

It is important to take note that LDH release should not be considered directly proportional to total DNA content. As previously mentioned, LDH release is caused by damage to cell membranes, which causes leakage of intracellular components to the media. The half-life of LDH is approximately 9 hours, though it varies according to the enzyme isoform. Therefore, it is best used as a representation of the total damage sustained by cells at a specific timepoint [338]. In comparison, DNA quantification is a much more sensitive detection method based on the specific binding of the Picogreen dye to dsDNA as it can detect as few as 50 cells, taking advantage of its >1000 fold increase in fluorescence when bound to dsDNA [339].

Light microscopy (LM)

Monitoring spheroid growth and hypoxic core formation

Light microscopy was used to monitor spheroid growth throughout several days, observing morphology to determine variations between wells. Hypoxic core formation has been reported to occur within 4 – 10 days, depending on cell type and initial seeding density. Oxygen deficiency has been shown to be a crucial part of cancer drug resistance and is linked to the overexpression of VEGF (angiogenesis) and CD44 (adhesion receptor) [323]. The appearance of the hypoxic core can be seen in Fig. 4.5, with the inner section of the spheroid becoming more pronounced as cell compaction separates the layers into proliferating, quiescent, and necrotic [340].

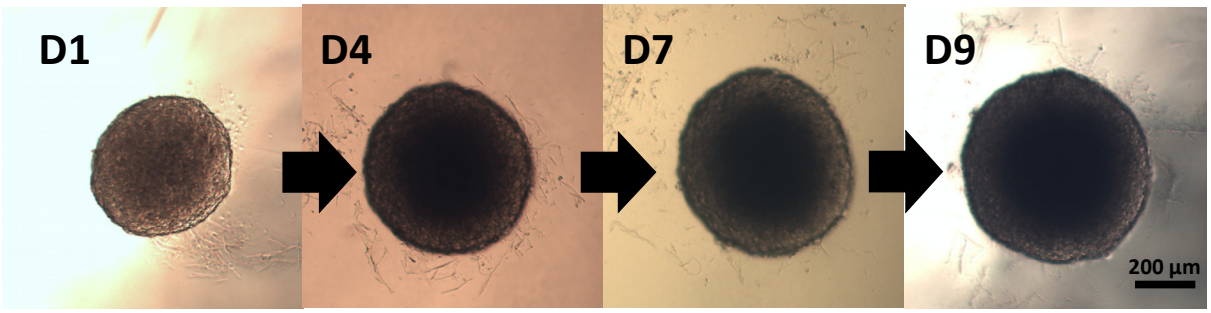

Fig. 4.5 – Progression of spheroid growth after initial aggregation. Spheroids reach a maximum diameter (~600 µm) and maintain their morphology until decaying.

The workflow of screening PDT parameters with spheroids requires frequent observation of individual samples to reduce the effect of cellular debris on biological assays (Fig. 4.6). Though PDT required spheroids to be outside of normal incubation conditions, prolonged exposure to stress caused a slight disruption in the outer layers. Spheroids of 450 – 500 µm were selected as they showed the presence of hypoxia in the core region while having outer layers of proliferating cells. Though larger spheroids could have been used (600 µm) these would have variations in drug response as cells pass from proliferation to quiescence.

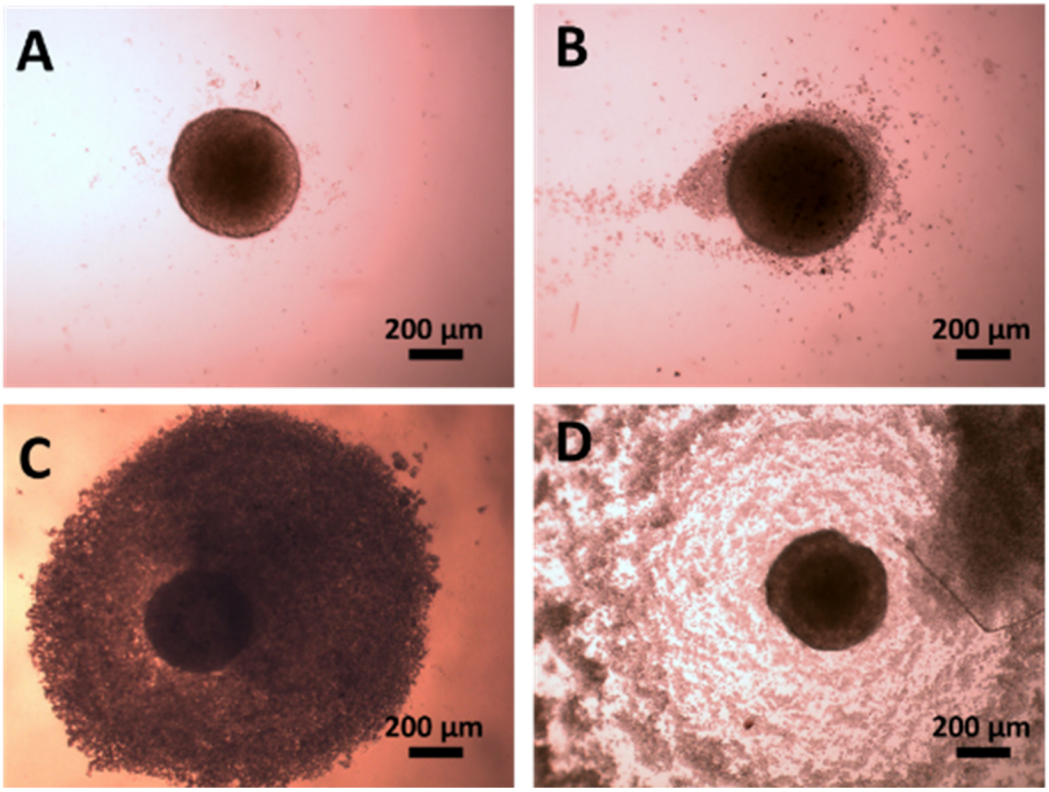

Fig. 4.6 – Multicellular tumour spheroids react differently to PDT. Spheroids were selected for use in PDT after reaching ~450 µm (A). Prolonged exposure to environmental stress in addition to conjugate dark toxicity caused slight damage to the outer cell layer (B). PDT caused significantly more damage, resulting in large seen as debris surrounding the spheroid (C). Debris can be removed to reveal the spheroid (D).

Dark toxicity

Spheroids show increased resistance to dark toxicity compared to cell monolayers

Dark toxicity in MCTS was re-evaluated to observe differences from monolayers and select an appropriate PpIX concentration range for PDT. PpIX showed a steady drop in spheroid viability as evidenced by the elevated LDH release. Nonetheless, the highest concentration of 10 µg/ml did not drop viability below 50%. In comparison, PpIX-CD and PpIX@CD consistently showed a decreased impact at all timepoints with concentrations over 1 µg/ml (Fig. 4.7). The adjustment of drug concentrations based on PpIX content was repeated to ensure a better comparison.

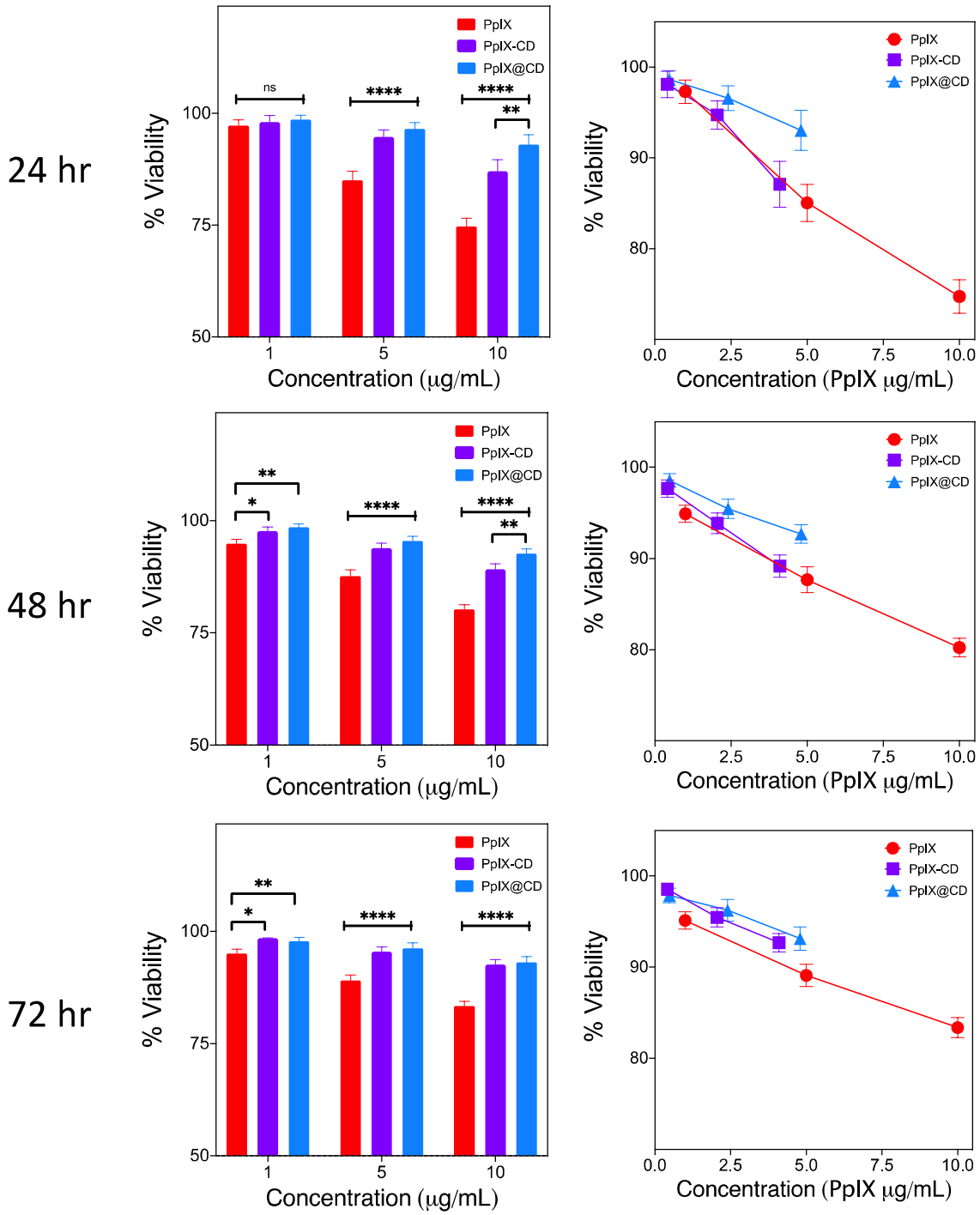

Fig. 4.7 – LDH release varies according to sample type and dose (μg/ml). PpIX-adjusted values show samples have similar dark toxicity in spheroids. Each sample was compared to the positive control PpIX. (n=6, N=3)

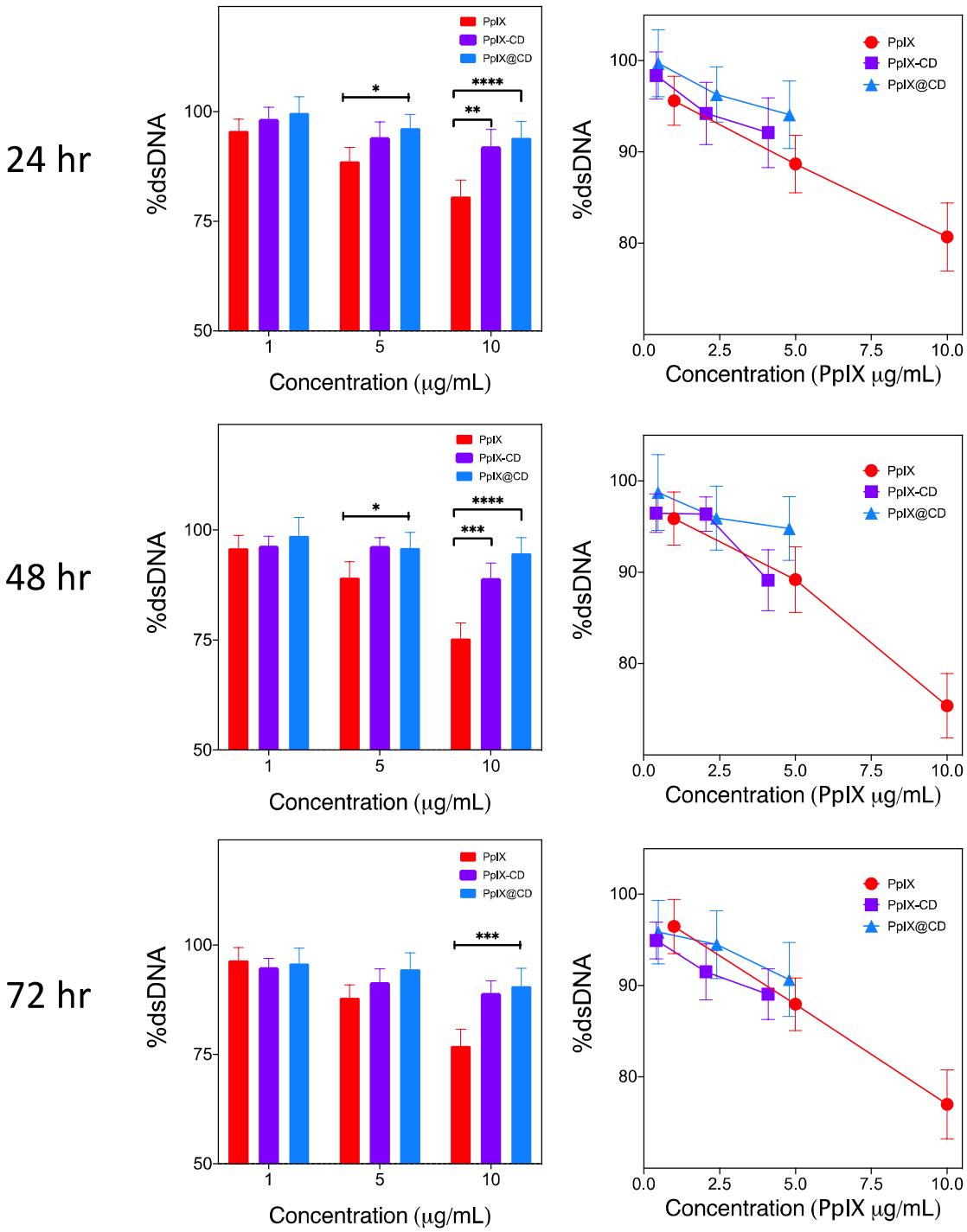

Fig. 4.8 – Total dsDNA concentration shows less variability between samples and concentrations. PpIX-adjusted concentrations show similar behaviour to LDH release, with no significant difference between conjugates and PpIX. Each sample was compared to the positive control PpIX. (n=6, N=3)

However, PpIX-adjusted values indicate there is no significant drop in viability based on total drug content, with the highest dose (10 μg/ml) only reducing around 20% of the spheroid viability. PpIX@CD initially showed slightly improved cytocompatibility at 24 hours post-exposure, though the difference ceased at later time points. These results are consistent with those found through the initial cytotoxicity evaluation of CD-PS conjugates in the previous chapter. Likewise, the slight recovery of viability after treatment (48-hour timepoint) was previously observed in cell monolayers.

DNA quantification showed a similar behaviour, with concentrations over 1 μg/ml showing significant difference between samples and control (Fig. 4.8). PpIX-CD once again showed very similar behaviour to the control with PpIX-adjusted concentrations at most timepoints. Interestingly, PpIX@CD continued to slightly outperform PpIX-CD with higher viability at 5 and 10 μg/ml. Spheroids began recovering after 48 hours post-PDT, as shown in Fig. 7, particularly at 10 μg/ml.

In summary, results appear to indicate doses of 1 – 5 μg/ml are ideal, though conjugates could be used up to >10 μg/ml. While PpIX showed a significantly improved PDT effect in 2D, the variability induced by high dark toxicity makes lower concentrations easier to evaluate. Spheroid DNA content and membrane damage are very near the values for control spheroids in this concentration range.

Variation between 2D and 3D cell culture is due to morphophysiological cues

Previously, results from 2D cell culture showed conjugates reduced metabolic activity by 50% at higher concentrations than PpIX (88.5 μg/ml PpIX-CD, 95.4 μg/ml PpIX@CD, 14.6 μg/ml PpIX). In comparison, spheroids demonstrated higher drug resistance than monolayers with all samples, particularly at the highest tested concentration of 10 μg/ml. LDH release and DNA quantification showed a similar trend, slightly decreasing as drug concentration increased.

Though a direct comparison between resazurin reduction and LDH or Picogreen is not ideal due to the characteristic differences in measured variables, there was one key difference that could be observed between 2D and 3D models. PpIX showed a significant difference in dark toxicity from 5 μg/ml compared to the conjugates in cell monolayers. This difference was not observed with MCTS, which only showed significant differences for PpIX@CD at PpIX-adjusted concentrations over 2.5 μg/ml on days 1 and 2 post-PDT for both LDH and Picogreen. Contrariwise, PpIX-CD showed very similar behaviour to PpIX at all timepoints with PpIX-adjusted concentrations.

There are different proposed mechanisms for increased drug resistance in spheroids which have been explored in the literature. The three-dimensional structure of spheroids has been previously shown to influence drug uptake depending on a multitude of factors such as spheroids size, cell type, and phase of cell cycle [341]. While the stroma and other cellular components are typically the focus of research, extracellular matrix and the interstitial fluid surrounding the main tumour mass have also been found to be an important factor in drug response. Normal tissue typically has 14-34% of its total volume occupied by interstitial fluid, while tumour tissue exhibits a much higher range of 36-53% [342]. This significantly affects drug and nanoparticle distribution as they typically rely on concentration gradients. Therefore, it is likely that spheroids present highly variable drug concentration [343].

Phototoxicity

Ultra-low fluence rates can be used to determine light toxicity thresholds

Initial light treatment (LT) tests showed a significantly different response from spheroids in comparison to cell monolayers after 5 minutes of exposure (0.83 J/cm^2). This was expected as MCTS showed consistently higher drug resistance during dark toxicity evaluation. Therefore, the total light exposure (irradiance) was adjusted to higher values (2.5 – 10 J/cm^2) where greater phototoxicity could be observed. While it is a 3 to 12-fold increase, total light exposure is still within the ultra-low fluence range [344].

Values for total light exposure in the literature range from 25 J/cm^2 in the low end to >350 J/cm^2 with high dose conditions, delivered through a laser light source instead of an LED [345]. Laser setups has the advantage of delivering a large amount of energy in less time without power loss due to light scattering and controlling laser power by adjusting the beam. However, high power output has also been shown to cause photobleaching and tissue damage. LEDs are a low-cost reliable alternative that has shown clinical success with PDT at various fluence rates [346]. Damage distribution to tumours also varies according to irradiance, with scar formation and other symptoms appearing after high fluence PDT [347].

In this chapter, fluence was adjusted to the ultra-low range (>10 J/cm^2). This range was previously utilised by Matthews et al. (2009) to deliver sub-lethal light doses to human glioma spheroids with 5-aminolevulenic acid at 1.5 – 6 J/cm^2 [297]. Additionally, photobleaching rates have been shown to vary according to light intensity (mW/cm^2) and refer to the point at which ~37% of fluorescence signal strength is lost. PpIX bleaching rates vary from 3.5 J/cm^2 at 5 mW/cm^2 to 6 J/cm^2 at 150 mW/cm^2 [298]. This intensity value is well below the 2.76 mW/cm^2 output of the mounted LED, which should circumvent PpIX photobleaching in the experiments.

Fractionated treatments were also carried out, in which the total light dose was separated by a 24-hour time interval. This is represented by the abbreviation "LT", which is short for light treatments. For example: 5 J/cm^2 (2LT) would correspond to a 30-minute (5 J) exposure on day 1, a 24-hour interval between doses, and a second exposure on day 2. Other abbreviations and explanations for PDT parameters can be found in Table 4.2. Fractionation in PDT has been proposed as a method for improving treatment outcome without requiring the use of longer timescales for irradiation or higher drug doses. This method has shown positive results in pre-clinical trials, with 2-fold illumination treatments showing a markedly improved complete response rate compared to the control [348].

Table 4.2. Explanation of PDT parameters screened with spheroids.

Parameter	Range	Summary
Fluence (J/cm^2)	2.5 / 5 / 10	Total energy delivered per area. Most common PDT parameter reported in literature.
Time (min)	15 / 30 / 60	Total time exposed to irradiation.
Light treatment (LT)	1 or 2	Number of light exposures throughout PDT (24-hour intervals)
Time after PDT (hours)	24 / 48 / 72	Timepoints chosen for analysis of spheroid viability.
Drug dose (µg/ml)	1 / 5 / 10	Concentration based on previously obtained results in Chapter 4.

Spheroids react to stressful environmental conditions after prolonged exposure

A separate experiment was carried out using spheroids without PS in order to determine potential drops in viability due to prolonged time outside standard incubation conditions. The effect of 405 nm light exposure was also investigated using the same methodology. Spheroids placed outside the incubator for 2 hours began to show some signs of stress as their morphology

changed, with some cells on the outer layers becoming detached. This happened regardless of light exposure duration. However, there was no significant difference after returning spheroids to the incubator for 24 hours (Fig. 4.9). Therefore, total light irradiation time had to be adjusted to a maximum of 60 minutes, corresponding to 10 J/cm^2. This ensured more light could be delivered without significantly altering results due to sample variability.

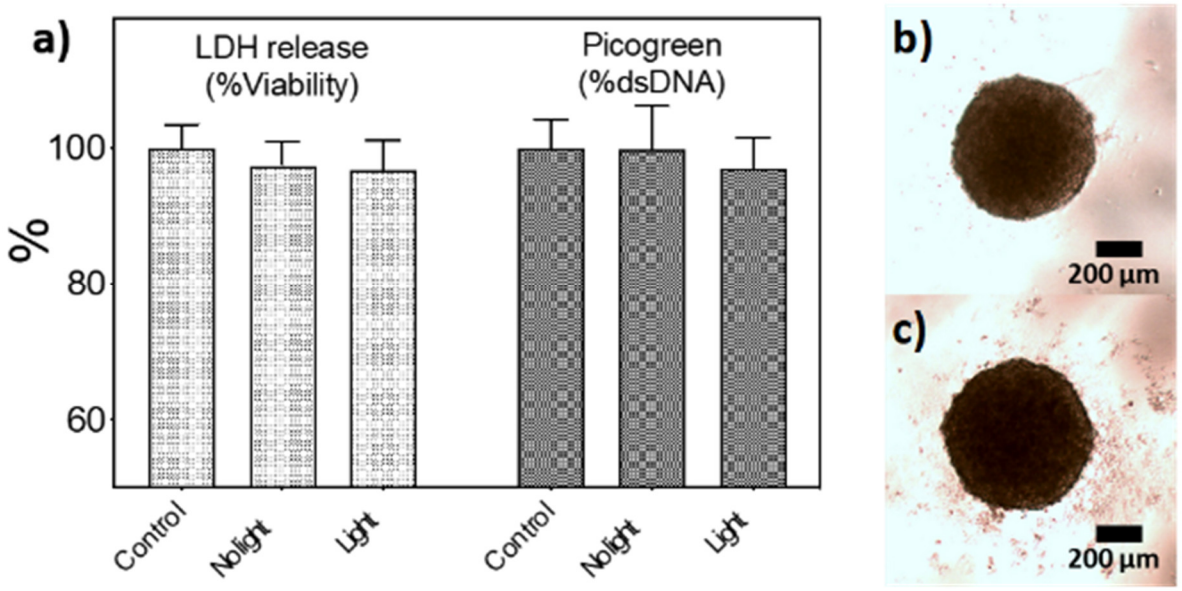

Fig. 4.9 – Effect of prolonged exposure to environmental stress on spheroid viability. Spheroids showed no significant difference in LDH release and total DNA content after a 2-hour period outside the incubator. Each sample was compared to spheroids left within incubation conditions. (n=3, N=3)

Light toxicity in spheroids caused varying degrees of cell death

Spheroids showed a significant increase in resistance to light-activated toxicity in comparison to 2D cell culture. Cell death can be seen easily through light microscopy (LM) as a halo of debris surrounding the spheroid. The quantity of debris changes depending on experimental conditions and sample used; typically, higher light and drug doses induce greater PDT effect (Fig. 4.10). Spheroids with extensive damage undergo changes in their morphology, losing their spherical shape and becoming deformed as lysis occurs [349]. Media changes can be used

to slowly remove debris from each well, though this becomes more difficult with increasing damage. Spheroids with the highest parameters (10 μg/ml, 10 J/cm^2, 2LT) were prone to complete disruption after trying to rinse out their well. All spheroids used in light toxicity experiments were washed to lessen variability due to remaining dsDNA or LDH within debris.

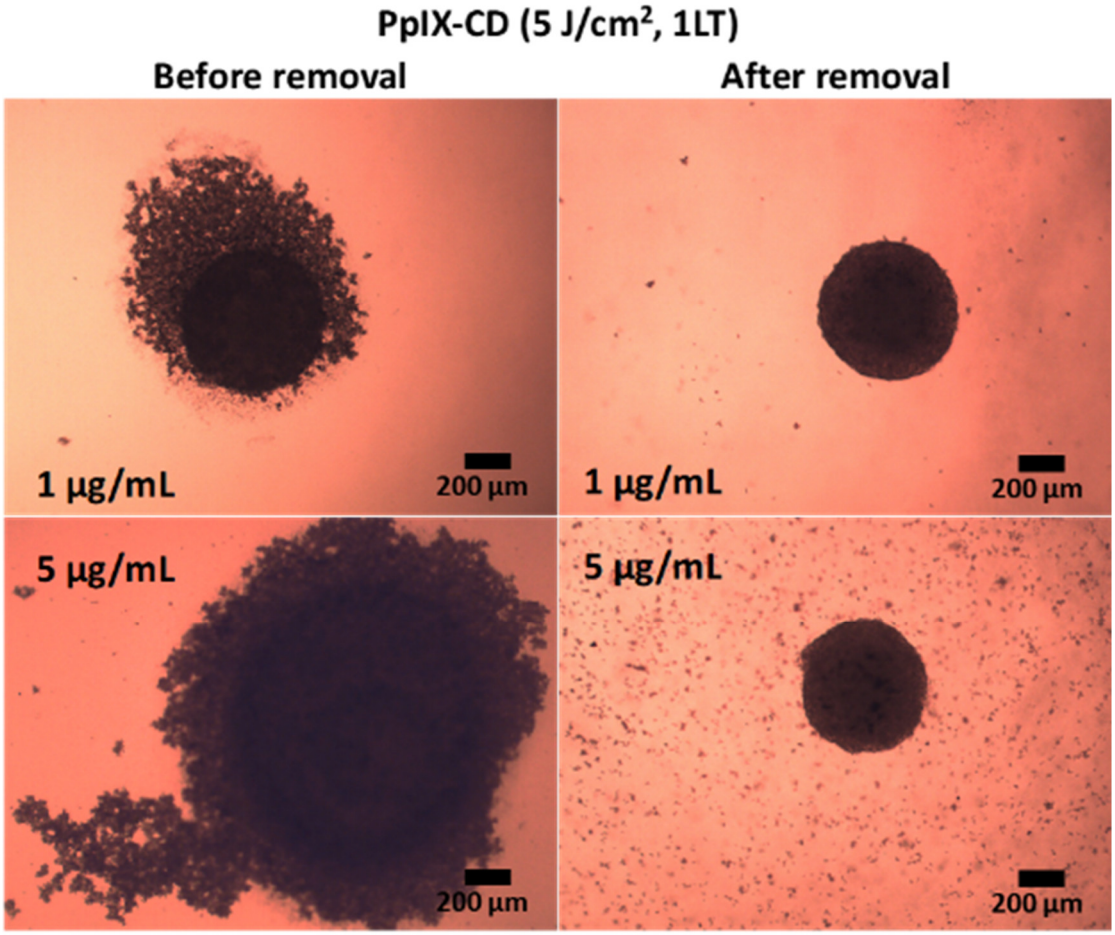

Fig. 4.10 – PDT-induced phototoxicity in spheroids after 24 hrs (PpIX-CD 5 μg/ml, 5 J/cm^2, 1LT). Cell debris precipitates to the bottom of the well, obscuring the spheroid. Removal must be done with care to avoid spheroid disruption.

All evaluated conditions showed a decrease in both viability and total DNA content after PDT. As expected, low drug doses (1 μg/ml) combined with low irradiance (2.5 J/cm^2) did not show a strong PDT effect. The increase of both dose and irradiance significantly increased treatment effectiveness. Double light treatments showed significant difference from single treatments at most experimental conditions, which is consistent with the literature [350].

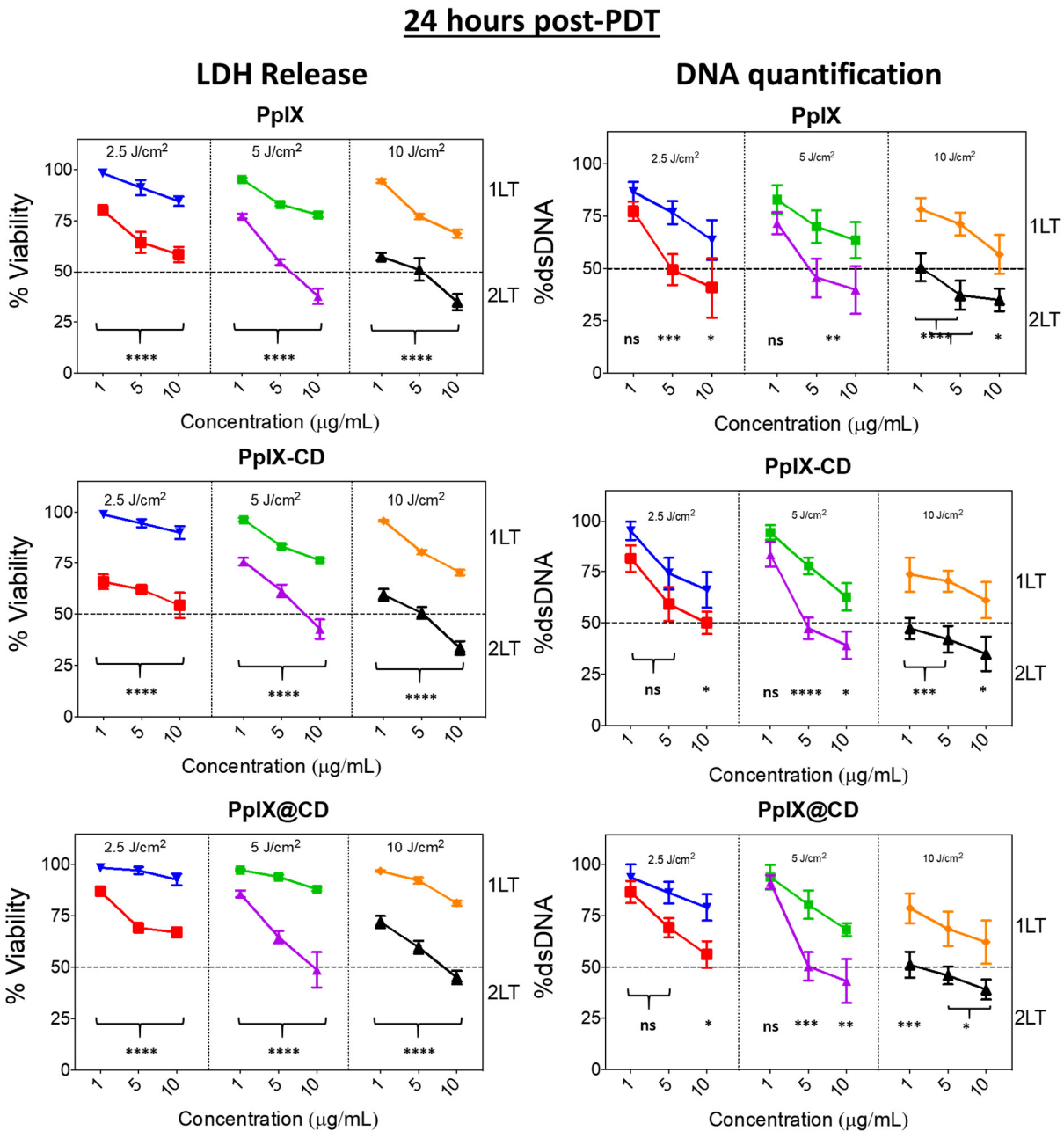

Fig. 4.11 – Light fractionation improves PDT outcome. Fractionated treatments (2LT) showed significant differences from single treatments (1LT) at concentrations >5 μg/ml. Higher irradiance and drug concentration significantly increased damage to spheroids regardless of sample type. (N=3, n=6)

There was a significant difference in observed values between LDH release and DNA concentration at low light doses and drug concentrations. As can be seen in Fig. 4.11, LDH values (% viability) consistently show significant difference between 1LT and 2LT, regardless

of sample or conditions. In contrast, total dsDNA has no significant change, particularly at 2.5 J/cm^2 and 1-5 μg/ml. 1LT was unable to consistently reduce spheroid viability and DNA content below the 50% threshold, though high drug/light combinations (1LT with >5 μg/ml and 5 J/cm^2) were shown to be significantly more effective compared to low doses.

Low-fluence as an alternative to high-fluence PDT

Clinically, PDT treatments tend to have high fluence values. These are generally preferred due to their increased and proven effectiveness as more power leads to increased $O_2{}^1$ production. Photofrin, also known as the FDA-approved 5-aminolevulenic acid, has standard clinical treatment parameters of 1 mg/kg (body weight), 630 nm light, and 150 mW/cm^2 specific power (215 J/cm^2 in total). Interestingly, it has been found that the tissue microenvironment undergoes a rapid depletion of oxygen during at least 40% of the total treatment duration, making it highly inefficient.

In comparison, a lower power of 30 mW/cm^2 has been previously shown to be as effective at disrupting tumour growth [351]. However, oxygen depletion and subsequent hypoxia in the treated area may limit further PS activation as the concentration of immediately available O_2 is rapidly diminished after irradiation. In particular, cells with low PS concentration or insufficient light exposure have been shown to have minimal PDT-induced death, even with high fluence (360 J/cm^2, 200 mW/cm^2) [352].

There are several factors that may intervene in these similar outcomes between high and low power intensities. Endothelial and cancerous cells within the tumour periphery are more likely to have a normal blood supply and oxygen partial pressure values compared to those found within the tumour core [353]. While PDT focused on destroying tumour vasculature may be highly effective, it will not be enough to cause total tumour ablation. It is also highly likely that high-fluence light irradiation causes oxygen depletion in the area and, more importantly, rapid

PS photobleaching [354]. This can explain the discrepancies in treatment effectiveness. Photochemical consumption of oxygen and the subsequent production of singlet oxygen are directly linked to PS concentration, oxygen availability, and light fluence. Thus, PS excited with a high-intensity light source would be steadily bleached, effectively reducing its concentration until oxygen consumption could keep up with available molecules in the tumour microenvironment. The spacing of light doses is meant to enable reoxygenation in affected tissue while maintaining PS function [355].

Fractionated PDT varies in effectiveness according to compounds and light activation

Fractionated PDT showed a slight variation between light doses, as seen in Fig. 4.12. While LDH release is significantly higher in fractionated treatments, this is not always observed with dsDNA quantification. Some variations can be seen at higher concentrations (> 5ug/ml) or light exposure (>5 J/cm^2), though they vary between samples.

There are conflicting reports regarding the usefulness of fractionated light doses. Babilas et al. (2003) stated that fractionated PDT using PpIX with different specific power ranges (25 – 100 mW/cm^2) were not as effective in comparison to single high-dose treatments [350]. There are some key differences in their methodology from other protocols. Their method of light fractionation consisted in an initial 20 J dose, followed by a 15-minute interval to allow oxygenation, and finished with a final 80 J dose. Irradiation was also carried out using a non-coherent light source (580 – 740 nm) as opposed to a monochromatic light source with a specific wavelength. Similar results were found by de Bruijn et al. (2007) using methyl-5-aminolevulinate (MAL) in a mouse skin model [356]. Their results suggest PS localisation prior to PDT is a key factor in not only treatment effectiveness, but in determining differences between single and multiple light doses. Compounds which do not reach their targets can greatly diminish PDT effectiveness, regardless of the total energy applied.

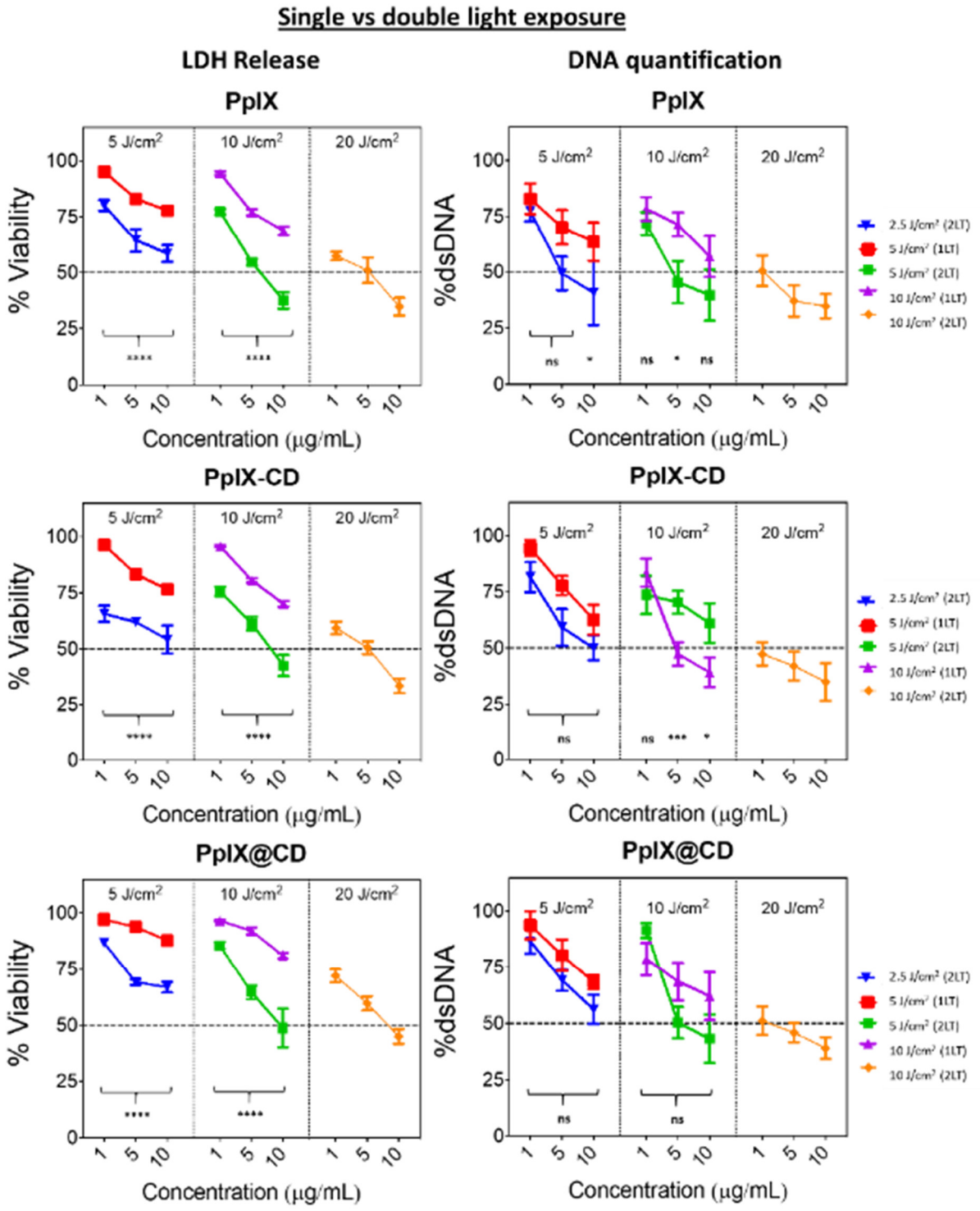

Fig. 4.12 – Fractionation of light exposure increases PDT effectiveness. Treatments with 1LT show slightly decreased damage to spheroids in comparison to 2LT, even with lower fluence in each repeat exposure. (N=3, n=6)

However, the experiments that were carried out using PpIX and its CD-based conjugates greatly differ in methodology. The use of a 405 nm LED with a low bandwidth (405 ± 13 nm) ensured more efficient absorption at the PpIX maxima. Most importantly, the time between light doses was greatly increased from 15-minute intervals to a 24-hour period. As was previously mentioned in Chapter 4, PpIX sensitizes cancer cells to PDT by interaction with p53, tumour suppression protein. They showed that cells treated with 2 J/cm^2 and 1 μg/ml PpIX caused a significant increase in p53-mediated and independent apoptosis. Fluorescence-activated cell sorting confirmed PDT induced apoptosis through the activation of the HDM2-p53 complex [312]. In comparison to necrosis, apoptosis is an ordered sequence of events leading to cell death. It is generally thought to occur within a period of 12 to 24 hours after signalling, though the exact duration is hard to determine as it depends on the activation pathway [357]. The experimental conditions which were used in the present study are like those reported by Ouyang et al. (2018). They selected a treatment based on the percentage of early apoptotic cells in comparison to necrosis, which corresponded to 4 μg/ml PpIX and a 5 J/cm^2 light dose [358].

Concentration adjustment show equivalent PDT effect between samples

PpIX-adjusted concentrations reveal a similar trend to that found previously with 2D cell culture. PpIX-CD consistently outperformed other samples at most conditions, particularly at 10 μg/ml, though this was only observed at 24 and 48 hrs post PDT. PpIX@CD showed poor effectiveness at 1 μg/ml for LDH release, but consistently demonstrated an equal effect to both PpIX-CD and PpIX during DNA quantification. In general, PpIX-loaded conjugates appeared to be like PpIX in both assays (Fig. 4.13).

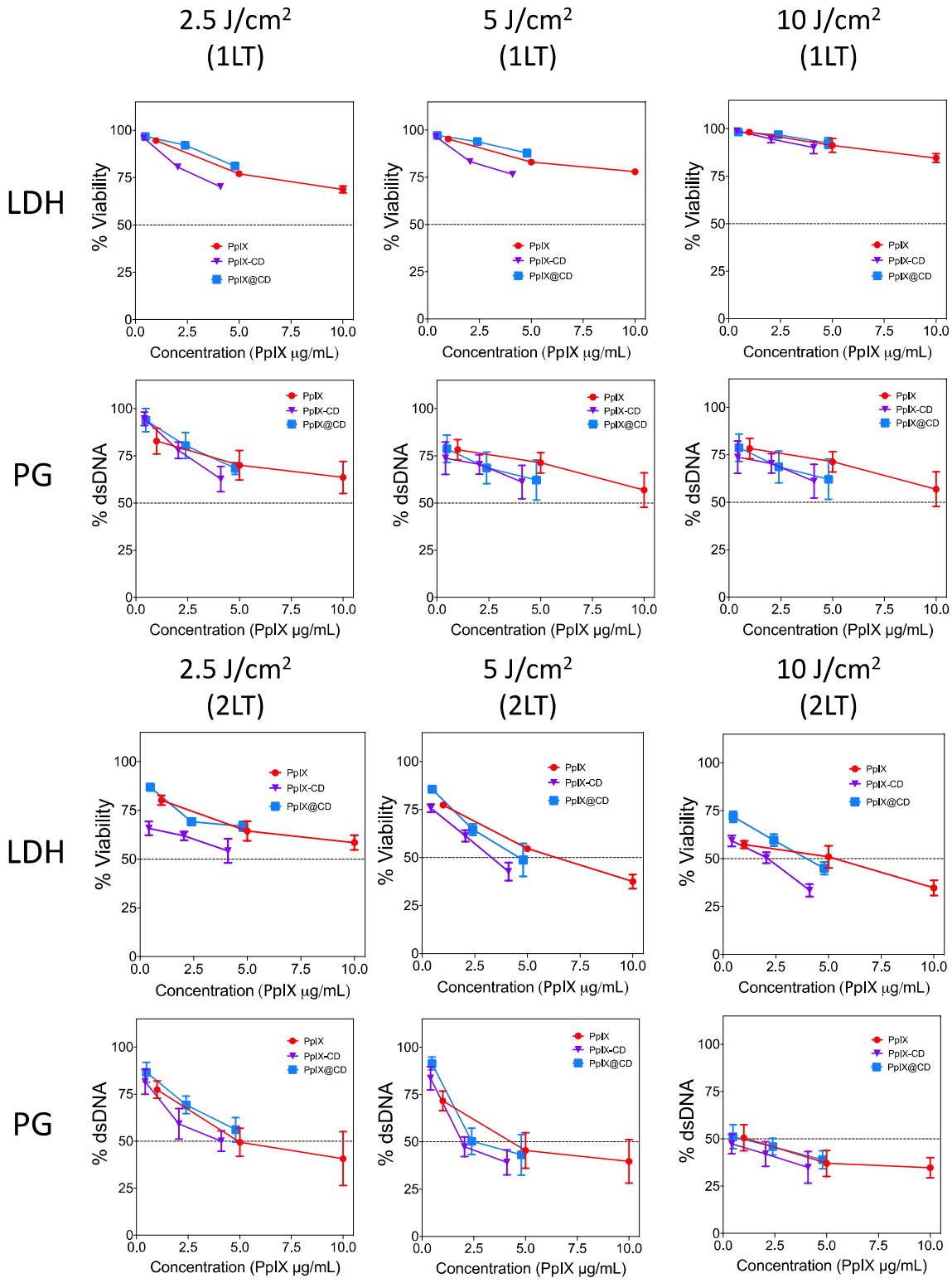

Fig. 4.13 – PpIX-adjusted values show similar behaviour between PpIX and conjugates. This trend can be seen in LDH release and total DNA content in samples treated with single (top) and double (bottom) light treatments. (N=3, n=6)

Summary of PDT parameter screening

In total, 54 parameter combinations were evaluated using MCTS at three distinct timepoints. Fig. 4.14 shows the variation in spheroid viability according to treatments. Single light treatments (1LT) proved to be unreliable unless higher drug concentrations were added, which adds additional variation due to innate dark toxicity from samples. 2LT was shown to be slightly more effective at lower drug concentrations. Therefore, ideal PDT conditions would require 2LT with a drug concentration of around 5 µg/ml, which is enough to cause considerable damage without substantial dark toxicity.

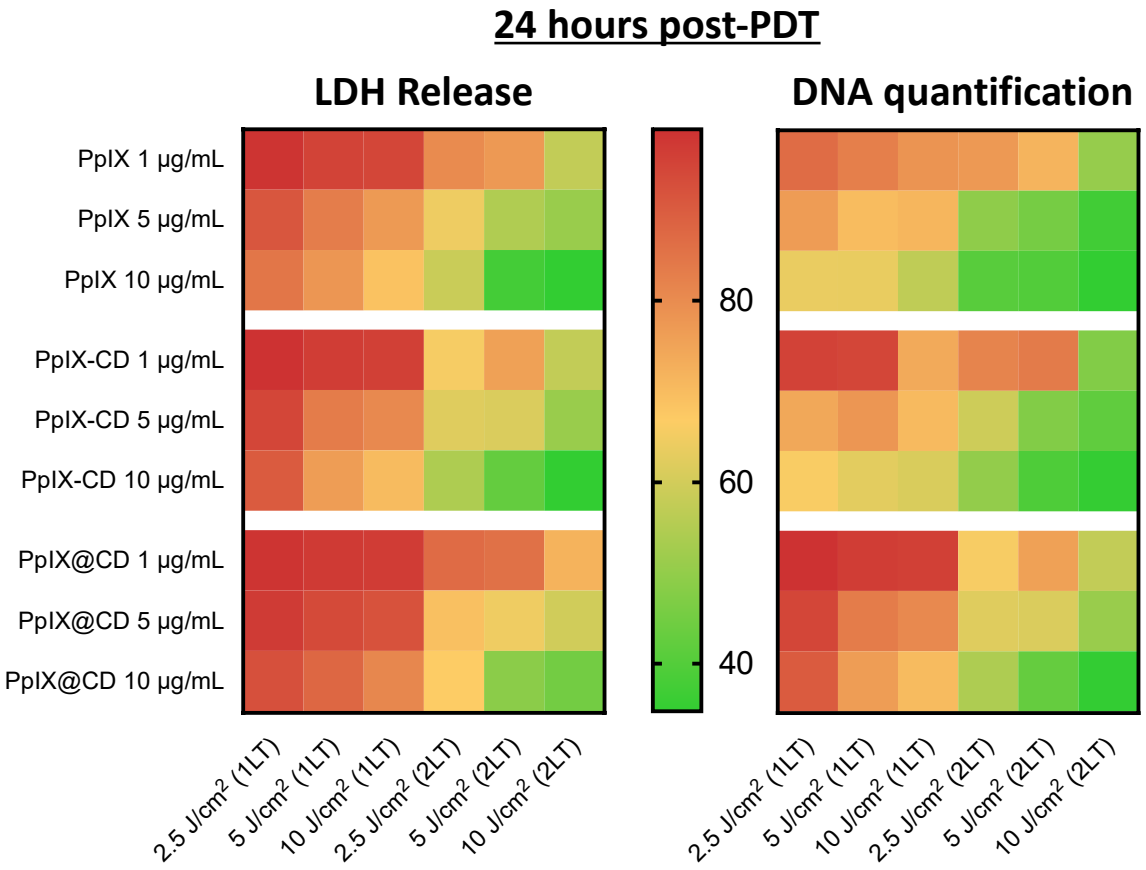

Fig. 4.14– Heatmap of all treatment combinations. Values correspond to % viability (LDH release) or %dsDNA (DNA quantification). Treatments with best outcomes are shown in green.

High fluence PDT using a laser

A 405 nm laser (Vortran Laser Technology, USA) was used to evaluate the effect of increased power output on the PDT effect in spheroids. The laser power was measured at the point of contact with the 96-well plate using a power meter, ensuring output was consistent. In comparison to the previously used LED, the 405 nm laser has the capability of providing up to 200 mW of stable output. The positioning of the laser spot was difficult as the adjacent mirror had to be adjusted for light to reflect onto the complete area of each well (Fig. 1.15c and 1.15d). The irradiance was adjusted to values considered standard (25 J/cm^2) and high (100 J/cm^2). PDT effect was evaluated using LDH release as a marker for damage and cell death.

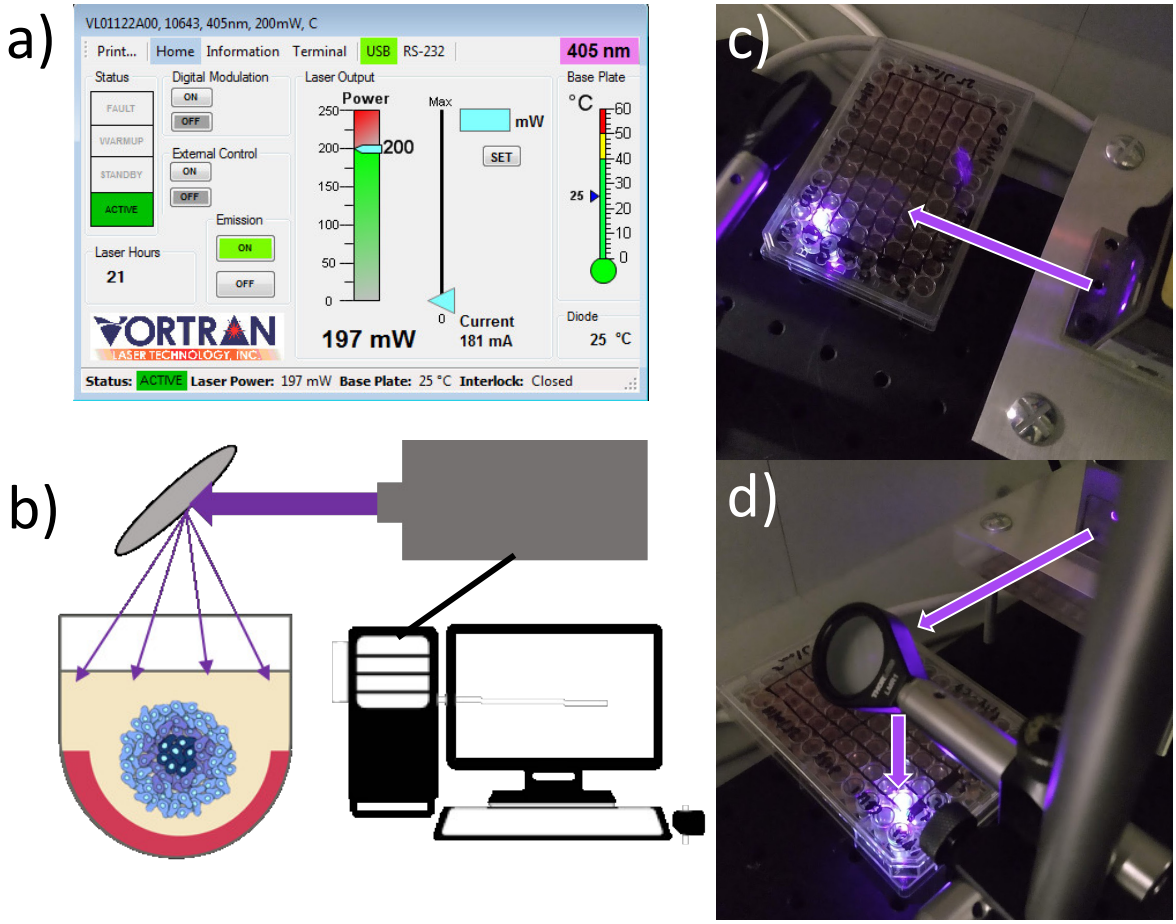

Fig. 4.15 – Schematic of 405 nm laser setup. The laser was controlled through software (a) and directed towards the spheroids using a mirror (b).

Results demonstrate high irradiance does not cause significantly higher cell membrane damage compared to the standard treatment. PpIX and PpIX-CD both showed decreased effectiveness after a 100 J/cm^2 dose at 5 µg/ml. In contrast, PpIX@CD did not show a significant change between treatments. Nonetheless, all high irradiance treatments resulted in much higher sample variability, which can be seen in Fig 4.16. This discrepancy has been previously reported in the literature as high fluence rates (>100 mW/cm^2) were shown to significantly reduce oxygen levels in carcinomas, with depletion occurring during approximately 40% of the total light exposure duration [359].

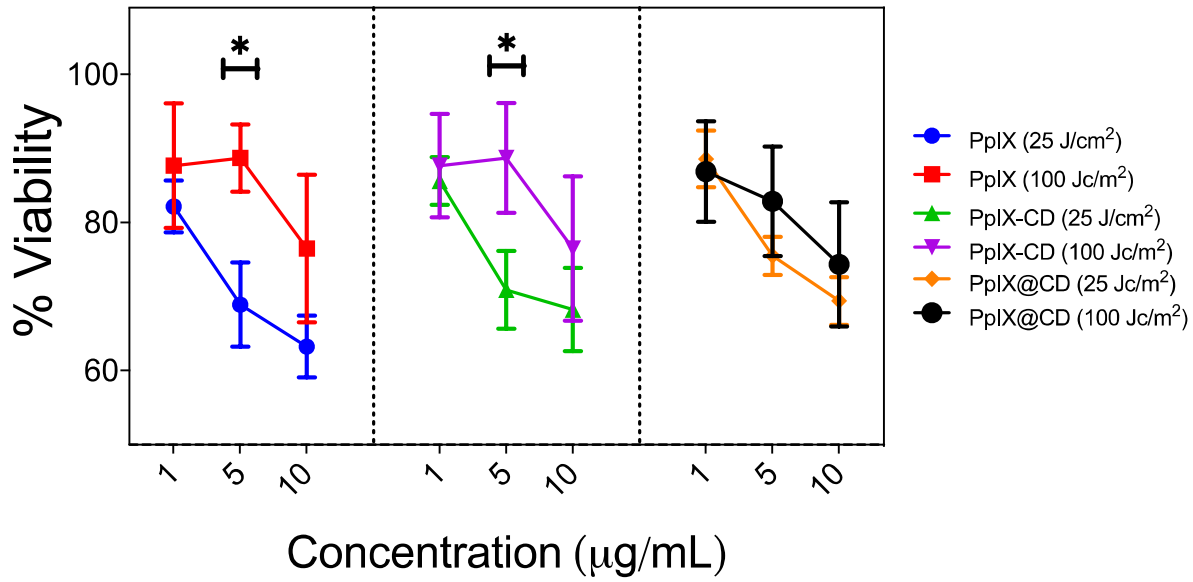

Fig. 4.16 – PDT effect does not scale with high irradiance. The increase of irradiance does not lead to significantly different treatment outcomes in multicellular tumour spheroids using a 405 nm laser (25 and 100 J/cm^2). (N=3, n=6)

Drug/light product has a lower threshold for effective PDT

PDT is composed of a drug and a light dose, which can be expressed as drug/light product. This can be reciprocal in some cases: for example, 1 mg/kg PpIX (150 J) and 3 mg/kg PpIX (50 J). In ideal conditions (i.e. no oxygen depletion), tumour destruction has been found to be

strongly linked to this parameter. However, the drug and light doses have been found to have a specific threshold below which reciprocity does not occur [360]. This effect was later confirmed by Seshadri et al. (2008) as they evaluated the effectiveness of PDT with high (100 mW) and low (7 mW) laser power regimens while adjusting PS concentrations. They did not observe a significant change in the total area of necrosis after PDT, observing intermittent hypoxia in the 100 mW ultimately leading to reduced effectiveness compared to 7 mW [361]. This indicates that light delivery over longer periods of time with lower power enhances the effectiveness of PDT.

Light sheet fluorescence microscopy (LSFM)

PpIX uptake can be observed throughout the inner layers of spheroids

Light sheet fluorescence microscopy was carried out using fixed spheroids incubated with all samples for 3 hours to estimate drug uptake. LSFM has been shown to be a much more efficient method for evaluating drug uptake in MCTS. While confocal laser scanning microscopy has been widely used to observe spheroids, it lacks enough imaging depth (~100 μm maximum) to accurately monitor drug distribution. In contrast, LSFM was capable of analysing spheroids up to 1 mm in diameter and determine drug penetration [362].

Spheroids typically exhibit some autofluorescence at 405 nm excitation, but the use of the long pass filter ensured the control did not show any appreciable fluorescence emission after 600 nm. Conversely, spheroids incubated with all samples and doses (1 – 10 μg/ml) for 3 hours showed emission peaks. Low sample concentrations (1 μg/ml) showed the presence of PpIX on the spheroid periphery, with slightly increased fluorescence in the control and PpIX-CD (Fig. 4.17). PpIX@CD showed aggregation within one side of the outermost layer of the spheroid, with low emission in other areas.

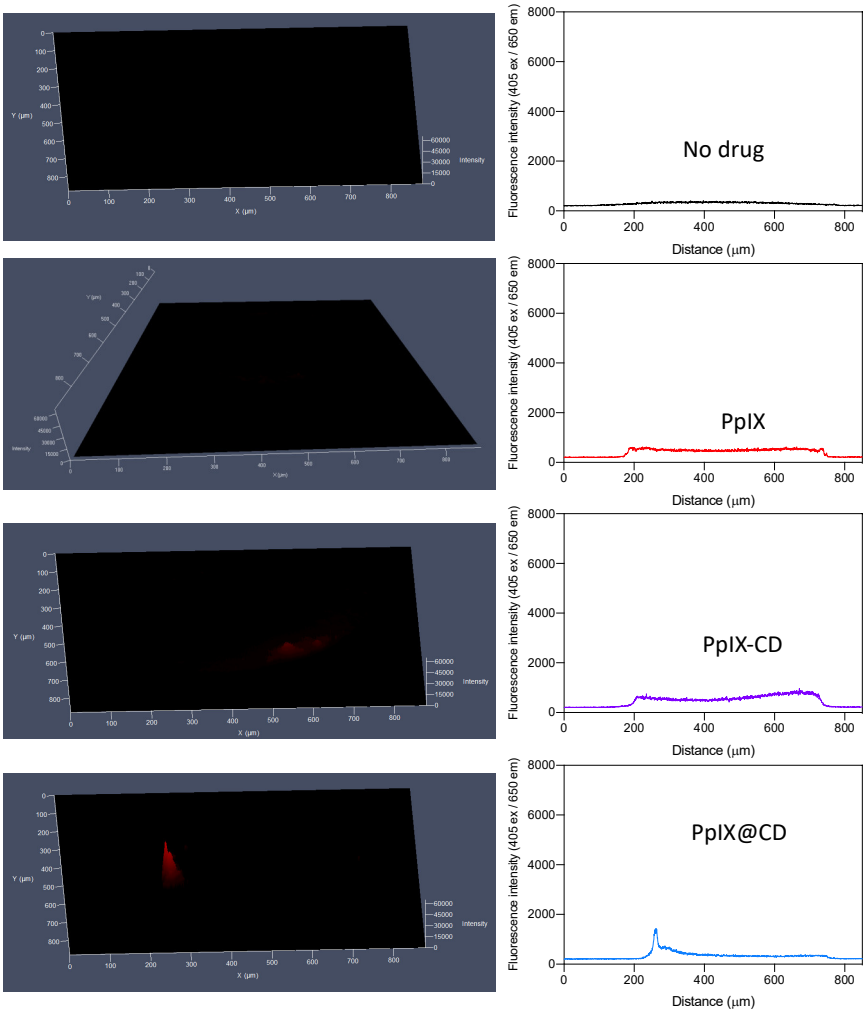

Fig. 4.17 – Conjugate uptake in spheroids at 1 μg/ml. Drug uptake with 1 μg/ml is an insufficient dose for PDT as uptake is limited to outer spheroid layers.

The increase of dosage to 5 μg/ml corresponds to a sizeable increase of fluorescence from all samples (Fig. 4.18). PpIX-CD displayed markedly higher emission in comparison to the control PpIX, with approximately 28% more uptake. PpIX-CD also showed similar values along the innermost part of the spheroid. In comparison, PpIX@CD continued to show much lower PpIX accumulation, with only 49 – 60 % emission in comparison to PpIX and PpIX-CD, respectively. The embedded conjugate once again showed higher uptake in one side of the spheroid, with drastically reduced emissions in the opposite sides.

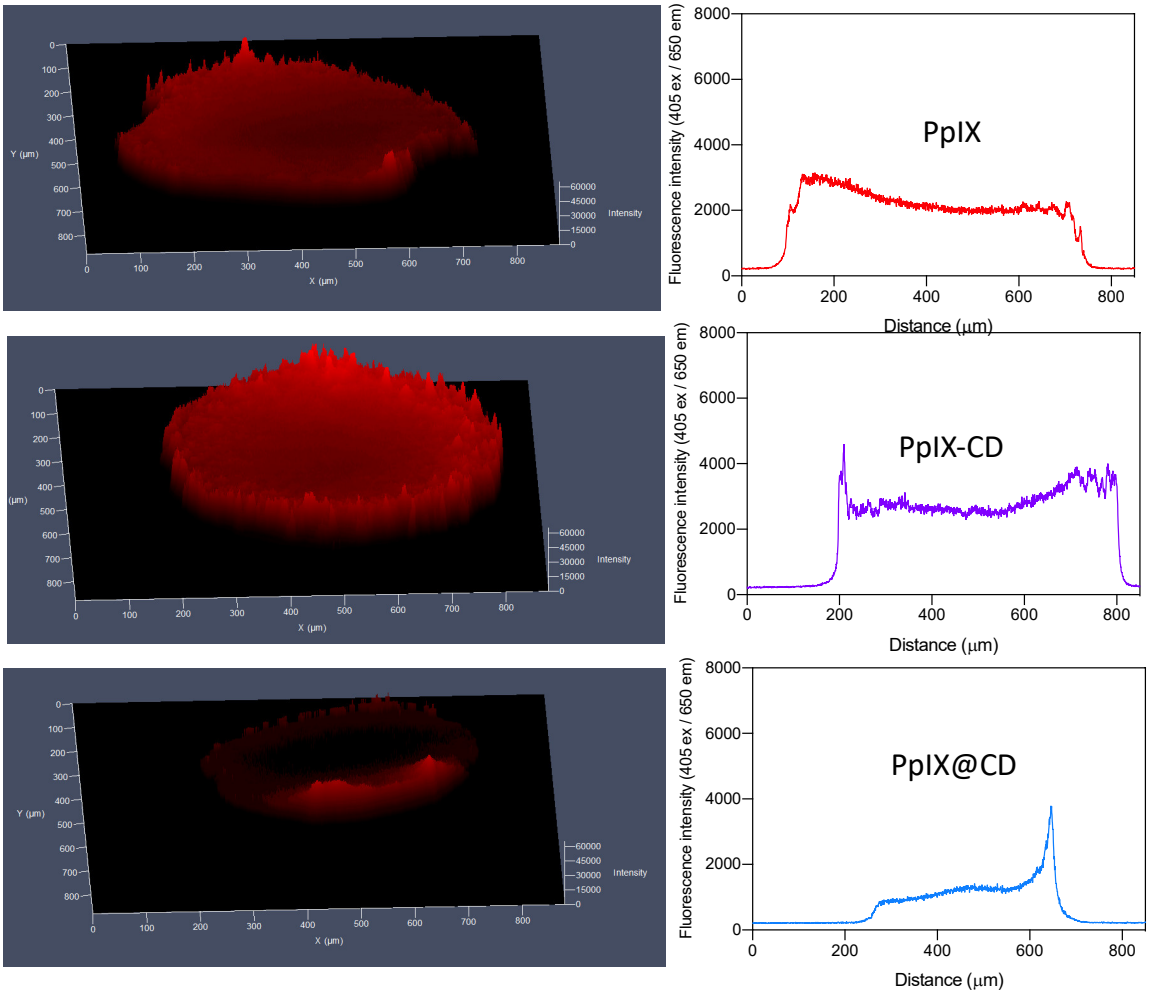

Fig. 4.18 – Conjugate uptake in spheroids at 5 µg/ml Drug uptake and signal emission are significantly improved after increasing dose to 5 µg/ml. PpIX@CD shows signs of aggregation or quenching.

This behaviour continued as conjugate concentration increased to 10 µg/ml. PpIX-CD continued to show significantly higher PpIX accumulation, with approximately 31% more drug in comparison to the control at equal nanoparticle concentrations (Fig. 4.19). Interestingly, PpIX-CD shows increased accumulation within the spheroid core at around 150 – 200 µm depth while PpIX shows a steady decrease after the initial 50 µm. PpIX@CD showed an even greater decline in PpIX uptake, with only around 37% accumulation of the PpIX control. Spheroids showed an initial high uptake until ~50 µm, after which it steadily dropped.

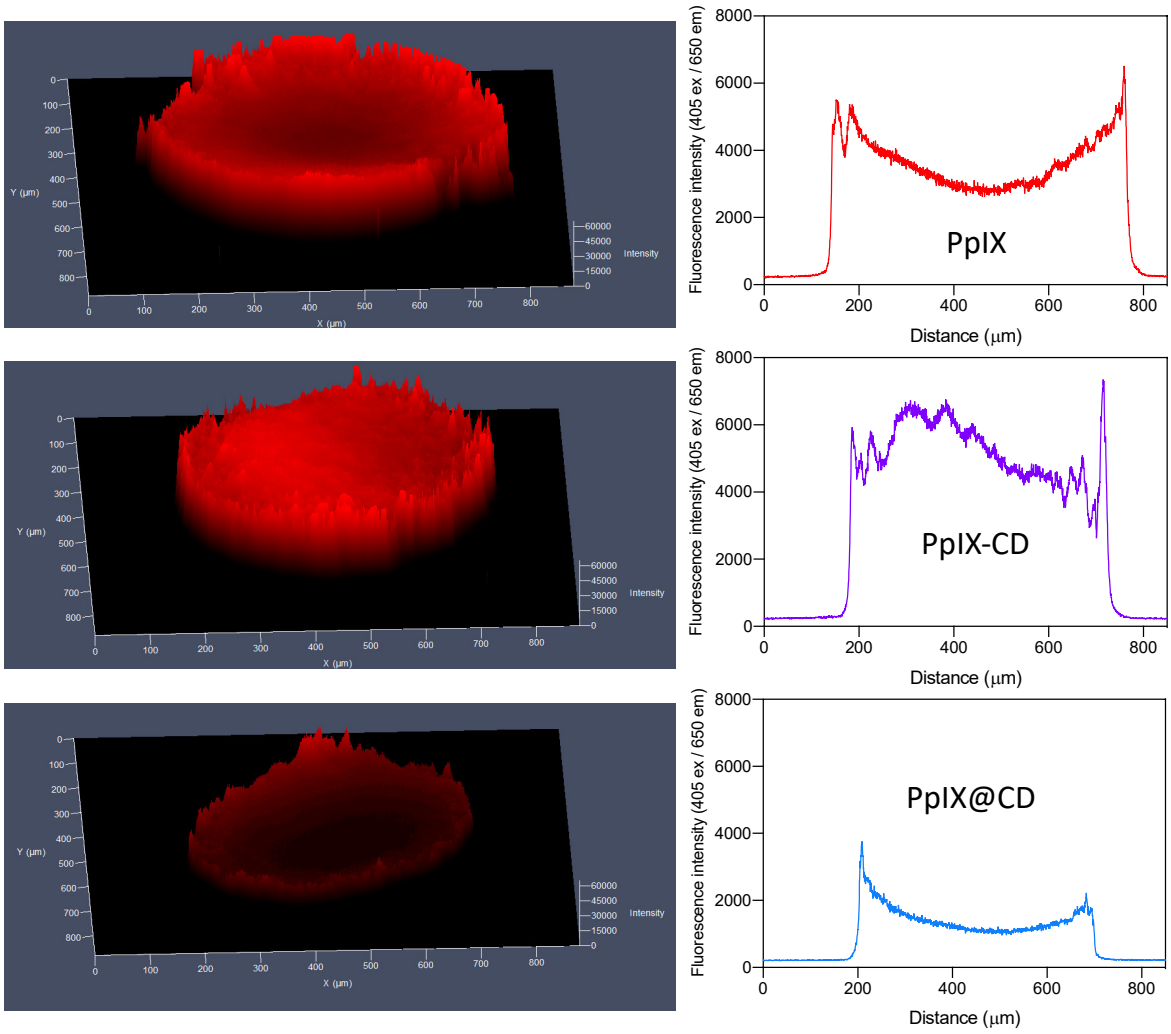

Fig. 4.18 – Conjugate uptake in spheroids at 10 µg/ml. PpIX-based emissions with 10 µg/ml show drug uptake throughout the spheroid diameter and within the hypoxic core.

The fluorescence intensity found from PpIX and PpIX-CD was very similar at all concentrations while PpIX@CD reached a maximum around 5 µg/ml. In comparison, PpIX@CD showed a significant difference in fluorescence over 5 µg/ml. Nonetheless, it is also possible that PpIX@CD suffers from self-quenching, as previously detailed in Chapter 3. The embedding of PpIX on its surface can both obstruct surface traps (CD fluorescence) and limit PpIX fluorescence.

Live/dead staining shows spatially directed PDT damage in spheroids

The observation of PDT-induced damage to spheroids is difficult due to their growth conditions. Spheroids rest within the bottom of a 96-well plate with agar, which aids in the formation of spherical aggregates. Typically, light microscopy (LM) or fluorescence microscopy used to observe spheroids, especially in high-throughput screening as they are fast, reliable, and inexpensive. Imaging shows treated spheroids have reduced size and slightly irregular morphology, but generally keep their roundness regardless of light treatment as shown previously. However, only inverted microscopes can observe the bottom of the plates – spheroids would lose sterility if the cover is removed and the focal length is inadequate as the objective cannot approach samples.

In comparison, light sheet fluorescence microscopy (LSFM) can be used to observe the 3D structure of samples. Samples are placed within a glass capillary and embedded in agarose, which allows the equipment to rotate spheroids along the X axis. Imaging of spheroids can reveal more information about physical changes to their structure after PDT (Fig. 4.20). LSFM of PDT-treated spheroids can be improved by live/dead staining to observe damage at various time points. This stain uses two components to differentiate between live (calcein AM, green) and dead (ethidium homodimer-1, red). Calcein AM is a cell-permeant compound that is transformed into the fluorescent calcein after uptake, showing a characteristic green colour, while ethidium homodimer-1 is cell-impermeant, emitting red fluorescence after binding to DNA.

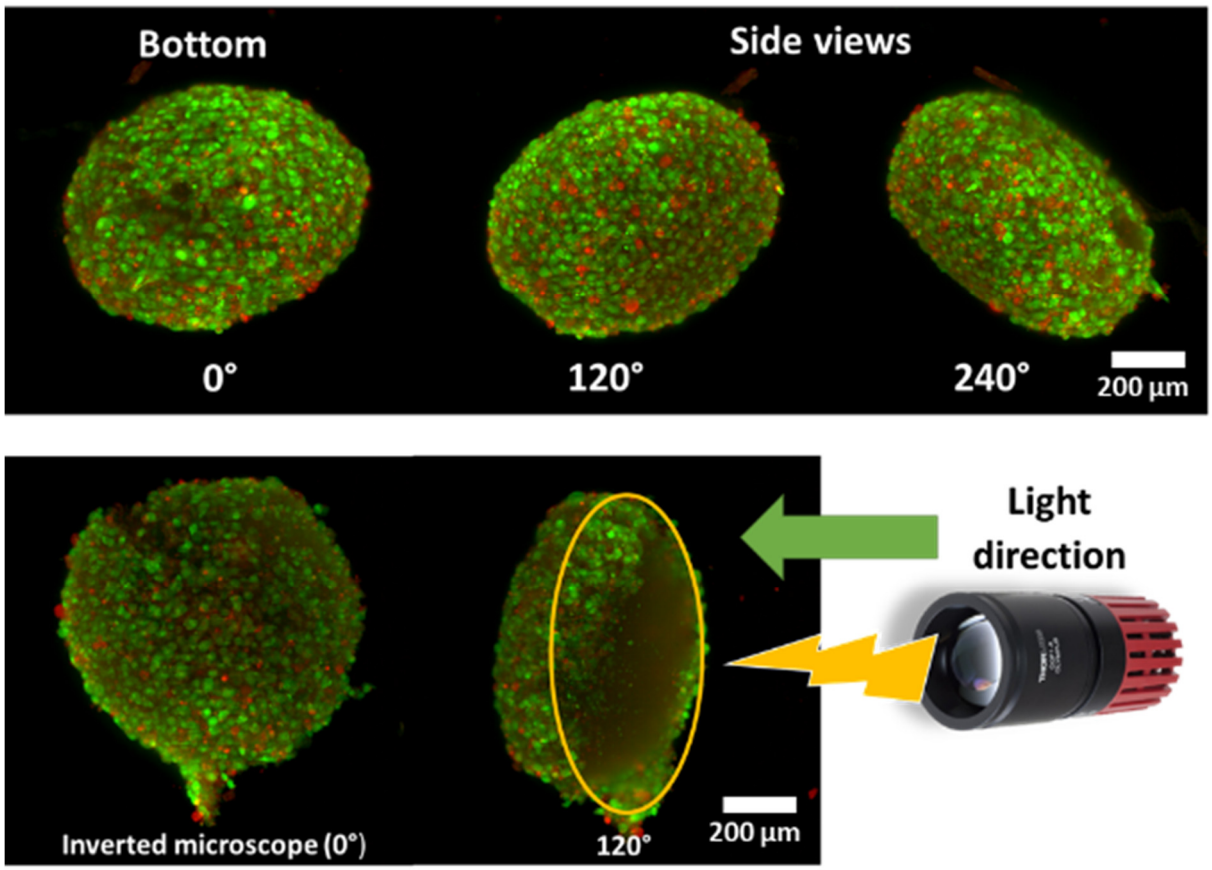

Fig. 4.20 – Sample rotation within LSFM permits more detailed evaluation of spheroid morphology. Live (green) and dead(red) cells can be seen throughout the spheroid at all angles (top). PDT damage can be seen in some samples, with spheroids showing sloughing and loss of sphericity after treatment (bottom). Image at 0° corresponds to the point of view seen with light microscopy.

The distribution of live/dead cells within MCTS was observed using LSFM. Spheroids were washed to remove cellular debris, fixed, and stained 24 and 48 hours after delivering final light dose. While spheroid morphology appeared to remain intact from initial viewing angles, with some irregularities being apparent on their surface. Changes in viewing angles demonstrate the extent of PDT-induced damage. A test was done using a small quantity of Tris-EDTA buffer to induce cell lysis within the sample chamber. After 30 minutes of incubation, a weak signal was obtained from the red channel, corresponding to ethidium homodimer-1 entering the nuclei of dead cells, seen in Fig. 4.21. Spheroids did not show significant changes in morphology.

While it is possible to use LSFM to image live samples, image quality differed between spheroids. Live imaging was not used for further work and fixed samples were obtained for all timepoints.

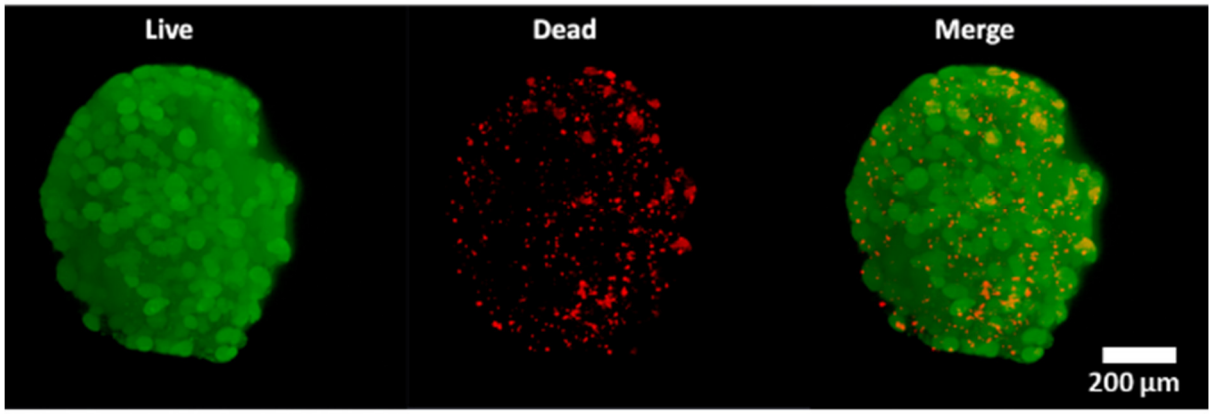

Fig. 4.21 – Live LSFM imaging of spheroid treated with lysis buffer. Images were separated by channel (calcein-AM, ethidium homodimer-1, and the merged image).

Images were obtained from three separate angles to observe morphology after PDT with 5 J/cm^2, which was a light dose which produced significant damage to spheroids while reducing time spent outside the incubator. Drug doses (1 – 10 µg/ml) and fractionated light exposures (1LT and 2LT) were left unchanged from the previous methodology. An additional light treatment (3LT) was added to observe continuous light activation and spheroid response to PpIX-triggered sensitization to PDT [363]. Samples using 1 µg/ml did not show significant changes to roundness, with only small sections being affected, regardless of light dose. Nonetheless, sample rotation revealed changes in spheroid thickness, which was reduced from ~450 µm to ~400 µm as a result of PDT-induced cell death.

PDT with a concentration of 5 µg/ml significantly increased damage to spheroids and caused disruption in their spherical shape, shown in Fig. 4.22. PpIX and PpIX-CD show damage throughout the spheroid surface, appearing as large grooves that run across its diameter and missing sections corresponding to the area which was in contact by light. The core area of all

spheroids showed a high number of dead cells, which corresponds to the hypoxic region formed during initial growth and compaction. Spheroid shape was also influenced by sample manipulation during fixing and mounting: samples frequently needed to be swapped as too much force caused the spheroid to begin falling apart.

In comparison, spheroids treated with 10 μg/ml show more pronounced damage and a similar loss of shape and roundness, as can be seen in Fig. 4.23. However, it should be noted that not all spheroids within the same conditions show the same degree of damage. This is likely because of the variability within groups, which is present even with close monitoring of spheroid growth kinetics and preselection of suitable spheroids prior to drug uptake. Das et al. (2016) determined that these variations occur in part due to edge effects from uneven agarose surfaces within individual wells and evaporation-induced liquid media loss at the plate periphery [364]. Nonetheless, spheroid morphology cannot be completely observed through widefield microscopy. The structural changes that spheroids undergo after PDT suggest that low-fluence PDT is capable of tumour ablation at nontoxic PS doses.

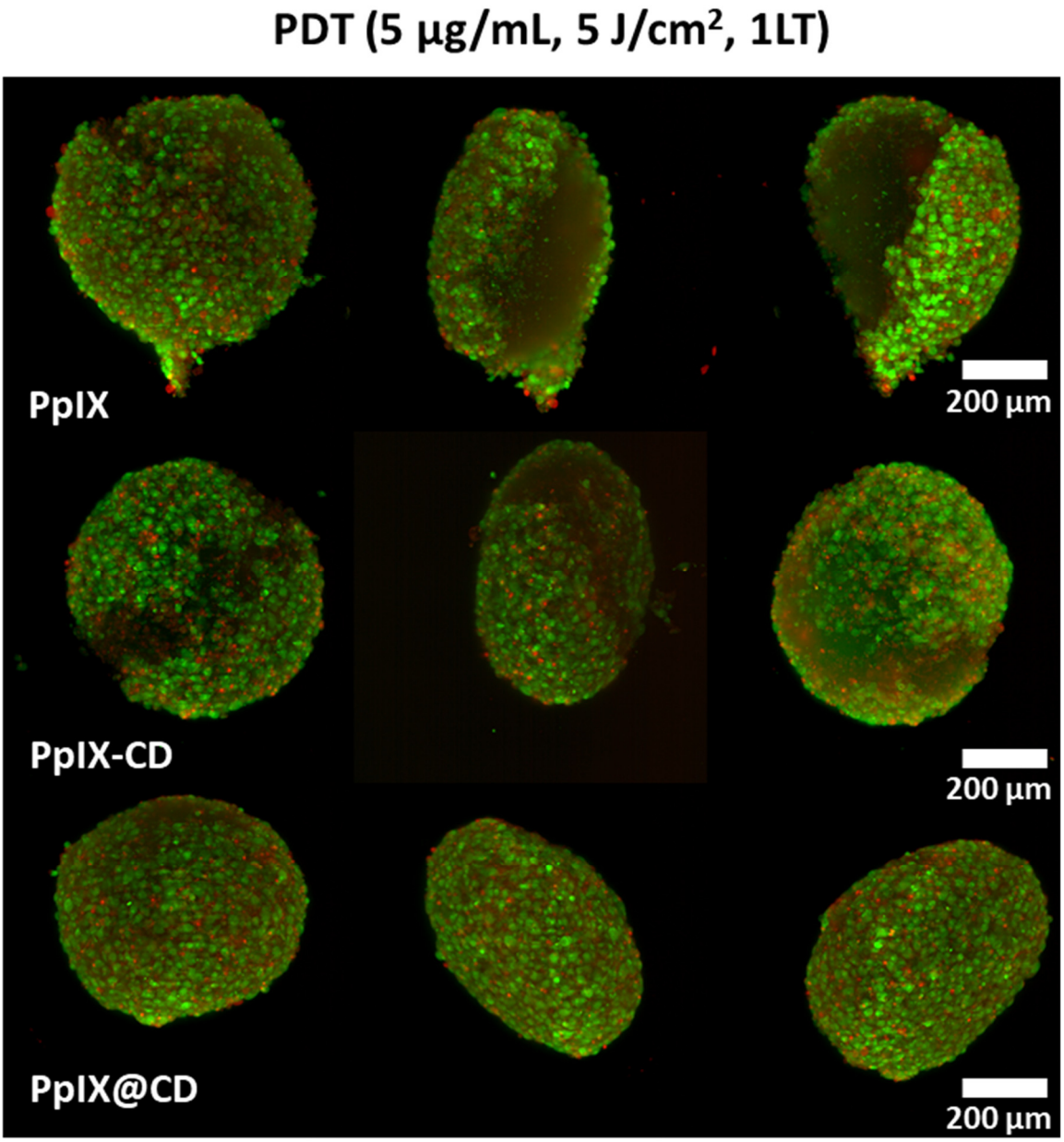

Fig. 4.22 – Spheroids show directional ablation after PDT. Post-PDT morphology varies according to viewing angle, with parts of spheroids becoming ablated due to significant cell death.

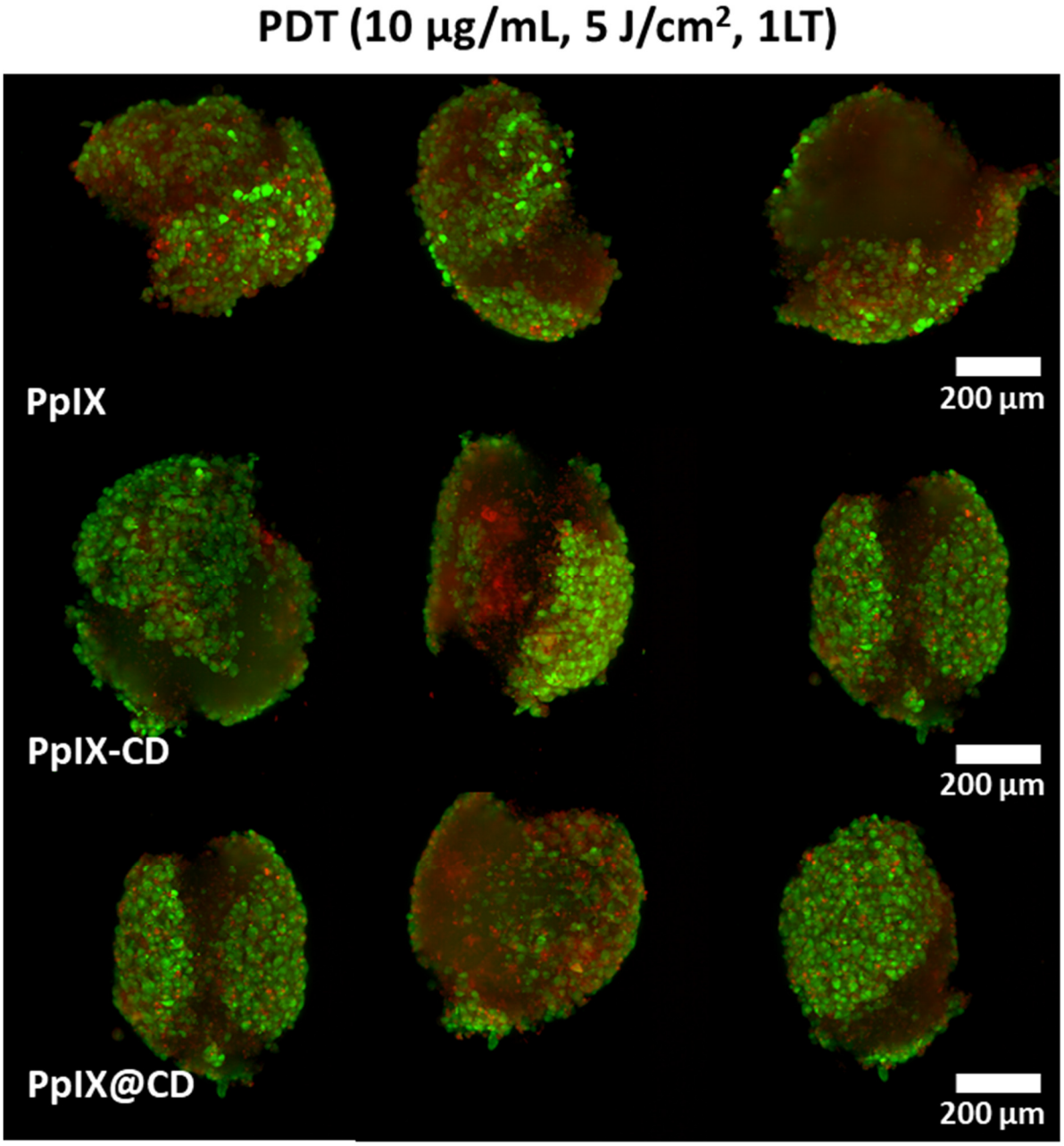

Fig. 4.23 – Drug dose increases damage to spheroids. Increased drug doses destabilise spheroid morphology and cause ongoing cell death after 24 hours of PDT.

Light fractionation caused significant damage after 48 hrs

Spheroids treated with 2LT showed a much more pronounced reduction in size and higher degree of cell death than those with 1LT. This was expected as both LDH release and DNA content indicate lower sample viability with repeat light exposure. Prolonged damage to spheroids was also observed in all conditions, reflecting results found previously, where toxicity reduced spheroid viability for up to 72 hours after PDT, shown in Fig. 4.23. This is likely caused by the aforementioned mechanism of PpIX-induced cell death, which promotes apoptosis through the activation of the p53 pathway [312].

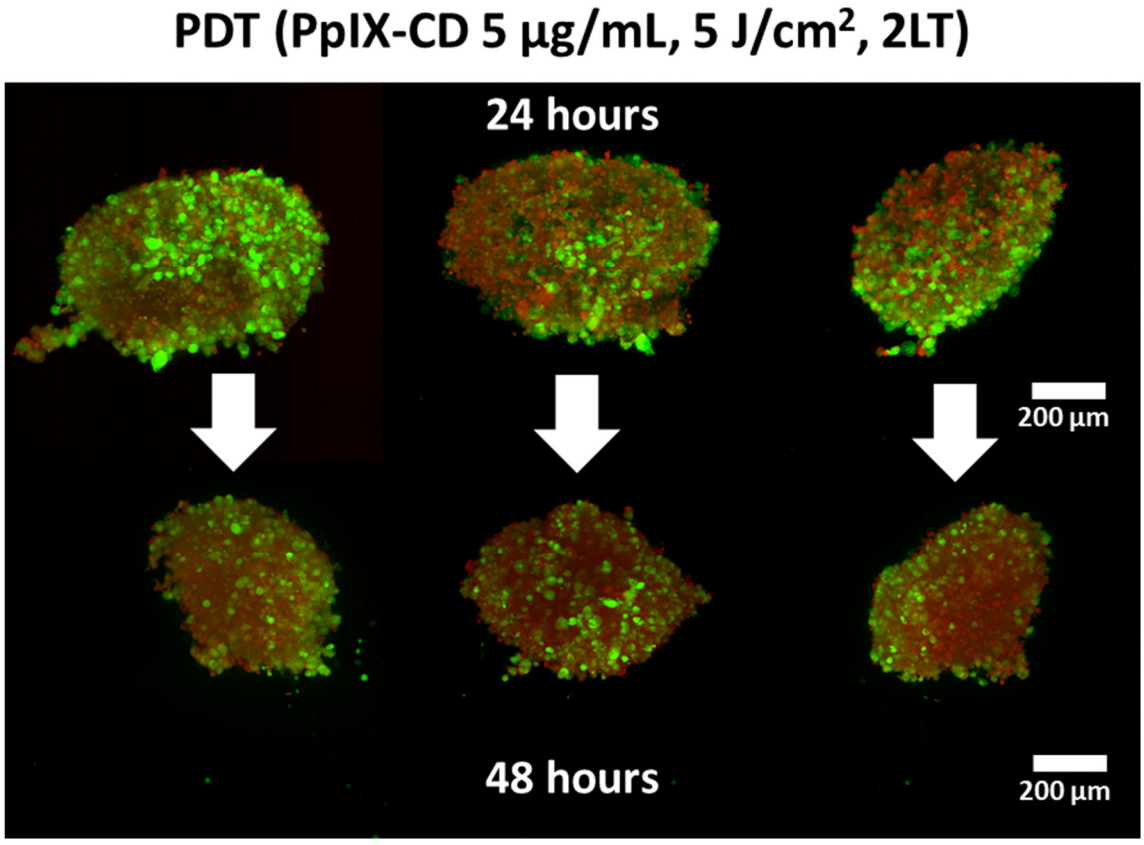

Fig. 4.23 – Spheroids showed prolonged response to phototoxicity. Continuous cell death could be observed up to 48 hours after the final light treatment. Initial damage was similar to that found in 1LT (top) and continued to reduce spheroid size while increasing cell death (bottom).

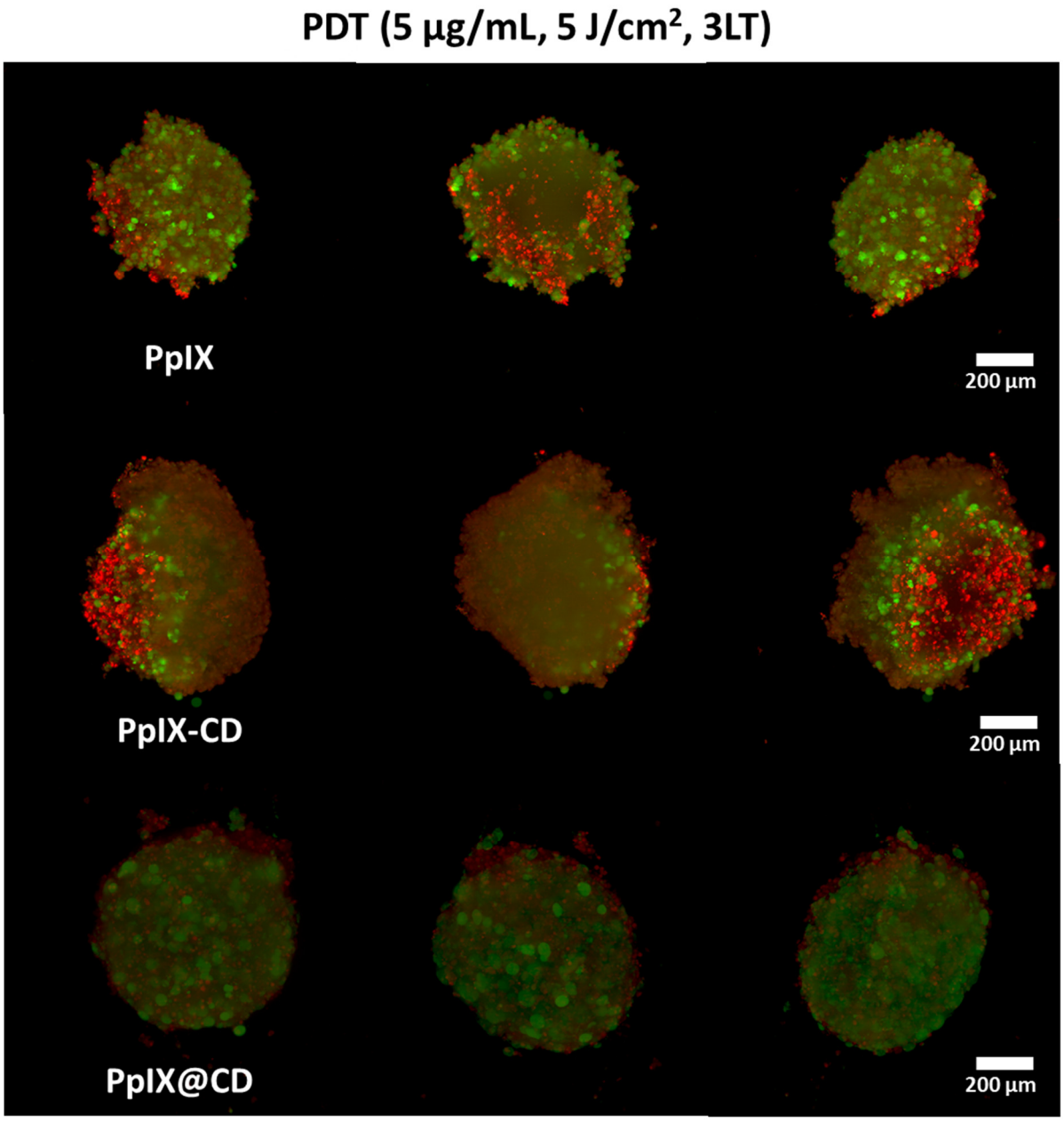

Fig. 4.24 – 3LT causes significant PDT damage compared to 1LT and 2LT. Live imaging of 3LT PDT (24 hrs) shows significantly increased cell death and localised damage on the top section of the spheroid. Outer layers begin to detach after sequential light treatments.

As expected, 3LT showed a significant increase in spheroid damage as can be seen in Fig. 24. However, the PDT effect was not as consistent as with previous conditions (Fig. 4.24). While some spheroids suffered complete disruption and were unable to be imaged, others retained their morphology and showed similar morphology to that seen with 2LT (5 or 10 μg). However, the dead or damaged cells on the top section of spheroids were much more prominent in spheroids treated with PpIX-CD in comparison to PpIX and PpIX@CD.

In summary, LSFM was used to observe the morphology of PDT-treated spheroids, showing varied morphological changes occurred after light activation. Spheroid thickness was consistently reduced with all samples and concentration, though differential drug uptake may cause variation between samples with identical treatment conditions. Live imaging was also used to observe *in situ* PDT damage without compromising spheroid viability.

Scanning electron microscopy (SEM)

SEM imaging has been previously used to observe fine details in spheroid morphology. The surface roughness can indicate the amount of produced extracellular matrix [365]. It can also be used to observe cell-cell interactions and growth progression with higher magnifications. Most importantly, the surface morphology can be used to observe morphological changes which are not immediately apparent with LM. However, it requires the use of glutaraldehyde or formaldehyde fixing and immersion in osmium tetroxide before samples can be successfully imaged.

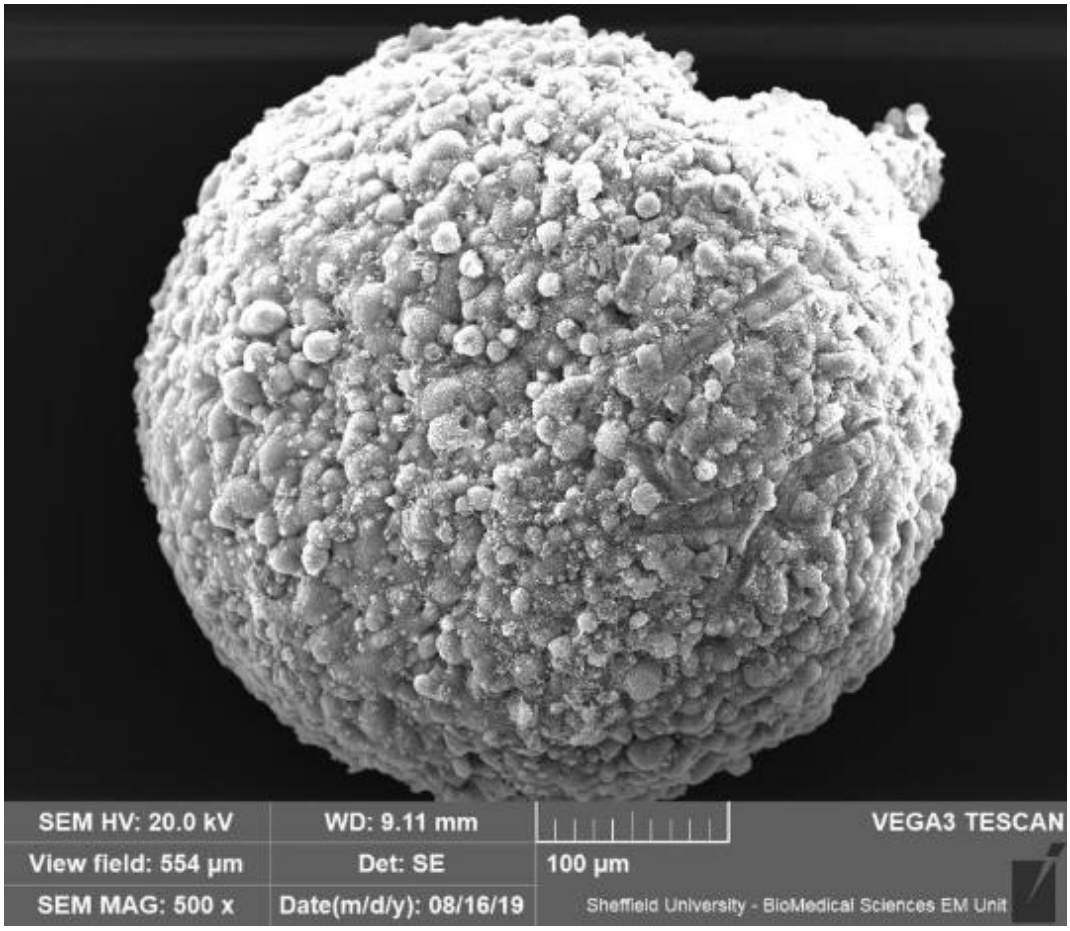

Fig. 4.25 – Standard C8161 melanoma spheroid imaged using SEM. Slight damage visible in the top right corner due to manipulation during fixation.

Control spheroids show a clear round morphology which is reminiscent of images obtained with LM, seen in Fig. 4.25. However, PDT-treated spheroids show key differences as ablation deforms spheroid morphology (Fig. 4.26). The outer layers of spheroids appear to have been sloughed off due to extensive cell death and have not been reformed after 48 hours post light exposure. This shedding of layers has been previously observed in spheroids which have passed their stationary phase as a sign of entering their death phase [366]. In summary, the combination of LSFM and SEM was used to observe subtle changes in spheroid morphology, which is summarised in Fig. 4.27.

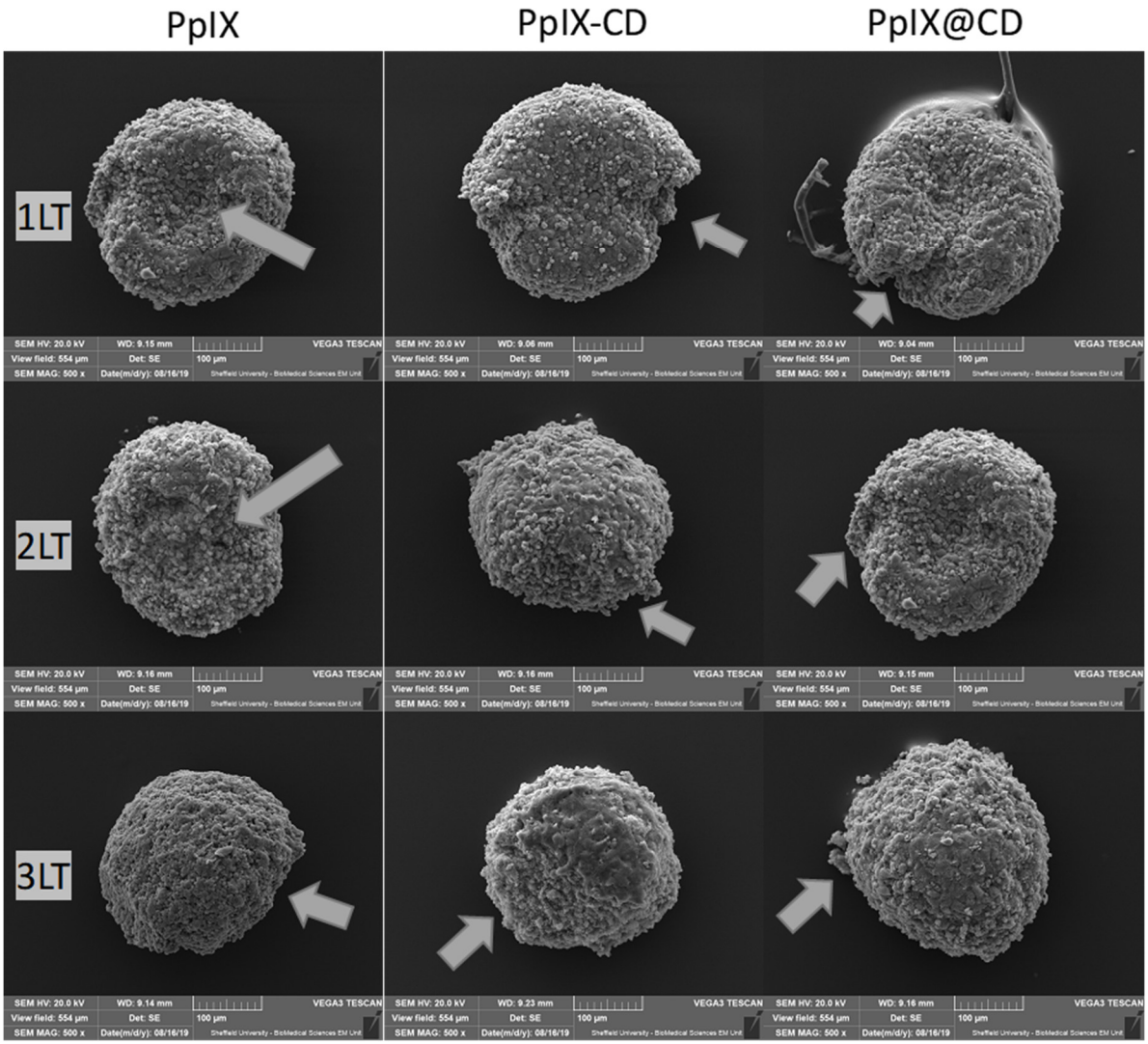

Fig. 4.26 – PDT-induced damage is visible using SEM. In comparison to the previously shown untreated spheroid (Fig. 4.25), treated spheroids show a significantly reduced size and loss of sphericity. PDT caused sloughing of outer layers as damage increased due to fractionated light treatments, indicated with arrows for all samples.

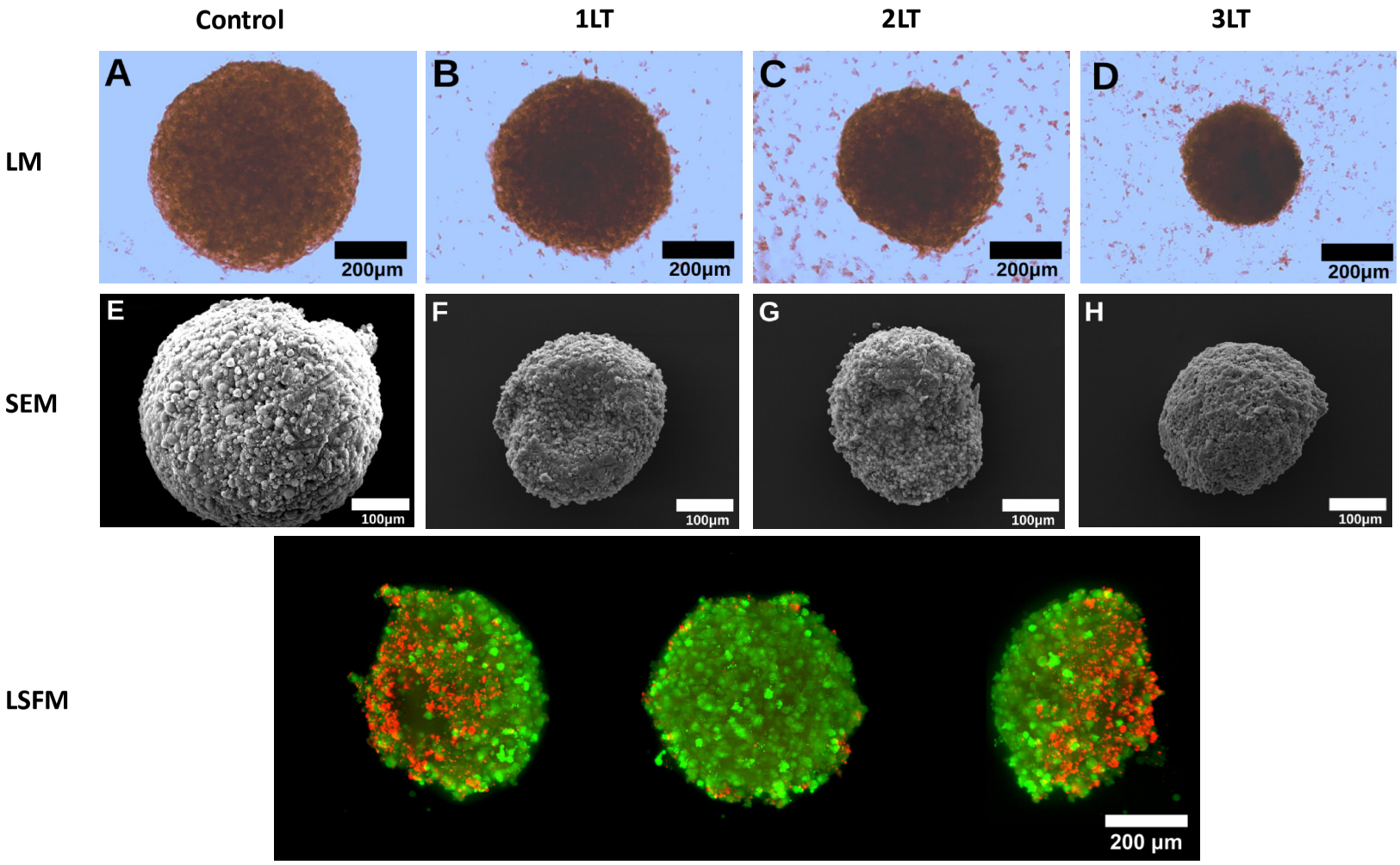

Fig. 4.27 – Cancer spheroid microscopy for evaluating PDT damage. Fractionated light treatments significantly alter spheroid morphology, greatly reducing their size.

Conclusion

Currently, the gold standard for cancer drug testing is the *in vivo* tumour xenograft mouse model. Cell line and patient-derived xenografts have been shown to accurately replicate tumour morphophysiological characteristics. However, the use of animal models is not suitable for exploring the effect of individual treatment parameters due to their intrinsic complexity. Furthermore, large-scale screening experiments are costly, time-consuming, and face issues with ethical concerns.

In this study, a total of 18 combinations of different PDT parameters (drug concentration, fluence, and light fractionation) were tested with PpIX, PpIX-CD, and PpIX@CD, totalling 54 combinations. These treatment conditions were evaluated using two different assays to determine viability after PDT (LDH release and dsDNA quantification) and monitored at 3 time points (24, 48, and 72 hours post-PDT). This led to the pre-screening of unsuccessful PDT conditions such as 1 μg/ml drug doses or 1LT, which would not have been apparent with only 2D cell culture. Furthermore, light sheet microscopy was used to obtain information regarding drug penetration into spheroids, with PpIX and PpIX-CD showing higher uptake compared to PpIX@CD. Spheroid morphology was also shown to be irregular due to varying response to PDT-induced damage resulting in the shedding of the outer proliferating cell layer.

In conclusion, PDT parameter pre-screening was able to rule out multiple conditions previously thought to be successful with cell monolayers. The results presented here highlight the importance for custom models tailored for PDT. As research continues, high-throughput analysis of experimental conditions will be needed in order to adequately assess the efficiency of novel PDT agents such as CD-based conjugates.

Chapter 5 – Automated parameter acquisition and comparison to metabolic activity data

Introduction

3D cell culture models can replicate *in vivo* conditions such as hypoxia, dormancy, and cell-cell interactions more accurately than 2D models. In the previous chapter, spheroids were shown to be a better screening tool for optimising PDT parameters. However, this model is highly variable, being affected by parameters such as partial oxygen pressure, compactness, diffusion, and nutrient gradients [367]. In some cases, conventional methods for evaluating 2D cell cultures have been shown to be unsuitable for 3D cell cultures, further increasing variability [368]. This has caused some to question the validity and reproducibility of acquired data. Thus, there is a lack of standardized, easily accessible methods to provide quantification of drug-responsiveness tailored for use with MCTS [369]. Moving forward, this may place limitations for the extended use of spheroids; there is a special interest in high-content screening, where thousands of chemical compounds are tested with standardized conditions.

Spheroid morphology has been found to be a key parameter in experimental standardisation, ensuring other factors like microenvironment to be more similar between samples. These morphological parameters (i.e. diameter, volume, sphericity, etc.) can be obtained through imaging with various types of microscopy, such as light, fluorescence, and light sheet microscopies [370]. They can then be used to observe variations in growth kinetics, improving experimental reproducibility [335]. Image-processing software such as AnaSP (open-source) or ImageXpress Micro XLS (proprietary) can also be utilised to automatically process multiple image sets simultaneously, allowing users to quickly obtain data regarding spheroid variability prior to starting experiments [371].

Furthermore, the same morphological parameters have been shown to be related to drug-responsiveness. Thakuri et al. (2019) demonstrated that size-based analysis closely matched traditional assay-based analysis in evaluating drug responsiveness. They also observed that spheroid growth could be linked to resazurin reduction [372]. A similar trend was also observed by Ivanov et al. (2014) with the acid phosphatase assay, though it can only be performed as an endpoint assay due to requiring cell lysis [373]. However, there has not been any attempt to determine correlation between drug response and spheroid morphology using assays such as LDH release and DNA quantification.

As previously mentioned, most software is centred on high-throughput screening, which relies on costly automated equipment, limiting its use by non-specialised users. The development of open-source alternatives is a key step in the introduction of reliable computer-assisted image analysis to researchers working with MCTS. Piccinini (2015) developed a MATLAB-based suite for analysing various spheroid parameters: AnaSP (ANAlyse SPheroids) [371]. Likewise, the visualization and estimation of spheroid volume has seen advances and has been shown to be possible to recreate based on a projection from a 2D image using ReViSP (Reconstruction and Visualization from a Single Projection) [374]. In comparison to other methods of volume assessment, reconstruction from a simple light microscopy image is less labour and time intensive.

In this chapter, MCTS morphological parameters with LDH release and DNA content will be compared to determine a possible correlation. Furthermore, the use of automated image analysis for improving MCTS-based models for PDT-induced toxicity will be discussed.

Aim: Demonstrate a link between spheroid morphometric parameters and PDT-induced cell death in previously evaluated treatment combinations.

Objectives:

- Reduce spheroid variability in groups by pre-screening samples based on morphology.
- Select best morphometric parameters to differentiate between damage and control spheroids.
- Investigate the relationship between morphometric parameters and previously obtained biological assay data.
- Evaluate the effect of triple light fractionation (3LT) on spheroid morphology.

Experimental

Materials

Materials used for spheroid culture, LDH assay, Picogreen DNA quantification, live/dead staining, and microscopy were identical to those previously mentioned in Chapter 5.

Automated parameter acquisition

Images were obtained using an AE2000 inverted light microscope (Motic, United States) fitted with a Moticam 2.0 camera with a 4× objective. Images were obtained before and after clearing cellular debris from each well. White balance was used increase spheroid contrast against the background. AnaSP version 1.2 (https://sourceforge.net/projects/anasp/) was downloaded from the source webpage. The scripts were loaded onto MATLAB R2019b (Version 9.7) with Image Processing Toolbox. Spheroid images were only utilised in data analysis if image segmentation was performed automatically. The standard morphological parameters were extracted: Area, Convexity, Equivalent Diameter, Length of Major Diameter Through Centroid, Length of Minor Diameter Through Centroid, Perimeter, Solidity, Sphericity, and Volume.

Statistical analysis

Experiments carried out with three independent repeats in triplicates (N=3, n=6) and results were normalized using untreated controls. Statistical analysis was carried out using GraphPad Prism version 8.3.0. A normality test was performed on each data set to confirm the use of ANOVA. The comparison of metabolic activity was evaluated by 2-way ANOVA analysis with Dunnett's test for multiple comparisons, with adjusted P values < 0.05 were considered statistically significant. Data was presented as means ± SD (standard deviation). Charts include symbols representing adjusted P values, which are shown below.

Table 5.1 – List of symbols used to represent statistical significance.

P value	***Symbol***
>0.05	ns (non-significant)
<0.05	*
<0.01	**
<0.001	***
<0.0001	****

Results and Discussion

3LT was added to PDT evaluation

Spheroids were grown as previously described in Chapter 5, using agar-coated 96-well plates to prevent cell adhesion. PDT was carried out using PpIX and PpIX-CD based on results obtained in the previous chapter. Drug concentration was adjusted to >5 μg/ml and 5 J/cm^2. This was based on the previously observed drug response and subsequent reduction in spheroid viability with all samples in these conditions. An additional 3-step light dose was performed in addition to 1LT and 2LT. Fig. 5.1 shows the workflow for a typical spheroid PDT experiment with automated parameter acquisition.

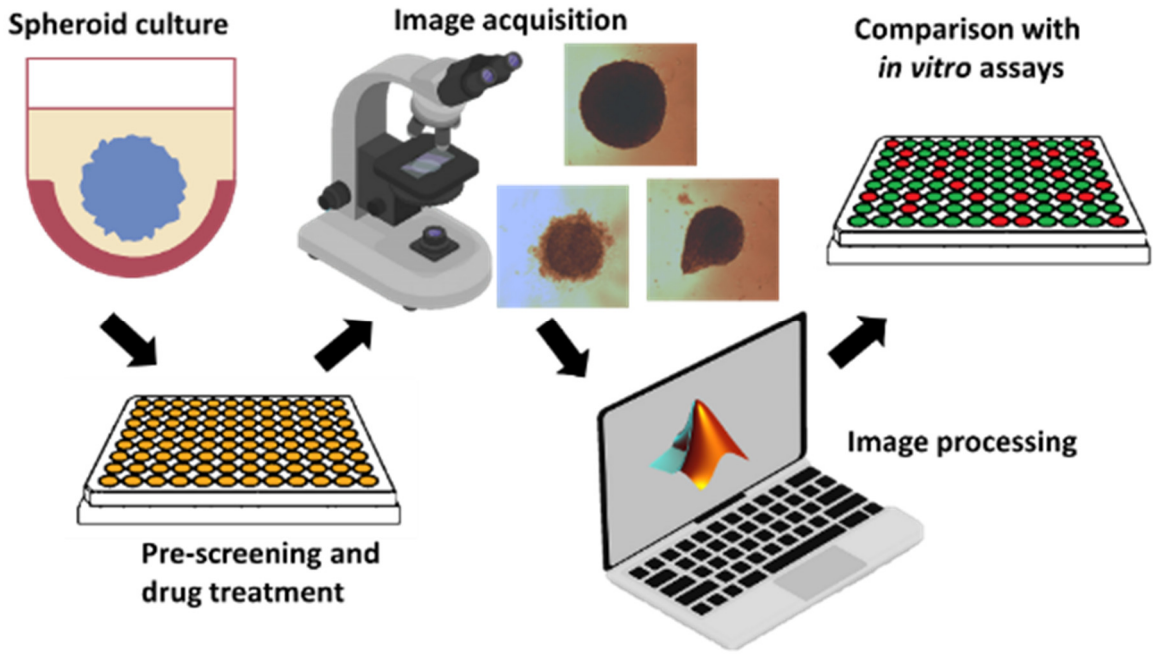

Fig. 5.1 – Automated parameter acquisition using multicellular tumour spheroids. Spheroids were cultured, pre-screened, and treated with various PDT combinations. Image acquisition was done using widefield microscopy and automatic segmentation with AnaSP led to parameter extraction. Finally, morphometric parameters were compared with *in vitro* assays.

Automatic image processing and parameter acquisition with AnaSP

The open-source software AnaSP can extract morphological parameters from spheroids by pre-processing suitable images and identifying the area of interest based on histogram intensity and automatic triangle segmentation. There are several parameters that are calculated by default, which are listed below in Table 5.2. Although new parameters can be programmed, it was determined that predetermined values were enough for analysis.

Table 5.2. List of morphological parameters extracted from multicellular tumour spheroids using AnaSP.

Parameter	Explanation
Area (*A)*	Total number of pixels in foreground
Volume (*V*)	Volume estimated from segmented image projection (ReViSP) [374]
LMajorDTC	Maximum length of axis through centre of spheroid mass
LMinorDTC	Minimum length of axis through centre of spheroid mass
Convexity	Degree of spheroid curvature
Equivalent Diameter	Diameter corresponding to a circle with equivalent area
Perimeter (*P*)	Total number of pixels in outer border
Solidity	Degree of spheroid compaction after growth (Area/Convexity*Area)
Sphericity	Degree of similitude to a perfect sphere (1 = perfect sphere)

Modification to AnaSP workflow due to image processing errors

Initially, AnaSP was unable to convert images to binary format: this process changes colour values to binary values. Instead, image pre-processing returned greyscale images, which were not able to be successfully segmented. It is unclear what caused this issue as the command for binary image conversion was correct in the source files. In order to continue with automatic segmentation, an extra step was introduced to obtain binary images. The following script was run within the folder containing the images (Input) and converted images were manually moved to the "mask" folder:

```
% Run START SEGMENTATION
% This script will convert .jpg "mask" images to true binary in .tif format
% Change Spheroid to image filename in Output folder
% Script has to be in the same folder as masks in order to work
% Must move images from Output folder to Mask folder
% Run DATA EXTRACTION after moving images and selecting new folder
file_name='1';
im=imread([file_name '.jpg']);
im2=im2bw(im); %#ok<IM2BW>
imwrite(im2,[file_name '.tif'])
```

Early variations in spheroid growth significantly change morphology

Spheroid morphology was monitored throughout their initial growth period to determine differences between samples before undergoing PDT. In general, high sphericity (how close an object approximates a perfect sphere) is a desirable parameter for pre-screening spheroids. Diffusion kinetics of nutrients, oxygen, and drugs within spheroids are significantly changed by both shape and cell compaction, with irregular/elongated shapes being generally undesirable [375]. Furthermore, oxygen consumption drastically changes as cells begin compacting, resulting in an approximately 8-fold increase as spheroid size stabilizes. In turn, this increases the size of the hypoxic zone, a key factor of *in vivo* tumour microenvironments. Leung et al. (2014) determined sphericity and compactness are highly linked to a uniform solute gradient within MCTS [376]. Therefore, the evaluation of PDT response and parameter screening

should be performed with samples presenting low variation in morphology, with sphericity being closely monitored as the main parameter for selection, as shown in Fig. 5.2.

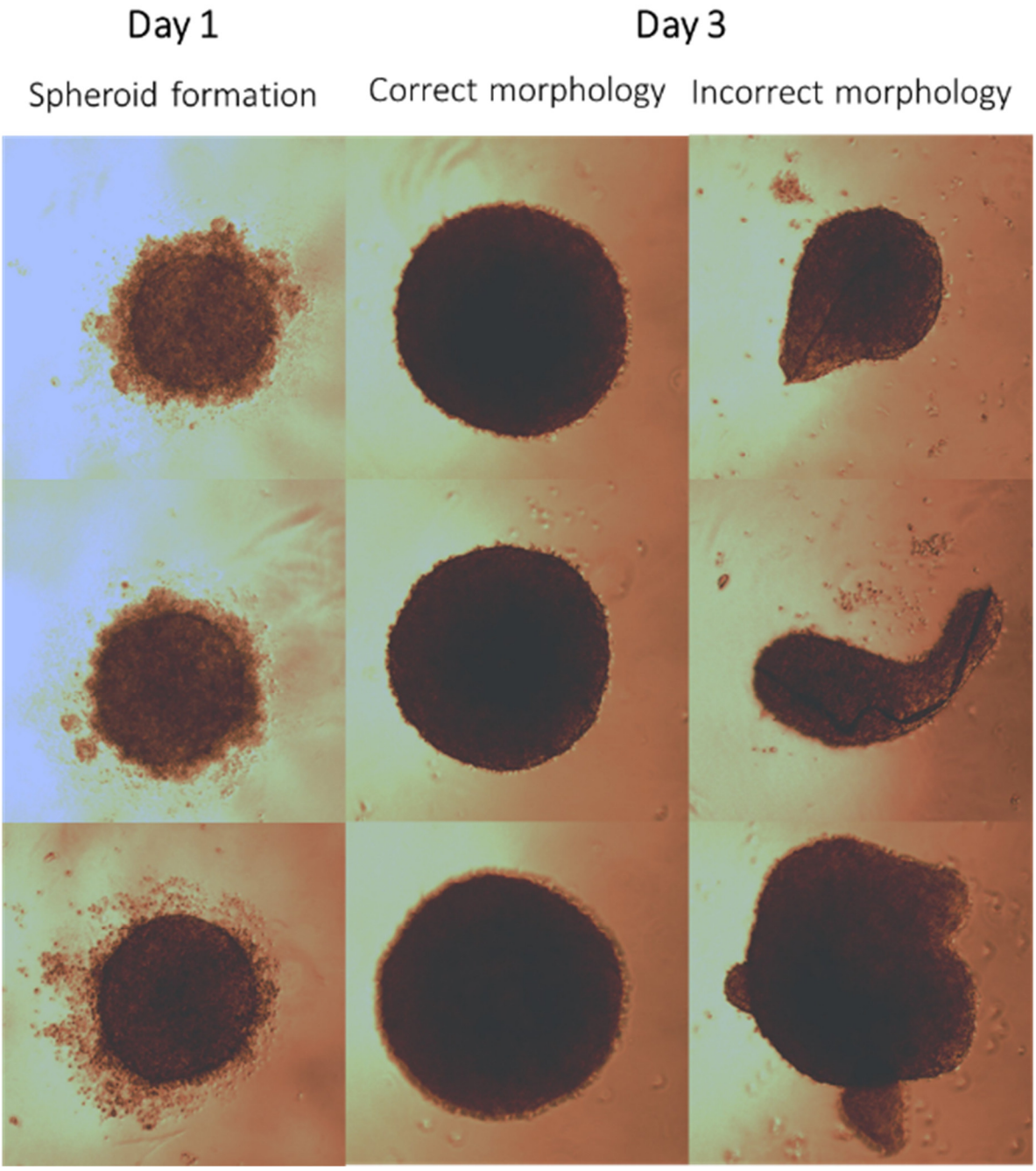

Fig. 5.2 – Spheroid growth and morphology depends on agarose coating quality. Spheroids initially may show irregular morphology as cells begin to aggregate in Day 1. Steady growth eventually leads to a more spherical shape with no irregularities by Day 3. Defects in the agarose coating or incubation conditions led to irregular morphology.

Automatic segmentation versus manual (freehand) segmentation

Image pre-processing is an essential step in parameter acquisition as it influences all obtained data. Manual segmentation done through free-hand drawing using a stylus or mouse cursor can be attempted instead of the automatic segmentation, though results are significantly different. Fig. 5.3. shows a comparison between manual and automatic image processing and its impact on extracted parameters. Initially, parameters like sphericity and convexity appear to increase in manual segmentation, which conflicts with the reduction of other data with manual segmentation. However, this is caused by the lack of jagged edges seen in the automatic processing that cannot be replicated with freehand contouring. In contrast, the parameters area (-28.25%), perimeter (-30.95%), and volume (-39.87%) were reduced by as a result of imprecise outlines. Furthermore, the use of manually segmented spheroids within experiments increased variability within groups. Therefore, only automatically segmented images were used in analysis.

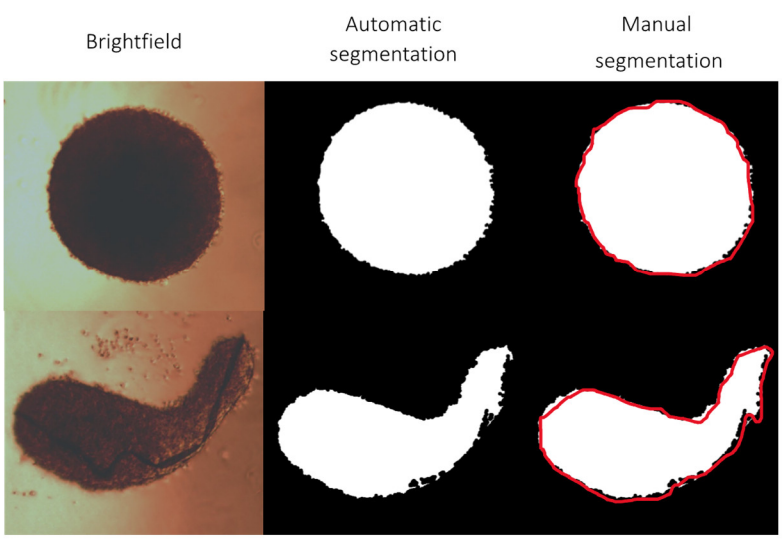

Segmentation	%Change (Manual to Automatic)
Area	- 28.25
Convexity	13.92
Eq. Diameter	15.13
LMajorDTC	14.70
LMinorDTC	15.91
Perimeter	- 30.95
Solidity	4.51
Sphericity	- 17.69
Volume	- 39.87

Fig. 5.3 – Automatic segmentation reduces variability during image pre-processing. Manual segmentation results for area, perimeter, and volume showed high variation after multiple segmentation attempts with the same image.

Parameter extraction requires clearer images to avoid errors

As previously mentioned, PDT-induced cell death could be observed by the formation of a debris halo surrounding each spheroid. In addition to possible variability in biological assays, the presence of this cellular debris significantly impacts parameter acquisition as segmentation does not adequately detect spheroid contours. This was confirmed after comparing acquired images from spheroids after PDT (2.5 μg/ml PpIX, 5 J/cm^2, 1LT) before and after debris removal (Fig. 5.4). Parameters based on spheroid sphericity showed an increase of approximately 32-59%, while those based on area were reduced by over 27-46%. Additionally, automatic segmentation in AnaSP did not produce consistent image outputs for extraction as debris was counted as part of the main spheroid mass. Therefore, clearing cell debris is a crucial step in successful parameter acquisition.

Parameter	% Change (Before vs after removal)
Area	-46.51
Convexity	32.62
EquivalentDiameter	-25.57
LMajorDTC	-56.21
LMinorDTC	-36.78
Perimeter	-34.57
Solidity	45.31
Sphericity	59.22
Volume	-27.57

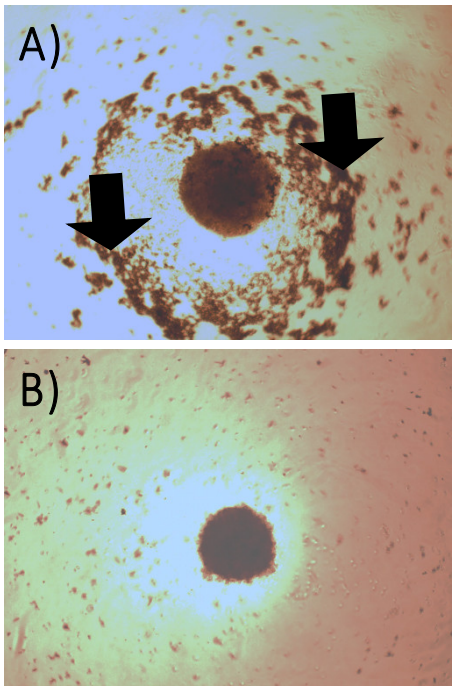

Fig. 5.4 – Parameter extraction improves as debris is cleared from the well. Automatic segmentation depends on initial binary conversion and accuracy decreases as more opaque objects are present in the foreground alongside spheroids.

Extracted parameters vary depending in spheroids after PDT damage

Pre-screened spheroids show no significant difference between replicates

A significant challenge in spheroid-based platforms for drug screening is the inherent variability found between samples, regardless of consistency in growth conditions. Recent advances in culture techniques include spinner flasks, rotary culture vessels, and microfluidic devices, which aim to tightly control spheroid growth. However, the maintenance of these systems is both expensive and time-consuming [326]. The use of non-adherent surfaces like agarose typically leads to heterogeneous spheroid morphology. However, the selection of homogeneous spheroid groups before PDT improved the consistency of results. Fig. 5.5 shows the variation in total area between groups of treated spheroids.

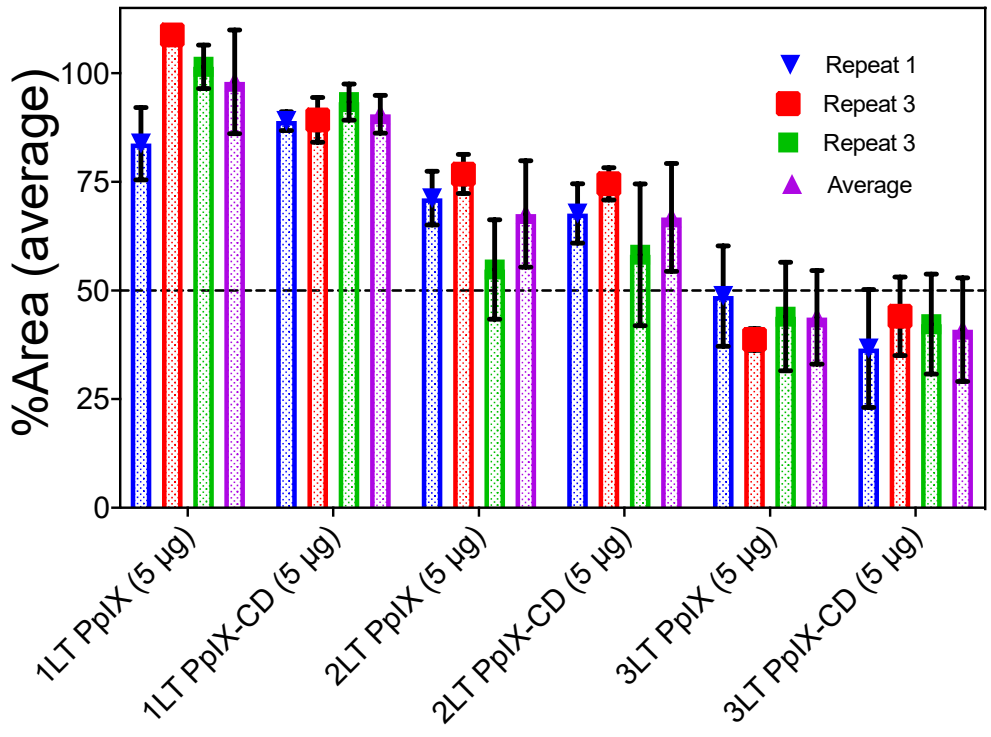

Fig. 5.5 – Group variability was lowered with spheroid pre-screening. Area values from extracted morphological data did not show significant variability between spheroid and treatment groups. (N=3, n=6).

Parameters show variable response to PDT-induced damage

Spheroids showed increasingly more LDH release and lower dsDNA concentrations as PDT damage increased. Parameters such as area and volume showed significant changes exhibiting a similar trend to results from biological assays. This is expected as spheroid size is strongly linked to cell number, which is reduced with more effective treatments [324]. In contrast, parameters related to spheroid roundness (sphericity, convexity, solidity) did not show significant difference between treatments, as shown in Fig. 5.6.

The variation in morphological parameters was also observed by Mittler et al. (2017). They used lipid vesicles carrying doxorubicin, docetaxel, etoposide, and ARN-509 to treat prostate cancer spheroids. Interestingly, they determined automated image analysis was inconclusive for determining drug-induced chemotoxicity as growth was arrested without affecting sphericity. Furthermore, they observed that size or roundness-based analysis was not enough to distinguish between drug doses (50 and 500 nM) [377]. However, their results suggest that spheroid selection and treatment conditions were not ideal to observe significant differences between groups.

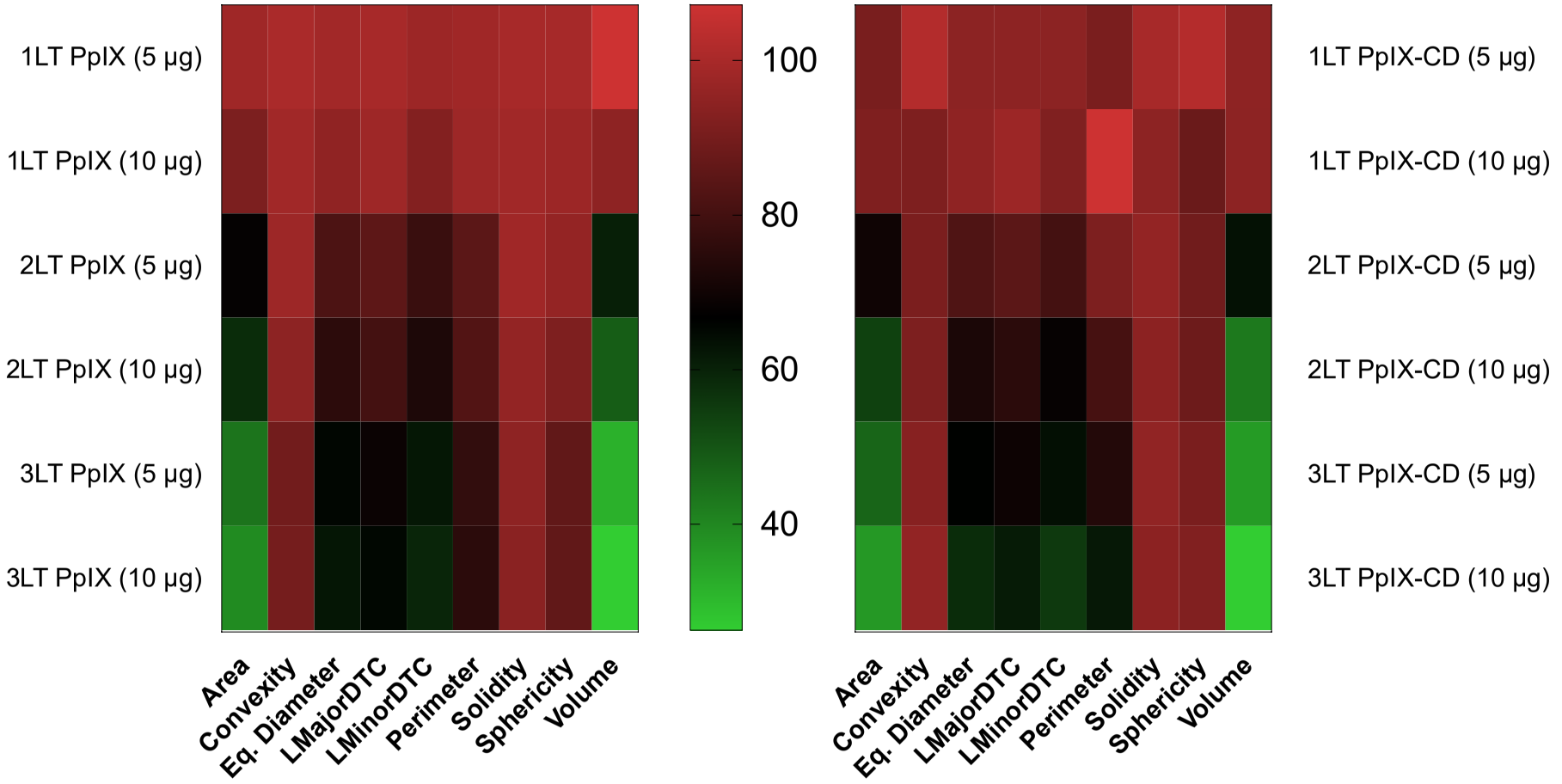

Fig. 5.6 – Variability in spheroid morphology at 24 hours post-PDT. Greater variations in colours indicate which parameters can be used to distinguish treatments known to cause significantly different damage to spheroids, such as 5 µg 1LT versus 10 µg 3LT.

Morphological parameters can be linked to LDH release and dsDNA content

LDH release and dsDNA quantification were repeated using PpIX and PpIX-CD with the best-performing conditions (5-10 μg/ml, 5 J/cm^2, 1-3 LT). The data was then plotted against the spheroid area, showing the variation in size after PDT based on total area of control spheroids not exposed to drug or light irradiation. Fig. 5.8 shows 1LT can be clearly separated from 2LT and 3LT-based treatments using only area as the primary indicator of PDT-induced damage. However, distinguishing between two very similar treatments, such as 2LT (10 μg) and 3LT (5 μg) proved to be very difficult due to the variability of acquired data.

Results show variation between experimental groups in the same conditions. Although spheroids were preselected based on their area and sphericity, variations occurred in similar treatment conditions. However, most of the variability was shown to be statistically insignificant, with some exceptions. PpIX showed greater variance in both LDH release and dsDNA content than PpIX-CD, particularly at 10 μg/ml, which can be seen in Fig. 5.8.

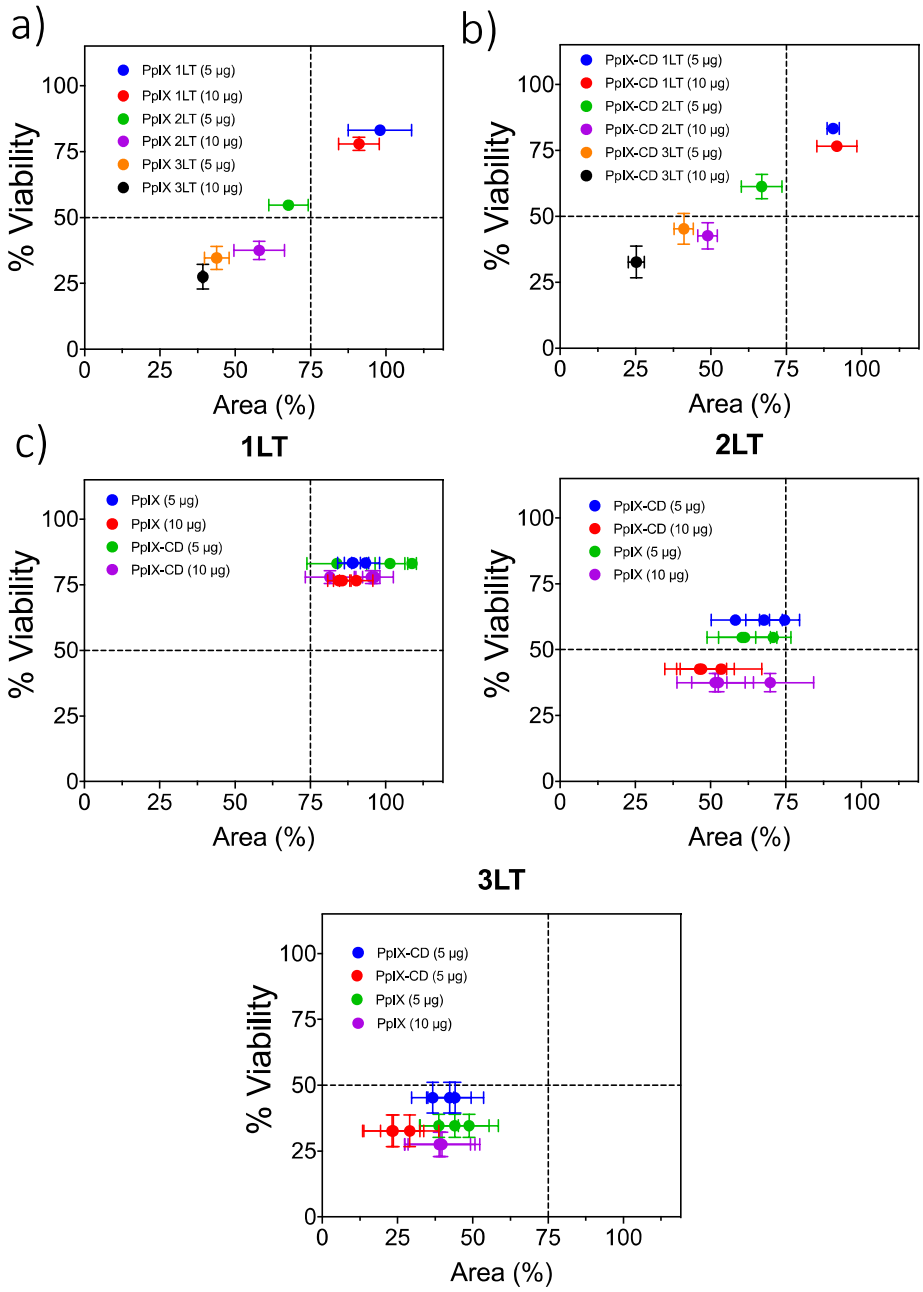

Fig. 5.7 – PpIX and PpIX-CD show similar reductions to viability and area with equivalent treatment conditions (a, b). Light fractionated treatments caused very similar effects regardless of drug dosages (c).

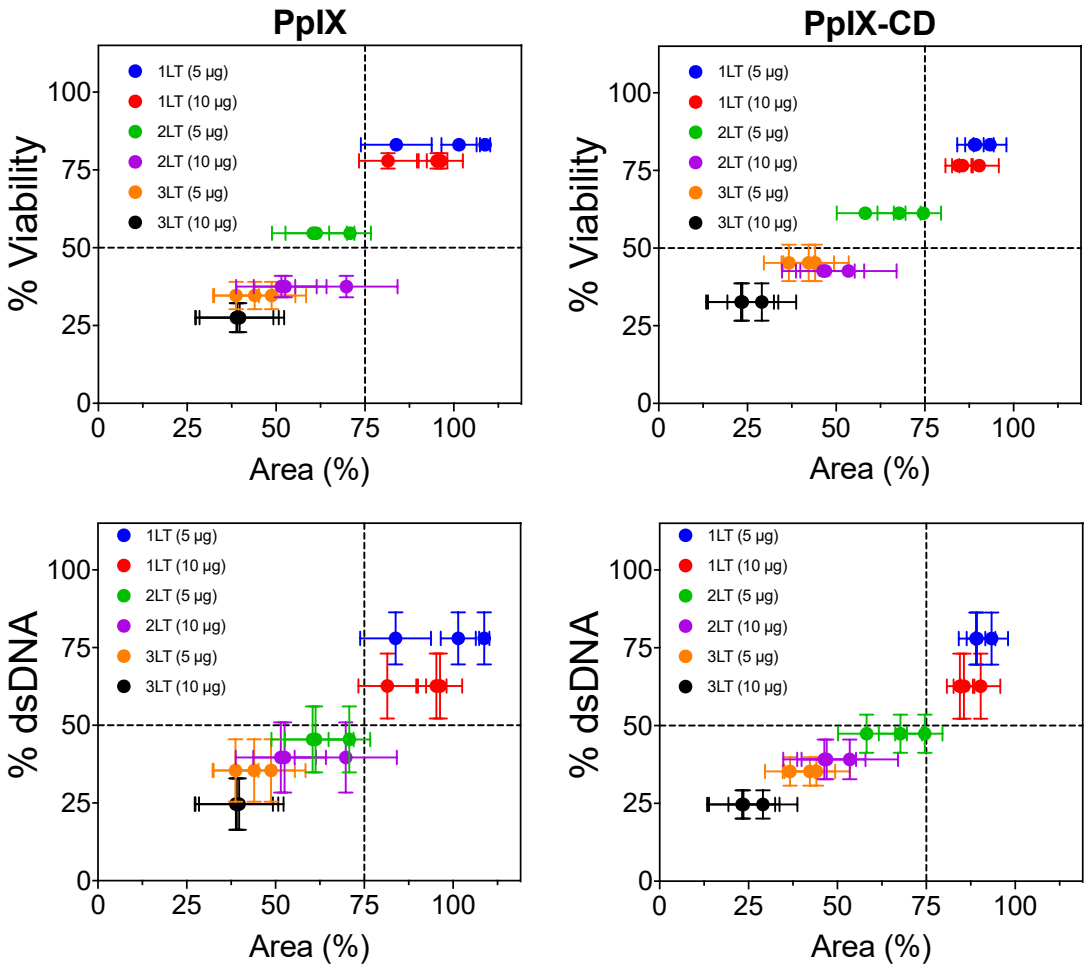

Fig. 5.8 – Spheroid area can be used to predict viability and DNA content. Each point on the graph corresponds to an independent repeat; the same spheroid was monitored through imaging (parameter acquisition) and biological assays (LDH release and total dsDNA content). (N=3, n=6)

Previously, sphericity was shown to be an important parameter to determine spheroid population homogeneity as it influences oxygen and drug diffusion. However, PDT-induced damage was not able to be estimated by spheroid roundness or other parameters such as LMinDTC, as shown in Fig. 5.9. This is caused by variations in size and the fragility of remaining aggregates; the acquisition of images from heavily damaged spheroids resulted in many samples being lost due to complete disaggregation during of debris removal. It is also possible that image quality plays an important factor. Although images were captured using a 2.0 MP Moticam 2.0 camera, they lack the detail found in other microscopy techniques.

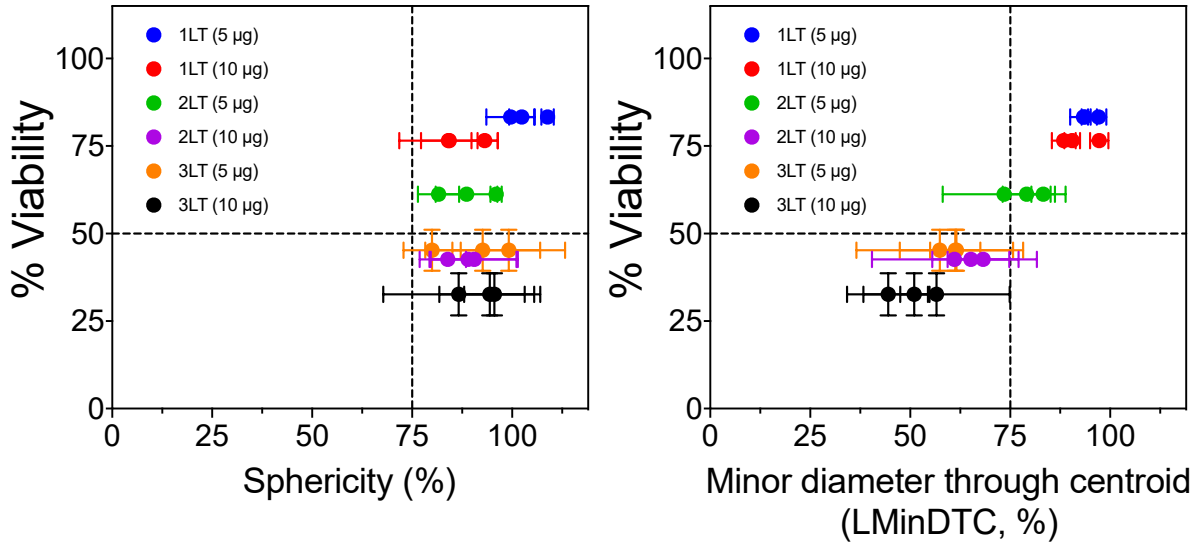

Fig. 5.9 – Spheroid curvature is not linked to viability. Morphological parameters based on spheroid curvature (sphericity) and diameter (LMinDTC) showed significant variability compared to area or volume.

In summary, morphology-based analysis has been shown to be unsuitable as a complete alternative to replace of biological assays as it is unable to reliably distinguish between similar drug treatments with the same level of accuracy. Nonetheless, its speed, cost-effectiveness, and capability of processing large groups of samples make it ideal for its use within PDT parameter screening.

Automated image analysis with alternative image sources

Light sheet microscopy significantly increases acquired image detail

Light sheet fluorescence microscopy (LSFM) has been shown to be a reliable tool for imaging cancer spheroids. Schmitz et al. (2017) demonstrated LSFM could be used to produce three-dimensional high-quality spheroid models for analysing growth kinetics and inner morphological features [378]. Image analysis using LSFM is complex due to the amount of data that is generated; each stack can contain anywhere from 250 – 400 individual images depending on the slice interval. Volume estimation can greatly vary depending on the type of

staining that is performed, sample quality (fixing and staining), and signal intensity. This requires an optimization for each spheroid type and staining protocol, further increasing complexity, as shown by Smyrek and Steltzer (2017) [379]. The analysis of individual spheroids can also be changed by the type of 3D projection that is used as finer features become visible, as shown in Fig. 5.11.

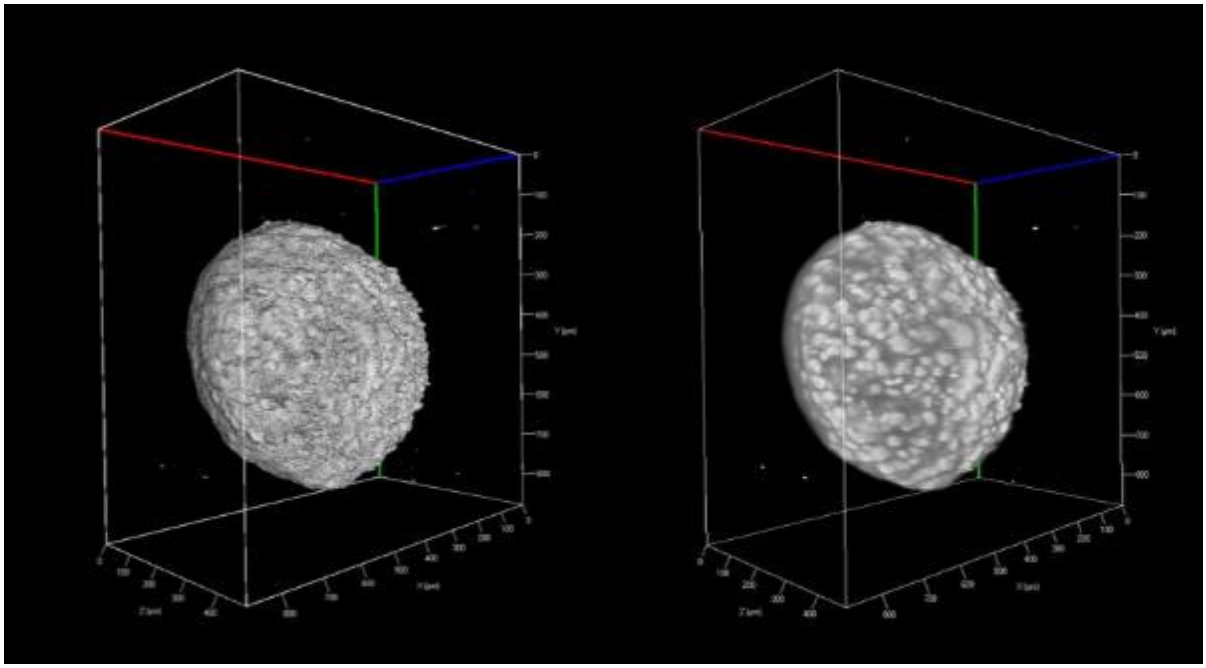

Fig. 5.11 – Variations in surface roughness based on different models for 3D projection: (a) roughness and (b) mixed from Zeiss ZEN 2014 software. Data such as total fluorescence intensity, size, and volume can be extracted from each Z-stack.

A similar approach was used by Barbier et al. (2016), analysing light-attenuated image stacks obtained by confocal laser scanning microscopy (CSLM) [380]. Though these tools produce detailed images, they are unsuitable for larger-scale experiments requiring hundreds of spheroids analysed at specific time points as image processing is severely limited due to hardware constraints. Recently, high-throughput confocal imaging has become available and has been used for morphological analysis of 3D cell cultures. Boutin et al. (2018) demonstrated high-content imaging with U87 spheroids could be achieved within lower timescales (1 hour

per 384 well plate) [381]. However, their protocol required an increase in slice interval (5 μm compared to 1.8 μm for confocal/light sheet within Chapters 4 and 5), resulting in reduced detail. Therefore, more precise microscopy tools are ideal for observing small changes in morphology and can be used to more accurately measure morphological parameters. As was observed in the previous chapter, spheroids subjected to PDT often present significant damage to their outer layers, shedding them after repeated light treatments and leading to irregular shapes. Nonetheless, it is not clear if this is an effect of spheroid manipulation during fixing: repeated light treatments have been shown to reduce spheroid solidity, making them prone to bursting if not handled carefully.

Conclusion

In the previous chapter, spheroids were shown to be a better screening model for PDT parameters due to their more relevant morphophysiological conditions such as hypoxia, cell-cell interactions, and increased drug resistance. However, the inherent variability between individual spheroids in groups needs to be reduced in order to properly determine the effect of treatment parameters, as spheroid shape and size influence drug diffusion and ultimately PDT response.

Computer-assisted analysis is a valuable tool for drug discovery in combination with cancer spheroids. Morphological parameters like volume and sphericity can be automatically obtained through imaging with multiple systems ranging from widefield microscopy to light sheet fluorescence microscopy. Automated segmentation and subsequent image processing allow accurate parameter extraction from a single image, leading to significantly more information being obtained for each condition. Additionally, single spheroid variability can be slightly diminished by pre-screening samples with high sphericity and low variation in area or volume.

In this chapter, automatic image analysis was used to determine results obtained from *in vitro* assays (LDH release and dsDNA concentration) have a connection with some extracted morphometric parameters. Measurements based on spheroid curvature were not found to be significantly linked to treatment response. In contrast, area and volume demonstrated a link with these values and were shown to be capable of differentiating most PDT treatment combinations. The continuation of this work would focus on the improvement of spheroid segmentation, reduction of variability due to cellular debris, and the use of additional microscopy tools in order to improve PDT parameter pre-screening.

Future work

Currently, *in vivo* tumour xenograft mouse models are the gold standard for PDT evaluation. However, they are limited by high costs and strict regulatory controls. Furthermore, evaluating multiple PDT parameters and treatment combinations becomes increasingly more difficult due to the number of animals required. Thus, there is an urgent need for better models of PDT for PS evaluation prior to in vivo testing.

Based on the data obtained in this dissertation, future work should be focused on four key areas:

2.1. Expand and refine the current spheroid protocol for estimating spheroid viability post-light exposure.
2.2. Improve automated image processing to handle larger image sets and additional source images from other various microscopy techniques.
2.3. Develop a protocol for *ex ovo* PDT evaluation using cancer xenografts within CAM assay to observe the effect of tumour vascularisation.
2.4. Validate previous results using a mouse cancer xenograft model for PDT.

Protocol for evaluating PDT with spheroids

The expansion of the spheroid PDT protocol would be highly beneficial for the improvement of PDT parameter screening. Spheroids are rapidly grown, cost-effective, and can be imaged in high-content microscopes. Likewise, they do not need specialised equipment and can be readily used with a wide variety of well-known assays. Currently, there are several areas of opportunity within the previously established protocol.

1. Expansion of PDT evaluation

Although the combination of LDH release and dsDNA concentration showed interesting variations during PDT, the addition of other assays will lead to better understanding of spheroid response to PDT. There are several assays which could be included, such as intracellular oxygen content (Intracellular Oxygen Concentration Assay), intracellular ROS generation (observed by 2,7-DCF-diacetate hydrolysis), and extracellular matrix staining (observing collagen deposition). These could be easily integrated into the spheroid workflow to provide more information about spheroid response post-PDT. Likewise, gene and protein expression can be used to further standardise produced MCTS and monitor heterogeneity while observing key differences during PDT. Finally, the use of light sheet microscopy to observe spheroid response to PDT has been highly beneficial. Live imaging, either through LSFM or widefield microscopy, can provide additional information about spheroid response to nanoparticles and PDT during the initial 24 hours.

2. Mass density evaluation in collaboration with CellDynamics

In addition, the new physical parameter of spheroid mass density can be evaluated as a possible marker for treatment effectiveness. This parameter varies according to the degree of cell compaction found in spheroids: “younger” spheroids are aggregated more loosely than “older” spheroids, which have produced more ECM. This work could be done in collaboration with CellDynamics, a company specialised in the fabrication of equipment for 3D cell biology. The use of mass density could reveal small variations in similar conditions such as equal drug dosage or irradiance with different compounds (e.g. PpIX-CD vs PpIX@CD, 5 µg/ml, 2LT, 5 J/cm^2). However, spheroid culture would have to be readjusted as the maximum size for measurement is 250 µm. In turn, this change will require a re-evaluation of previously measured LDH and dsDNA content values for the smaller spheroids.

3. Adaptations to spheroid protocol for PDT

The conditions used for spheroid culture in this project were standard incubation conditions. However, they can be further adjusted to reflect *in vivo* tumour microenvironment. The change in oxygen content would be extremely important to improve the relevance of obtained data, as 20% (160 mmHg) is extremely high, even compared to arterial blood (9.5%, 70 mmHg). In comparison, physiological hypoxia found in tumours is much lower and typically ranges from 2-0.4%, depending on the type of tissue: melanoma tumours have been shown to possess approximately 1.5% oxygen (11.6 mmHg). This is around 13-fold less oxygen than what is currently used in cell culture and could significantly impact spheroid growth. Likewise, PDT response is linked to oxygen availability within cells, making this an extremely important parameter that needs to be adjusted. This could be achieved by using a separate incubator for spheroid growth and performing PDT within incubation conditions.

Improvement of automated parameter acquisition

Improving automated image processing will lead to better turnaround time for large datasets. Currently, there is a high degree of manual input needed in between sections, which slows the comparison of multiple PDT parameters. Currently, graphs and statistics were manually input and created using Microsoft Excel after obtaining morphometric parameters from AnaSP. However, it is possible to perform these tasks using MATLAB. Although this is an area of opportunity, it requires programming knowledge in order to integrate all steps in the workflow (image acquisition, naming of widefield images, parameter extraction, comparison of conditions).

Automated parameter acquisition can also be expanded upon by making use of other imaging tools such as high content microscopes (widefield, fluorescence, and confocal images) and

LSFM. Although widefield fluorescence images could likely be processed with AnaSP, other images require different software for processing, such as ReViMS for LSFM and confocal images. The advantage of acquiring image stacks in comparison to single images is the possibility of reconstructing the true 3D morphology and extracting morphometric parameters for comparison. This could further improve the correlation between biological assays with PDT-treated spheroids.

Ex ovo CAM assay for evaluation of cancer xenograft tumours

Chick Chorioallantoic Membrane (CAM) Assay is another model based on the use of fertilised chicken eggs. Drug delivery evaluation with CAM assay coupled with cancer xenografts is a highly reproducible and cost-effective alternative to traditional animal models. Implanted tumours develop additional characteristics such as angiogenesis and vascularization, which are key areas of early tumour development. Tumour xenografts on CAM can proliferate after implantation using MCTS or cell suspensions and can become vascularised within the 4-day window for growth after implantation. CAM experiments must take place within the 14-day period before chick termination. An *ex ovo* model for cancer xenografts has already been established within the Biomaterials group. This model is more advantageous than the standard *in ovo* model due to the ease of implantation and image acquisition.

A modified waterproof mounted LED system within the incubator could be used to ensure less stress within the CAM from temperature changes and improve chick survival rate before PDT. Once standardised, this model could test multiple conditions simultaneously in a two-week period. An experienced user can manage 12-48 eggs with 1-3 implantation sites. The use of an aggressive melanoma xenograft in combination with PDT will enable a closer observation of tumour neoangiogenesis inhibition by PDT. Additionally, CAM tissue samples can be further analysed through microscopy and histology to compare results with MCTS. Furthermore,

xenografts can be made using both cell lines (such as C8161) or patient-derived tissue. This assay is an ideal step up from spheroids instead of choosing CSC or CTOS organoids.

Validation of PpIX-CD conjugates using an *in vivo* mouse model

The validation of the screening would be the final step in the evaluation of PpIX-loaded CDs. In addition to PDT parameters obtained from the literature, newly obtained ultra-low fluence conditions could be evaluated *in vivo*. BALB/c nude mice with GFP-expressing tumour xenografts can be used to monitor cancer progression through fluorescence microscopy and determine PS localisation, uptake, and circulation lifetime. The experiments can use standard conditions: 5-week old mice are subcutaneously injected with a cell suspension containing ~5×10^6 cells. The progression of tumour growth can be seen through optical and *in vivo* fluorescence imaging in a 3 to 8-day period, with tumours growing to ~100 mm^3 in size prior to PDT. Pharmacokinetic studies can be carried out using blood drawn at various time intervals after administration. Finally, *ex vivo* imaging and histological analysis of tissue will yield more information regarding photosensitiser uptake and circulation lifetimes. Validation in a small study with mice would greatly benefit our understanding of PpIX conjugate pharmacokinetics and *in vivo* efficiency.

In summary, the combination of in vitro (MCTS), *ex ovo* (CAM assay), and automated image analysis (widefield/LSFM) will enable the determination of better treatment conditions prior to *in vivo* trials. The evaluation of low-fluence and fractionated PDT is an area of research opportunity which can be exploited using a combination of *in vitro/ex ovo* models. Furthermore, this model could be used to observe treatment efficiency of various parameters in treatments such as chemotherapy, photothermal therapy, or nitric oxide production. Finally, it is also possible to build on previous work by evaluating novel nanoparticle and other PDT agents, such as transition metal-compounds.

Final remarks

Current research is focused on the improvement of existing PS through chemical modifications or using carriers like nanoparticles. CD-based conjugates are becoming increasingly more accepted in biomedical applications but are not usually compared between each other due to difficulties in replicating experimental methodologies. Furthermore, testing these novel agents is more complex than for many non-light activated small molecules by the requirement for light and oxygen for activity, hence the need custom models of PDT. However, the complex interaction between tissue oxygenation, vascularisation, light absorption, and drug biodistribution makes selecting ranges for PDT parameters difficult.

In this work, protoporphyrin IX and CD-based conjugates were successfully produced via two distinct loading strategies. Characterisation revealed crucial differences in water solubility and drug loading efficiency, with conjugates showing similar behaviour to PpIX. *In vitro* PDT evaluation with cell monolayers revealed conjugates significantly improved PpIX efficiency through the decrease of dark toxicity.

Cancer spheroids showed localised cell death and differential drug uptake to cell monolayers, demonstrating the requirement and validation of complex *in vitro* models. Preliminary studies also demonstrated the feasibility of multiple parameter testing - multiple combinations were carried out, evaluating the impact of drug dose, colloidal stability, light intensity, and sequential irradiation. A combination of biological assays, microscopy, and automated image analysis was used to establish a link between treatment response and morphological parameters, with a total of 54 conditions were evaluated at three distinct timepoints. This represents a substantial increase in screening speed and capability in comparison to in vivo mouse cancer xenograft models. In conclusion, this work showed the importance of intermediate models for PDT with novel compounds before *in vivo* trials.

References

1. Xu X, Ray R, Gu Y, Ploehn HJ, Gearheart L, Raker K, et al. Electrophoretic Analysis and Purification of Fluorescent Single-Walled Carbon Nanotube Fragments. J Am Chem Soc. 2004;126(40):12736–7.

2. Gao J, Zhu M, Huang H, Liu Y, Kang Z. Advances, challenges and promises of carbon dots [Internet]. Vol. 4, Inorganic Chemistry Frontiers. Royal Society of Chemistry; 2017. p. 1963–86.

3. Wang Y, Hu A. Carbon quantum dots: synthesis, properties and applications. J Mater Chem C. 2014 Jun 17;2(34):6921–39.

4. Khan S, Li W, Karedla N, Thiart J, Gregor I, Chizhik AM, et al. Charge-Driven Fluorescence Blinking in Carbon Nanodots. J Phys Chem Lett. 2017 Dec 7;8(23):5751–7.

5. Barati A, Shamsipur M, Abdollahi H. A misunderstanding about upconversion luminescence of carbon quantum dots. J Iran Chem Soc. 2015 Mar 24;12(3):441–6.

6. Song SH, Jang M, Yoon H, Cho YH, Jeon S, Kim BH. Size and pH dependent photoluminescence of graphene quantum dots with low oxygen content. RSC Adv. 2016 Oct 12;6(100):97990–4.

7. Dutta Choudhury S, Chethodil JM, Gharat PM, Praseetha PK, Pal H. PH-Elicited Luminescence Functionalities of Carbon Dots: Mechanistic Insights. J Phys Chem Lett. 2017;8(7):1389–95.

8. Yao B, Huang H, Liu Y, Kang Z. Carbon Dots: A Small Conundrum. Trends Chem. 2019 May 1;1(2):235–46.

9. Poland CA, Duffin R, Kinloch I, Maynard A, Wallace WAH, Seaton A, et al. Carbon nanotubes introduced into the abdominal cavity of mice show asbestos-like pathogenicity in a pilot study. Nat Nanotechnol [Internet]. 2008;3(7):423–8.

10. Gordon S. Phagocytosis: An Immunobiologic Process. Vol. 44, Immunity. Cell Press; 2016. p. 463–75.

11. Alshehri R, Ilyas AM, Hasan A, Arnaout A, Ahmed F, Memic A. Carbon Nanotubes in Biomedical Applications: Factors, Mechanisms, and Remedies of Toxicity. J Med Chem. 2016 Sep 22;59(18):8149–67.

12. Chauhan S, Jain N, Nagaich U. Nanodiamonds with powerful ability for drug delivery and biomedical applications: Recent updates on in vivo study and patents. Journal of Pharmaceutical Analysis. Xi'an Jiaotong University; 2019.

13. Neburkova J, Vavra J, Cigler P. Coating nanodiamonds with biocompatible shells for applications in biology and medicine. Curr Opin Solid State Mater Sci. 2017 Feb 1;21(1):43–53.

14. Zhao L, Nakae Y, Qin H, Ito T, Kimura T, Kojima H, et al. Polyglycerol-functionalized

nanodiamond as a platform for gene delivery: Derivatization, characterization, and hybridization with DNA. Beilstein J Org Chem. 2014 Mar 24;10:707–13.

15. Chen F, Gao W, Qiu X, Zhang H, Liu L, Liao P, et al. Graphene quantum dots in biomedical applications: Recent advances and future challenges. Front Lab Med. 2017 Dec 1;1(4):192–9.

16. Sun Y, Zheng Y, Pan H, Chen J, Zhang W, Fu L, et al. Magnetism of graphene quantum dots. npj Quantum Mater [Internet]. 2017 Dec 1;2(1).

17. Chen N, He Y, Su Y, Li X, Huang Q, Wang H, et al. The cytotoxicity of cadmium-based quantum dots. Biomaterials. 2012 Feb 1;33(5):1238–44.

18. Anderson SD, Gwenin V V, Gwenin CD. Magnetic Functionalized Nanoparticles for Biomedical, Drug Delivery and Imaging Applications. Nanoscale Res Lett. 2019 May 30;14(1):188.

19. Dibaba ST, Xiaoqian Ge, Ren W, Sun L. Recent progress of energy transfer and luminescence intensity boosting mechanism in Nd3+-sensitized upconversion nanoparticles. Vol. 37, Journal of Rare Earths. Chinese Society of Rare Earths; 2019. p. 791–805.

20. Del Rosal B, Jaque D. Upconversion nanoparticles for in vivo applications: limitations and future perspectives [Internet]. Vol. 7, Methods and applications in fluorescence. IOP Publishing; 2019. p. 022001.

21. Li H, Kang Z, Liu Y, Lee ST. Carbon nanodots: Synthesis, properties and applications. J Mater Chem. 2012 Nov 6;22(46):24230–53.

22. Tsoi KM, Dai Q, Alman BA, Chan WCW. Are quantum dots toxic? Exploring the discrepancy between cell culture and animal studies. Acc Chem Res. 2013 Mar 19;46(3):662–71.

23. Farshbaf M, Davaran S, Rahimi F, Annabi N, Salehi R, Akbarzadeh A. Carbon quantum dots: recent progresses on synthesis, surface modification and applications [Internet]. Vol. 46, Artificial Cells, Nanomedicine and Biotechnology. Taylor & Francis; 2018. p. 1331–48.

24. Tuerhong M, XU Y, YIN XB. Review on Carbon Dots and Their Applications [Internet]. Vol. 45, Chinese Journal of Analytical Chemistry. Elsevier; 2017. p. 139–50.

25. Wang R, Lu KQ, Tang ZR, Xu YJ. Recent progress in carbon quantum dots: synthesis, properties and applications in photocatalysis [Internet]. Vol. 5, Journal of Materials Chemistry A. Royal Society of Chemistry; 2017. p. 3717–34.

26. Williams DF. On the mechanisms of biocompatibility. Biomaterials [Internet]. 2008 Jul;29(20):2941–53.

27. Mervin LH, Cao Q, Barrett IP, Firth MA, Murray D, McWilliams L, et al. Understanding Cytotoxicity and Cytostaticity in a High-Throughput Screening Collection. 2020;13:51.

28. Sukhanova A, Bozrova S, Sokolov P, Berestovoy M, Karaulov A, Nabiev I. Dependence

of Nanoparticle Toxicity on Their Physical and Chemical Properties. Vol. 13, Nanoscale Research Letters. Springer New York LLC; 2018.

29. Schaeublin NM, Braydich-Stolle LK, Schrand AM, Miller JM, Hutchison J, Schlager JJ, et al. Surface charge of gold nanoparticles mediates mechanism of toxicity. Nanoscale. 2011 Feb 10;3(2):410–20.

30. Jiang J, Oberdörster G, Elder A, Gelein R, Mercer P, Biswas P. Does nanoparticle activity depend upon size and crystal phase? Nanotoxicology. 2008 Mar;2(1):33–42.

31. Derfus AM, Chan WCW, Bhatia SN. Probing the Cytotoxicity of Semiconductor Quantum Dots. Nano Lett. 2004 Jan 1;4(1):11–8.

32. Huang YW, Cambre M, Lee HJ. The Toxicity of Nanoparticles Depends on Multiple Molecular and Physicochemical Mechanisms [Internet]. Vol. 18, International journal of molecular sciences. Multidisciplinary Digital Publishing Institute (MDPI); 2017.

33. Lewinski N, Colvin V, Drezek R. Cytotoxicity of nanoparticles [Internet]. Vol. 4, Small. John Wiley & Sons, Ltd; 2008. p. 26–49.

34. Panessa-Warren BJ, Warren JB, Wong SS, Misewich JA. Biological cellular response to carbon nanoparticle toxicity. J Phys Condens Matter. 2006 Aug 23;18(33):S2185–201.

35. Moore TL, Urban DA, Rodriguez-Lorenzo L, Milosevic A, Crippa F, Spuch-Calvar M, et al. Nanoparticle administration method in cell culture alters particle-cell interaction. Sci Rep. 2019 Dec 29;9(1):900.

36. Ray SC, Jana NR. Toxicology and Biosafety of Carbon Nanomaterials. In: Carbon Nanomaterials for Biological and Medical Applications. Elsevier; 2017. p. 205–29.

37. Tao H, Yang K, Ma Z, Wan J, Zhang Y, Kang Z, et al. In vivo NIR fluorescence imaging, biodistribution, and toxicology of photoluminescent carbon dots produced from carbon nanotubes and graphite. Small. 2012 Jan 23;8(2):281–90.

38. Huang H, Li C, Zhu S, Wang H, Chen C, Wang Z, et al. Histidine-derived nontoxic nitrogen-doped carbon dots for sensing and bioimaging applications. Langmuir. 2014 Nov 18;30(45):13542–8.

39. Xu X, Zhang K, Zhao L, Li C, Bu W, Shen Y, et al. Aspirin-Based Carbon Dots, a Good Biocompatibility of Material Applied for Bioimaging and Anti-Inflammation. ACS Appl Mater Interfaces. 2016 Dec 7;8(48):32706–16.

40. Jiang K, Sun S, Zhang L, Wang Y, Cai C, Lin H. Bright-Yellow-Emissive N-Doped Carbon Dots: Preparation, Cellular Imaging, and Bifunctional Sensing. ACS Appl Mater Interfaces. 2015 Oct 21;7(41):23231–8.

41. Ray SC, Saha A, Jana NR, Sarkar R. Fluorescent carbon nanoparticles: Synthesis, characterization, and bioimaging application. J Phys Chem C. 2009 Oct 29;113(43):18546–51.

42. Cui Y, Zhang C, Sun L, Hu Z, Liu X. Simple and efficient synthesis of strongly green

fluorescent carbon dots with upconversion property for direct cell imaging. Part Part Syst Charact. 2015 May 1;32(5):542–6.

43. Hill SA, Benito-Alifonso D, Morgan DJ, Davis SA, Berry M, Galan MC. Three-minute synthesis of sp3 nanocrystalline carbon dots as non-toxic fluorescent platforms for intracellular delivery. Nanoscale. 2016 Nov 10;8(44):18630–4.

44. Yang ZC, Wang M, Yong AM, Wong SY, Zhang XH, Tan H, et al. Intrinsically fluorescent carbon dots with tunable emission derived from hydrothermal treatment of glucose in the presence of monopotassium phosphate. Chem Commun. 2011 Oct 18;47(42):11615–7.

45. Shereema RM, Sruthi T V., Kumar VBS, Rao TP, Shankar SS. Angiogenic Profiling of Synthesized Carbon Quantum Dots. Biochemistry. 2015 Oct 20;54(41):6352–6.

46. Yang ST, Wang X, Wang H, Lu F, Luo PG, Cao L, et al. Carbon dots as nontoxic and high-performance fluorescence imaging agents. J Phys Chem C. 2009 Oct 22;113(42):18110–4.

47. Vedamalai M, Periasamy AP, Wang CW, Tseng YT, Ho LC, Shih CC, et al. Carbon nanodots prepared from o-phenylenediamine for sensing of Cu2+ ions in cells. Nanoscale. 2014 Aug 28;6(21):13119–25.

48. Zhang X, Wang S, Zhu C, Liu M, Ji Y, Feng L, et al. Carbon-dots derived from nanodiamond: Photoluminescence tunable nanoparticles for cell imaging. J Colloid Interface Sci. 2013 May 1;397:39–44.

49. Du F, Zhang M, Ju H, Zhang L, Sun M, Zhou Z, et al. Engineering iodine-doped carbon dots as dual-modal probes for fluorescence and X-ray CT imaging. Int J Nanomedicine. 2015;10:6943.

50. Liu C, Zhang P, Zhai X, Tian F, Li W, Yang J, et al. Nano-carrier for gene delivery and bioimaging based on carbon dots with PEI-passivation enhanced fluorescence. Biomaterials. 2012 May 1;33(13):3604–13.

51. Havrdova M, Hola K, Skopalik J, Tomankova K, Petr M, Cepe K, et al. Toxicity of carbon dots-Effect of surface functionalization on the cell viability, reactive oxygen species generation and cell cycle. Carbon N Y. 2016 Apr 1;99:238–48.

52. Li Q, Ohulchanskyy TY, Liu R, Koynov K, Wu D, Best A, et al. Photoluminescent carbon dots as biocompatible nanoprobes for targeting cancer cells in vitro. J Phys Chem C. 2010 Jul 22;114(28):12062–8.

53. Zhai X, Zhang P, Liu C, Bai T, Li W, Dai L, et al. Highly luminescent carbon nanodots by microwave-assisted pyrolysis. Chem Commun. 2012 Jul 16;48(64):7955–7.

54. Zhou J, Shan X, Ma J, Gu Y, Qian Z, Chen J, et al. Facile synthesis of P-doped carbon quantum dots with highly efficient photoluminescence. RSC Adv. 2014 Jan 6;4(11):5465–8.

55. Parvin N, Mandal TK. Dually emissive P,N-co-doped carbon dots for fluorescent and photoacoustic tissue imaging in living mice. Microchim Acta. 2017 Apr 7;184(4):1117–

25.

56. Mohammadinejad R, Dadashzadeh A, Moghassemi S, Ashrafizadeh M, Dehshahri A, Pardakhty A, et al. Shedding light on gene therapy: Carbon dots for the minimally invasive image-guided delivery of plasmids and noncoding RNAs - A review. Vol. 18, Journal of Advanced Research. Elsevier B.V.; 2019. p. 81–93.

57. Vinci JC, Ferrer IM, Seedhouse SJ, Bourdon AK, Reynard JM, Foster BA, et al. Hidden properties of carbon dots revealed after HPLC fractionation. J Phys Chem Lett. 2013 Jan 17;4(2):239–43.

58. Donaldson K, Borm PJ, Castranova V, Gulumian M. The limits of testing particle-mediated oxidative stress in vitro in predicting diverse pathologies; relevance for testing of nanoparticles [Internet]. Vol. 6, Particle and Fibre Toxicology. BioMed Central; 2009. p. 13.

59. Yang ST, Cao L, Luo PG, Lu F, Wang X, Wang H, et al. Carbon dots for optical imaging in vivo. J Am Chem Soc. 2009 Aug 19;131(32):11308–9.

60. Dong X, Moyer MM, Yang F, Sun YP, Yang L. Carbon Dots' Antiviral Functions Against Noroviruses. Sci Rep [Internet]. 2017 Dec 1;7(1).

61. Huang X, Zhang F, Zhu L, Choi KY, Guo N, Guo J, et al. Effect of injection routes on the biodistribution, clearance, and tumor uptake of carbon dots. ACS Nano. 2013 Jul 23;7(7):5684–93.

62. Wenhao Liu, Hak Soo Choi, John P. Zimmer, Eiichi Tanaka, John V. Frangioni, and, Moungi Bawendi. Compact Cysteine-Coated CdSe(ZnCdS) Quantum Dots for in Vivo Applications. 2007;

63. Gandorfer A, Haritoglou C, Gandorfer A, Kampik A. Retinal damage from indocyanine green in experimental macular surgery. Investig Ophthalmol Vis Sci. 2003 Jan 1;44(1):316–23.

64. Wang K, Gao Z, Gao G, Wo Y, Wang Y, Shen G, et al. Systematic safety evaluation on photoluminescent carbon dots [Internet]. Vol. 8, Nanoscale Research Letters. Springer New York; 2013. p. 1–9.

65. He H, Wang X, Feng Z, Cheng T, Sun X, Sun Y, et al. Rapid microwave-assisted synthesis of ultra-bright fluorescent carbon dots for live cell staining, cell-specific targeting and in vivo imaging. J Mater Chem B. 2015 Jun 10;3(24):4786–9.

66. Bao X, Yuan Y, Chen J, Zhang B, Li D, Zhou D, et al. In vivo theranostics with near-infrared-emitting carbon dots—highly efficient photothermal therapy based on passive targeting after intravenous administration. Light Sci Appl [Internet]. 2018 Dec 1;7(1):1–11.

67. Zheng M, Li Y, Liu S, Wang W, Xie Z, Jing X. One-Pot To Synthesize Multifunctional Carbon Dots for Near Infrared Fluorescence Imaging and Photothermal Cancer Therapy. ACS Appl Mater Interfaces. 2016 Sep 14;8(36):23533–41.

68. Hunt PR. The C. elegans model in toxicity testing [Internet]. Vol. 37, Journal of Applied

Toxicology. Wiley-Blackwell; 2017. p. 50–9.

69. Singh V, Rawat KS, Mishra S, Baghel T, Fatima S, John AA, et al. Biocompatible fluorescent carbon quantum dots prepared from beetroot extract for in vivo live imaging in C. elegans and BALB/c mice. J Mater Chem B. 2018 May 23;6(20):3366–71.

70. McGrath P, Li CQ. Zebrafish: a predictive model for assessing drug-induced toxicity [Internet]. Vol. 13, Drug Discovery Today. Elsevier Current Trends; 2008. p. 394–401.

71. Kang Y-FF, Li Y-HH, Fang Y-WW, Xu Y, Wei X-MM, Yin X-BB. Carbon Quantum Dots for Zebrafish Fluorescence Imaging. Sci Rep. 2015 Dec 2;5(1):11835.

72. Li S, Skromne I, Peng Z, Dallman J, Al-Youbi AO, Bashammakh AS, et al. "Dark" carbon dots specifically "light-up" calcified zebrafish bones. J Mater Chem B. 2016 Nov 23;4(46):7398–405.

73. Mangir N, Raza A, Haycock JW, Chapple C, Macneil S. An improved in vivo methodology to visualise tumour induced changes in vasculature using the chick chorionic allantoic membrane assay. In Vivo (Brooklyn). 2018;32(3):461–72.

74. Schomann T, Qunneis F, Widera D, Kaltschmidt C, Kaltschmidt B. Improved Method for Ex Ovo -Cultivation of Developing Chicken Embryos for Human Stem Cell Xenografts. Stem Cells Int. 2013 Mar 11;2013:1–9.

75. Mangir N, Dikici S, Claeyssens F, Macneil S. Using ex Ovo Chick Chorioallantoic Membrane (CAM) Assay to Evaluate the Biocompatibility and Angiogenic Response to Biomaterials. ACS Biomater Sci Eng. 2019 Jul 8;5(7):3190–200.

76. Sayes CM, Reed KL, Warheit DB. Assessing Toxicity of Fine and Nanoparticles: Comparing In Vitro Measurements to In Vivo Pulmonary Toxicity Profiles. Toxicol Sci. 2007 May 1;97(1):163–80.

77. Langhans SA. Three-dimensional in vitro cell culture models in drug discovery and drug repositioning [Internet]. Vol. 9, Frontiers in Pharmacology. Frontiers; 2018. p. 6.

78. Knight E, Przyborski S. Advances in 3D cell culture technologies enabling tissue-like structures to be created *in vitro*. J Anat. 2015 Dec;227(6):746–56.

79. Zhao C, Danish E, Cameron NR, Kataky R. Emulsion-templated porous materials (PolyHIPEs) for selective ion and molecular recognition and transport: applications in electrochemical sensing.

80. Chandra A, Singh N. Cell Microenvironment pH Sensing in 3D Microgels Using Fluorescent Carbon Dots. ACS Biomater Sci Eng. 2017 Dec 11;3(12):3620–7.

81. Hamill OP, Martinac B. Molecular basis of mechanotransduction in living cells. Vol. 81, Physiological Reviews. American Physiological Society; 2001. p. 685–740.

82. Lin CH, Jokela T, Gray J, LaBarge MA. Combinatorial Microenvironments Impose a Continuum of Cellular Responses to a Single Pathway-Targeted Anti-cancer Compound. Cell Rep. 2017 Oct 10;21(2):533–45.

83. Fröhlich E. Comparison of conventional and advanced in vitro models in the toxicity testing of nanoparticles [Internet]. Vol. 46, Artificial Cells, Nanomedicine and Biotechnology. Taylor & Francis; 2018. p. 1091–107.

84. Perche F, Torchilin VP. Cancer cell spheroids as a model to evaluate chemotherapy protocols. Cancer Biol Ther [Internet]. 2012 Oct;13(12):1205–13.

85. Griner LM, Gampa K, Do T, Nguyen H, Farley D, Hogan CJ, et al. Generation of high-throughput three-dimensional tumor spheroids for drug screening. J Vis Exp [Internet]. 2018 Sep 5;2018(139).

86. Scialabba C, Sciortino A, Messina F, Buscarino G, Cannas M, Roscigno G, et al. Highly Homogeneous Biotinylated Carbon Nanodots: Red-Emitting Nanoheaters as Theranostic Agents toward Precision Cancer Medicine. ACS Appl Mater Interfaces. 2019;11(22):19854–66.

87. Wang H-JJ, He X, Luo T-YY, Zhang J, Liu Y-HH, Yu X-QQ. Amphiphilic carbon dots as versatile vectors for nucleic acid and drug delivery. Nanoscale. 2017 May 11;9(18):5935–47. Available from: http://xlink.rsc.org/?DOI=C7NR01029J

88. Bulin AL, Broekgaarden M, Hasan T. Comprehensive high-throughput image analysis for therapeutic efficacy of architecturally complex heterotypic organoids. Sci Rep [Internet]. 2017 Dec 1;7(1):1–12.

89. Kondo J, Inoue M. Application of Cancer Organoid Model for Drug Screening and Personalized Therapy. Cells [Internet]. 2019 May 17;8(5):470.

90. Gilmore AP. Anoikis. Cell Death Differ [Internet]. 2005;12:1473–7.

91. DiMasi JA, Grabowski HG, Hansen RW. Innovation in the pharmaceutical industry: New estimates of R&D costs. J Health Econ. 2016 May 1;47:20–33.

92. Brayden DJ. Controlled release technologies for drug delivery. In: Drug Discovery Today. Elsevier Current Trends; 2003. p. 976–8.

93. Rodrigues T, Reker D, Schneider P, Schneider G. Counting on natural products for drug design [Internet]. Vol. 8, Nature Chemistry. Nature Publishing Group; 2016. p. 531–41.

94. Sliwoski G, Kothiwale S, Meiler J, Lowe EW, Jr. Computational methods in drug discovery. Pharmacol Rev. 2014;66(1):334–95.

95. Hu ZZ, Huang H, Wu CH, Jung M, Dritschilo A, Riegel AT, et al. Omics-based molecular target and biomarker identification. Methods Mol Biol [Internet]. 2011;719:547–71.

96. Martinho N, Damgé C, Reis CP. Recent Advances in Drug Delivery Systems. J Biomater Nanobiotechnol. 2011 Dec 9;02(05):510–26.

97. Vo TN, Kasper FK, Mikos AG. Strategies for controlled delivery of growth factors and cells for bone regeneration. Adv Drug Deliv Rev. 2012 Sep;64(12):1292–309.

98. Onoue S, Yamada S, Chan HK. Nanodrugs: Pharmacokinetics and safety [Internet]. Vol.

9, International Journal of Nanomedicine. Dove Press; 2014. p. 1025–37.

99. Milton Harris J, Chess RB. Effect of pegylation on pharmaceuticals [Internet]. Vol. 2, Nature Reviews Drug Discovery. Nature Publishing Group; 2003. p. 214–21.

100. Wu ZL, Liu ZX, Yuan YH. Carbon dots: materials, synthesis, properties and approaches to long-wavelength and multicolor emission. J Mater Chem B. 2017 May 31;5(21):3794–809.

101. Zuo J, Jiang T, Zhao X, Xiong X, Xiao S, Zhu Z. Preparation and Application of Fluorescent Carbon Dots [Internet]. Vol. 2015, Journal of Nanomaterials. Hindawi; 2015. p. 1–13.

102. Huh AJ, Kwon YJ. "Nanoantibiotics": A new paradigm for treating infectious diseases using nanomaterials in the antibiotics resistant era [Internet]. Vol. 156, Journal of Controlled Release. Elsevier; 2011. p. 128–45.

103. Thakur M, Pandey S, Mewada A, Patil V, Khade M, Goshi E, et al. Antibiotic conjugated fluorescent carbon dots as a theranostic agent for controlled drug release, bioimaging, and enhanced antimicrobial activity. J Drug Deliv. 2014 Mar 18;2014:282193.

104. Yang J, Zhang X, Ma YH, Gao G, Chen X, Jia HR, et al. Carbon Dot-Based Platform for Simultaneous Bacterial Distinguishment and Antibacterial Applications. ACS Appl Mater Interfaces. 2016 Nov 30;8(47):32170–81.

105. Gogoi N, Chowdhury D. Novel carbon dot coated alginate beads with superior stability, swelling and pH responsive drug delivery. J Mater Chem B. 2014 Jun 11;2(26):4089–99.

106. Muller HE. Oligodynamic action of 17 different metals on Bacillus subtilis, Enterobacteriaceae, Legionellaceae, Micrococcaceae and Pseudomonas aeruginosa. Zentralbl Bakteriol Mikrobiol Hyg B. 1985;182(1):95–101. Available from: http://www.ncbi.nlm.nih.gov/pubmed/3939057

107. Fang H-Y, Huang W-M, Chen D-H. One-step synthesis of positively charged bifunctional carbon dot/silver composite nanoparticles for killing and fluorescence imaging of Gram-negative bacteria. Nanotechnology. 2019 Sep 6;30(36):365603.

108. Priyadarshini E, Rawat K, Prasad T, Bohidar HB. Antifungal efficacy of Au@carbon dots nanoconjugates against opportunistic fungal pathogen, Candida albicans. Colloids Surfaces B Biointerfaces. 2018 Mar 1;163:355–61.

109. Kumari S, Rajit Prasad S, Mandal D, Das P. Carbon dot-DNA-protoporphyrin hybrid hydrogel for sustained photoinduced antimicrobial activity. J Colloid Interface Sci. 2019 Oct 1;553:228–38.

110. Meziani MJ, Dong X, Zhu L, Jones LP, Lecroy GE, Yang F, et al. Visible-Light-Activated Bactericidal Functions of Carbon "quantum" Dots. ACS Appl Mater Interfaces. 2016 May 4;8(17):10761–6.

111. Jijie R, Barras A, Bouckaert J, Dumitrascu N, Szunerits S, Boukherroub R. Enhanced

antibacterial activity of carbon dots functionalized with ampicillin combined with visible light triggered photodynamic effects. Colloids Surfaces B Biointerfaces. 2018 Oct 1;170:347–54.

112. Belkahla H, Boudjemaa R, Caorsi V, Pineau D, Curcio A, Lomas JS, et al. Carbon dots, a powerful non-toxic support for bioimaging by fluorescence nanoscopy and eradication of bacteria by photothermia. Nanoscale Adv [Internet]. 2019;1(7):2571–9.

113. Zou L, Wang H, He B, Zeng L, Tan T, Cao H, et al. Current approaches of photothermal therapy in treating cancer metastasis with nanotherapeutics [Internet]. Vol. 6, Theranostics. Ivyspring International Publisher; 2016. p. 762–72.

114. Kang EB, Phuong PTM, Lee G, Lee S, In I, Park SY. pH-Selective Fluorescent Probe with Photothermal Ablation of Bacteria Based NIR Dye-Embedded Zwitterionic Carbon Dots. Macromol Res. 2019 Jul 25;27(7):720–8.

115. Ganesh AN, Aman A, Logie J, Barthel BL, Cogan P, Al-Awar R, et al. Colloidal Drug Aggregate Stability in High Serum Conditions and Pharmacokinetic Consequence. ACS Chem Biol. 2019 Apr 19;14(4):751–7.

116. Doak AK, Wille H, Prusiner SB, Shoichet BK. Colloid formation by drugs in simulated intestinal fluid. J Med Chem. 2010 May 27;53(10):4259–65.

117. Zhang M, Yuan P, Zhou N, Su Y, Shao M, Chi C. pH-Sensitive N-doped carbon dots–heparin and doxorubicin drug delivery system: preparation and anticancer research. RSC Adv. 2017 Jan 30;7(15):9347–56.

118. Feng T, Ai X, An G, Yang P, Zhao Y. Charge-Convertible Carbon Dots for Imaging-Guided Drug Delivery with Enhanced in Vivo Cancer Therapeutic Efficiency. ACS Nano. 2016 Apr 26;10(4):4410–20.

119. Zeng Q, Shao D, He X, Ren Z, Ji W, Shan C, et al. Carbon dots as a trackable drug delivery carrier for localized cancer therapy in vivo. J Mater Chem B. 2016 Jul 27;4(30):5119–26.

120. Kong T, Hao L, Wei Y, Cai X, Zhu B. Doxorubicin conjugated carbon dots as a drug delivery system for human breast cancer therapy. Cell Prolif. 2018 Oct 1;51(5):e12488.

121. Wang Z, Liao H, Wu H, Wang B, Zhao H, Tan M. Fluorescent carbon dots from beer for breast cancer cell imaging and drug delivery. Anal Methods. 2015 Oct 8;7(20):8911–7.

122. Yang L, Wang Z, Wang J, Jiang W, Jiang X, Bai Z, et al. Doxorubicin conjugated functionalizable carbon dots for nucleus targeted delivery and enhanced therapeutic efficacy. Nanoscale. 2016 Mar 17;8(12):6801–9.

123. Yuan Y, Guo B, Hao L, Liu N, Lin Y, Guo W, et al. Doxorubicin-loaded environmentally friendly carbon dots as a novel drug delivery system for nucleus targeted cancer therapy. Colloids Surfaces B Biointerfaces. 2017 Nov 1;159:349–59.

124. Pandey S, Thakur M, Mewada A, Anjarlekar D, Mishra N, Sharon M. Carbon dots functionalized gold nanorod mediated delivery of doxorubicin: tri-functional nano-

worms for drug delivery, photothermal therapy and bioimaging. J Mater Chem B. 2013;1(38):4972.

125. Hettiarachchi SD, Graham RM, Mintz KJ, Zhou Y, Vanni S, Peng Z, et al. Triple conjugated carbon dots as a nano-drug delivery model for glioblastoma brain tumors. Nanoscale. 2019 Mar 28;11(13):6192–205.

126. Yan Q, Zheng HN, Jiang C, Li K, Xiao SJ. EDC/NHS activation mechanism of polymethacrylic acid: Anhydride versus NHS-ester. RSC Adv [Internet]. 2015 Aug 3;5(86):69939–47.

127. Dobson PD, Kell DB. Carrier-mediated cellular uptake of pharmaceutical drugs: An exception or the rule? Nat Rev Drug Discov [Internet]. 2008 Mar;7(3):205–20.

128. Zhao S, Sun S, Jiang K, Wang Y, Liu Y, Wu S, et al. In Situ Synthesis of Fluorescent Mesoporous Silica–Carbon Dot Nanohybrids Featuring Folate Receptor-Overexpressing Cancer Cell Targeting and Drug Delivery. Nano-Micro Lett [Internet]. 2019 Apr 1;11(1).

129. Li S, Amat D, Peng Z, Vanni S, Raskin S, De Angulo G, et al. Transferrin conjugated nontoxic carbon dots for doxorubicin delivery to target pediatric brain tumor cells. Nanoscale. 2016 Sep 22;8(37):16662–9.

130. Tang J, Kong B, Wu H, Xu M, Wang Y, Wang Y, et al. Carbon nanodots featuring efficient FRET for real-time monitoring of drug delivery and two-photon imaging. Adv Mater. 2013 Dec 1;25(45):6569–74.

131. Mewada A, Pandey S, Thakur M, Jadhav D, Sharon M. Swarming carbon dots for folic acid mediated delivery of doxorubicin and biological imaging. J Mater Chem B. 2014 Jan 15;2(6):698–705.

132. Zheng M, Liu S, Li J, Qu D, Zhao H, Guan X, et al. Integrating oxaliplatin with highly luminescent carbon dots: An unprecedented theranostic agent for personalized medicine. Adv Mater. 2014 Jun 1;26(21):3554–60.

133. Feng T, Ai X, Ong H, Zhao Y. Dual-Responsive Carbon Dots for Tumor Extracellular Microenvironment Triggered Targeting and Enhanced Anticancer Drug Delivery. ACS Appl Mater Interfaces. 2016 Jul 27;8(29):18732–40.

134. Wang Q, Huang X, Long Y, Wang X, Zhang H, Zhu R, et al. Hollow luminescent carbon dots for drug delivery. Carbon N Y. 2013 Aug 1;59:192–9.

135. Gong X, Zhang Q, Gao Y, Shuang S, Choi MMF, Dong C. Phosphorus and Nitrogen Dual-Doped Hollow Carbon Dot as a Nanocarrier for Doxorubicin Delivery and Biological Imaging. ACS Appl Mater Interfaces. 2016 May 11;8(18):11288–97.

136. Wang H, Mukherjee S, Yi J, Banerjee P, Chen Q, Zhou S. Biocompatible Chitosan-Carbon Dot Hybrid Nanogels for NIR-Imaging-Guided Synergistic Photothermal-Chemo Therapy. ACS Appl Mater Interfaces. 2017 Jun 7;9(22):18639–49.

137. He L, Wang T, An J, Li X, Zhang L, Li L, et al. Carbon nanodots@zeolitic imidazolate framework-8 nanoparticles for simultaneous pH-responsive drug delivery and

fluorescence imaging. CrystEngComm. 2014 Mar 24;16(16):3259.

138. Xu L, Fang G, Liu J, Pan M, Wang R, Wang S. One-pot synthesis of nanoscale carbon dots-embedded metal-organic frameworks at room temperature for enhanced chemical sensing. J Mater Chem A [Internet]. 2016;4(41):15880–7.

139. Fahmi MZ, Chen JK, Huang CC, Ling YC, Chang JY. Phenylboronic acid-modified magnetic nanoparticles as a platform for carbon dot conjugation and doxorubicin delivery. J Mater Chem B. 2015 Jul 1;3(27):5532–43.

140. Mitra A, Stables GI. Topical photodynamic therapy for non-cancerous skin conditions [Internet]. Vol. 3, Photodiagnosis and Photodynamic Therapy. Elsevier; 2006. p. 116–27.

141. Izak-Nau E, Huk A, Reidy B, Uggerud H, Vadset M, Eiden S, et al. Impact of storage conditions and storage time on silver nanoparticles' physicochemical properties and implications for their biological effects. RSC Adv [Internet]. 2015;5(102):84172–85.

142. Baer DR. The Chameleon effect: Characterization challenges due to the variability of nanoparticles and their surfaces. Front Chem. 2018;6(MAY).

143. Hwang HS, Shin H, Han J, Na K. Combination of photodynamic therapy (PDT) and anti-tumor immunity in cancer therapy. Vol. 48, Journal of Pharmaceutical Investigation. Springer Netherlands; 2018. p. 143–51.

144. Fowley C, Nomikou N, McHale AP, McCaughan B, Callan JF. Extending the tissue penetration capability of conventional photosensitisers: a carbon quantum dot-protoporphyrin IX conjugate for use in two-photon excited photodynamic therapy. Chem Commun (Camb). 2013;49(79):8934–6.

145. Wu F, Yue L, Su H, Wang K, Yang L, Zhu X. Carbon Dots @ Platinum Porphyrin Composite as Theranostic Nanoagent for Efficient Photodynamic Cancer Therapy. Nanoscale Res Lett. 2018 Dec 8;13(1):357.

146. Wu H, Zeng F, Zhang H, Xu J, Qiu J, Wu S. A nanosystem capable of releasing a photosensitizer bioprecursor under two-photon irradiation for photodynamic therapy. Adv Sci. 2015 Feb 1;3(2):1500254.

147. Yu G, Chen X. Host–guest chemistry in supramolecular theranostics [Internet]. Vol. 9, Theranostics. 2019. p. 3041–74.

148. Sun Y-P, Wang P, Lu Z, Yang F, Meziani MJ, LeCroy GE, et al. Host-Guest Carbon Dots for Enhanced Optical Properties and Beyond. Sci Rep. 2015;5(1):12354.

149. He H, Zheng X, Liu S, Zheng M, Xie Z, Wang Y, et al. Diketopyrrolopyrrole-based carbon dots for photodynamic therapy. Nanoscale. 2018 Jun 14;10(23):10991–8.

150. Li Y, Zheng X, Zhang X, Liu S, Pei Q, Zheng M, et al. Porphyrin-Based Carbon Dots for Photodynamic Therapy of Hepatoma. Adv Healthc Mater. 2017 Jan 1;6(1):1600924.

151. Aguilar Cosme JR, Bryant HE, Claeyssens F. Carbon dot-protoporphyrin IX conjugates for improved drug delivery and bioimaging. Hamblin MR, editor. PLoS One. 2019 Jul

25;14(7):e0220210.

152. Choi Y, Kim S, Choi MH, Ryoo SR, Park J, Min DH, et al. Highly biocompatible carbon nanodots for simultaneous bioimaging and targeted photodynamic therapy in vitro and in vivo. Adv Funct Mater. 2014 Oct 1;24(37):5781–9.

153. Beack S, Kong WH, Jung HS, Do IH, Han S, Kim H, et al. Photodynamic therapy of melanoma skin cancer using carbon dot - Chlorin e6 - Hyaluronate conjugate. Acta Biomater. 2015 Oct 15;26:295–305.

154. Hua XW, Bao YW, Chen Z, Wu FG. Carbon quantum dots with intrinsic mitochondrial targeting ability for mitochondria-based theranostics. Nanoscale. 2017 Aug 3;9(30):10948–60.

155. Huang P, Lin J, Wang X, Wang Z, Zhang C, He M, et al. Light-triggered theranostics based on photosensitizer-conjugated carbon dots for simultaneous enhanced-fluorescence imaging and photodynamic therapy. Adv Mater. 2012 Sep 25;24(37):5104–10.

156. Fowley C, McHale AP, McCaughan B, Fraix A, Sortino S, Callan JF. Carbon quantum dot-NO photoreleaser nanohybrids for two-photon phototherapy of hypoxic tumors. Chem Commun. 2015 Dec 2;51(1):81–4.

157. Jia Q, Ge J, Liu W, Zheng X, Chen S, Wen Y, et al. A Magnetofluorescent Carbon Dot Assembly as an Acidic H2O2-Driven Oxygenerator to Regulate Tumor Hypoxia for Simultaneous Bimodal Imaging and Enhanced Photodynamic Therapy. Adv Mater. 2018 Mar 1;30(13):1706090.

158. Zheng DW, Li B, Li CX, Fan JX, Lei Q, Li C, et al. Carbon-Dot-Decorated Carbon Nitride Nanoparticles for Enhanced Photodynamic Therapy against Hypoxic Tumor via Water Splitting. ACS Nano. 2016 Sep 27;10(9):8715–22.

159. Wang H, Shen J, Li Y, Wei Z, Cao G, Gai Z, et al. Magnetic iron oxide-fluorescent carbon dots integrated nanoparticles for dual-modal imaging, near-infrared light-responsive drug carrier and photothermal therapy. Biomater Sci. 2014 May 7;2(6):915–23.

160. Guo XL, Ding ZY, Deng SM, Wen CC, Shen XC, Jiang BP, et al. A novel strategy of transition-metal doping to engineer absorption of carbon dots for near-infrared photothermal/photodynamic therapies. Carbon N Y. 2018 Aug 1;134:519–30.

161. Peng X, Wang R, Wang T, Yang W, Wang H, Gu W, et al. Carbon Dots/Prussian Blue Satellite/Core Nanocomposites for Optical Imaging and Photothermal Therapy. ACS Appl Mater Interfaces. 2018 Jan 10;10(1):1084–92.

162. Nandi S, Bhunia SK, Zeiri L, Pour M, Nachman I, Raichman D, et al. Bifunctional Carbon-Dot-WS2 Nanorods for Photothermal Therapy and Cell Imaging. Chem - A Eur J. 2017 Jan 18;23(4):963–9.

163. Ge J, Jia Q, Liu W, Lan M, Zhou B, Guo L, et al. Carbon Dots with Intrinsic Theranostic Properties for Bioimaging, Red-Light-Triggered Photodynamic/Photothermal

Simultaneous Therapy In Vitro and In Vivo. Adv Healthc Mater. 2016 Mar 1;5(6):665–75.

164. Jia Q, Ge J, Liu W, Guo L, Zheng X, Chen S, et al. Self-Assembled Carbon Dot Nanosphere: A Robust, Near-Infrared Light-Responsive, and Vein Injectable Photosensitizer. Adv Healthc Mater. 2017 Jun 1;6(12):1601419.

165. Sun S, Chen J, Jiang K, Tang Z, Wang Y, Li Z, et al. Ce6-Modified Carbon Dots for Multimodal-Imaging-Guided and Single NIR Laser Triggered Photothermal / Photodynamic Synergistic Cancer Therapy by Reduced Irradiation Power. ACS Appl Mater Interfaces. 2019 Feb 13;11(6):5791–803.

166. Zhang Y, Satterlee A, Huang L. In vivo gene delivery by nonviral vectors: Overcoming hurdles [Internet]. Vol. 20, Molecular Therapy. American Society of Gene & Cell Therapy; 2012. p. 1298–304.

167. Nakayama T, Otsuka S, Kobayashi T, Okajima H, Matsumoto K, Hagiya Y, et al. Dormant cancer cells accumulate high protoporphyrin IX levels and are sensitive to 5-aminolevulinic acid-based photodynamic therapy. Sci Rep. 2016 Dec 18;6(1):36478.

168. Begum AA, Toth I, Hussein WM, Moyle PM. Advances in Targeted Gene Delivery. Curr Drug Deliv [Internet]. 2019 May 30;16(7):588–608.

169. Cao X, Wang J, Deng W, Chen J, Wang Y, Zhou J, et al. Photoluminescent Cationic Carbon Dots as efficient Non-Viral Delivery of Plasmid SOX9 and Chondrogenesis of Fibroblasts. Sci Rep. 2018 Dec 4;8(1):7057.

170. Zhou J, Deng W, Wang Y, Cao X, Chen J, Wang Q, et al. Cationic carbon quantum dots derived from alginate for gene delivery: One-step synthesis and cellular uptake. Acta Biomater. 2016 Sep 15;42:209–19.

171. Dou Q, Fang X, Jiang S, Chee PL, Lee TC, Loh XJ. Multi-functional fluorescent carbon dots with antibacterial and gene delivery properties. RSC Adv. 2015 May 26;5(58):46817–22.

172. Kim S, Choi Y, Park G, Won C, Park YJ, Lee Y, et al. Highly efficient gene silencing and bioimaging based on fluorescent carbon dots in vitro and in vivo. Nano Res. 2017;10(2):503–19.

173. Liu J, Jiang T, Li C, Wu Y, He M, Zhao J, et al. Bioconjugated Carbon Dots for Delivery of si *Tnfα* to Enhance Chondrogenesis of Mesenchymal Stem Cells by Suppression of Inflammation. Stem Cells Transl Med. 2019 Mar 28;8(7):sctm.18-0289.

174. Zhao H, Duan J, Xiao Y, Tang G, Wu C, Zhang Y, et al. Microenvironment-Driven Cascaded Responsive Hybrid Carbon Dots as a Multifunctional Theranostic Nanoplatform for Imaging-Traceable Gene Precise Delivery. Chem Mater. 2018 May 22;30(10):3438–53.

175. Cheng L, Li Y, Zhai X, Xu B, Cao Z, Liu W. Polycation-b-polyzwitterion copolymer grafted luminescent carbon dots as a multifunctional platform for serum-resistant gene delivery and bioimaging. ACS Appl Mater Interfaces. 2014 Nov 26;6(22):20487–97.

176. Das S, Debnath N, Cui Y, Unrine J, Palli SR. Chitosan, Carbon Quantum Dot, and Silica Nanoparticle Mediated dsRNA Delivery for Gene Silencing in Aedes aegypti: A Comparative Analysis. ACS Appl Mater Interfaces. 2015 Sep 9;7(35):19530–5.

177. Riley MK, Vermerris W. Recent advances in nanomaterials for gene delivery—A review [Internet]. Vol. 7, Nanomaterials. Multidisciplinary Digital Publishing Institute (MDPI); 2017.

178. Jaleel JA, Ashraf SM, Rathinasamy K, Pramod K. Carbon dot festooned and surface passivated graphene-reinforced chitosan construct for tumor-targeted delivery of TNF-α gene. Int J Biol Macromol. 2019 Apr 15;127:628–36.

179. Wu Y-F, Wu H-C, Kuan C-H, Lin C-J, Wang L-W, Chang C-W, et al. Multi-functionalized carbon dots as theranostic nanoagent for gene delivery in lung cancer therapy. Sci Rep. 2016;6(1):21170.

180. Xiao PJ, Li C, Neumann A, Samulski RJ. Quantitative 3D tracing of gene-delivery viral vectors in human cells and animal tissues. Mol Ther. 2012 Feb 1;20(2):317–28.

181. Pierrat P, Wang R, Kereselidze D, Lux M, Didier P, Kichler A, et al. Efficient invitro and invivo pulmonary delivery of nucleic acid by carbon dot-based nanocarriers. Biomaterials. 2015 May 1;51:290–302.

182. Hu L, Sun Y, Li S, Wang X, Hu K, Wang L, et al. Multifunctional carbon dots with high quantum yield for imaging and gene delivery. Carbon N Y. 2014 Feb 1;67:508–13.

183. Noh EH, Ko HY, Lee CH, Jeong MS, Chang YW, Kim S. Carbon nanodot-based self-delivering microRNA sensor to visualize microRNA124a expression during neurogenesis. J Mater Chem B. 2013 Aug 14;1(35):4438–45.

184. Liu Y, Gong X, Dong W, Zhou R, Shuang S, Dong C. Nitrogen and phosphorus dual-doped carbon dots as a label-free sensor for Curcumin determination in real sample and cellular imaging. Talanta. 2018 Jun 1;183:61–9.

185. Wang J, Liu S, Chang Y, Fang L, Han K, Li M. High efficient delivery of siRNA into tumor cells by positively charged carbon dots. J Macromol Sci Part A Pure Appl Chem. 2018 Dec 2;55(11–12):770–4.

186. Zuo G, Xie A, Pan X, Su T, Li J, Dong W. Fluorine-Doped Cationic Carbon Dots for Efficient Gene Delivery. ACS Appl Nano Mater. 2018 May 25;1(5):2376–85.

187. Sharma P, Brown S, Walter G, Santra S, Moudgil B. Nanoparticles for bioimaging [Internet]. Vols. 123–126, Advances in Colloid and Interface Science. Elsevier; 2006. p. 471–85.

188. Sun YP, Zhou B, Lin Y, Wang W, Fernando KAS, Pathak P, et al. Quantum-sized carbon dots for bright and colorful photoluminescence. J Am Chem Soc. 2006;128(24):7756–7.

189. Guo H, You B, Zhao S, Wang Y, Sun G, Bai Y, et al. Full-color tunable photoluminescent carbon dots based on oil/water interfacial synthesis and their applications. RSC Adv. 2018 Jul 2;8(42):24002–12.

190. Bhunia SK, Saha A, Maity AR, Ray SC, Jana NR. Carbon nanoparticle-based fluorescent bioimaging probes. Sci Rep. 2013;3:1473.

191. Ya-Ping Sun, Bing Zhou, Yi Lin, Wei Wang, K. A. Shiral Fernando, Pankaj Pathak, et al. Quantum-Sized Carbon Dots for Bright and Colorful Photoluminescence. 2006;

192. Cao L, Wang X, Meziani MJ, Lu F, Wang H, Luo PG, et al. Carbon dots for multiphoton bioimaging. J Am Chem Soc. 2007;129(37):11318–9.

193. Lu Y, Zhang L, Lin H. The Use of a Microreactor for Rapid Screening of the Reaction Conditions and Investigation of the Photoluminescence Mechanism of Carbon Dots. Chem - A Eur J. 2014 Apr 7;20(15):4246–50.

194. Jiang K, Sun S, Zhang L, Lu Y, Wu A, Cai C, et al. Red, Green, and Blue Luminescence by Carbon Dots: Full-Color Emission Tuning and Multicolor Cellular Imaging. Angew Chemie. 2015 Apr 27;127(18):5450–3.

195. Meiling TT, Cywiński PJ, Bald I. White carbon: Fluorescent carbon nanoparticles with tunable quantum yield in a reproducible green synthesis. Sci Rep. 2016 Sep 23;6(1):28557.

196. Kenry, Duan Y, Liu B. Recent Advances of Optical Imaging in the Second Near-Infrared Window. Adv Mater. 2018 Nov;30(47):1802394.

197. Geng B, Yang D, Pan D, Wang L, Zheng F, Shen W, et al. NIR-responsive carbon dots for efficient photothermal cancer therapy at low power densities. Carbon N Y. 2018 Aug 1;134:153–62.

198. Huang Q, Liu Y, Zheng L, Wu L, Zhou Z, Chen J, et al. Biocompatible iron(II)-doped carbon dots as T 1-weighted magnetic resonance contrast agents and fluorescence imaging probes. Microchim Acta [Internet]. 2019 Aug 1;186(8).

199. Gong X, Lu W, Liu Y, Li Z, Shuang S, Dong C, et al. Low temperature synthesis of phosphorous and nitrogen co-doped yellow fluorescent carbon dots for sensing and bioimaging. J Mater Chem B. 2015 Aug 12;3(33):6813–9.

200. DaCosta M V., Doughan S, Han Y, Krull UJ. Lanthanide upconversion nanoparticles and applications in bioassays and bioimaging: A review. Anal Chim Acta. 2014 Jun 17;832:1–33.

201. Wen X, Yu P, Toh YR, Ma X, Tang J. On the upconversion fluorescence in carbon nanodots and graphene quantum dots. Chem Commun [Internet]. 2014 May 11;50(36):4703–6.

202. Wu F, Su H, Zhu X, Wang K, Zhang Z, Wong W-K. Near-infrared emissive lanthanide hybridized carbon quantum dots for bioimaging applications. J Mater Chem B. 2016 Sep 28;4(38):6366–72.

203. Chen Y, Xu J, Liu B, Li J, Fang X, Xiong L, et al. Enhanced Photoluminescence Properties of Carbon Dots by Doping with Europium. J Nanosci Nanotechnol. 2016 Apr 1;16(4):3735–8.

204. Zhang T, Zhai Y, Wang H, Zhu J, Xu L, Dong B, et al. Facilely prepared carbon dots and rare earth ion doped hybrid composites for ratio-metric pH sensing and white-light emission. RSC Adv. 2016 Jun 28;6(66):61468–72.

205. Alexiades-Armenakas M. Laser-mediated photodynamic therapy. Clin Dermatol. 2006 Jan 1;24(1):16–25.

206. Robertson CA, Evans DH, Abrahamse H. Photodynamic therapy (PDT): A short review on cellular mechanisms and cancer research applications for PDT [Internet]. Vol. 96, Journal of Photochemistry and Photobiology B: Biology. Elsevier; 2009. p. 1–8.

207. Kennedy JC, Pottier RH, Pross DC. Photodynamic therapy with endogenous protoporphyrin. IX: Basic principles and present clinical experience. J Photochem Photobiol B Biol. 1990 Jun 1;6(1–2):143–8.

208. Loewen GM, Pandey R, Bellnier D, Henderson B, Dougherty T. Endobronchial photodynamic therapy for lung cancer [Internet]. Vol. 38, Lasers in Surgery and Medicine. Wiley Subscription Services, Inc., A Wiley Company; 2006. p. 364–70.

209. Bader MJ, Stepp H, Beyer W, Pongratz T, Sroka R, Kriegmair M, et al. Photodynamic Therapy of Bladder Cancer - A Phase I Study Using Hexaminolevulinate (HAL). Urol Oncol Semin Orig Investig. 2013 Oct 1;31(7):1178–83.

210. Hu X-H, Feng Y, Lu JQ, Allison RR, Cuenca RE, Downie GH, et al. Modeling of a Type II Photofrin-mediated Photodynamic Therapy Process in a Heterogeneous Tissue Phantom. Photochem Photobiol. 2005 Nov 1;81(6):1460.

211. Hong EJ, Choi DG, Shim MS. Targeted and effective photodynamic therapy for cancer using functionalized nanomaterials. Vol. 6, Acta Pharmaceutica Sinica B. Chinese Academy of Medical Sciences; 2016. p. 297–307.

212. Huang Z. A Review of Progress in Clinical Photodynamic Therapy. Technol Cancer Res Treat. 2005 Jun;4(3):283–93.

213. Allison RR, Downie GH, Cuenca R, Hu XH, Childs CJH, Sibata CH. Photosensitizers in clinical PDT [Internet]. Vol. 1, Photodiagnosis and Photodynamic Therapy. Elsevier; 2004. p. 27–42.

214. Detty MR, Gibson SL, Wagner SJ. Current clinical and preclinical photosensitizers for use in photodynamic therapy [Internet]. Vol. 47, Journal of Medicinal Chemistry. American Chemical Society; 2004. p. 3897–915.

215. Konan-Kouakou YN, Boch R, Gurny R, Allémann E. In vitro and in vivo activities of verteporfin-loaded nanoparticles. J Control Release. 2005 Mar 2;103(1):83–91.

216. Allison RR, Bagnato VS, Sibata CH. Future of oncologic photodynamic therapy. Future Oncol. 2010 Jun;6(6):929–40.

217. Maeda H, Wu J, Sawa T, Matsumura Y, Hori K. Tumor vascular permeability and the EPR effect in macromolecular therapeutics: A review [Internet]. Vol. 65, Journal of Controlled Release. 2000. p. 271–84.

218. Bechet D, Couleaud P, Frochot C, Viriot ML, Guillemin F, Barberi-Heyob M. Nanoparticles as vehicles for delivery of photodynamic therapy agents [Internet]. Vol. 26, Trends in Biotechnology. Elsevier Current Trends; 2008. p. 612–21.

219. Li X, Lee S, Yoon J. Supramolecular photosensitizers rejuvenate photodynamic therapy. Vol. 47, Chemical Society Reviews. Royal Society of Chemistry; 2018. p. 1174–88.

220. Uehlinger P, Zellweger M, Wagnières G, Juillerat-Jeanneret L, Van Den Bergh H, Lange N. 5-Aminolevulinic acid and its derivatives: Physical chemical properties and protoporphyrin IX formation in cultured cells. J Photochem Photobiol B Biol. 2000 Jan 30;54(1):72–80.

221. Sazgarnia A, Shanei A, Eshghi H, Hassanzadeh-Khayyat M, Esmaily H, Shanei MM. Detection of sonoluminescence signals in a gel phantom in the presence of Protoporphyrin IX conjugated to gold nanoparticles. Ultrasonics. 2013 Jan 1;53(1):29–35.

222. Homayoni H, Jiang K, Zou X, Hossu M, Rashidi LH, Chen W. Enhancement of protoporphyrin IX performance in aqueous solutions for photodynamic therapy. Photodiagnosis Photodyn Ther. 2015 Jun 1;12(2):258–66.

223. Wu L, Luderer M, Yang X, Swain C, Zhang H, Nelson K, et al. Surface passivation of carbon nanoparticles with branched macromolecules influences near infrared bioimaging. Theranostics. 2013;3(9):677–86.

224. Zhou N, Zhu S, Maharjan S, Hao Z, Song Y, Zhao X, et al. Elucidating the endocytosis, intracellular trafficking, and exocytosis of carbon dots in neural cells. RSC Adv. 2014 Nov 12;4(107):62086–95.

225. Wang J, Qiu J. A review of carbon dots in biological applications [Internet]. Vol. 51, Journal of Materials Science. Springer US; 2016. p. 4728–38.

226. Mandani S, Sharma B, Dey D, Sarma TK. White light emission by controlled mixing of carbon dots and rhodamine B for applications in optical thermometry and selective Fe^{3+} detection. RSC Adv. 2016 Sep 6;6(88):84599–603.

227. Wang Q, Zhang C, Shen G, Liu H, Fu H, Cui D. Fluorescent carbon dots as an efficient siRNA nanocarrier for its interference therapy in gastric cancer cells. J Nanobiotechnology. 2014 Dec 30;12(1):58.

228. Thakur M, Pandey S, Mewada A, Patil V, Khade M, Goshi E, et al. Antibiotic conjugated fluorescent carbon dots as a theranostic agent for controlled drug release, bioimaging, and enhanced antimicrobial activity. J Drug Deliv. 2014;2014:282193.

229. Li L, Dong T. Photoluminescence tuning in carbon dots: Surface passivation or/and functionalization, heteroatom doping. J Mater Chem C. 2018;6(30):7944–70.

230. Jazayeri MH, Amani H, Pourfatollah AA, Pazoki-Toroudi H, Sedighimoghaddam B. Various methods of gold nanoparticles (GNPs) conjugation to antibodies. Sens Bio-Sensing Res. 2016 Jul 1;9:17–22.

231. Fischer MJE. Amine Coupling Through EDC/NHS: A Practical Approach. In Humana

Press; 2010. p. 55–73.

232. Tsay JM, Trzoss M, Shi L, Kong X, Selke M, Jung ME, et al. Singlet oxygen production by Peptide-coated quantum dot-photosensitizer conjugates. J Am Chem Soc. 2007 May 30;129(21):6865–71.

233. Fu M, Ehrat F, Wang Y, Milowska KZ, Reckmeier C, Rogach AL, et al. Carbon Dots: A Unique Fluorescent Cocktail of Polycyclic Aromatic Hydrocarbons. Nano Lett. 2015 Sep 9;15(9):6030–5.

234. Zhu H, Wang X, Li Y, Wang Z, Yang F, Yang X. Microwave synthesis of fluorescent carbon nanoparticles with electrochemiluminescence properties. Chem Commun. 2009 Sep 14;(34):5118.

235. Devi S, Gupta RK, Paul AK, Kumar V, Sachdev A, Gopinath P, et al. Ethylenediamine mediated luminescence enhancement of pollutant derivatized carbon quantum dots for intracellular trinitrotoluene detection: soot to shine. RSC Adv. 2018 Sep 21;8(57):32684–94.

236. De B, Karak N. Recent progress in carbon dot-metal based nanohybrids for photochemical and electrochemical applications. J Mater Chem A [Internet]. 2017;5(5):1826–59.

237. Reyes D, Camacho M, Camacho M, Mayorga M, Weathers D, Salamo G, et al. Laser Ablated Carbon Nanodots for Light Emission. Nanoscale Res Lett. 2016 Dec 22;11(1):424.

238. Liu Y, Xiao N, Gong N, Wang H, Shi X, Gu W, et al. One-step microwave-assisted polyol synthesis of green luminescent carbon dots as optical nanoprobes. Carbon N Y. 2014 Mar 1;68:258–64.

239. Liu H, Ye T, Mao C. Fluorescent Carbon Nanoparticles Derived from Candle Soot. Angew Chemie Int Ed. 2007 Aug 27;46(34):6473–5.

240. Zhang H, Chen Y, Liang M, Xu L, Qi S, Chen H, et al. Solid-Phase Synthesis of Highly Fluorescent Nitrogen-Doped Carbon Dots for Sensitive and Selective Probing Ferric Ions in Living Cells. Anal Chem. 2014 Oct 7;86(19):9846–52.

241. Liu M, Xu Y, Niu F, Gooding JJ, Liu J. Carbon quantum dots directly generated from electrochemical oxidation of graphite electrodes in alkaline alcohols and the applications for specific ferric ion detection and cell imaging. Analyst. 2016 Apr 25;141(9):2657–64.

242. Campos BB, Oliva MM, Contreras-Cáceres R, Rodriguez-Castellón E, Jiménez-Jiménez J, da Silva JCGE, et al. Carbon dots on based folic acid coated with PAMAM dendrimer as platform for Pt(IV) detection. J Colloid Interface Sci. 2016 Mar 1;465:165–73.

243. Sachdev A, Gopinath P. Green synthesis of multifunctional carbon dots from coriander leaves and their potential application as antioxidants, sensors and bioimaging agents. Analyst. 2015 Jun 2;140(12):4260–9.

244. Cheng F, An X, Zheng C, Cao S. Green synthesis of fluorescent hydrophobic carbon quantum dots and their use for 2,4,6-trinitrophenol detection. RSC Adv. 2015 Oct 29;5(113):93360–3.

245. Gu J, Li X, Hu D, Liu Y, Zhang G, Jia X, et al. Green synthesis of amphiphilic carbon dots from organic solvents: application in fluorescent polymer composites and bio-imaging. RSC Adv. 2018 Apr 3;8(23):12556–61.

246. Shu Y, Lu J, Mao Q-X, Song R-S, Wang X-Y, Chen X-W, et al. Ionic liquid mediated organophilic carbon dots for drug delivery and bioimaging. Carbon N Y. 2017 Apr 1;114:324–33.

247. Gawande MB, Shelke SN, Zboril R, Varma RS. Microwave-Assisted Chemistry: Synthetic Applications for Rapid Assembly of Nanomaterials and Organics. Acc Chem Res. 2014 Apr 15;47(4):1338–48.

248. Reimbert C, Minzoni AA, Smynth NF. Effect of radiation losses on hotspot formation and propagation in microwave heating. IMA J Appl Math. 1996 Oct 1;57(2):165–79.

249. Polshettiwar V, Varma RS. Green chemistry by nano-catalysis. Green Chem. 2010 May 11;12(5):743.

250. Yildiz I, Deniz E, McCaughan B, Cruickshank SF, Callan JF, Raymo FM. Hydrophilic CdSe−ZnS Core−Shell Quantum Dots with Reactive Functional Groups on Their Surface. Langmuir. 2010 Jul 6;26(13):11503–11.

251. Gunter EW, Turner WE, Huff DL. Investigation of protoporphyrin IX standard materials used in acid-extraction methods, and a proposed correction for the millimolar absorptivity of protoporphyrin IX. Clin Chem. 1989 Aug;35(8):1601–8. Available from: http://www.ncbi.nlm.nih.gov/pubmed/2758627

252. McKenzie LK, Sazanovich I V., Baggaley E, Bonneau M, Guerchais V, Williams JAG, et al. Metal Complexes for Two-Photon Photodynamic Therapy: A Cyclometallated Iridium Complex Induces Two-Photon Photosensitization of Cancer Cells under Near-IR Light. Chem - A Eur J [Internet]. 2017 Jan 5;23(2):234–8.

253. Naik VM, Gunjal DB, Gore AH, Pawar SP, Mahanwar ST, Anbhule P V., et al. Quick and low cost synthesis of sulphur doped carbon dots by simple acidic carbonization of sucrose for the detection of Fe3+ ions in highly acidic environment. Diam Relat Mater [Internet]. 2018 Sep 1;88:262–8.

254. Jaiswal A, Ghosh SS, Chattopadhyay A. One step synthesis of C-dots by microwave mediated caramelization of poly(ethylene glycol). Chem Commun. 2012 Dec 5;48(3):407–9.

255. Cheng C, Shi Y, Li M, Xing M, Wu Q. Carbon quantum dots from carbonized walnut shells: Structural evolution, fluorescence characteristics, and intracellular bioimaging. Mater Sci Eng C. 2017 Oct 1;79:473–80.

256. Prasannan A, Imae T. One-Pot Synthesis of Fluorescent Carbon Dots from Orange Waste Peels. Ind Eng Chem Res. 2013 Nov 6;52(44):15673–8.

257. Atkin P, Daeneke T, Wang Y, Carey BJ, Berean KJ, Clark RM, et al. 2D WS2/carbon dot hybrids with enhanced photocatalytic activity. J Mater Chem A. 2016 Aug 30;4(35):13563–71.

258. Fan RJ, Sun Q, Zhang L, Zhang Y, Lu AH. Photoluminescent carbon dots directly derived from polyethylene glycol and their application for cellular imaging. Carbon N Y [Internet]. 2014 May;71:87–93.

259. Gude V, Das A, Chatterjee T, Mandal PK. Molecular origin of photoluminescence of carbon dots: aggregation-induced orange-red emission. Phys Chem Chem Phys. 2016 Oct 12;18(40):28274–80.

260. Šimkovic I, Šurina I, Vričan M. Primary reactions of sucrose thermal degradation. J Anal Appl Pyrolysis. 2003;70(2):493–504.

261. Tostado-Plascencia MM, Sanchez-Tizapa M, Zamudio-Ojeda A, Suárez-Gómez A, Castañeda-Valderrama R, Carreón-Alvarez MA, et al. Synthesis and characterization of multiwalled carbon nanotubes-protoporphyrin IX composites using acid functionalized or nitrogen doped carbon nanotubes. Diam Relat Mater. 2016 Nov 1;70:65–75.

262. Friedman A, Claypool S, Liu R. The Smart Targeting of Nanoparticles. Curr Pharm Des. 2013;19(35):6315–29.

263. Hua X-WW, Bao Y-WW, Chen Z, Wu F-GG. Carbon quantum dots with intrinsic mitochondrial targeting ability for mitochondria-based theranostics. Nanoscale. 2017 Aug 3;9(30):10948–60.

264. Hua XW, Bao YW, Wu FG. Fluorescent Carbon Quantum Dots with Intrinsic Nucleolus-Targeting Capability for Nucleolus Imaging and Enhanced Cytosolic and Nuclear Drug Delivery. ACS Appl Mater Interfaces. 2018;10(13):10664–77.

265. Wu X, Sun S, Wang Y, Zhu J, Jiang K, Leng Y, et al. A fluorescent carbon-dots-based mitochondria-targetable nanoprobe for peroxynitrite sensing in living cells. Biosens Bioelectron. 2017 Apr 15;90:501–7.

266. Gilles V, Vieira MA, Lacerda V, Castro EVR, Santos RB, Orestes E, et al. A new, simple and efficient method of steglich esterification of juglone with long-chain fatty acids: Synthesis of a new class of non-polymeric wax deposition inhibitors for crude oil. J Braz Chem Soc [Internet]. 2015 Jan 1;26(1):74–83.

267. El-Shafey A. “Zero-length” cross-linking in solid state as an approach for analysis of protein-protein interactions. Protein Sci [Internet]. 2006 Feb 1;15(3):429–40.

268. Zhu L, Zhu Y, Meng X, Hao J, Li Q, Wei Y, et al. DCC-Assisted Esterification of a Polyoxometalate-Functionalized Phenol with Carboxylic Acids (DCC: Dicyclohexylcarbodiimide). Chem - A Eur J. 2008 Dec 8;14(35):10923–7.

269. Totaro KA, Liao X, Bhattacharya K, Finneman JI, Sperry JB, Massa MA, et al. Systematic Investigation of EDC/sNHS-Mediated Bioconjugation Reactions for Carboxylated Peptide Substrates. Bioconjug Chem. 2016 Apr 20;27(4):994–1004.

270. Zhao Y, Liu X, Yang Y, Kang L, Yang Z, Liu W, et al. Carbon Dots: From Intense

Absorption in Visible Range to Excitation-Independent and Excitation-Dependent Photoluminescence. Fullerenes Nanotub Carbon Nanostructures [Internet]. 2015 Nov 2;23(11):922–9.

271. Sharma A, Gadly T, Gupta A, Ballal A, Ghosh SK, Kumbhakar M. Origin of Excitation Dependent Fluorescence in Carbon Nanodots. J Phys Chem Lett [Internet]. 2016 Sep 15;7(18):3695–702.

272. Zhang J, Yu SH. Carbon dots: large-scale synthesis, sensing and bioimaging [Internet]. Vol. 19, Materials Today. Elsevier; 2016. p. 382–93.

273. Li X, Zhang S, Kulinich SA, Liu Y, Zeng H. Engineering surface states of carbon dots to achieve controllable luminescence for solid-luminescent composites and sensitive Be2+ detection. Sci Rep [Internet]. 2014 May 15;4.

274. Chen X, Zhang W, Wang Q, Fan J. C8-structured carbon quantum dots: Synthesis, blue and green double luminescence, and origins of surface defects. Carbon N Y. 2014 Nov 1;79(1):165–73.

275. Wang P, Liu JH, Gao H, Hu Y, Hou X, LeCroy GE, et al. Host-guest carbon dots as high-performance fluorescence probes. J Mater Chem C. 2017 Jun 29;5(25):6328–35.

276. Greiler LC, Haase H, Mahltig B. Microwave assisted conversion of an amino acid into a fluorescent solution. Acta Chim Slov [Internet]. 2018;65(4):865–74.

277. Peng Z, Han X, Li S, Al-Youbi AO, Bashammakh AS, El-Shahawi MS, et al. Carbon dots: Biomacromolecule interaction, bioimaging and nanomedicine. Coord Chem Rev. 2017 Jul 15;343:256–77.

278. Ding H, Yu SB, Wei JS, Xiong HM. Full-color light-emitting carbon dots with a surface-state-controlled luminescence mechanism. ACS Nano. 2016 Jan 26;10(1):484–91.

279. Sellitti C, Koenig JL, Ishida H. Surface characterization of graphitized carbon fibers by attenuated total reflection fourier transform infrared spectroscopy. Carbon N Y. 1990 Jan 1;28(1):221–8.

280. Lei Z, Xu S, Wan J, Wu P. Facile synthesis of N-rich carbon quantum dots by spontaneous polymerization and incision of solvents as efficient bioimaging probes and advanced electrocatalysts for oxygen reduction reaction. Nanoscale. 2016 Jan 21;8(4):2219–26.

281. Liu X, Pang J, Xu F, Zhang X. Simple Approach to Synthesize Amino-Functionalized Carbon Dots by Carbonization of Chitosan. Sci Rep. 2016 Nov 5;6(1):31100.

282. Wang H, Ning G, He X, Ma X, Yang F, Xu Z, et al. Carbon quantum dots derived by direct carbonization of carbonaceous microcrystals in mesophase pitch. Nanoscale. 2018 Nov 22;10(45):21492–8.

283. Lee WH, Lee JM, Lim C, Kim S, Kim SG. Structural requirements within protoporphyrin IX in the inhibition of heat shock protein 90. Chem Biol Interact. 2013 Jun;204(1):49–57.

284. Tong G, Wang J, Wang R, Guo X, He L, Qiu F, et al. Amorphous carbon dots with high two-photon fluorescence for cellular imaging passivated by hyperbranched poly(amino amine). J Mater Chem B [Internet]. 2015 Jan 28;3(4):700–6.

285. Ciriminna R, Meneguzzo F, Delisi R, Pagliaro M. Citric acid: Emerging applications of key biotechnology industrial product. Vol. 11, Chemistry Central Journal. BioMed Central Ltd.; 2017.

286. Stoddart MJ. Cell viability assays: introduction. Vol. 740, Methods in molecular biology (Clifton, N.J.). 2011. p. 1–6.

287. Barrera G. Oxidative Stress and Lipid Peroxidation Products in Cancer Progression and Therapy. ISRN Oncol [Internet]. 2012;2012:1–21.

288. Jena NR. DNA damage by reactive species: Mechanisms, mutation and repair. In: Journal of Biosciences [Internet]. 2012. p. 503–7.

289. Davies MJ. Reactive species formed on proteins exposed to singlet oxygen. Vol. 3, Photochemical and Photobiological Sciences. 2004. p. 17–25.

290. Allison RR, Moghissi K. Photodynamic therapy (PDT): PDT mechanisms. Clin Endosc [Internet]. 2013;46(1):24–9.

291. Zou Y, Celli A, Zhu H, Elmahdy A, Cao Y, Hui X, et al. Confocal laser scanning microscopy to estimate nanoparticles' human skin penetration in vitro. Int J Nanomedicine [Internet]. 2017 Oct 31;12:8035–41.

292. Postovit L-M, Seftor EA, Seftor REB, Hendrix MJC. A Three-Dimensional Model to Study the Epigenetic Effects Induced by the Microenvironment of Human Embryonic Stem Cells. Stem Cells [Internet]. 2006 Mar;24(3):501–5.

293. Xu H, Sun Y, Zhang Y, Wang W, Dan J, Yao J, et al. Protoporphyrin IX induces a necrotic cell death in human THP-1 macrophages through activation of reactive oxygen species/c-Jun N-terminal protein kinase pathway and opening of mitochondrial permeability transition pore. Cell Physiol Biochem. 2014;34(6):1835–48.

294. Zhao SG, Chen XF, Wang LG, Yang G, Han DY, Teng L, et al. Increased expression of ABCB6 enhances protoporphyrin ix accumulation and photodynamic effect in human glioma. Ann Surg Oncol [Internet]. 2013;20(13):4379–88.

295. Ding H, Sumer BD, Kessinger CW, Dong Y, Huang G, Boothman DA, et al. Nanoscopic micelle delivery improves the photophysical properties and efficacy of photodynamic therapy of protoporphyrin IX. J Control Release. 2011 May 10;151(3):271–7.

296. Schmidt MH, Meyer GA, Reichert KW, Cheng J, Krouwer HG, Ozker K, et al. Evaluation of photodynamic therapy near functional brain tissue in patients with recurrent brain tumors. J Neurooncol. 2004;67(1–2):201–7.

297. Mathews MS, Angell-Petersen E, Sanchez R, Sun CH, Vo V, Hirschberg H, et al. The effects of ultra low fluence rate single and repetitive photodynamic therapy on glioma spheroids. Lasers Surg Med [Internet]. 2009 Oct;41(8):578–84.

298. Robinson DJ, De Bruijn HS, Van Der Veen N, Stringer MR, Brown SB, Star WM. Fluorescence Photobleaching of ALA-induced Protoporphyrin IX during Photodynamic Therapy of Normal Hairless Mouse Skin: The Effect of Light Dose and Irradiance and the Resulting Biological Effect. Photochem Photobiol. 1998 Jan;67(1):140–9.

299. Braslavsky SE. Glossary of terms used in photochemistry 3rd edition: (IUPAC Recommendations 2006). Vol. 79, Pure and Applied Chemistry. 2007. p. 293–465.

300. Kah JCY, Wan RCY, Wong KY, Mhaisalkar S, Sheppard CJR, Olivo M. Combinatorial treatment of photothermal therapy using gold nanoshells with conventional photodynamic therapy to improve treatment efficacy: An in vitro study. Lasers Surg Med. 2008 Oct;40(8):584–9.

301. Cox GS, Whitten DG. Mechanisms for the Photooxidation of Protoporphyrin IX in Solution. J Am Chem Soc. 1982 Jan;104(2):516–21.

302. Tromberg BJ, Orenstein A, Kimel S, Barker SJ, Hyatt J, Nelson JS, et al. In vivo tumor oxygen tension measurements for the evaluation of the efficiency of photodynamic therapy. Photochem Photobiol. 1990 Aug;52(2):375–85.

303. Reibaldi M, Boscia F, Avitabile T, Russo A, Cannemi V, Uva MG, et al. Low-fluence photodynamic therapy in longstanding chronic central serous chorioretinopathy with foveal and gravitational atrophy. Eur J Ophthalmol [Internet]. 2009;19(1):154–8.

304. Ericson MB, Sandberg C, Stenquist B, Gudmundson F, Karlsson M, Ros AM, et al. Photodynamic therapy of actinic keratosis at varying fluence rates: Assessment of photobleaching, pain and primary clinical outcome. Br J Dermatol. 2004 Dec;151(6):1204–12.

305. Li M, Yu C, Hu C, Yang W, Zhao C, Wang S, et al. Solvothermal conversion of coal into nitrogen-doped carbon dots with singlet oxygen generation and high quantum yield. Chem Eng J [Internet]. 2017;320:570–5.

306. Charara M, Tovmasyan A, Batinic-Haberle I, Craik J, Benov L. Post-illumination cellular effects of photodynamic treatment. Hamblin M, editor. PLoS One. 2017 Dec 4;12(12):e0188535.

307. Chipuk JE, Green DR. How do BCL-2 proteins induce mitochondrial outer membrane permeabilization? Vol. 18, Trends in Cell Biology. 2008. p. 157–64.

308. Buytaert E, Dewaele M, Agostinis P. Molecular effectors of multiple cell death pathways initiated by photodynamic therapy. Vol. 1776, Biochimica et Biophysica Acta - Reviews on Cancer. 2007. p. 86–107.

309. Mroz P, Yaroslavsky A, Kharkwal GB, Hamblin MR. Cell death pathways in photodynamic therapy of cancer. Vol. 3, Cancers. 2011. p. 2516–39.

310. Chung J, Chen C, Paw BH. Heme metabolism and erythropoiesis [Internet]. Vol. 19, Current Opinion in Hematology. NIH Public Access; 2012. p. 156–62.

311. Hilf R. Mitochondria are targets of photodynamic therapy [Internet]. Vol. 39, Journal of Bioenergetics and Biomembranes. Kluwer Academic Publishers-Plenum Publishers;

2007. p. 85–9.

312. Zawacka-Pankau J, Issaeva N, Hossain S, Pramanik A, Selivanova G, Podhajska AJ. Protoporphyrin IX interacts with wild-type p53 protein in vitro and induces cell death of human colon cancer cells in a p53-dependent and -independent manner. J Biol Chem. 2007 Jan 26;282(4):2466–72.

313. Du F, Li J, Hua Y, Zhang M, Zhou Z, Yuan J, et al. Multicolor nitrogen-doped carbon dots for live cell imaging. J Biomed Nanotechnol [Internet]. 2015 May 1;11(5):780–8.

314. Gao G, Jiang YW, Yang J, Wu FG. Mitochondria-targetable carbon quantum dots for differentiating cancerous cells from normal cells. Nanoscale [Internet]. 2017 Dec 14;9(46):18368–78.

315. Zhou D, Li D, Jing P, Zhai Y, Shen D, Qu S, et al. Conquering Aggregation-Induced Solid-State Luminescence Quenching of Carbon Dots through a Carbon Dots-Triggered Silica Gelation Process. Chem Mater. 2017 Feb 28;29(4):1779–87.

316. Imamura Y, Mukohara T, Shimono Y, Funakoshi Y, Chayahara N, Toyoda M, et al. Comparison of 2D- and 3D-culture models as drug-testing platforms in breast cancer. Oncol Rep. 2015 Apr 1;33(4):1837–43.

317. Silva ZS, Bussadori SK, Santos Fernandes KP, Huang YY, Hamblin MR. Animal models for photodynamic therapy (PDT). Vol. 35, Bioscience Reports. Portland Press Ltd; 2015.

318. Noble JN, Mishra A. Development and Significance of Mouse Models in Lymphoma Research. Current Hematologic Malignancy Reports. Current Science Inc.; 2019.

319. Weiswald LB, Bellet D, Dangles-Marie V. Spherical Cancer Models in Tumor Biology. Vol. 17, Neoplasia (United States). Neoplasia Press, Inc.; 2015. p. 1–15.

320. Vaira V, Fedele G, Pyne S, Fasoli E, Zadra G, Bailey D, et al. Preclinical model of organotypic culture for pharmacodynamic profiling of human tumors. Proc Natl Acad Sci U S A [Internet]. 2010 May 4;107(18):8352–6.

321. Carletti E, Motta A, Migliaresi C. Scaffolds for tissue engineering and 3D cell culture. Vol. 695, Methods in molecular biology (Clifton, N.J.). 2011. p. 17–39.

322. Phan N, Hong JJ, Tofig B, Mapua M, Elashoff D, Moatamed NA, et al. A simple high-throughput approach identifies actionable drug sensitivities in patient-derived tumor organoids. Commun Biol [Internet]. 2019 Dec 1;2(1).

323. Gong X, Lin C, Cheng J, Su J, Zhao H, Liu T, et al. Generation of multicellular tumor spheroids with microwell-based agarose scaffolds for drug testing. Kerkis I, editor. PLoS One. 2015 Jun 19;10(6):e0130348.

324. Hagemann J, Jacobi C, Hahn M, Schmid V, Welz C, Schwenk-Zieger S, et al. Spheroid-based 3D Cell Cultures Enable Personalized Therapy Testing and Drug Discovery in Head and Neck Cancer. Anticancer Res. 2017;37(5):2201–10.

325. Ham SL, Joshi R, Thakuri PS, Tavana H. Liquid-based three-dimensional tumor models

for cancer research and drug discovery. Exp Biol Med. 2016 May 11;241(9):939–54.

326. Mehta G, Hsiao AY, Ingram M, Luker GD, Takayama S. Opportunities and challenges for use of tumor spheroids as models to test drug delivery and efficacy. J Control Release [Internet]. 2012 Dec 10;164(2):192–204.

327. Kim S-H, Kuh H-J, R. Dass C. The Reciprocal Interaction: Chemotherapy and Tumor Microenvironment. Curr Drug Discov Technol [Internet]. 2011 May 9;8(2):102–6.

328. Pereira PMR, Berisha N, Bhupathiraju NVSDK, Fernandes R, Tomé JPC, Drain CM. Cancer cell spheroids are a better screen for the photodynamic efficiency of glycosylated photosensitizers. Moreno-Sanchez R, editor. PLoS One. 2017 May 17;12(5):e0177737.

329. West CML. Size-dependent resistance of human tumour spheroids to photodynamic treatment. Br J Cancer [Internet]. 1989;59(4):510–4.

330. Aguilar Cosme, Jose Ricardo. Carbon dot – protoporphyrin IX conjugates for improved drug delivery and bioimaging. PLoS One [Internet]. 2019;

331. Chan FKM, Moriwaki K, De Rosa MJ. Detection of necrosis by release of lactate dehydrogenase activity. Methods Mol Biol [Internet]. 2013;979:65–70.

332. Rühland S, Wechselberger A, Spitzweg C, Huss R, Nelson PJ, Harz H. Quantification of in vitro mesenchymal stem cell invasion into tumor spheroids using selective plane illumination microscopy. J Biomed Opt [Internet]. 2015 Apr 3;20(4):040501.

333. Lin RZ, Chang HY. Recent advances in three-dimensional multicellular spheroid culture for biomedical research. Vol. 3, Biotechnology Journal. Wiley-VCH Verlag; 2008. p. 1172–84.

334. Däster S, Amatruda N, Calabrese D, Ivanek R, Turrini E, Droeser RA, et al. Induction of hypoxia and necrosis in multicellular tumor spheroids is associated with resistance to chemotherapy treatment. Oncotarget [Internet]. 2017;8(1):1725–36.

335. Friedrich J, Seidel C, Ebner R, Kunz-Schughart LA. Spheroid-based drug screen: Considerations and practical approach. Nat Protoc [Internet]. 2009;4(3):309–24.

336. Quent VMC, Loessner D, Friis T, Reichert JC, Hutmacher DW. Discrepancies between metabolic activity and DNA content as tool to assess cell proliferation in cancer research. J Cell Mol Med [Internet]. 2010 Apr;14(4):1003–13.

337. Ng KW, Leong DTW, Hutmacher DW. The challenge to measure cell proliferation in two and three dimensions. Tissue Eng [Internet]. 2005 Jan;11(1–2):182–91.

338. Riss T, Niles A, Moravec R, Karassina N, Vidugiriene J. Cytotoxicity Assays: In Vitro Methods to Measure Dead Cells [Internet]. Assay Guidance Manual. 2004. Available from: http://www.ncbi.nlm.nih.gov/pubmed/31070879

339. Otto WR. Fluorimetric DNA assay of cell number. Methods Mol Biol [Internet]. 2005;289:251–62.

340. Dufau I, Frongia C, Sicard F, Dedieu L, Cordelier P, Ausseil F, et al. Multicellular tumor

spheroid model to evaluate spatio-temporal dynamics effect of chemotherapeutics: application to the gemcitabine/CHK1 inhibitor combination in pancreatic cancer. BMC Cancer. 2012 Dec 13;12(1):15.

341. Olive PL, Durand RE. Drug and radiation resistance in spheroids: cell contact and kinetics. Cancer Metastasis Rev [Internet]. 1994 Jun;13(2):121–38.

342. Baronzio G, Schwartz L, Kiselevsky M, Guais A, Sanders E, Milanesi G, et al. Tumor interstitial fluid as modulator of cancer inflammation, thrombosis, immunity and angiogenesis. Vol. 32, Anticancer Research. 2012. p. 405–14.

343. Sriraman SK, Aryasomayajula B, Torchilin VP. Barriers to drug delivery in solid tumors. Vol. 2, Tissue Barriers. Taylor and Francis Inc.; 2014. p. e29528-1-e29528-10.

344. Madsen SJ, Sun C-H, Tromberg BJ, Wallace VP, Hirschberg H. Photodynamic Therapy of Human Glioma Spheroids Using 5-Aminolevulinic Acid ¶. Photochem Photobiol [Internet]. 2007 May 1;72(1):128–34.

345. Sitnik TM, Henderson BW. The Effect of Fluence Rate on Tumor and Normal Tissue Responses to Photodynamic Therapy. Photochem Photobiol. 1998 Apr;67(4):462–6.

346. Hempstead J, Jones DP, Ziouche A, Cramer GM, Rizvi I, Arnason S, et al. Low-cost photodynamic therapy devices for global health settings: Characterization of battery-powered LED performance and smartphone imaging in 3D tumor models. Sci Rep [Internet]. 2015 May 12;5.

347. Robinson DJ, De Bruijn HS, Van Der Veen N, Stringer MR, Brown SB, Star WM. Protoporphyrin IX fluorescence photobleaching during ALA-mediated photodynamic therapy of UVB-induced tumors in hairless mouse skin. Photochem Photobiol [Internet]. 1999;69(1):61–70.

348. De Vijlder HC, Sterenborg HJCM, Martino Neumann HA, Robinson DJ, De Haas ERM. Light fractionation significantly improves the response of superficial basal cell carcinoma to aminolaevulinic acid photodynamic therapy: Five-year follow-up of a randomized, prospective trial. Acta Derm Venereol [Internet]. 2012;92(6):641–7.

349. Foster TH, Hartley DF, Nichols MG, Hilf R. Fluence Rate Effects in Photodynamic Therapy of Multicell Tumor Spheroids. Cancer Res [Internet]. 1993;53(6):1249–54.

350. Babilas P, Schacht V, Liebsch G, Wolfbeis OS, Landthaler M, Szeimies RM, et al. Effects of light fractionation and different fluence rates on photodynamic therapy with 5-aminolaevulinic acid in vivo. Br J Cancer [Internet]. 2003 May 6;88(9):1462–9.

351. Korbelik M, Krosl G, Krosl J, Dougherty GJ. The role of host lymphoid populations in the response of mouse EMT6 tumor to photodynamic therapy. Cancer Res [Internet]. 1996 Dec 15;56(24):5647–52.

352. Foster TH, Murant RS, Bryant RG, Knox RS, Gibson SL, Hilf R. Oxygen Consumption and Diffusion Effects in Photodynamic Therapy. Radiat Res [Internet]. 1991 Jun;126(3):296.

353. Herman AB, van Savage M, West GB. A quantitative theory of solid tumor growth,

metabolic rate and vascularization. PLoS One [Internet]. 2011 Sep 29;6(9).

354. Jarvi MT, Patterson MS, Wilson BC. Insights into photodynamic therapy dosimetry: Simultaneous singlet oxygen luminescence and photosensitizer photobleaching measurements. Biophys J [Internet]. 2012 Feb 8;102(3):661–71.

355. Pogue BW, Braun RD, Lanzen JL, Erickson C, Dewhirst MW. Analysis of the Heterogeneity of pO2 Dynamics During Photodynamic Therapy with Verteporfin. Photochem Photobiol [Internet]. 2001;74(5):700.

356. De Bruijn HS, De Haas ERM, Hebeda KM, Van Der Ploeg - Van Den Heuvel A, Sterenborg HJCM, Neumann HAM, et al. Light fractionation does not enhance the efficacy of methyl 5-aminolevulinate mediated photodynamic therapy in normal mouse skin. In: Photochemical and Photobiological Sciences [Internet]. 2007. p. 1325–31.

357. Green DR. Apoptotic pathways: Ten minutes to dead. Vol. 121, Cell. 2005. p. 671–4.

358. Ouyang G, Xiong L, Liu Z, Lam B, Bui B, Ma L, et al. Inhibition of autophagy potentiates the apoptosis-inducing effects of photodynamic therapy on human colon cancer cells. Photodiagnosis Photodyn Ther [Internet]. 2018 Mar 1;21:396–403.

359. Henderson BW, Busch TM, Vaughan LA, Frawley NP, Babich D, Sosa TA, et al. Photofrin photodynamic therapy can significantly deplete or preserve oxygenation in human basal cell carcinomas during treatment, depending on fluence rate. Cancer Res [Internet]. 2000 Feb 1;60(3):525–9.

360. Fingar VH, Henderson BW. DRUG and LIGHT DOSE DEPENDENCE OF PHOTODYNAMIC THERAPY: A STUDY OF TUMOR and NORMAL TISSUE RESPONSE. Photochem Photobiol [Internet]. 1987;46(5):837–47.

361. Seshadri M, Bellnier DA, Vaughan LA, Spernyak JA, Mazurchuk R, Foster TH, et al. Light delivery over extended time periods enhances the effectiveness of photodynamic therapy. Clin Cancer Res [Internet]. 2008 May 1;14(9):2796–805.

362. Lazzari G, Vinciguerra D, Balasso A, Nicolas V, Goudin N, Garfa-Traore M, et al. Light sheet fluorescence microscopy versus confocal microscopy: in quest of a suitable tool to assess drug and nanomedicine penetration into multicellular tumor spheroids. Eur J Pharm Biopharm [Internet]. 2019 Sep 1;142:195–203.

363. Yamamoto J, Ogura SI, Shimajiri S, Nakano Y, Akiba D, Kitagawa T, et al. 5-Aminolevulinic acid-induced protoporphyrin IX with multi-doseionizing irradiation enhances host antitumor response and strongly inhibits tumor growth in experimental glioma in vivo. Mol Med Rep [Internet]. 2015 Mar 1;11(3):1813–9.

364. Das V, Fürst T, Gurská S, Džubák P, Hajdúch M. Reproducibility of uniform spheroid formation in 384-well plates: The effect of medium evaporation. J Biomol Screen [Internet]. 2016 Oct 1;21(9):923–30.

365. Amaral RLF, Miranda M, Marcato PD, Swiech K. Comparative analysis of 3D bladder tumor spheroids obtained by forced floating and hanging drop methods for drug screening. Front Physiol [Internet]. 2017 Aug 22;8(AUG).

366. Leek RD, Stratford I, Harris AL. The role of hypoxia-inducible factor-1 in three-dimensional tumor growth, apoptosis, and regulation by the insulin-signaling pathway. Cancer Res [Internet]. 2005 May 15;65(10):4147–52.

367. Kim TH, Mount CW, Gombotz WR, Pun SH. The delivery of doxorubicin to 3-D multicellular spheroids and tumors in a murine xenograft model using tumor-penetrating triblock polymeric micelles. Biomaterials [Internet]. 2010 Oct;31(28):7386–97.

368. Kepp O, Galluzzi L, Lipinski M, Yuan J, Kroemer G. Cell death assays for drug discovery. Vol. 10, Nature Reviews Drug Discovery. 2011. p. 221–37.

369. Vinci M, Gowan S, Boxall F, Patterson L, Zimmermann M, Court W, et al. Advances in establishment and analysis of three-dimensional tumor spheroid-based functional assays for target validation and drug evaluation. BMC Biol [Internet]. 2012 Mar 22;10.

370. Sant S, Johnston PA. The production of 3D tumor spheroids for cancer drug discovery. Vol. 23, Drug Discovery Today: Technologies. Elsevier Ltd; 2017. p. 27–36.

371. Piccinini F. AnaSP: A software suite for automatic image analysis of multicellular spheroids. Comput Methods Programs Biomed [Internet]. 2015 Apr 1;119(1):43–52.

372. Thakuri PS, Gupta M, Plaster M, Tavana H. Quantitative Size-Based Analysis of Tumor Spheroids and Responses to Therapeutics. Assay Drug Dev Technol [Internet]. 2019 Apr 1;17(3):140–9.

373. Ivanov DP, Parker TL, Walker DA, Alexander C, Ashford MB, Gellert PR, et al. Multiplexing Spheroid Volume, Resazurin and Acid Phosphatase Viability Assays for High-Throughput Screening of Tumour Spheroids and Stem Cell Neurospheres. Mancini MA, editor. PLoS One. 2014 Aug 13;9(8):e103817.

374. Piccinini F, Tesei A, Arienti C, Bevilacqua A. Cancer multicellular spheroids: Volume assessment from a single 2D projection. Comput Methods Programs Biomed [Internet]. 2015;118(2):95–106.

375. Grimes DR, Currell FJ. Oxygen diffusion in ellipsoidal tumour spheroids. J R Soc Interface [Internet]. 2018;15(145).

376. Leung BM, Lesher-Perez SC, Matsuoka T, Moraes C, Takayama S. Media additives to promote spheroid circularity and compactness in hanging drop platform. Biomater Sci [Internet]. 2015 Feb 1;3(2):336–44.

377. Mittler F, Obeïd P, Rulina A V., Haguet V, Gidrol X, Balakirev MY. High-content monitoring of drug effects in a 3D spheroid model. Front Oncol [Internet]. 2017 Dec 11;7(Dec).

378. Schmitz A, Fischer SC, Mattheyer C, Pampaloni F, Stelzer EHK. Multiscale image analysis reveals structural heterogeneity of the cell microenvironment in homotypic spheroids. Sci Rep [Internet]. 2017 Mar 3;7.

379. Smyrek I, Stelzer EHK. Quantitative three-dimensional evaluation of immunofluorescence staining for large whole mount spheroids with light sheet microscopy. Biomed Opt Express [Internet]. 2017 Feb 1;8(2):484.

380. Barbier M, Jaensch S, Cornelissen F, Vidic S, Gjerde K, De Hoogt R, et al. Ellipsoid segmentation model for analyzing light-attenuated 3D confocal image stacks of fluorescent multi-cellular spheroids. PLoS One [Internet]. 2016 Jun 1;11(6).

381. Boutin ME, Voss TC, Titus SA, Cruz-Gutierrez K, Michael S, Ferrer M. A high-throughput imaging and nuclear segmentation analysis protocol for cleared 3D culture models. Sci Rep [Internet]. 2018 Dec 1;8(1).

382. Zhang M, Yuan P, Zhou N, Su Y, Shao M, Chi C. pH-Sensitive N-doped carbon dots-heparin and doxorubicin drug delivery system: preparation and anticancer research. RSC Adv. 2017 Jan 30;7(15):9347–56.

383. Rai S, Singh BK, Bhartiya P, Singh A, Kumar H, Dutta PKK, et al. Lignin derived reduced fluorescence carbon dots with theranostic approaches: Nano-drug-carrier and bioimaging. J Lumin. 2017 Oct 1;190:492–503.

Annex

Chapter 2

Table A2.1 Cytocompatibility studies of carbon dots in cell monolayers

Cell line	Surface passivation	CD synthesis	Concentration	Protocol used for cytotoxicity	Exposure	Toxic dose	Author
A549, MCF-10A and MDA-MB-231	None	Hydrothermal	0.3 – 300 µg/ml	Resazurin reduction	24 hours	~ 300 µg/ml (A549) > 300 µg/ml (MCF-10A and MDA-MB-231)	Vedamalai et al. (2014) [47]
COS-7 and HepG2	Branched PEI	Microwave	2 – 48 µg/ml	MTT assay	24 hours	24 µg/ml (CD-PEI-A) to > 48 µg/ml (CD-PEI-C)	Liu et al. (2012) [50]
HEK 293 and A549	None	Combustion	0 – 250 µg/ml	XTT assay	24 hours	HEK 293: > 250 µg/ml A549: 15.625 µg/ml	Shereema et al. (2015) [45]
NIH/3T3 and A549	None	Hydrothermal	0 – 320 µg/ml	CCK-8	24 and 48 hours	> 320 µg/ml	Zhang et al. (2013) [48]
293T	None	Acid reflux	16 – 500 µg/ml	CellTiter96	24 hours	> 500 µg/ml	Tao et al. (2012) [37]
AD-293	None	Microwave	50 – 200 µg/ml	MTT assay	4 and 24 hours	> 2 mg/ml	Huang et al. (2014) [38]
HeLa	None	Solvent-thermal reaction	0 – 100 µg/ml	MTT assay	24 hours	> 100 µg/ml	Zhou et al. (2014) [54]
HeLa	None	Hydrothermal	0 – 2 mg/ml	CCK-8	24 hours	> 2 mg/ml	Cui et al. (2015) [42]
HeLa	PEG_{1500N}, 4-arm PEG, and PEI-PEG-PEI, conjugates with transferrin	Hydrothermal and acid reflux	? (Unclear)	CellTiter96 and MTS assay	24 hours	? (Unclear)	Li et al. (2010) [52]
L929	Ethylenediamine, diethylamine, triethylamine, 1,4-butanediamine	Microwave	0.5 – 10 mg/ml	MTT assay	Not mentioned	> 10 mg/ml	Zhai et al. (2012) [53]
NIH/3T3	None (Pristine), PEG, PEI	Acid reflux	0 – 400 µg/ml	MTT assay and flow cytometry	24 hours	Pristine: ~300 µg/ml PEG: ~250 µg/ml PEI: ~50 µg//ml	Havrdova et al. (2016) [51]
A549 and 4T1	None	Hydrothermal	0 – 200 µg/ml	MTS assay	24 hours	> 200 µg/ml	Zhang et al. (2015) [49]
EAC	None	Acid reflux	0.1 – 1 mg/ml	MTT and trypan blue staining	24 hours	> 1 mg/ml	Ray et al. (2009) [41]
HepG2	KH_2PO_4	Hydrothermal	0 – 600 µg/ml	MTS assay	72 hours	> 625 µg/ml	Yang et al. (2011) [44]
MCF-7	None	Hydrothermal	0 – 50 µg/ml	MTT assay	24 hours	> 50 µg/ml	Jiang et al. (2015) [40]
MCF-7 and HT-29	PEG_{1500N}	Laser ablation	0 – 200 µg/ml	MTT assay	24 hours	~ 200 µg/ml	Yang et al. (2009) [46]
HeLa and MDA	TTDDA	Hydrothermal	10^{-6} – 2000 µg/ml	Resazurin reduction	1, 3, and 7 days	> 250 µg/ml	Hill et al. (2016) [43]
RAW264.7	N_2H_4 through amidation reaction	Microwave	0 – 100 µg/ml	MTT assay	24 hours	> 100 µg/ml	Xu et al. (2016) [39]
RAW264.7	None	Hydrothermal	0.1 – 1 mg/ml	MTT assay	4 hours	> 1 mg/ml	Parvin and Mandal (2017) [55]

Table A2.2 Biocompatibility studies of carbon dots in animal models

Animal model	Experimental design	Surface passivation	CD synthesis	Concentration	Protocol used for toxicity	Exposure	Author
Mouse	DBA/1	PEG_{1500N}, PPEI-EI	Laser ablation	Subcutaneous: 1 mg/ml (30 µl volume) Extremities: 1 mg/ml (10 µl volume) Intravenous: 2.2 mg/ml (200 µl volume)	In vivo/ex vivo fluorescence imaging and organ dissection (lymph nodes, kidneys, liver)	24 hours	Yang et al. (2009) [59]
Mouse, rat	BALB/c (60), Kunming (50), and Wistar (64)	PEG_{2000N}	Nitric acid oxidation	Intravenous (0.2 – 51 mg/kg body weight depending on the animal)	Blood sample analysis, histology (all major organs), bone marrow micronucleus test, body weight, genotoxicity	1, 3, 7, and 28 days	Wang et al. (2013) [64]
Mouse	BALB/c	None	Acid reflux	Subcutaneous (2 mg/ml, 20 µl volume)	*In vivo* fluorescence imaging, radiolabelling, blood sample analysis, histology (all major organs)	1, 7, 20, 40, and 90 days	Tao et al. (2012) [37]
Mouse	CD-1	PEG_{1500N}	Laser ablation	Intravenous (8 and 40 mg/kg body weight)	ALT and AST release, blood sample analysis, histology (liver, spleen, and kidneys)	1, 7, and 28 days exposure	Yang et al. (2009) [46]
Chicken	CAM assay	None	Combustion	Intravenous (100 µg, unknown volume)	Photomicrographic analysis of vasculature, relative expression of angiogenic cytokines	8 days	Shereema et al. (2015) [45]
Mouse	BALB/c (SCC-7 tumour cell injection)	Diamine-terminated oligomeric PEG_{1500N}	Laser ablation	Intravenous (2.5 mg/kg, 50 µl volume)	Blood sample analysis, NIR fluorescence imaging, histology (all major organs)	2 – 24 hours	Huang et al. (2013) and Sun et al. (2006) [61,188]
Mouse, rat	Wistar, nude mice	N_2H_4 through amidation reaction	Microwave	Intraperitoneally (25 mg/kg, 1 ml volume)	Blood sample analysis, histology (heart, liver, spleen, and kidney), *in vivo* fluorescence imaging	1, 3, and 7 days	Xu et al. (2016) [39]
Nematode and mouse	*C. elegans* and BALB/c	None	Hydrothermal	Nematodes: 1.5 mg/ml mixed with OP50 bacteria) Mice: Intravenous (400 mg/ml with 50 µl volume)	Confocal laser scanning microscopy, *in vivo* spectral imaging	5 minutes – 24 hours	Singh et al. (2018) [69]
Zebrafish	Wild-type (6 days old)	None	Acid reflux	Microinjection of heart or abdominal cavity (0.5 – 5 µg/ml, total volume 5 nL)	*In vivo* fluorescence imaging, confocal laser scanning microscopy, immunohistochemistry	30 minutes – 2 days	Li et al. (2016) [72]
Rat	Sprague Dawley	None	Hydrothermal	Intravenous (20 - 40 mg/kg, 1 ml volume)	*In vivo* computerized tomography, blood sample chemistry, histology (all major organs)	7 and 30 days	Zhang et al. (2015) [49]
Mouse	BALB/c (CT26 tumour)	PEG_{800}	Hydrothermal	Intratumorally (4 mg/kg body weight)	*In vivo* fluorescence imaging,	1 hour – 11 days	Zheng et al. (2016) [67]
Zebrafish	Embryos and larvae	None	Hydrothermal	Soaking embryo in solution (2.5 mg/ml, 5 ml volume) and microinjections (0.5 – 2.5 mg/ml, 2 µl volume)	Confocal laser scanning microscopy, brightfield microscopy	3 – 72 hours	Kang et al. (2015) [71]
Mouse	BALB/c (HeLa cell injection)	None	Microwave	Intravenous (8 mg/ml, 200 µl volume)	*In vivo* and *ex vivo* fluorescence imaging	24 hours	He at al. (2015) [65]

Table A2.3 CD conjugates for drug delivery

Components (CD)	Cargo	Application	Loading strategy	Effect	Author
Citric acid and PEG	Gold nanoparticles	Antifungal	Host-guest chemistry	Size-dependent toxicity	Priyadarshini et al. (2018) [108]
Aminoethylethanolamine (AEEA)	Lauryl betaine	Antimicrobial	Crosslinking (EDC/NHS)	Multicolour fluorescence, enhanced and selective toxicity in Gram-negative bacteria	Yang et al. (2016) [104]
Citric acid and ethylenediamine	Ampicillin	Antimicrobial	Crosslinking (EDC/NHS)	Enhanced antimicrobial activity	Jijie et al. (2018) [111]
Gum arabic	Ciproflaxin	Antimicrobial	Electrostatic interactions	High loading capacity and controlled drug release	Thakur et al. (2014) [228]
L-arginine	Silver nitrate	Antimicrobial	Host-guest chemistry	Enhanced antimicrobial activity	Fang et al. (2019) [107]
Citric acid and bPEI	Protoporphyrin IX	Antimicrobial	Crosslinking (EDC/Me-Imidazole)	Sustained drug release over several days and high loading capacity	Kumari et al. (2019) [109]
Sulfobetaine-functionalized poly((vinylpyrrolidone)	IR825	Antimicrobial	Electrostatic interactions	pH-dependent drug release and NIR-activated photothermal effect	Kang et al. (2019) [114]
Chitosan	Tetracycline	Antimicrobial	Electrostatic interactions	pH-dependent drug release and effective drug loading	Gogoi and Chowdhury (2014) [105]
Carbon nanopowder and EDA	None	Antimicrobial	None	Intrinsic ROS production and A-PDT with ambient light illumination	Meziani et al. (2016) [110]
Ethanol and sodium hydroxide	PEG, folic acid, and doxorubicin	Chemotherapy	Crosslinking (EDC/NHS) and π–π stacking interactions	pH-dependent drug release with real-time monitoring, increased stability	Tang et al. (2013) [130]
Beer	Doxorubicin	Chemotherapy	Electrostatic interactions	Controlled drug release	Wang et al. (2015) [121]
Sorbitol	Folic acid, BSA, doxorubicin	Chemotherapy	Electrostatic interactions	High loading efficiency and therapeutic efficiency	Mewada et al. (2014) [131]
Hydroxybutyric acid	Doxorubicin	Chemotherapy	Hydrazone-based bonding	Nucleus-targeting and increased efficiency (*in vitro* and *in vivo*)	Yang et al. (2019) [122]
Carbon nanopowder	Transferrin and doxorubicin	Chemotherapy	Crosslinking (EDC/NHS)	Increased uptake and cytotoxicity	Li et al. (2016) [129]
Carbon nanopowder	Transferrin and epirubicin or temozolomide	Chemotherapy	Crosslinking (EDC/NHS)	Synergistic effect between drugs and improved accumulation	Hettiarachchi et al. (2019) [125]
Citric acid and ethylenediamine	Doxorubicin	Chemotherapy	Electrostatic interactions	High loading efficiency and increased cytotoxicity	Kong et al. (2018) [120]
Citric acid and diethylenetriamine	Cisplatin(IV)	Chemotherapy	Crosslinking (EDC/NHS)	Charge-convertible behaviour, improved efficiency, prolonged blood circulation, controlled release	Feng et al. (2016) [118]
Gum arabic	Gold nanorods and doxorubicin	Chemotherapy	Crosslinking (DCC/NHS) and electrostatic interactions	High loading efficiency and rapid burst release under NIR irradiation	Pandey et al. (2013) [124]
Polyethyleneimine and ethanol	Doxorubicin	Chemotherapy	Hydrophobic interactions	Controlled drug release and nucleus targeting	Wang et al. (2017) [87]
Milk	Doxorubicin	Chemotherapy	Hydrophobic interactions	pH-sensitive drug release, lower cytotoxicity to non-cancer cells, increased uptake	Yuan et al. (2017) [123]
Citric acid and polyene polyamine	Oxaliplatin	Chemotherapy	Crosslinking (EDC/NHS)	Simultaneous imaging and therapeutic effect, real-time monitoring of distribution	Zheng et al. (2014) [132]
Chitosan	Heparin and doxorubicin	Chemotherapy	Crosslinking (EDC/NHS) and electrostatic interactions	pH-dependent drug release profiles and increased stability	Zhang et al. (2017) [382]
Bovine serum albumin	Doxorubicin	Chemotherapy	Hydrophobic interactions	pH-dependent drug release and rapid cellular uptake	Wang et al. (2013) [134]
Citric acid and urea	Doxorubicin	Chemotherapy	Electrostatic interactions	pH-dependent drug release, increased stability and cellular uptake	Zeng et al. (2016) [119]
Glucose, ethylenediamine, and phosphoric acid	Doxorubicin	Chemotherapy	Electrostatic and hydrophobic interactions	Intranuclear delivery, high drug loading capacity, pH-dependent release	Gong et al. (2016) [135]
Citric acid, urea, and zeolitic imidazolate	5-fluorouracil	Chemotherapy	Electrostatic interactions	pH-dependent drug release	He et al. (2014) [137]
Citric acid	Manganese ferrite nanoparticles and doxorubicin	Chemotherapy	π–π stacking interactions	pH-dependent drug release and functionality as MRI and fluorescence contrast agents	Fahmi et al. (2015) [139]
Glucose and chitosan	Doxorubicin	Chemotherapy	π–π stacking and electrostatic interactions	pH-dependent drug release, high loading capacity and colloidal stability	Wang et al. (2017) [136]
Citric acid and diethylenetriamine	Cisplatin(IV) and RGD peptide	Chemotherapy	Crosslinking (EDC/NHS and HBTU/DIPEA)	Enhanced intracellular uptake and therapeutic efficiency	Feng et al. (2016) [133]
Hydrazine	Aspirin	Drug delivery	Host-guest chemistry	*In vitro* and *in vivo* anti-inflammatory effect	Xu et al. (2016) [39]
Lignosulfonate lignin powder	Curcumin	Drug delivery	Hydrophobic interactions	Increased solubility, high drug loading and rapid uptake	Rai et al. (2017) [383]

Table A2.4 CD conjugates for PDT and PTT

Components (CD)	Cargo	Application	Loading strategy	Effect	Author
α-cyclodextrin, PEG, and folic acid	Zinc phthalocyanine	PDT	π–π stacking interactions	Targeted delivery, increased efficiency and distribution	Choi et al. (2014) [152]
Citric acid or sucrose and ethylenediamine	Protoporphyrin IX	PDT	Host-guest chemistry and crosslinking (EDC/NHS)	Decreased dark toxicity, increased efficiency at lower drug concentrations, increased solubility	Aguilar Cosme et al. (2019) [151]
Carbon nanopowder	Protoporphyrin IX	PDT	Crosslinking (EDC/NHS)	PDT under two-photon excitation, high loading efficiency	Fowley et al. (2013) [144]
Chitosan	Diketopyrrolopyrrole	PDT	Host-guest chemistry	Maintains photostability under laser irradiation and high biocompatibility	He et al. (2018) [149]
Sodium hyaluronate	Chlorin e6 and hyaluronate	PDT	Crosslinking (EDC/NHS)	Increased transdermal delivery and efficiency	Beack et al. (2015) [153]
Soot and PEG 2000N	Chlorin e6	PDT	Crosslinking (EDC/NHS)	Improved singlet oxygen generation, water stability, and efficiency	Huang et al. (2012) [155]
Citric acid and ethylenediamine	PtPor (Tetraplatinated porphyrin complex)	PDT	Electrostatic interaction	Improved singlet oxygen generation, cellular uptake, and efficiency	Wu et al. (2018) [145]
PEG800	CyOH	PTT	Host-guest chemistry	Improved accumulation in target site and tumour inhibition	Zheng et al. (2016) [67]
Citric acid and urea	5-aminolevulinic acid, coumarin, and triphenylphosphonium	PDT	Crosslinking (Bromide)	Two-photon triggered drug release, low compound toxicity	Wu et al. (2015) [146]
Citric acid and urea	Carbon nitride, PpIX-PEG-RGD polymer	PDT	π–π stacking interactions	Improved efficiency in hypoxic environment, water-splitting effect, and targeted delivery	Zheng et al. (2016) [158]
Citric acid and polyethyleneimine	Chlorin e6	PDT/PTT	Crosslinking (DMT/MM)	High efficiency with low loading ratios and dual PDT/PTT effect with NIR excitation	Sun et al. (2019) [165]
Manganese(II) phthalocyanine and DSPE-PEG	None	PDT	None	*In situ* oxygen generation and enhanced efficiency in hypoxic environment	Jia et al. (2018) [157]
Polythiophene benzoic acid	None	PDT and PTT	None	Intrinsic singlet oxygen generation and heat conversion	Ge et al. (2016) [163]
Polythiophene	Sodium dodecylbenzenesulphonate	PDT	Ionic self-assembly	Intrinsic singlet oxygen generation and efficient *in vivo* distribution	Jia et al. (2017) [164]
Carbon nanopowder	Nitroaniline derivative NO photodonor	PDT	Crosslinking (EDC/NHS)	Two-photon excitation and nitric oxide production in hypoxic environment	Fowley et al. (2015) [156]
Magnetic Fe_3O_4 nanocrystals	Doxorubicin	PTT / drug delivery	Host-guest chemistry and interactions with surface	Magnetic responsive properties, detection by magnetic resonance imaging, heat conversion and NIR-triggered drug release	Wang et al. (2014) [159]
EDTA·2Na	Copper chloride	PDT/PTT	Doping	NIR absorption, high biocompatibility, dual effect	Guo et al. (2018) [160]
Citric acid and urea	Prussian Blue nanoparticles	PTT	Host-guest chemistry	NIR absorption, high photothermal efficiency, stable heat production	Peng et al. (2018) [161]
Chitosan	Triphenylporphyrin	PDT	Host-guest chemistry	Increased photostability and rapid cellular uptake leading to efficient PDT effect	Li et al. (2016) [150]
Chitosan, ethylenediamine, and mercaptosuccinic acid	Rose Bengal	PDT	Crosslinking (DCC/HOBt)	Mitochondria targeting capability, rapid cellular uptake, decreased cytotoxicity	Hua et al. (2017) [154]
m-phenylenediamine and *l*-cysteine	Protoporphyrin IX	PDT	Crosslinking (DCC/HOBt)	Nucleus targeting capability, enhanced PDT effect, increased blood circulation time	Hua et al. (2018) [264]
Quasi-gemini glucose surfactant	Tungsten sulphide	PTT	CD synthesis on WS_2 nanorod surface	Targeted PTT effect under NIR irradiation and multicolour fluorescence imaging	Nandi et al. (2017) [162]

Table A2.5 CD conjugates in gene delivery

Components (CD)	Cargo	Loading strategy	Effect	Author
Citric acid, ethylenediamine, and 2-bromoisobutyric acid	pGL3-control (loaded with PDMAEMA-b-PMPDSAH)	Electrostatic interactions	Decreased protein adsorption, superior stability in blood, higher transfection efficiency with serum	Cheng et al. (2015) [175]
Glycerol and branched PEI 25k	pGL3-control	Electrostatic interactions	Decreased cytotoxicity and increased transfection efficiency	Liu et al. (2012) [50]
PEI 600	pUC19, pEGFP-N1, or siRNA (survivin)	Electrostatic interactions	Increased transfection and gene silencing efficiency	Wang et al. (2017) [87]
PEG-200 and polyethyleneimine	siRNA (NF7, SRC, or GFP)	Electrostatic interactions	Effective gene silencing and high pH stability	Das et al. (2015) [176]
Glycerol and PEI	siRNA (cyclin B1 or EGFR)	Electrostatic interactions	Selective targeting for lung cancer and increased gene silencing efficiency	Wu et al. (2016) [179]
Citric acid and bPEI25k	pGL3	Electrostatic interactions	Significantly lower cytotoxicity after transgene expression	Pierrat et al. (2015) [181]
Citric acid, PPD, and HPAP	pGL3	Electrostatic interactions	Decreased protein adsorption, GSH-triggered release	Zhao et al. (2018) [174]
Citric acid and branched PEI	siRNA (Cy5 and GFP)	Electrostatic interactions	Enhanced intracellular uptake, decreased immune response to siRNA delivery *in vivo*	Kim et al. (2017) [172]
Arginine and glucose	pSOX9	Electrostatic interactions	Intracellular tracking, high transfection efficiency	Cao et al. (2018) [169]
Citric acid and tryptophan	siRNA (survivin) with PEI	Electrostatic interactions	Rapid intracellular uptake and improved gene silencing efficiency	Wang et al. (2014) [227]
PEI	EGFP (plasmid)	Electrostatic interactions	Intracellular tracking, high transfection efficiency	Hu et al. (2014) [182]
Alginate	pTGF-β1	Electrostatic interactions	Strong DNA condensation ability, low toxicity, and high transfection efficiency	Zhou et al. (2016) [170]
Glucose, PEI, and benzyl bromide	pRL-CMV	Electrostatic interactions	High transfection efficiency	Dou et al. (2015) [171]
Tetrafluoroterephthalic acid and 1.8k bPEI	EGFP (plasmid)	Electrostatic interactions	Maintained transfection efficiency at high serum concentrations and low DNA dose	Zuo et al. (2018) [186]
Candle soot	miRNA (miR124a)	Electrostatic interactions	High biocompatibility and rapid intracellular uptake	Noh et al. (2013) [183]
Unspecified	siRNA (*Tnfα*)	Crosslinking (sulfo-SMCC)	High biocompatibility and transfection efficiency	Liu et al. (2019) [173]
Glucose and tetraethylene pentamine	siRNA (Cy3)	Electrostatic interactions	High pH stability and enhanced gene silencing	Wang et al. (2018) [185]
Folic acid (CDs loaded on a chitosan – graphene oxide construct)	pDNA-TNF-α	Electrostatic interactions	High transfection efficiency *in ovo*	Jaleel et al. (2019) [178]

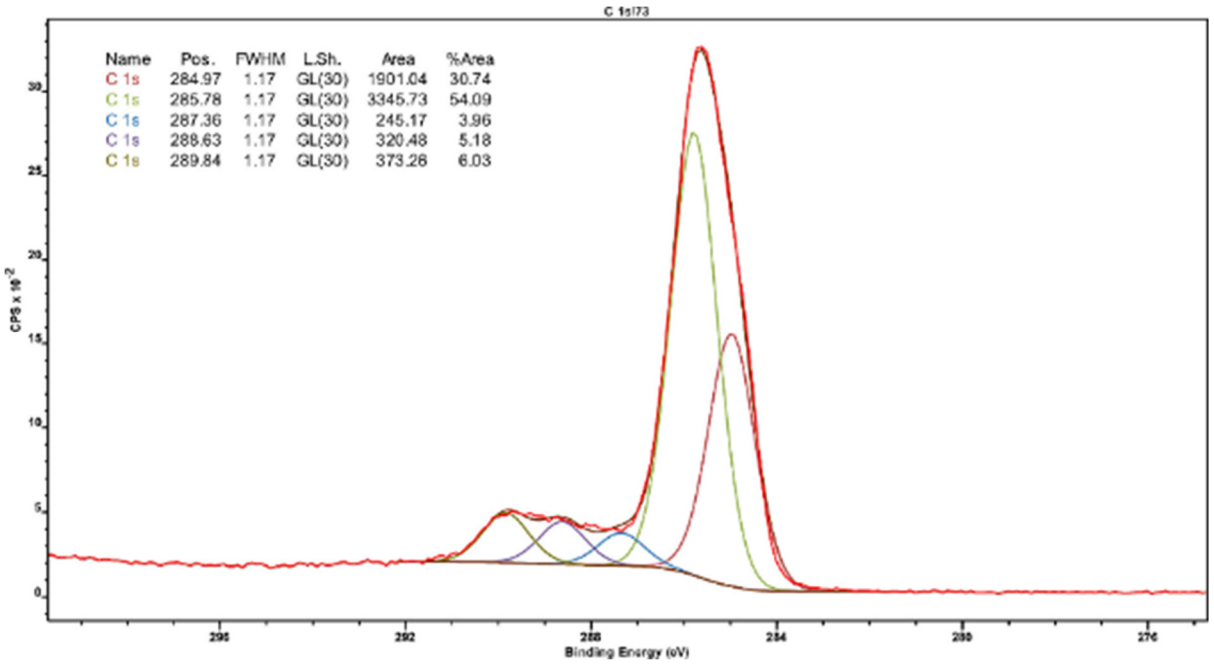

XPS C 1s scan of PpIX.

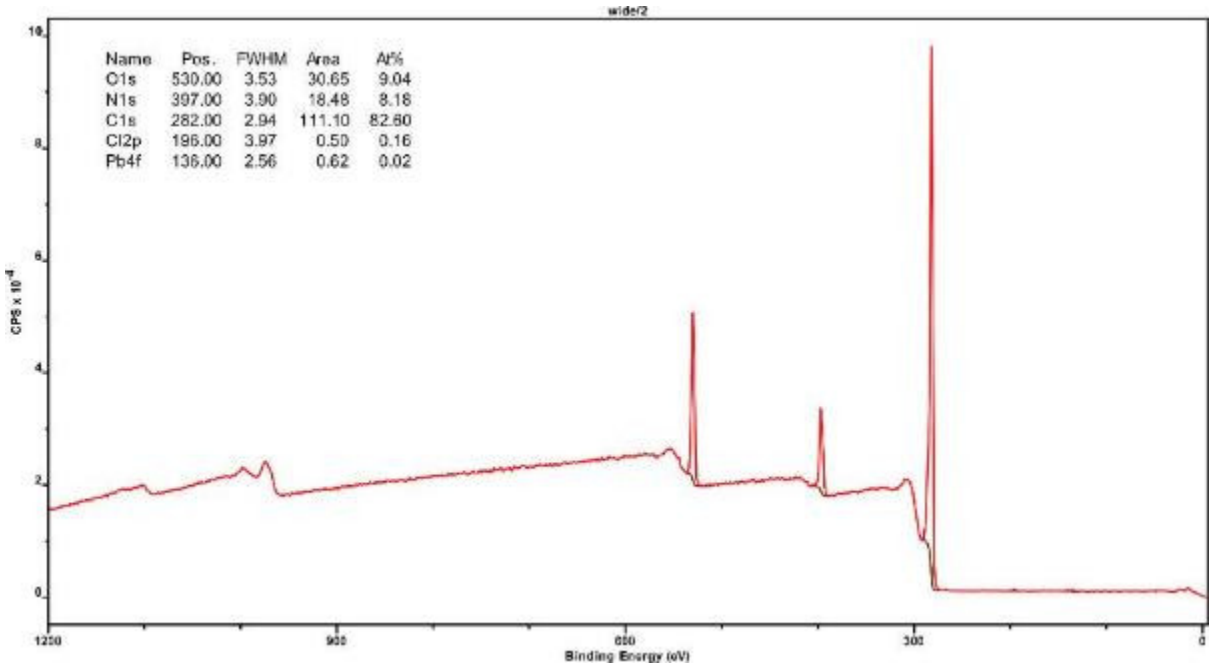

XPS survey scan of PpIX.

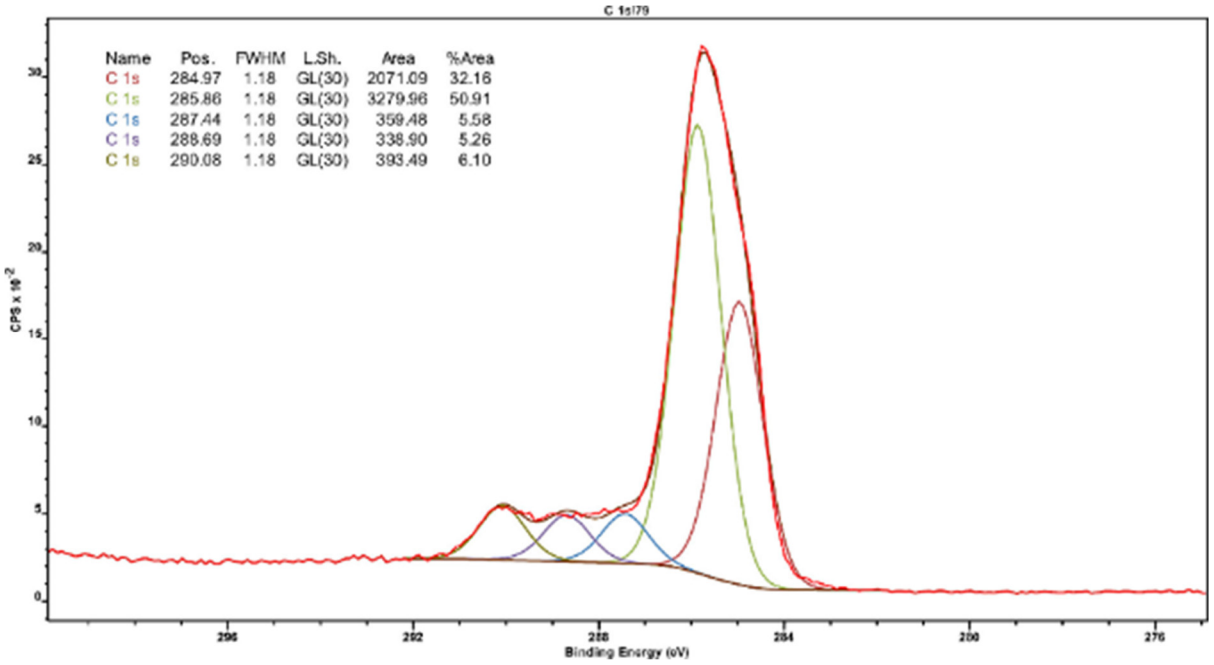

XPS C 1s scan of PpIX-CD.

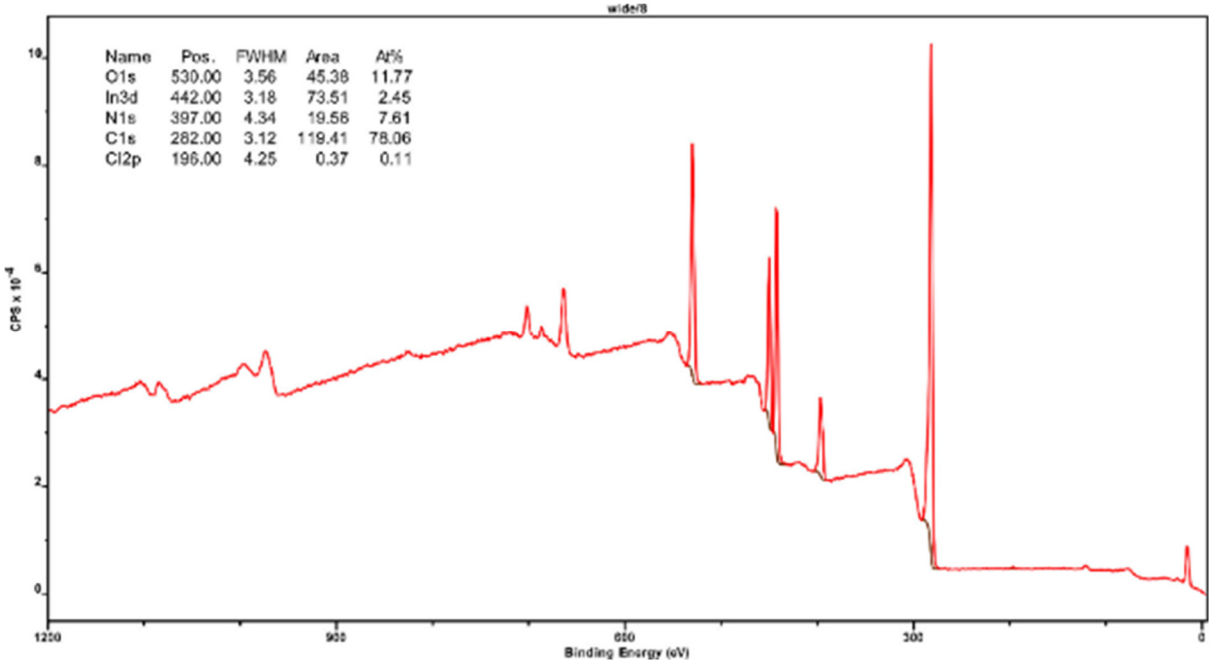

XPS survey scan of PpIX-CD.

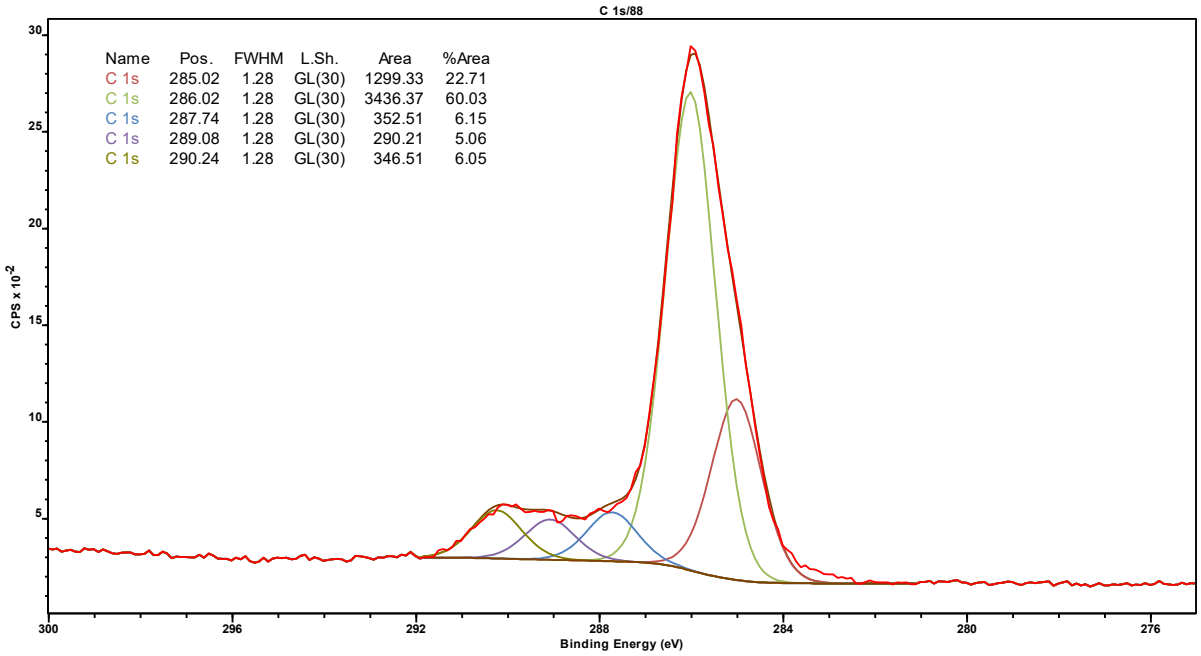

XPS C 1s scan of (PpIX-CD)p

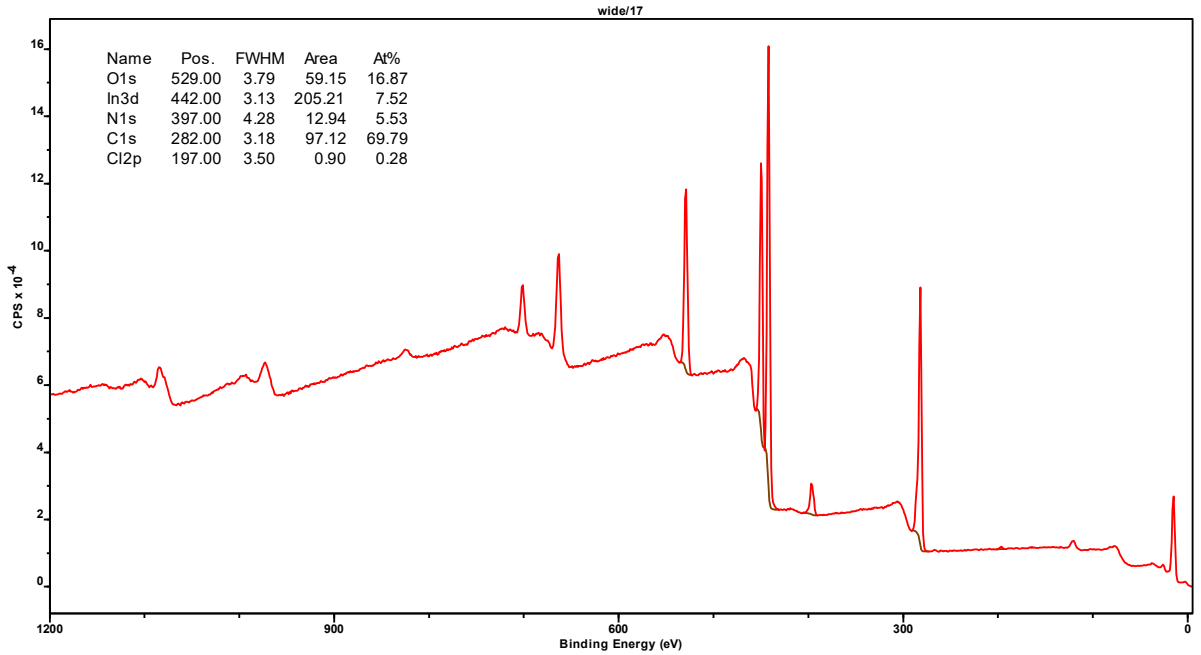

XPS survey scan of (PpIX-CD)p

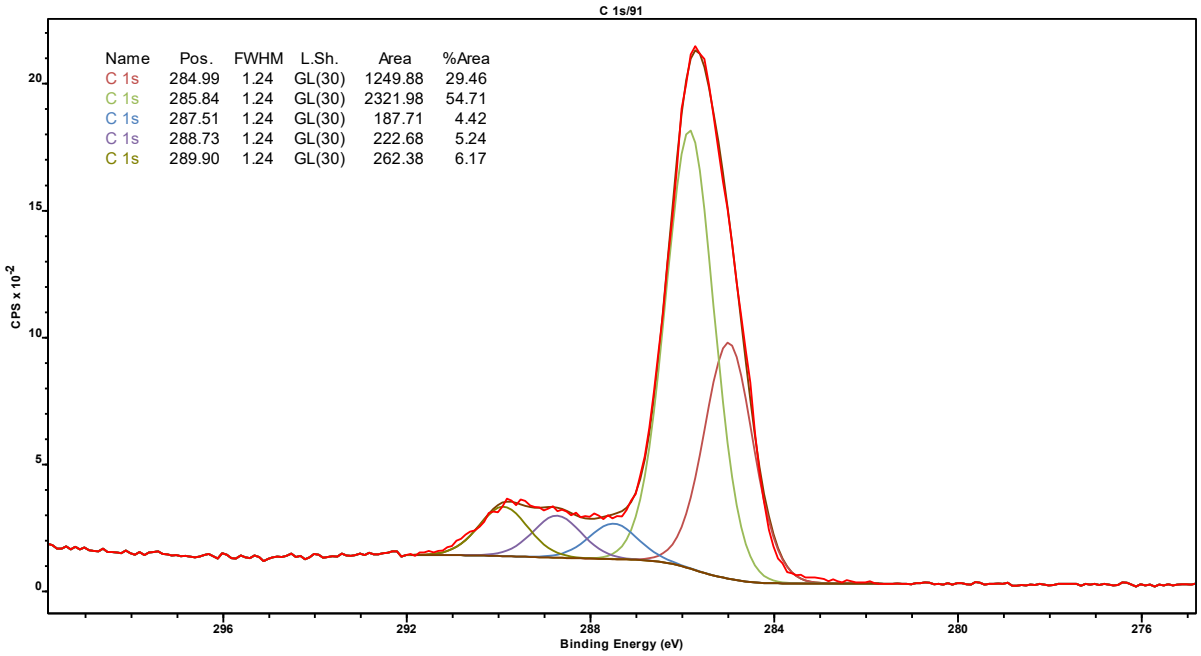

XPS C 1s scan of PpIX@CD

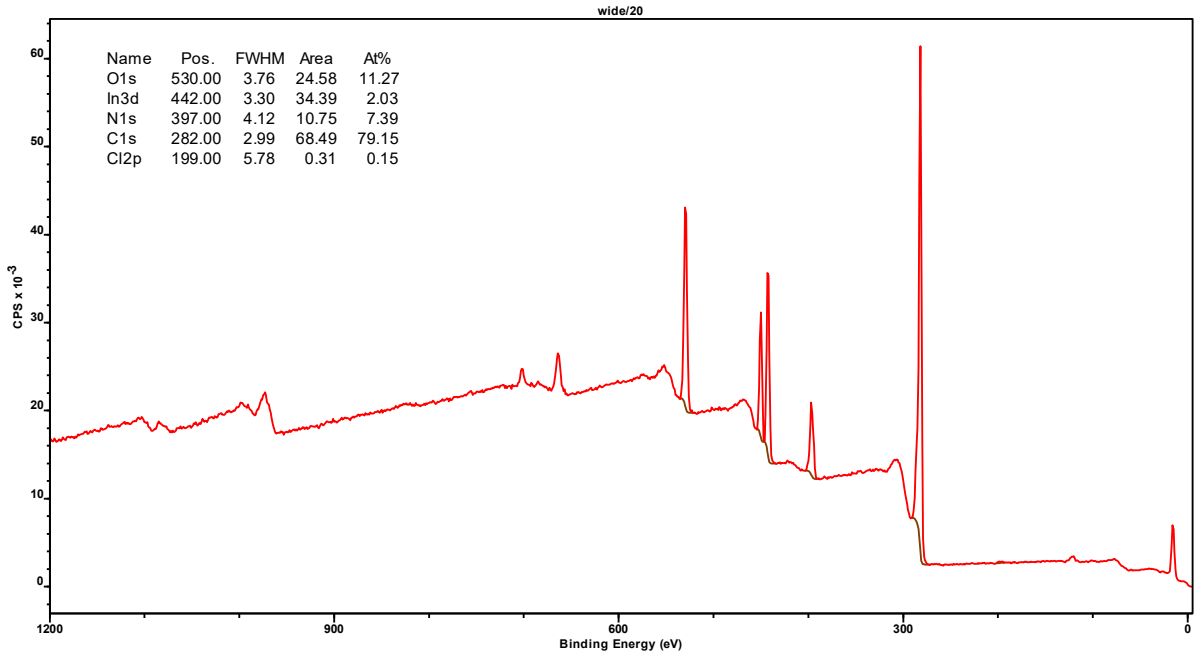

XPS survey scan of PpIX@CD

Sample	FWHM	B.E. (eV)	%At Conc.	B.E. (eV)	%At Conc.	B.E. (eV)	%At Conc.	B.E. (eV)	%At Conc.	B.E. (eV)	%At Conc.
PpIX	1.17	285.0	30.7	285.8	54.1	287.4	4.0	288.6	5.2	289.8	6.0
PpIX-CD	1.18	285.0	32.1	285.9	50.9	287.5	5.6	288.8	5.3	290.1	6.1
(PpIX-CD)p	1.28	285.0	22.7	286.0	60.0	287.5	6.2	288.5	5.1	290.1	6.1
PpIX@CD	1.25	285.0	28.4	285.8	56.0	287.6	4.4	288.6	5.0	28.9	6.2

High resolution C1s spectra. Curve fitting of the C 1S high resolution spectra of PpIX and CD-conjugates.

Sample	O	In	C
Indium foil	26.8	19.4	53.8

XPS of indium foil. Surface composition (atomic%) of indium foil.

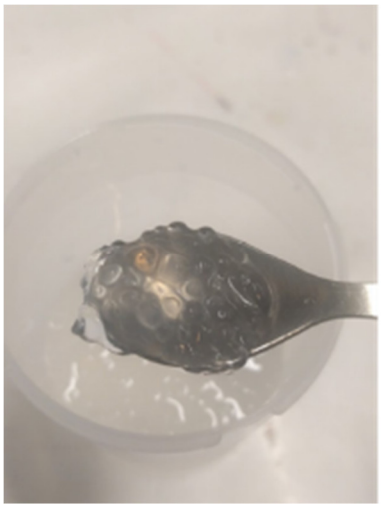

Synthesis of Eu-doped CDs with microwave pyrolysis. Europium was used to crosslink alginic acid at 10 mM. Hydrogel pyrolysis resulted in CD formation.

Acetone did not produce efficient PpIX crosslinking with EDC/NHS, causing precipitation and sample aggregation.

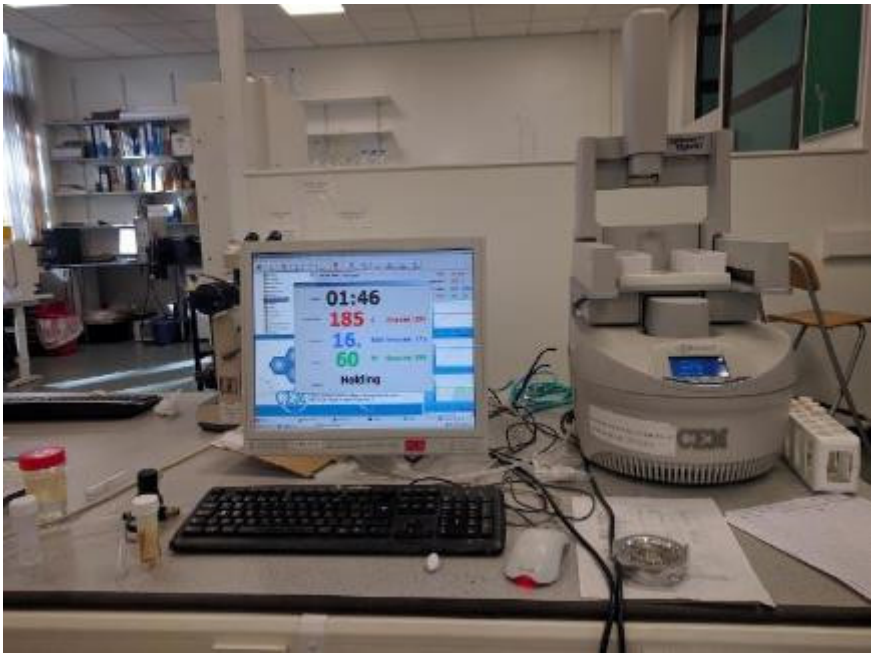

Discover SP microwave reactor setup.

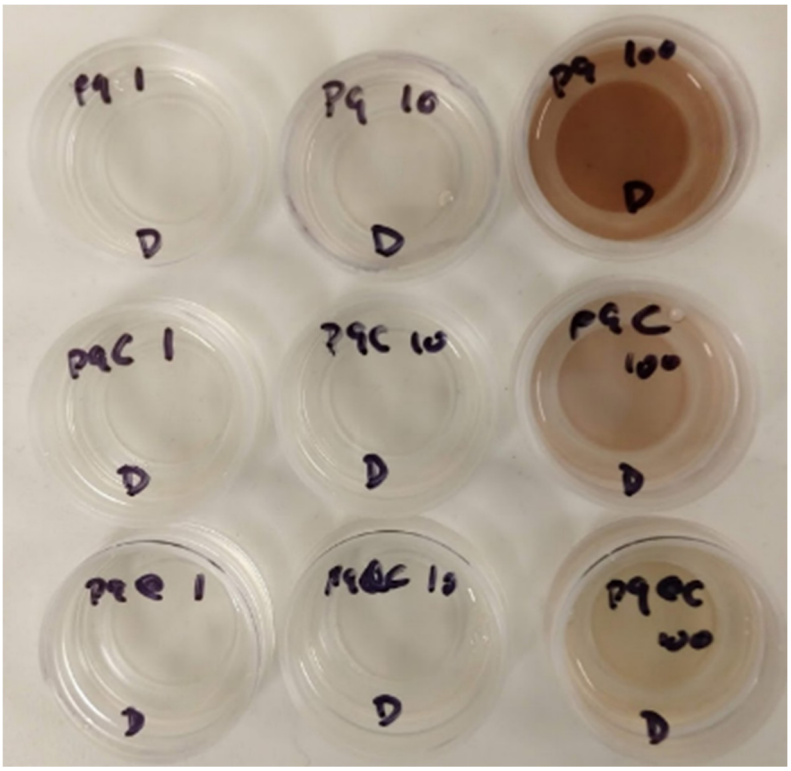

PpIX shows significantly lower stability in water. Precipitation can be seen at 4 hours in concentrations of 100 µg/ml.

Chapter 4

Table A4.1 – Light activated toxicity at 48 hours post irradiation.

ug/ml	PpIX		PpIX-CD		(PpIX-CD)p		PpIX@CD		No light	
	Average	SEM	Average	SEM	Average	SEM	Average	SEM	Average	SEM
0.5	78.76	2.33	72.30	3.91	89.54	2.03	78.95	5.57	100.00	0.57
1	59.85	4.64	64.21	4.80	67.86	2.03	68.89	5.08	100.00	0.57
2.5	46.27	1.12	49.72	3.57	64.17	0.83	42.35	2.09	100.00	0.57
5	42.56	0.94	41.80	3.67	62.58	1.84	40.21	1.71	100.00	0.57
10	41.32	0.97	39.81	1.71	56.64	3.41	39.96	1.37	100.00	0.57

Table A4.2 – Light activated toxicity at 48 hours post irradiation.

ug/ml	PpIX		PpIX-CD		(PpIX-CD)p		PpIX@CD		No light	
	Average	SEM	Average	SEM	Average	SEM	Average	SEM	Average	SEM
0.5	103.17	3.92	96.97	1.44	98.34	1.93	102.60	1.57	100.00	0.57
1	66.57	6.09	89.33	2.57	100.26	0.74	89.64	2.05	100.00	0.57
2.5	43.43	1.53	50.07	2.83	92.14	3.89	42.47	0.65	100.00	0.57
5	41.49	1.94	40.93	2.30	85.51	3.96	39.88	0.48	100.00	0.57
10	40.10	2.88	38.47	0.93	69.06	8.31	40.00	0.50	100.00	0.57

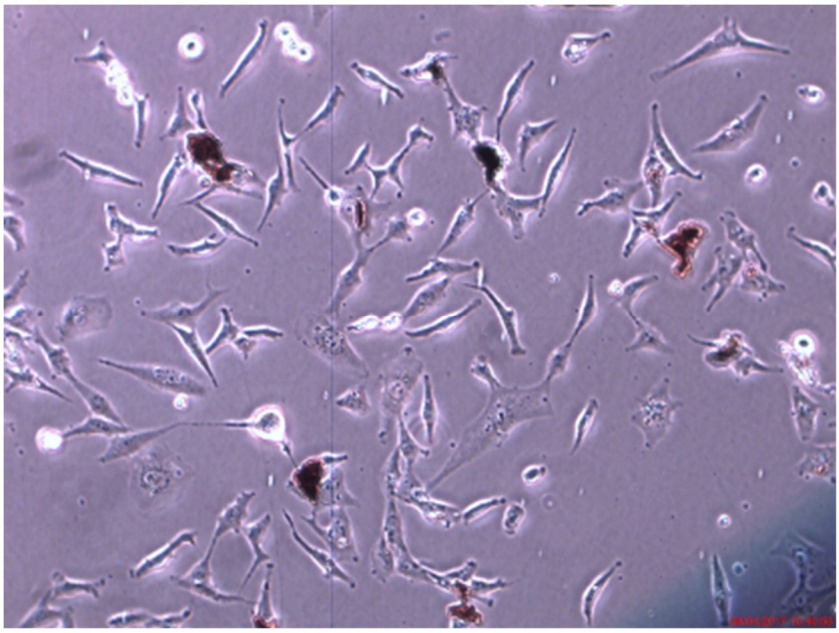

PpIX-loaded conjugates quickly aggregate in cell monolayers at concentrations >50 µg/ml.

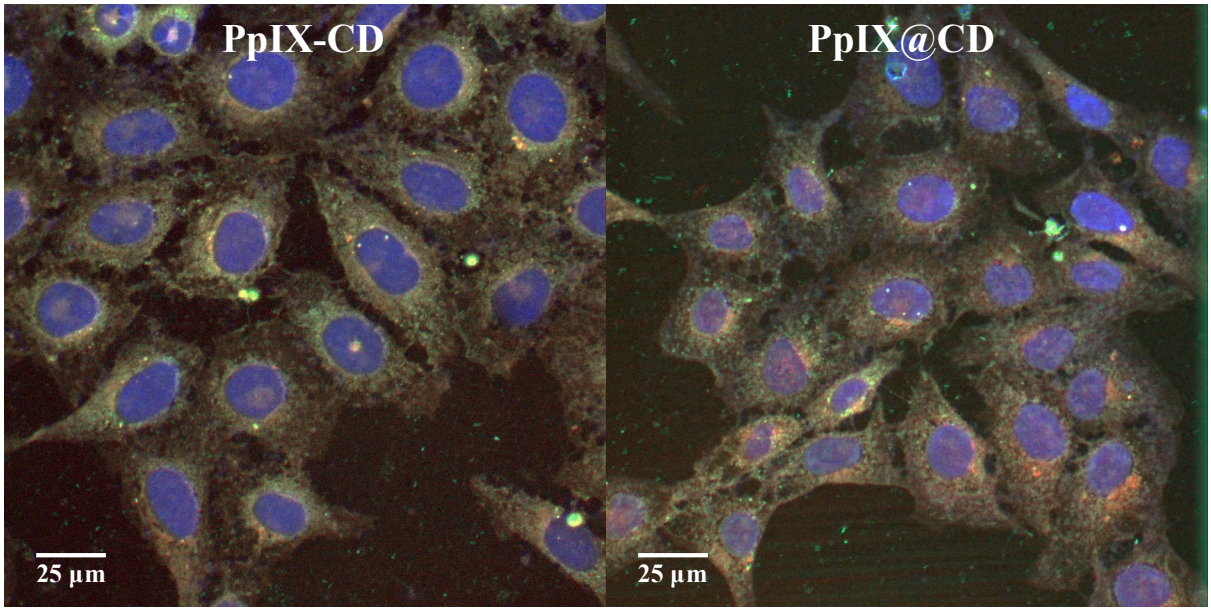

CSLM imaging of PpIX-CD and PpIX@CD with 250 µg/mL.

Chapter 5

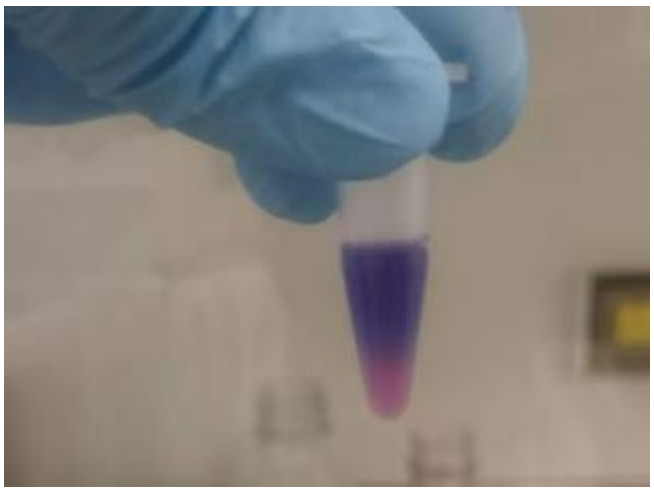

Initial tests with resazurin reduction with spheroids. Standardisation was difficult due as the assay could not be done within agar-coated wells, which absorbed resazurin. Spheroid movement into microcentrifuge plates proved difficult and time-consuming.

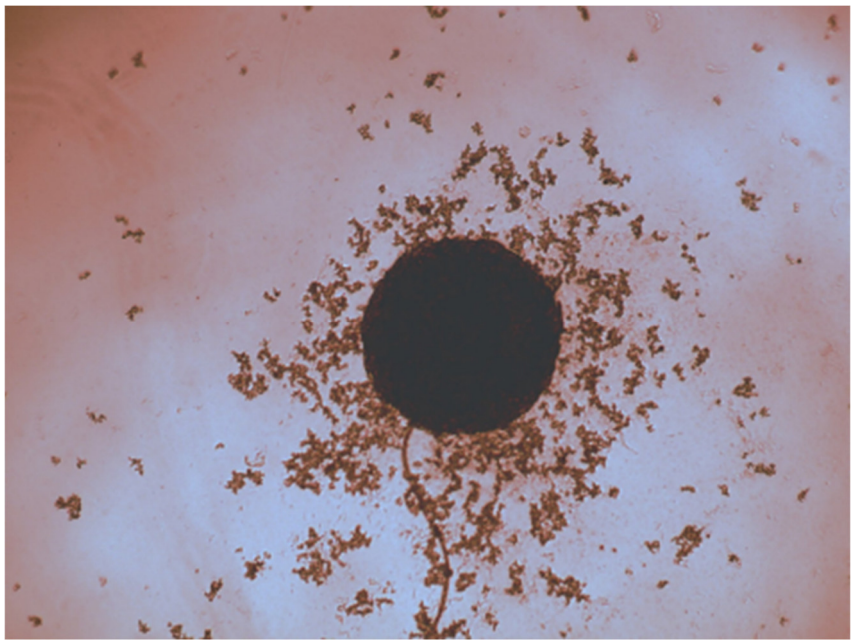

Monolayer PDT parameters (single 3-minute exposure at 0.87 $mW.cm^2$) do not cause significant damage in spheroids.

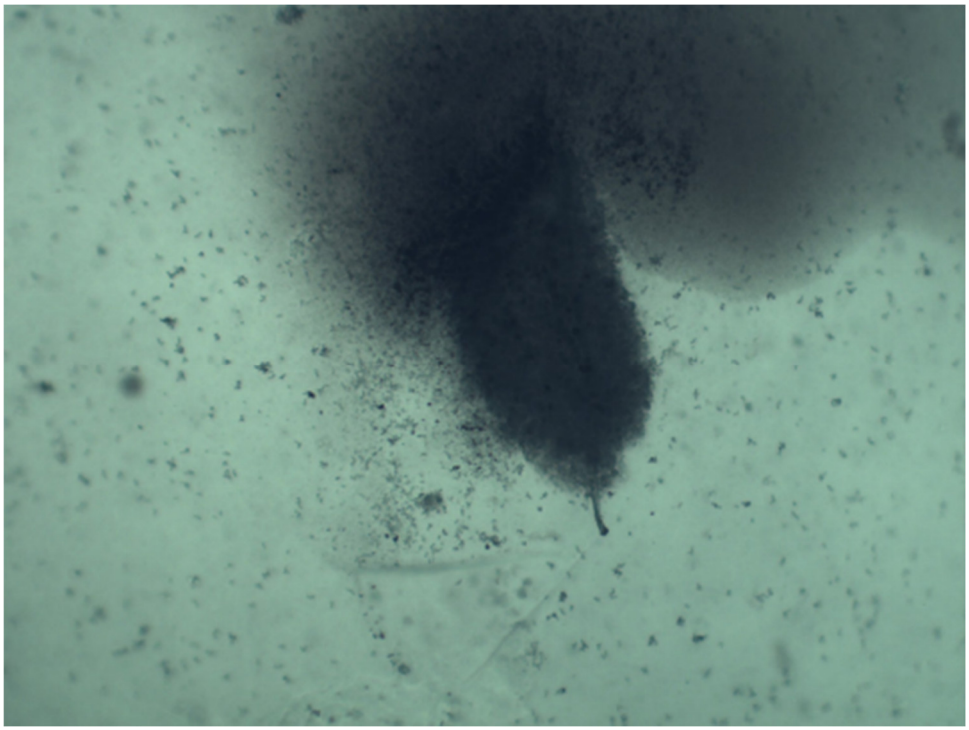

Spheroid damage (2LT, PpIX-CD 5 μg/ml) caused deformation and required care during manipulation.

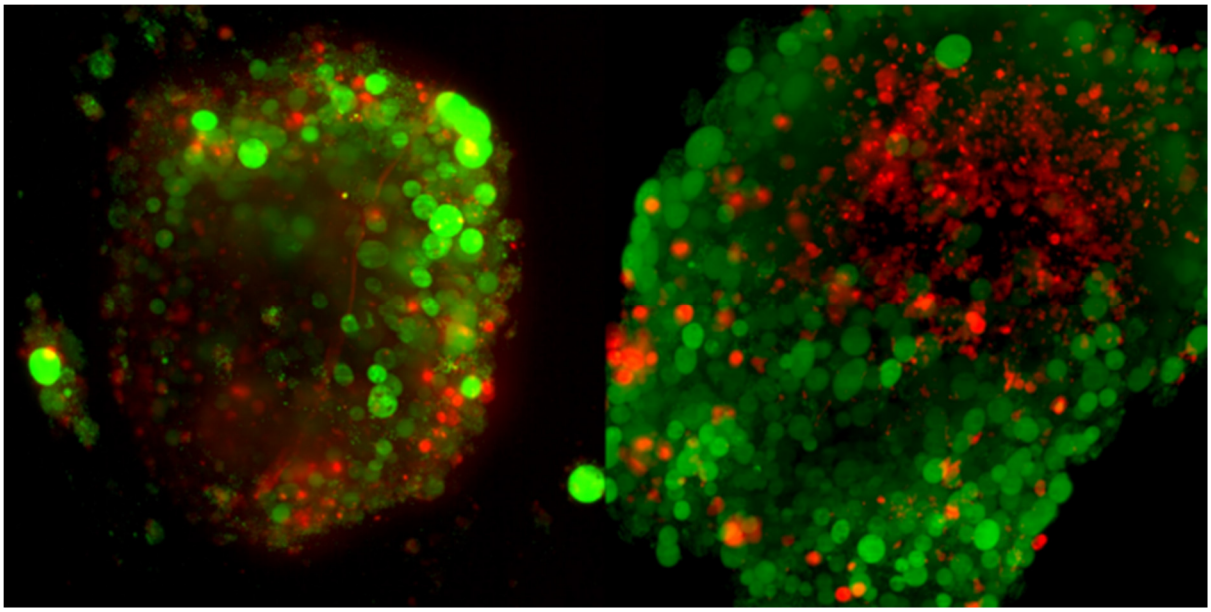

Live/dead staining required optimisation and LSFM filter adjustment (left – before, right – after).

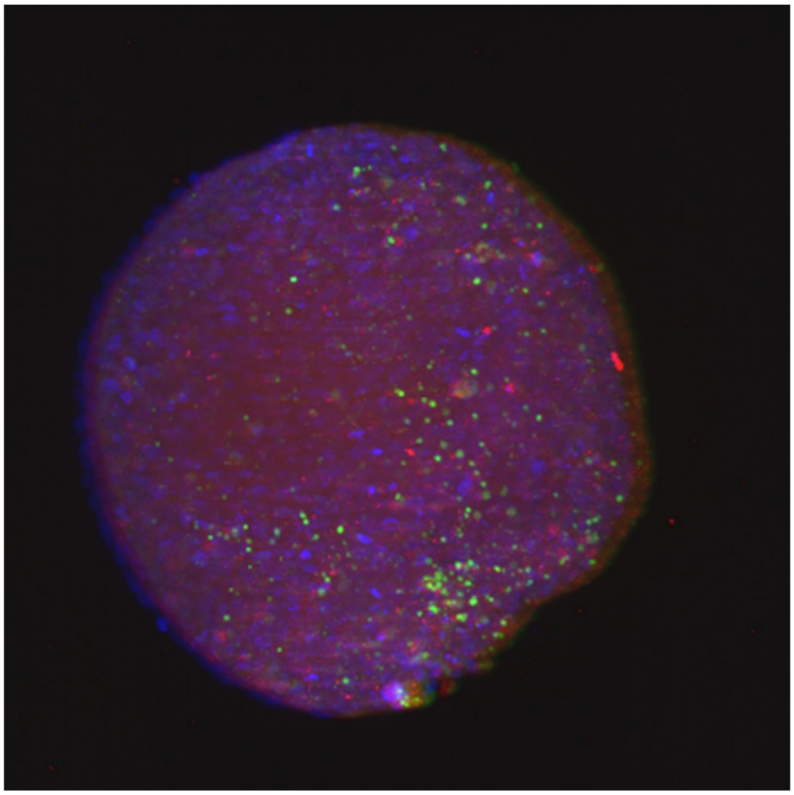

Spheroids show limited autofluorescence without staining in LSFM.

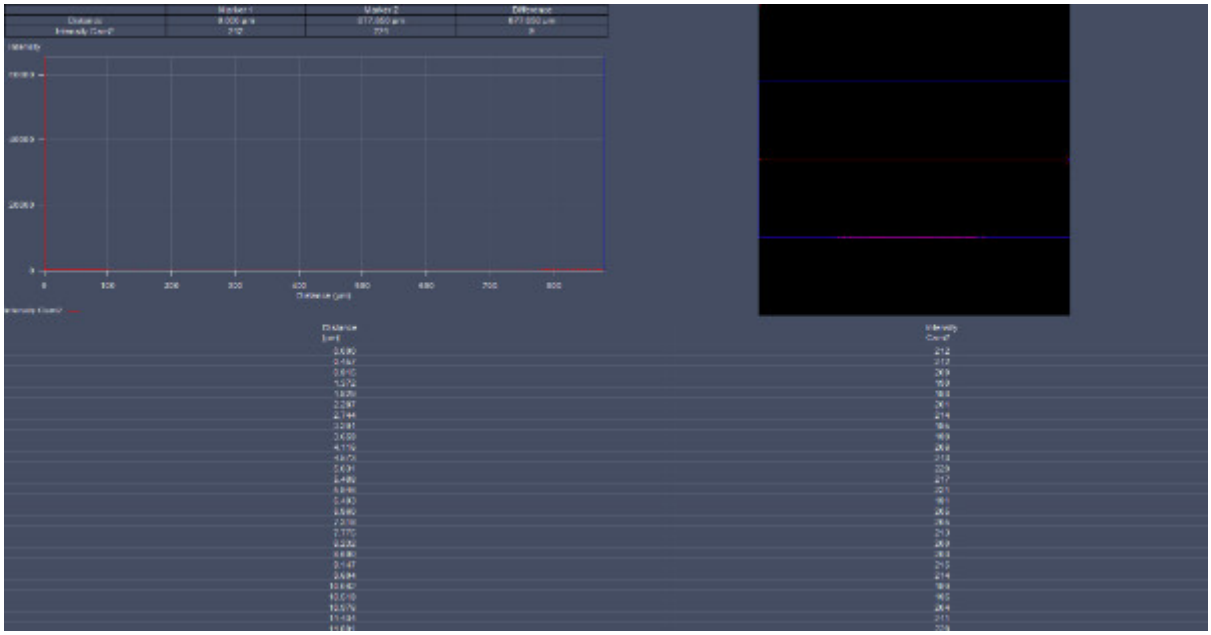

Selection of LSFM z-slice for control spheroid during drug uptake evaluation.

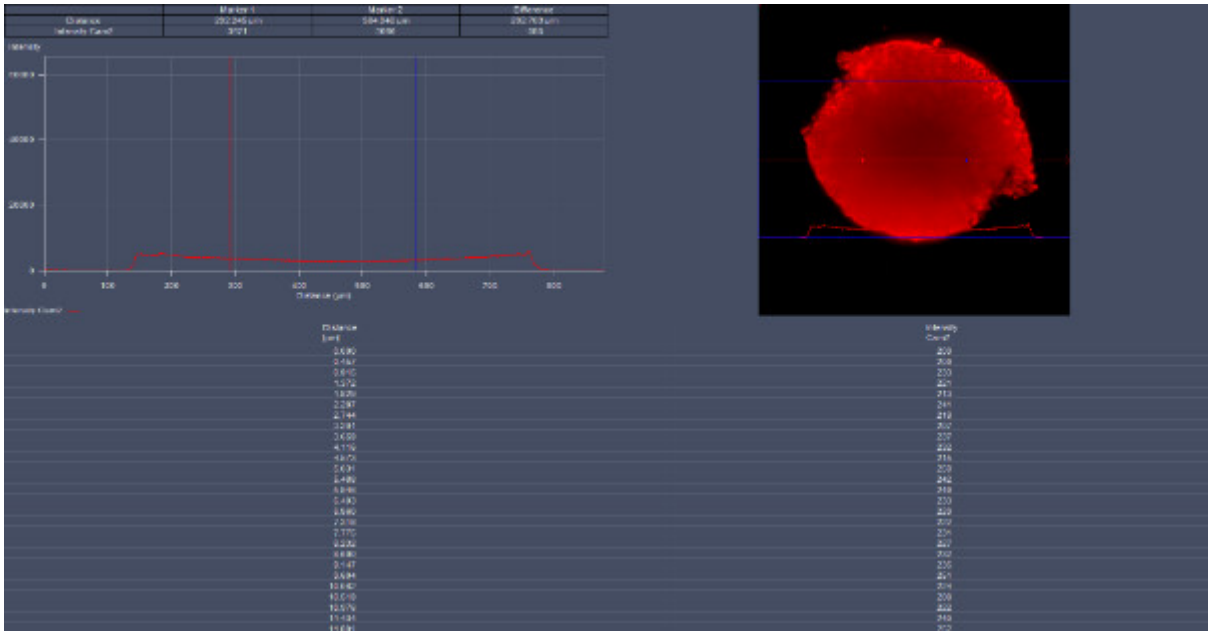

Selection of LSFM z-slice for 10 µg/ml PpIX spheroid during drug uptake evaluation.

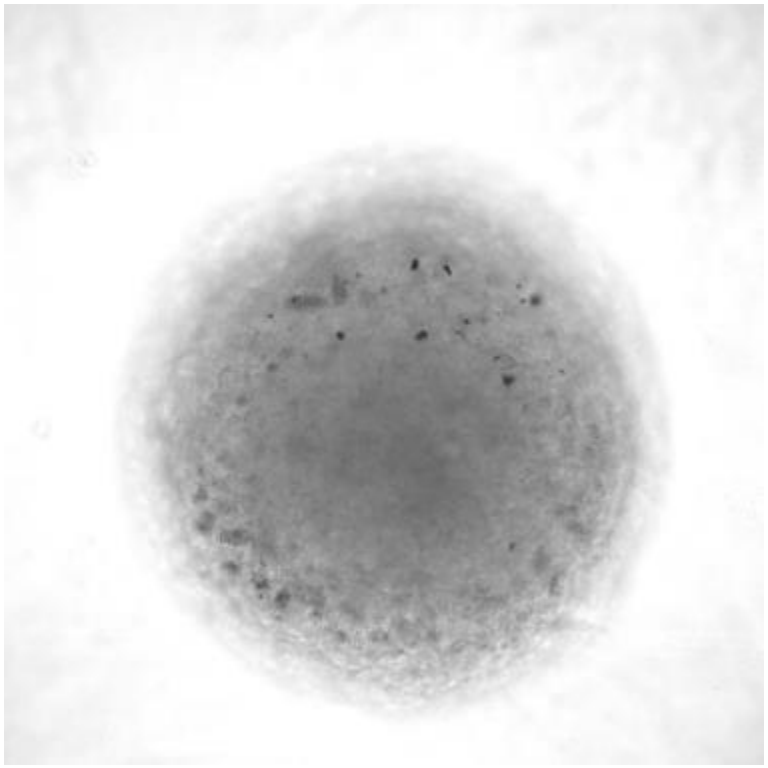

Transmission image obtained in LSFM showing PpIX aggregation on the spheroid surface at 5 µg/ml.

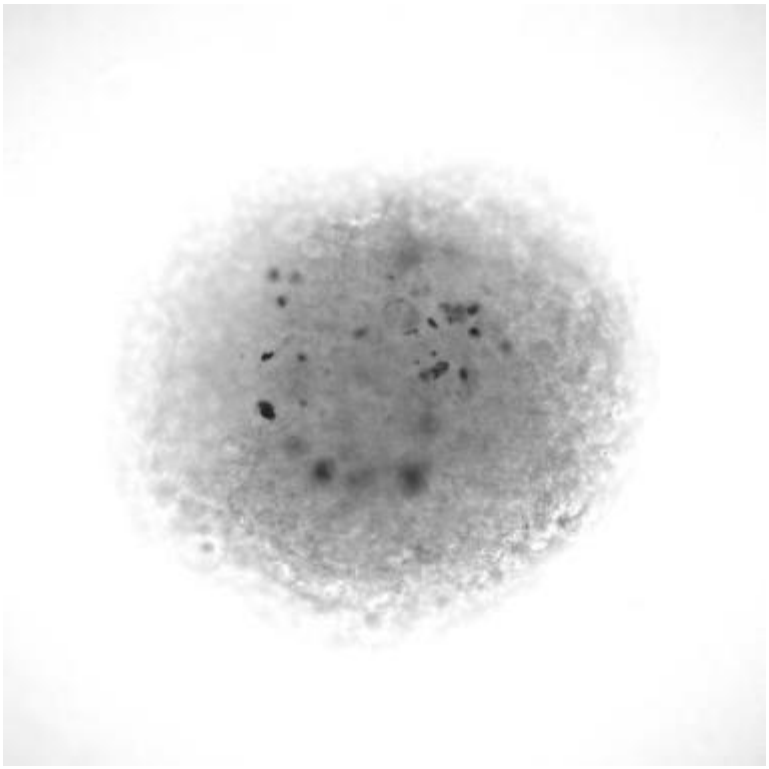

Transmission image obtained in LSFM showing PpIX aggregation on the spheroid surface at 10 μg/ml.

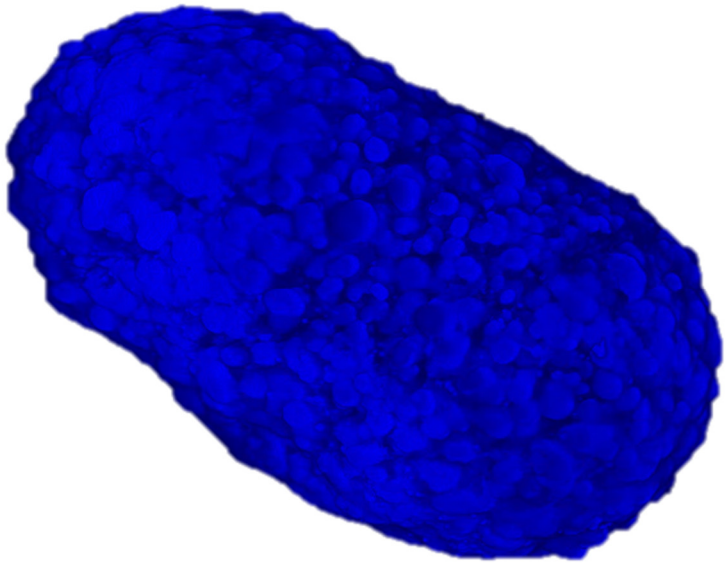

Spheroid treated with 5 μg/mL PpIX@CD rendered using mixed 3D projection in LSFM. The sample was stained with DAPI and phalloidin prior to imaging.

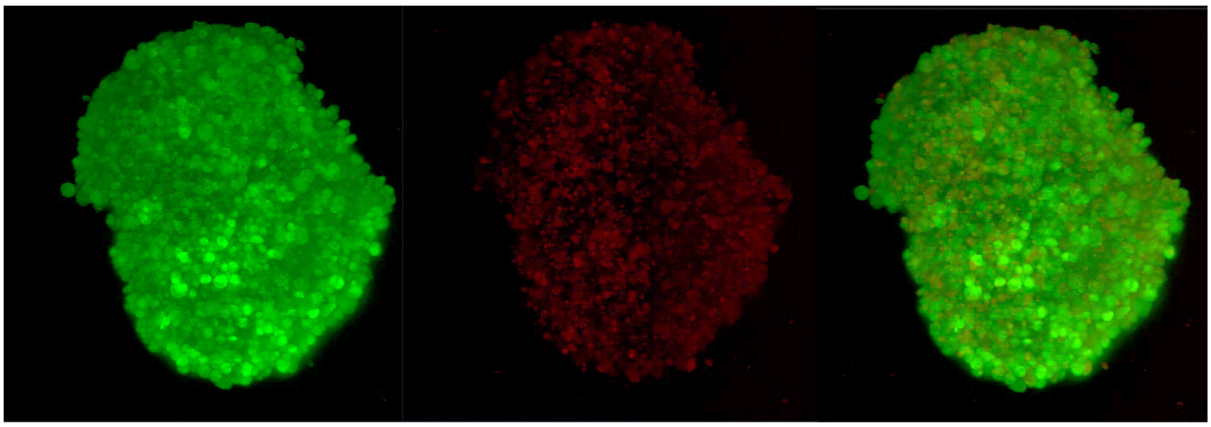

Control spheroids showed low frequency of cell death. Dead cells were concentrated in the inner region which corresponds to the hypoxic core.

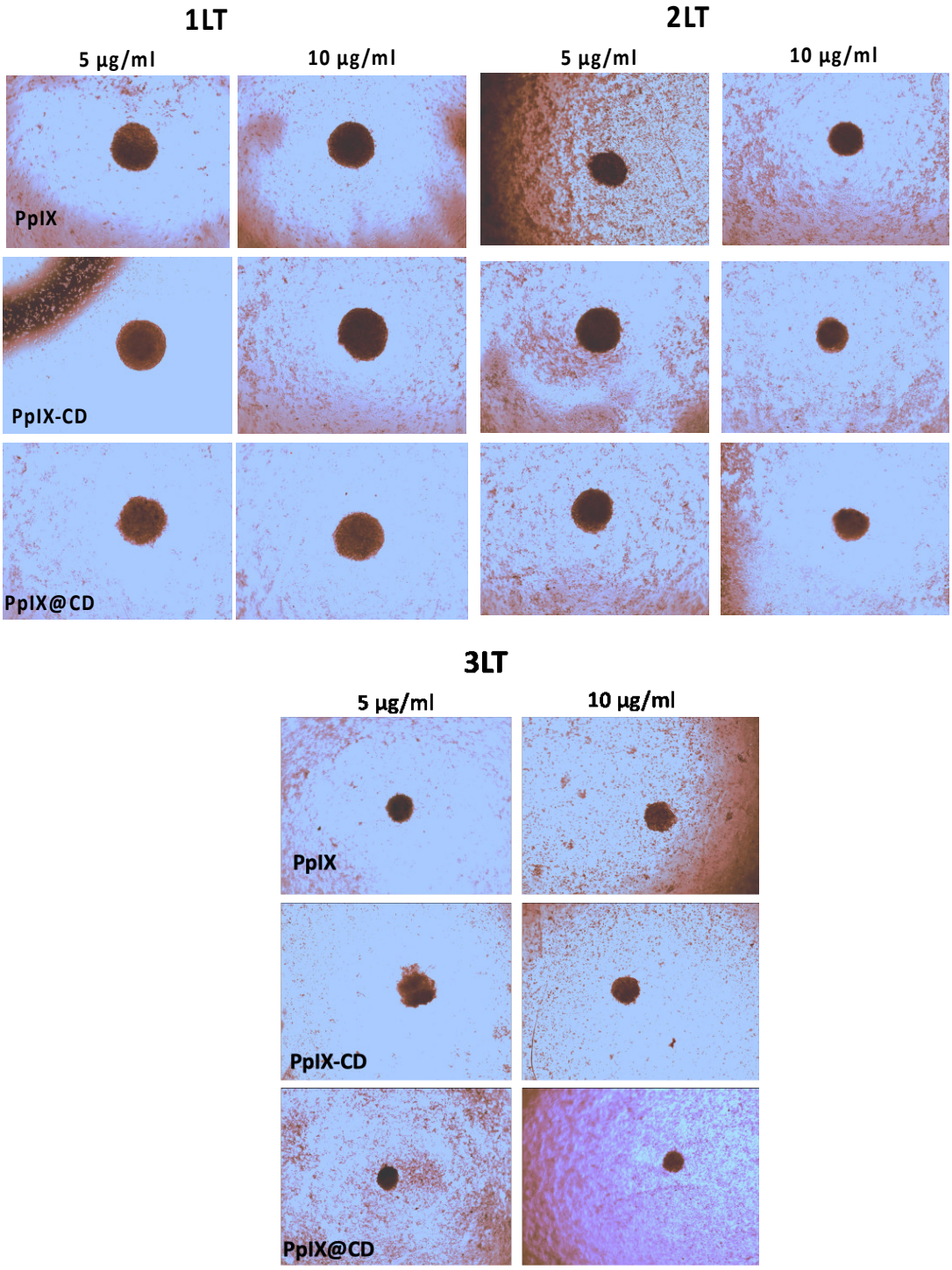

Representative light microscopy images of all PDT combinations.

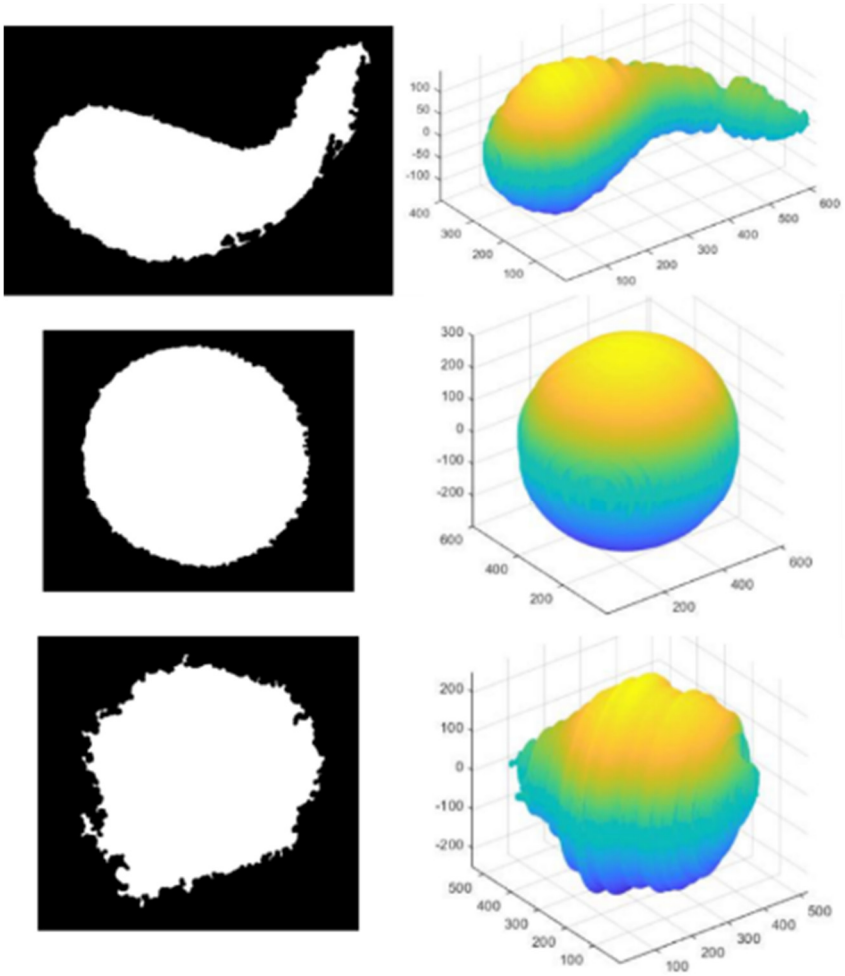

ReViSP projections of spheroid images can be used to predict morphology without the use of LSFM.

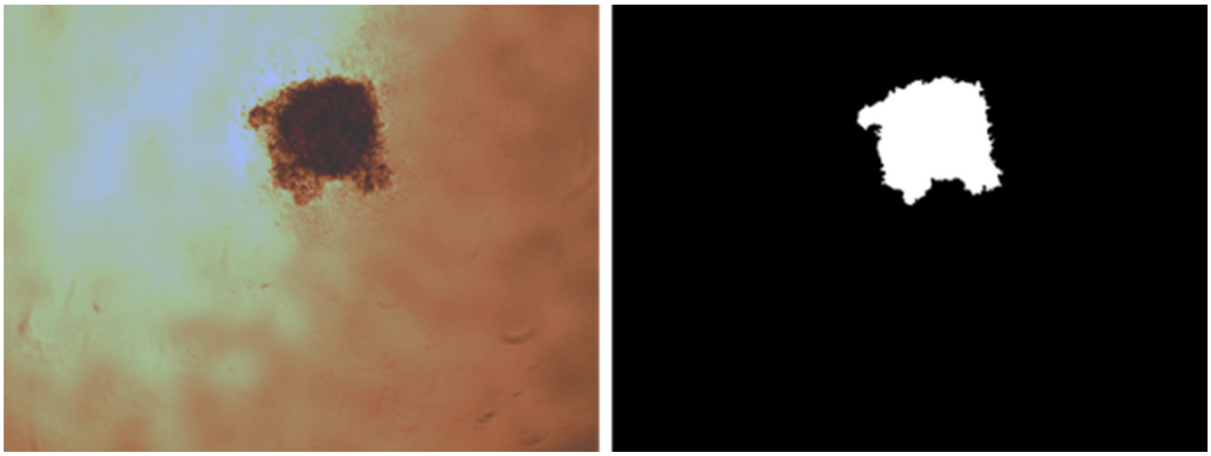

Example of image processing. Masks are made after initial binary image conversion and automatic segmentation.

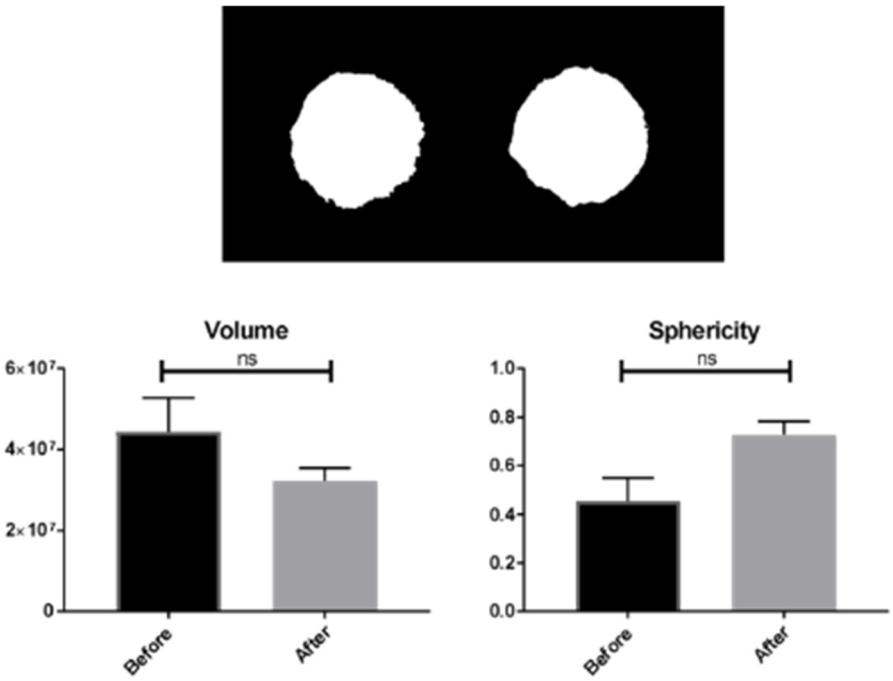

Control spheroids do not show significant changes to morphological parameters area and diameter after debris clearing.

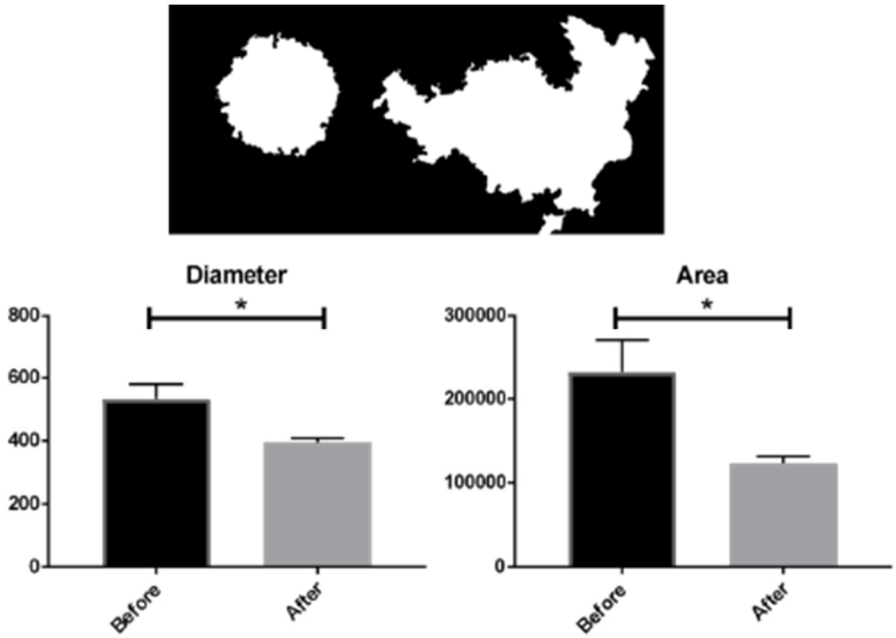

Treated spheroids do show significant changes to morphological parameters area and diameter after debris clearing.